Design and optimization of the Grating Monochromator for Soft X-Ray Self-Seeding FELs

Dissertation

zur Erlangung des Doktorgrades an der Fakultät

für Mathematik, Informatik und Naturwissenschaften

Fachbereich Physik

der Universität Hamburg

vorgelegt von

SVITOZAR SERKEZ

Hamburg

2015

The work described in this thesis is done at the Photon Science division of
Deutsches Elektronen-Synchrotron, a Research Centre of the Helmholtz Association.

Acknowledgments

First of all, I would like to express the deepest appreciation to my supervisors:

Evgeni Saldin for noticing me as a summer student and offering me a great opportunity to join his team. Also for a time we spent discussing things both related and not related to physics and giving me the basis for understanding all I learned during PhD studies. He was always ready and glad to answer my questions. Thanks to him I had a lot of research freedom during my studies.

Henry Chapman for accepting me as a responsible professor, his interest in the subject and support of my trips to SLAC.

I greatly appreciate all my referees and members of the examination commission for their time and efforts.

Also I thank **Edgar Weckert** for hiring me in HASYLAB (now FS-PS) during my studies and **Massimo Altarelli** with **Serguei Molodtsov** for their interest in this work.

Thanks to **Sven Reiche** I could carry out simulations with the GENESIS code. **Ilya Agapov** and **Vitali Kocharyan** gave lots of useful tips including ones about FEL simulations. **Olexandr Yefanov** shared his knowledge of coherent imaging and corresponding simulation techniques. **Gianluca Geloni** helped me a lot by reading text of this thesis and giving numerous advises.

I appreciate **Daniele Cocco** and **Yiping Feng** for designing an excellent monochromator. Also I thank **Jacek Krzywinski, Zhirong Huang** and **Daniel Ratner** for inviting me to an LCLS SXRSS monochromator commissioning and keeping me busy there. It was a great time and experience to collaborate with them along with **Yuantao Ding, Paul Emma, Claudio Emma, Kun Fang, Jerry Hastings, Gabriel Marcus, Juhao Wu** and the rest of SXRSS team.

Finally I'd like to thank my parents **Bogdan Serkez** and **Uliana Sus** for their patience and support, and **Yaryna Mykhyalyshyn** for being part of my life.

Kurzfassung

Design und Optimierung des Gitter Monochromators für Soft X-Ray Self-Seeding FELs

Freie Elektronen Laser (FEL) sind bahnbrechende Lichtquellen der vierten Generation. FELs für den Röntgenspektralbereich (XFEL) ermöglichen völlig neuartige Experimente, von denen die meisten Naturwissenschaften profitieren können. Selbstverstärkte spontane Emission (Self-amplified spontaneous emission, SASE) ist der Standart Arbeitsmodus eines FELs. Der Strahlungspuls ensteht durch spontane Emission aus dem Elektronenbündel und wird verstärkt bis Sättigung eintritt. Die SASE FEL Strahlung hat üblichweise mangelhafte Eigenschaften bezüglich ihrer spektralen Bandbreit oder longitudinalen Kohärenz. Self-seeding ist ein vielversprechender Ansatz die SASE Bandbreite von XFELs signifikant zur schmälern und tranformationslimitierte Pulse zu erzeugen. Self-seeding wird durch die Monochromatisierung des Strahlungspulses während der FEL Verstärkung erreicht.

Nach der erfolgreich demonstrierten self-seeding Konfiguration im harten Röntgenspektrum an der Linear Coherent Light Source (LCLS), soll nun auch das self-seeding für den weichen Röntgenspektralbereich erweitert werden.

Hier werden numerische Methoden vorgestellt, um die Monochromatorleistung für das soft X-ray self-seeding (SXRSS) zu simulieren. Sie erlauben eine Anfang bis Ende self-seeding FEL Simulation. Basierend auf dieser Methode wurde die Leistung des LCLC self-seeding Betriebs in Einklang mit den Experiment simuliert. Weiterhin wurde das bei SLAC entwickelte SXRSS Monochromatordesign für die SASE3 Undulator Station des European XFEL.

Das optische System wurde mit Hilfe von Gausstrahlen Optik, wellenoptischer Propagation und Ray Tracing behandelt um die Leistung des Monochromator zu beschreiben. Wellenoptische Analysen berücksichtigen die Wellenfront kohärenter FEL Quellen, Aberrationen dritter Ordnung und Höhenfehler jedes optischen Elements.

Das Monchromatordesign basiert auf einen toroidialen Gitter mit variablem Linienabstand bei einem festen Eintrittswinkel ohne Eintrittsspalt. Im optimierte Spektralbereich zwischen $300 - 1200$ eV erreicht man Auflösungen von über 7000. Der vorgeschlagene Monochromator besteht aus drei Spiegeln und dem Gitter. Weiterhin wird die Anfang zu Ende Simulation als Fallstudie der self-seeded European XFEL Leistungsfähigkeit vorgestellt. Sie zeigt Laserpuls Leistungen im TW-Bereich und einer im Vergleich zu konventionellen SASE Pulsen 80-fach höheren spektralen Leistungsdichte.

Abstract

The emergence of Free Electron Lasers (FEL) as a fourth generation of light sources is a breakthrough. FELs operating in the X-ray range (XFEL) allow one to carry out completely new experiments that probably most of the natural sciences would benefit. Self-amplified spontaneous emission (SASE) is the baseline FEL operation mode: the radiation pulse starts as a spontaneous emission from the electron bunch and is being amplified during an FEL process until it reaches saturation. The SASE FEL radiation usually has poor properties in terms of a spectral bandwidth or, on the other side, longitudinal coherence. Self-seeding is a promising approach to narrow the SASE bandwidth of XFELs significantly in order to produce nearly transform-limited pulses. It is achieved by the radiation pulse monochromatization in the middle of an FEL amplification process.

Following the successful demonstration of the self-seeding setup in the hard X-ray range at the LCLS, there is a need for a self-seeding extension into the soft X-ray range.

Here a numerical method to simulate the soft X-ray self seeding (SXRSS) monochromator performance is presented. It allows one to perform start-to-end self-seeded FEL simulations along with (in our case) GENESIS simulation code. Based on this method, the performance of the LCLS self-seeded operation was simulated showing a good agreement with an experiment. Also the SXRSS monochromator design developed in SLAC was adapted for the SASE3 type undulator beamline at the European XFEL.

The optical system was studied using Gaussian beam optics, wave optics propagation method and ray tracing to evaluate the performance of the monochromator itself. Wave optics analysis takes into account the actual beam wavefront of the radiation from the coherent FEL source, third order aberrations and height errors from each optical element.

The monochromator design is based on a toroidal VLS grating working at a fixed incidence angle mounting without both entrance and exit slits. It is optimized for the spectral range of $300 - 1200$ eV providing resolving power above 7000. The proposed monochromator is composed of three mirrors and the grating. Start-to-end simulation as a case study of the self-seeded European XFEL performance with a proposed SXRSS monochromator is presented. It shows that the laser pulse power reaches a TW-level with its spectral density about eighty times higher than that of the conventional SASE pulse at saturation.

Contents

Chapter 1

Introduction

Current Chapter presents the brief introduction to the Free Electron Lasers: some milestones of history of the development and working principle of FEL (Section 1.1). In Section 1.2 SASE and Seeded operation regimes of the laser are outlined. Seeding and self-seeding techniques and their comparison are presented.

Chapter 2 contains the theory, required to solve tasks of designing the monochromator and study its performance at the self-seeding operation regime. Wave optics approach is presented in Section 2.1, where the spatial-frequency transfer function and the Gaussian optics relations are derived. In the following chapters the Gaussian optics approach is used for the analytical design of the self-seeding monochromator, while the spatial frequency transfer function is necessary in order to perform the numerical simulations of both the monochromator performance and the self-seeded Free Electron laser operation. Propagation of the radiation in an inhomogeneous medium with a split-step method is discussed in Section 2.2. It was used to prove the applicability of the phase-shifter approach to simulate height errors of optical components. A way to describe a variable space grating with a toroidal shape is discussed in Section 2.3. Analytical derivation of resolution of such grating (Section 2.4) is presented and resolution demands of the self-seeding monochromator are discussed. In Section 2.5 a way to simulate surface errors of reflective optical components is described.

In **Chapter 3** the self-seeding scheme installed at the LCLS free electron laser is described (Sec. 3.1) and studied. Monochromator is analyzed analytically (Sec. 3.2) and numerically: two numerical simulation approaches were developed to simulate the monochromator performance (Sec 3.3). They are compared with each other and with an experiment (Sec. 3.4). Self-seeding commissioning challenges at the LCLS are presented as well in Sec 3.5.

Chapter 4 is devoted to the self seeding monochromator perspectives at the European XFEL. Facility and SASE beamline features are presented in Sections 4.1 and 4.2 respectively. In the latter section an attention to both the source specification of the SASE3 beamline and its response to the reimaging were paid. In Section 4.3 the proposed Self-seeding monochromator design is described in details. Its performance is calculated both analytically - with Gaussian optics (Sec. 4.4.1) and numerically (with both ray tracing (Sec. 4.4.2) and wave optics meth-

ods). With a start-to-end simulation the technical feasibility of the self-seeding scheme for the European XFEL is shown in Section 4.4.3. Grating heat load and single shot damage, which are of the great importance for the high repetition rate European XFEL facility, are discussed in Section 4.6.

1.1 X-Ray Free Electron Lasers

1.1.1 Brief history of the FEL technology development

The Free electron lasing concept was proposed by John M.J. Madey [1] in **1971** and confirmed experimentally later in **1977** as a working FEL *oscillator* [2]. Theoretical work on the possibility of a *single pass* gain FEL was developed by N. Kroll and W. Mc Mullin in **1978** [3].

In **1979** M. Kondratenko and E. Saldin proposed [4, 5] to use the FEL collective instability to produce optical radiation using a single pass amplifier starting from shot noise. The first proposal to use this instability in a single pass amplifier starting from shot noise for a soft X-ray FEL was published by Ya. S. Drebenev, A. M. Kondratenko and E. Saldin [6]. The term *"Self amplified spontaneous emission (SASE)"* appeared in **1986** work by R. Bonifacio and others [7] and was accepted by the physics community.

First experimental results of the high-gain linear regime of the SASE FEL were obtained in **1997** [8]. In **1998** statistical properties of the High-gain FEL were predicted by E.Saldin, E.Schneidmiller and M.Yurkov [9].

Saturation of a SASE FEL in visible region *(390 nm)* was reached in **2000** in Argonne National Laboratory (ANL) [10], and in **2001** saturation was achieved at *98 nm* in Tesla Test Facility (TTF) in DESY [11]. *Angstrom*-wavelength lasing was reached in **2009** in LCLS setting up a new milestone in FEL wavelength range [12, 13]. In **2011** sub-angstrom lasing was reported in SACLA facility [14].

1.1.2 The principle of Free Electron Laser operation

First of all, FEL is a vacuum tube device. The essential difference between conventional lasers and the FEL is that laser medium is the bunch of unbounded electrons in vacuum. In conventional LASER (Light Amplification by Stimulated Emission of Radiation), the amplification comes from the stimulated emission of electrons bound to atoms at a certain resonant frequencies forming energy levels. In the FEL the electrons are responsible for the light emission as well, but via the synchrotron radiation mechanism. This way, the FEL was developed from the synchrotron technology, being referred to as a light source of the 4-th generation.

Charged particle radiates energy in the form of electromagnetic radiation when it is being accelerated. Electromagnetic energy may be effectively extracted from the kinetic energy of a relativistic electron beam by propagating it along the axis of a periodic lattice of alternating magnetic dipolar fields, known as an "undulator" [15]. This forces the beam to undulate

transversely, thus causing the electrons to emit electromagnetic radiation [16]. When electron propagates in an undulator, a co-propagating radiation will always move ahead of it. Based on wave interference considerations, only those wavelengths that propagate ahead of the electron by an integer number of wavelengths in one undulator period will constructively interfere (see Figs. 1.1. Time required for an electron propagating in an undulator with mean speed $\bar{v}_e$ to
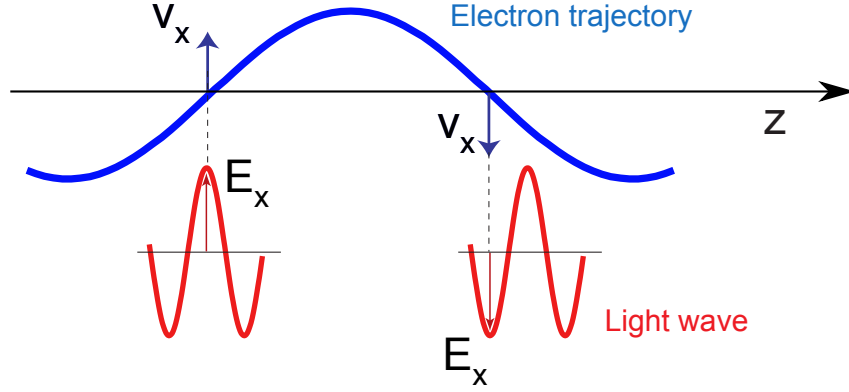

Figure 1.1: Condition for sustained energy transfer from electron to light wave in an undulator: The light wave has to slip forward by per half-period of the electron trajectory. Adapted from [17]

travel one undulator period λ_u is $t = \lambda_u/\bar{v}_e$. Interference takes place when the radiation wavefront at a wavelength λ_n travels the distance $\lambda_u + n\lambda_n$, during the time $t = (\lambda_u + n\lambda_n)/c$, where c is the speed of light and n is an integer number. By equating the relations tor t the resonant wavelength is obtained:

$$\lambda_n = \frac{\lambda_u}{n} \left(\frac{1 - \bar{v}_e/c}{\bar{v}_e/c} \right) \simeq \frac{\lambda_u}{2n\gamma^2}(1 + K^2) \, , \tag{1.1}$$

where $\bar{v}_e = c \left(1 - \frac{1+K^2}{2\gamma^2} \right)$, K is the RMS of undulator parameter, dependent on the undulator period λ_u and the magnetic field B.

$$K = \frac{\lambda_u e B}{2\sqrt{2}\pi m_e c} \, . \tag{1.2}$$

The electron charge is e mass - m_e and γ is a Lorenz factor. Equation (1.1) is called the *undulator equation*, and it shows that the resonance can take place at harmonics n of the resonant wavelength, which is called fundamental at $n = 1$.

Electron bunch with $N \gg 1$ electrons in an undulator emits the power [16]:

$$P \sim \left| \sum_{j=1}^{N} E_j e^{i\phi_j} \right|^2 = \sum_{j=1}^{N} E_j^2 + \left| \sum_{j=1}^{N} \sum_{k \neq j} E_j E_k e^{i(\phi_j + \phi_k)} \right| \, , \tag{1.3}$$

where ϕ_i are relative phases of the emitted radiation electric fields E_j. For a system with uncorrelated phases, the second sum of $\sim N^2$ terms tends to destructively interfere. In this case a radiation of the "spontaneous" source is observed with a power emitted approximately equal to the sum of powers from N independently emitting electrons, which is valid for undulator

radiation in synchrotron. In case when electron phases are correlated, i.e. periodically bunched at resonant wavelength, the coherent term $\sim N^2$ predominates, giving a major increase of power, observed in an FEL.

Bunching of the electron beam appears and is preserved due to a positive feedback process - intrinsic property of a free electron laser. Lorentz equation describes the motion of the electrons in combined undulator and radiation fields, while Maxwell's wave equation provides the electric field of radiation generated by a current from electrons transverse motion. Following equations are self-consistently coupled.

$$
\frac{d\vec{v}}{dt} = -\frac{e}{\gamma m}\left(\vec{E} + \vec{v} \times \vec{B}\right)
$$
$$
\nabla^2 \vec{E} - \frac{1}{c^2}\frac{\partial^2 \vec{E}}{\partial t^2} = \frac{4\pi}{c^2}\frac{\partial \vec{j}}{\partial t} \,, \tag{1.4}
$$

This self-consistency leads to the positive feedback - FEL collective instability. Electrons in the beam interact with emitted light and are grouped in bunches by resulting periodical pondero-motive potential. Electrons become strongly bunched, what results in domination of N^2 term in Equation. (1.3). This way we can conclude that a resonant interaction in an undulator causes an energy modulation of the electron beam, leading to a density modulation of the latter (an undulator magnetic field causes dispersion). The resulting density modulation (e.g. bunching) causes even higher intensity of the radiation since electrons radiate coherently within a bunches. It leads to even stronger resonant interaction.

Another very useful way do describe FEL is to treat it as an *electromagnetic radiation amplifier*. An electron beam is an active medium of the amplifier and an undulator is an interaction region. If the length of an electron beam is finite (which is the case for FELs), then amplifier is parametric, e.g. it's properties change with time, so electron beam length defines pulse duration. The key specification of the FEL amplifier is the Pierce parameter ρ [18]. It is a measure of radiation-electron interaction efficiency, ranging typically around $10^{-4} < \rho < 10^{-3}$ for XFELs and is inversely proportional to undulator periods on the gain length N_{l_g}

$$
\rho \sim \frac{\lambda_u}{l_g} \,, \tag{1.5}
$$

Also FEL gain is dependent on input signal wavelength, with its maximum at the resonant one. Frequency response bandwidth is defined by ρ parameter as well:

$$
\frac{\Delta\lambda}{\lambda} \sim \rho \tag{1.6}
$$

As any amplifier, it has linear and non-linear operation regime. Variation of input signal power affects amplified signal proportionally when linearly amplified. Non-linear amplification regime is called saturation. If we provide a monochromatic electromagnetic radiation as an input signal with an effective power P_0 and observe the amplified output P in a linear am-

plification regime we can measure the gain of an amplifier. Amplified power grows along an undulator length z exponentially.

$$P = P_0 \exp \frac{2z}{l_g} \,, \tag{1.7}$$

where l_g is defined as a gain length.

The energy efficiency of an FEL at the saturation is quite low, as it is roughly given by ρ parameter in the X-ray region. Once the fractional energy loss of the electron beam becomes comparable to the FEL parameter ρ, most of the electrons fall out of the resonant bandwidth of the radiation, leading to the FEL saturation. Nevertheless, one can then gradually change (taper) the undulator strength parameter (parameter K) to maintain the resonant condition as the electron beam loses energy:

$$\frac{1 + K(z)^2}{2\gamma(z)^2} = constant. \tag{1.8}$$

The strong radiation field produces a ponderomotive well which is deep enough to trap the electrons. The radiation produced by these captured particles increases the depth of the ponderomotive well, so that electrons are effectively decelerated, leading to growth of the radiated power. Tapering thus results in a much higher output power compared to the case of a uniform undulator. This way one can extract an additional energy from the electron beam after reaching the saturation [19, 20]. A further increase in power is achievable by starting the FEL process from the monochromatic seed, rather than from shot noise. The reason is the higher degree of coherence of the radiation in the seed case, thus involving, with tapering, a larger portion of the bunch in the energy-wavelength synchronism [21].

1.2 FEL operation regimes

1.2.1 Self Amplified Spontaneous Emission (SASE)

In the FEL amplifier there is an intrinsic noise. When the electron passes the undulator, it interacts with the electromagnetic field produced by other electrons and also emits radiation. If we consider the microstructure of the electron current, we can find that electrons enter the undulator randomly in time. This noise is caused by quantum nature of electron emission from the gun - shot noise. Its spectral power is frequency independent, which means the noise is white.

If we assume there are no neither initial radiation overlapped with an electron beam nor the externally imposed electron beam modulations (which is the nominal case for convenient XFELs), the high gain amplification starts from the shot noise in electron beam or, in other words, spontaneous undulator radiation. FEL instability leads to bunching of an initially nearly uniformly distributed electron beam thanks to a Poisson distribution of electrons in the beam. This process is called Self-Amplified Spontaneous Emission (SASE) [4, 7]. During the SASE
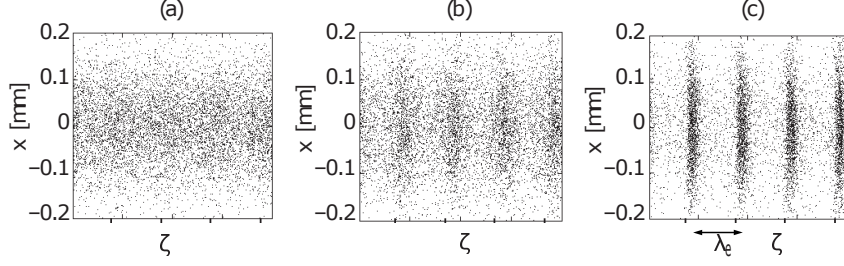
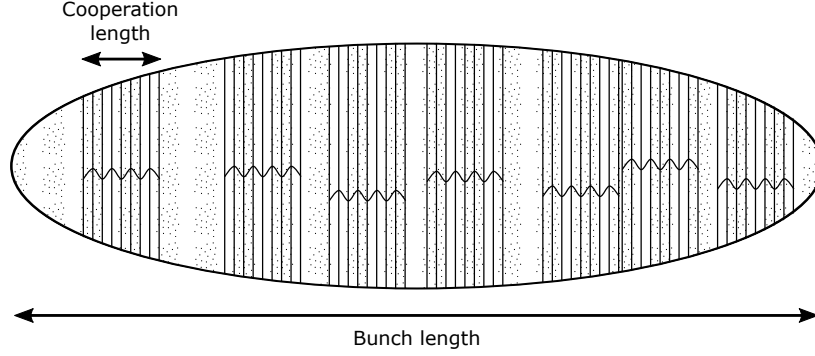Figure 1.2: Simulation of microbunching by Sven Reiche, SLS (code GENESIS)

Figure 1.3: Presence of numerous independent longitudinal modes is a natural property of SASE FEL operation

FEL operation regime, the radiation and bunching develop at different parts of the electron beam simultaneously and independently (see Figs 1.2 and 1.3). Due to radiation slippage electrons communicate with ones in front only if their separation is smaller than the total slippage. This length is known as cooperation or coherence length [22]:

$$l_c = \frac{\lambda}{4\pi\rho} \sim \frac{l_g}{2\gamma^2} \qquad (1.9)$$

Electrons emit radiation coherently within these regions, but phase differences of bunching between any two of them are independent, thus uniformly distributed from 0 to 2π. It results as a numerous longitudinal modes of the radiation in both time and frequency domains.

In other words, SASE is the operation of the FEL amplifier, when it's intrinsic noise is being amplified. After amplification power is distributed within FEL gain curve with bandwidth ρ given by Equation (1.6). An effective power of shot noise is given by [23, 24]

$$P_n \simeq \rho^2 \omega_0 \gamma m c^2 / 2 \ . \qquad (1.10)$$

FEL radiation produced with a SASE mechanism reveals shot-to-shot fluctuations of the pulse energy when operates in a linear amplification regime. A probability density distribution of the SASE FEL pulse energy after the monochromator is described rather well by a gamma probability density function [9]. In a linear amplification regime it tends towards the negative exponential distribution.
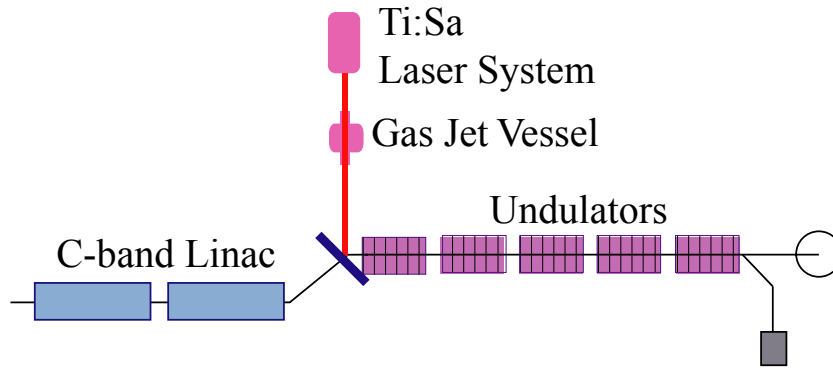
Figure 1.4: Layout of the HHG experiment. The C-band linac modules are the two last units of the SCSS whole accelerator. Reprinted from the original article [36].

1.2.2 Seeding schemes

In fact, the main interest in FEL, as well as in other lasers is to obtain the high-intensity radiation with controlled wavelength, pulse length and intensity within narrow spectral bandwidth. As mentioned before, FEL amplification line (or gain curve) is defined by Pierce parameter (Eq. 1.5), and in SASE FEL all frequencies present in noise are amplified within this $\sim 10^{-3}$ bandwidth. In terms of time domain, electron bunch length is usually much larger than the cooperation length. This way SASE radiation of XFELs has relatively poor temporal (i.e. longitudinal) coherence. A significant increase in power and spectral density is achievable by starting the FEL process from a monochromatic seed rather than from shot noise [20, 21, 25–30]. The most used and acknowledged seeding techniques are outlined below, as direct seeding with radiation (HHG), seeding by electron beam manipulation (HGHG, EEHG), and self-seeding. Essentially they are all focused on increasing cooperation length. There are other methods to increase that time based on SASE FEL - with introduction of additional phase-shifts along undulator (iSASE [31], HB-SASE [32]), or amplifying SASE at combination of fundamental and n-th harmonic FEL (pSASE [33]). Extensive overview of seeding methods can be found in [23], and following subsection is based on that reference, including [34] and [35].

Direct seeding

Seeding FEL with radiation, that has the same wavelength as the resonance wavelength of the FEL and the power level above shot noise is called "direct seeding". **High-order Harmonic Generation (HHG)** seeding was described in [36] and essentially lies in direct seeing the FEL with radiation at it's fundamental harmonic (see Fig. 1.4). Seed radiation at the resonant wavelength is obtained via interaction of infra-red Ti:sapphire laser with gas [37]. A successful experiment has been carried out at the SPring-8 Compact SASE Source (SCSS) test accelerator at 160 nm FEL fundamental harmonic [38]. 38 nm wavelength seeding was reached at FLASH [39].
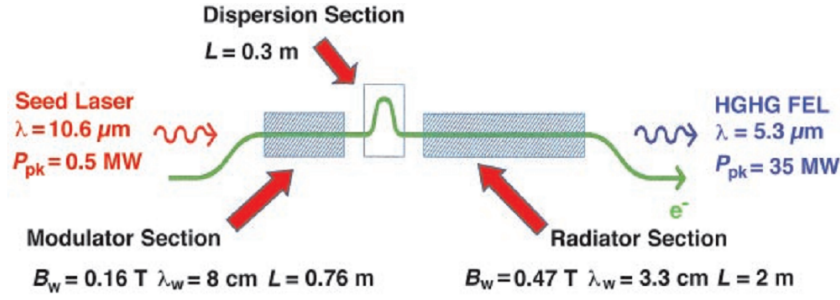
7

Figure 1.5: Configuration for the HGHG FEL experiment as carried out at the Accelerator Test Facility at Brookhaven National Laboratory. The 40-MeV electron beam had a current of 120 A (0.8 nC in 6 ps) with a normalized emittance of 5 mm-mrad. L, length; l, wavelength; P_{pk}, peak power; B_w, peak undulator magnetic field; λ_w, undulator period. Reprinted from the original article [41].

Seeding by electron beam manipulation

FEL can be seeded by introduction of a coherent bunching to the electron beam at the resonant wavelength. One of the methods is a so-called **High-Gain Harmonic Generation (HGHG)** process [40–43]. Working principle of HGHG is well described in [42]: "A small energy modulation is imposed on the electron beam by its interaction with a seed laser in a short undulator (the modulator) tuned to the seed frequency ω; the resulting energy modulation is then converted into a longitudinal density modulation as the electron beam traverses a magnetic dispersion; in a second undulator (the radiator), which is tuned to the n-th harmonic of the seed frequency, the microbunched electron beam emits coherent radiation at the harmonic frequency $n\omega$, which is then amplified in the radiator until saturation is reached. The output property of the HGHG FEL is a direct map of the seed laser's attributes which can have a high degree of temporal coherence. The additional benefits derived from this configuration are superior stability and control of the central wavelength, narrower bandwidth, and much smaller energy fluctuations than SASE."

Bunching created in the modulator at n-th harmonics is given by $b_n = \exp\left[-(n\sigma_\gamma/\Delta\gamma)^2/2\right]$ and it drops quickly when the induced energy modulation $\Delta\gamma$ gets smaller than the product of intrinsic energy spread σ_γ and harmonic number n. At higher harmonics a very large energy modulation needs to be applied to the electron beam in order to obtain bunching above shot noise level. A high stability HGHG seeding was demonstrated at FERMI lasing at 32 nm wavelength in 2012 [44].

Another method to create density modulation of the electron beam is the **Echo-Enabled Harmonic Generation (EEHG)**, proposed in [45] and extensively studied in [46]. It is similar to HGHG, but uses two modulators with two chicanes in order to introduce electron density modulation at significantly higher frequencies. In modulators the electron beam interacts with two laser pulses which may have the same or different frequencies.

After the magnetic chicane of the first modulation stage, phase space of the beam is strongly filamented. After the consecutive energy modulation by the second laser in modulator 2 and passing through the second chicane it exhibits a numerous peaks in the electron density. Fourier spectrum of this energy density extends to very high frequencies.
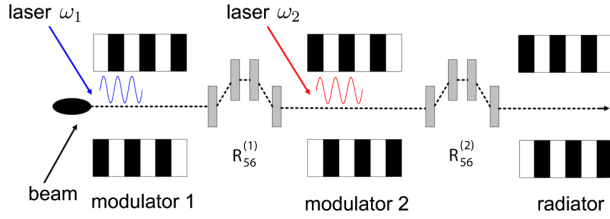
Figure 1.6: Schematic of the EEHG FEL. The beam energy is modulated in the first undulator (modulator 1) tuned at frequency ω_1 due to the interaction with the first laser beam. After passing through the first dispersion section, the beam energy is then modulated in the second undulator (modulator 2) tuned at frequency ω_2 due to the interaction with the second laser beam. The beam passes through the second dispersion section and emits radiation in the last undulator (radiator). Reprinted from the original article [46].
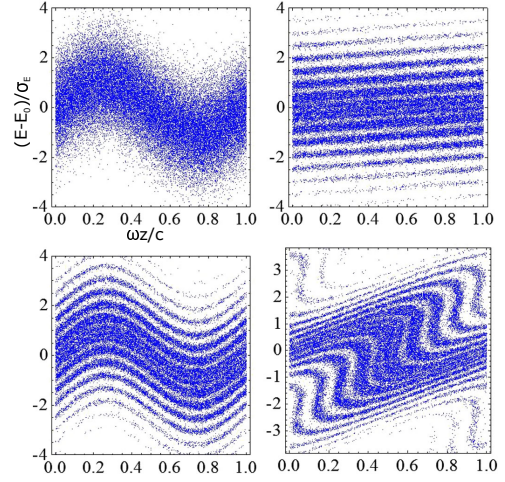

Figure 1.7: Longitudinal phase space distribution in a EEHG after the first undulator (top left), the first dispersive element (top right), the second undulator (bottom left), and the second dispersive element (bottom right). Horizontal axes in the plots are dimentionless coordinates along the beam, and the vertical axes are relative electron energies. Reprinted from the original article [45].

Two proof-of-principle experiments of the EEHG technique have been carried out at SDUV-FEL [47] and NLCTA [48] independently.

Self-seeding

One of main problems with seeding FEL externally along with obtaining short-wavelength seed pulses is the temporal synchronization of the FEL electron bunch. This problem is automatically solved if the same electron bunch both creates seeding radiation and amplifies the seed.

This scheme is referred to as a "**self-seeding**" and was proposed in [49] in soft X-ray and in the hard X-ray regimes [50–52]. Such scheme was successfully realized in LCLS in both wavelength ranges [53, 54].

In general, a self-seeding setup consists of two undulators separated by a photon monochromator and an electron bypass, normally a four-dipole chicane (see Figures 1.8).

The two undulators are resonant at the same radiation wavelength. The SASE radiation is generated by the first undulator before reaching saturation. Then it passes through the narrow-band monochromator. In case of the SXRSS the key element of the monochromator is a grating (Fig. 1.8), while in HXRSS, FEL pulse is monochromatized with a single diamond crystal (Figs. 1.9,1.10). In both cases pulses close to transform-limited are created, which are used as a coherent seed in the second undulator. Chromatic dispersion effect in the bypass chicane smears out the microbunching in the electron bunch produced by the SASE lasing in the first undulator. The electrons and the monochromatized photon beam are recombined at the entrance of the
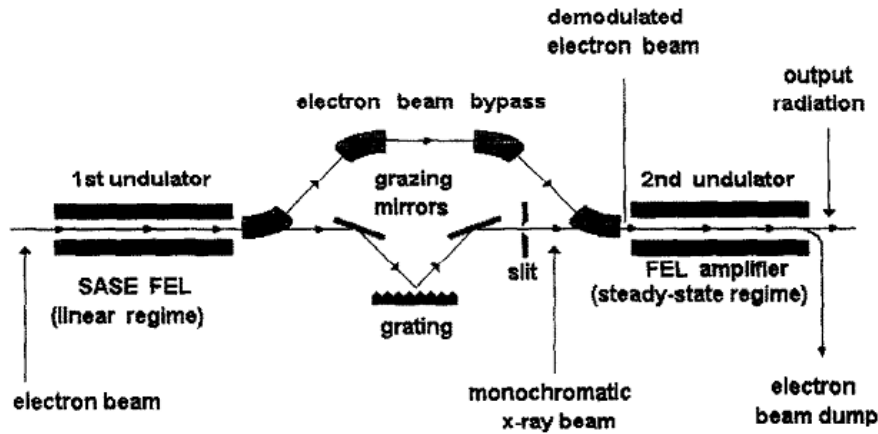
Figure 1.8: The principal scheme of the self-seeded FEL with a monochromator. Reprinted from the original article [49].
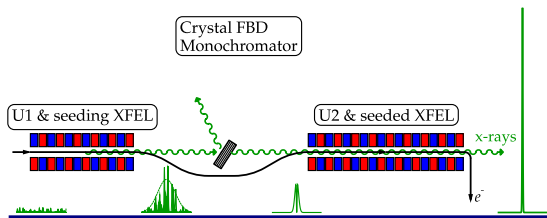

Figure 1.9: Hard x-ray FEL self-seeding scheme uses x rays from the first half of the magnetic undulator system U1 to seed the electron bunch in the second half U2 via a single crystal x-ray monochromator. The monochromator produces the delayed monochromatic seed under the forward Bragg diffraction (FBD) conditions. Reprinted from [55].
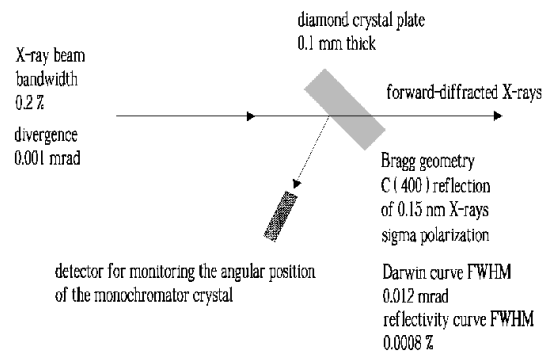

Figure 1.10: Wake monochromator based on a 0.1 mm-thick diamond crystal at 8 keV for self-seeded operation of the LCLS baseline hard X-ray FEL. Reprinted from the original article [51].

second undulator, and radiation is amplified by the electron bunch until saturation is reached. The required seed power at the beginning of the second undulator must dominate over the shot noise power within the FEL gain curve. Shot noise effective power is in order of a kW in the soft X-ray range.

The comparison of the seeding methods is outlined in Table 1.1

Method	Direct seeding (HHG)	HGHG or EEHG	Self-Seeding
Wavelength limit	>20 nm	>1 nm	**>0.1 Å**
Synchronization requirement	Good	Good	None
Brilliance	Similar to SASE	Better than SASE	Much better than SASE
Pulse length	∼10 fs	10-100 fs	As electron bunch
Signal to background	Poor	Moderate	Good
Complexity	Moderate	High	Moderate
Electron beam requirements	Arrival time, energy stability	Arrival time, energy stability, energy spread	Energy stability
Undulator length	Less than SASE FEL	Comparable with SASE FEL	50% longer than SASE FEL

Table 1.1: Comparison of seeding methods. Reprinted from [34]

Chapter 2

Theoretical background for designing a grating monochromator

2.1 Wave optics approach

Wave optics is a very promising straightforward approach to characterize the propagation of the FEL pulse through the optical system of the monochromator. It is good for both analytical calculations and numerical simulations. In this section we derive the spatial frequency transfer function for wave propagation and the Fresnel diffraction formula commonly used in Fourier optics. Then the propagation of a Gaussian beam through ideal lenses and mirrors spaced apart from each other is analyzed.

2.1.1 Wave equation

The fundamental theory of electromagnetic fields is based on the Maxwell equations. In differential form and in the space-time domain, these can be written as[1]:

$$\vec{\nabla} \cdot \vec{E} = 4\pi\rho \, , \tag{2.1a}$$

$$\vec{\nabla} \cdot \vec{B} = 0 \, , \tag{2.1b}$$

$$\vec{\nabla} \times \vec{E} = -\frac{1}{c}\frac{\partial \vec{B}}{\partial t} \, , \tag{2.1c}$$

$$\vec{\nabla} \times \vec{B} = \frac{4\pi}{c}\vec{j} + \frac{1}{c}\frac{\partial \vec{E}}{\partial t} \, . \tag{2.1d}$$

Here $\vec{j}$ is the current density and ρ denotes the electric charge density. $\vec{E}$ and $\vec{B}$ are the electric and magnetic fields in the time domain.

Maxwell equations can be manipulated mathematically in many ways in order to yield derived equations more suitable for certain applications. For example, from Maxwell equations

---

[1]For reasons of simplicity, in this thesis we will work with the Gaussian unit system

we can obtain an equation which depends only on the electric field vector $\vec{E}$ by taking curl of both sides Eq. 2.1c and implying Eq. 2.1d:

$$\vec{\nabla} \times (\vec{\nabla} \times \vec{E}) = -\frac{4\pi}{c^2} \frac{\partial \vec{j}}{\partial t} - \frac{1}{c^2} \frac{\partial^2 \vec{E}}{\partial t^2} \; . \tag{2.2}$$

the $\vec{\nabla} \times (\vec{\nabla} \times (\cdot))$ operator is not very easy to use, so that it is advantageous to use the vector identity

$$\vec{\nabla} \times (\vec{\nabla} \times \vec{E}) = \vec{\nabla}(\vec{\nabla} \cdot \vec{E}) - \nabla^2 \vec{E} \; , \tag{2.3}$$

which holds if we use a cartesian coordinate system. Exploiting Eq. (2.3) and incorporating Eq. (2.1a), we rewrite Eq. (2.2) as

$$\nabla^2 \vec{E} - \frac{1}{c^2} \frac{\partial^2 \vec{E}}{\partial t^2} = \frac{4\pi}{c^2} \frac{\partial \vec{j}}{\partial t} + 4\pi \vec{\nabla} \rho \; . \tag{2.4}$$

This is the wave equation in the most general form. It separates terms which are present in *free-space* (on the left hand side) from terms related with the propagation through the *dielectric medium* (on the right-hand side).

2.1.2 Spatial frequency transfer function

We will start with the basic treatment of radiation: propagation in a free space.

Let us consider the inhomogeneous wave equation for the electric field in the space-time domain (Eq. (2.4)). In space free of all sources and medium ($\vec{j} = 0, \rho = 0$) it reduces to the homogeneous wave equation:

$$\nabla^2 \vec{E} - \frac{1}{c^2} \frac{\partial^2 \vec{E}}{\partial t^2} = 0 \; . \tag{2.5}$$

Here c indicates the speed of light in vacuum, t is the time and $\vec{r}$ is a 3D spatial vector identified by cartesian coordinates x, y, z. As a consequence, the following equation for the field $\vec{\tilde{E}}(\omega, \vec{r})$ in the space-frequency domain holds:

$$\nabla^2 \vec{\tilde{E}} + k_0^2 \vec{\tilde{E}} = 0 \; , \tag{2.6}$$

where $k_0 = \omega/c$. Eq. (2.6) is the well-known Helmholtz equation. Here $\vec{\tilde{E}}(\omega, \vec{r})$ is a temporal Fourier transform of the electric field. The definitions of the Fourier transform and inverse Fourier transform for a function $\vec{\tilde{E}}(\omega, x, y)$ are defined below.

$$\vec{\tilde{E}}(\omega, x, y) = \int_{-\infty}^{\infty} \vec{E}(t, x, y) \exp[i\omega t] dt \; ,$$

$$\vec{E}(t, x, y) = \frac{1}{2\pi} \int_{-\infty}^{\infty} \vec{\tilde{E}}(\omega, x, y) \exp[-i\omega t] d\omega \; . \tag{2.7}$$

Similarly, the 2D spatial Fourier transform of $\vec{E}(x, y, z, \omega)$, with respect to the two transverse coordinates x and y will be written as

$$\vec{\hat{E}}(\omega, k_x, k_y, z) = \int_{-\infty}^{\infty} dx \int_{-\infty}^{\infty} dy \vec{\hat{E}}(\omega, x, y) \exp[ik_x x + ik_y y] , \qquad (2.8)$$

so that

$$\vec{\hat{E}}(\omega, x, y, z) = \frac{1}{4\pi^2} \int_{-\infty}^{\infty} dk_x \int_{-\infty}^{\infty} dk_y \vec{\hat{E}}(\omega, k_x, k_y) \exp[-ik_x x - ik_y y] . \qquad (2.9)$$

With the help of this transformation the Helmholtz equation, which is a partial differential equation in three dimensions, reduces to a one-dimensional ordinary differential equation for the spectral amplitude $\vec{\hat{E}}(\omega, k_x, k_y, z)$. In fact, by taking the 2D Fourier transform of Eq. (2.6), we have

$$\frac{d^2 \vec{\hat{E}}}{dz^2} + k_0^2 \left(1 - \frac{k_x^2}{k_0} - \frac{k_y^2}{k_0^2} \right) \vec{\hat{E}} = 0 . \qquad (2.10)$$

We then obtain straightforwardly

$$\vec{\hat{E}}(\omega, k_x, k_y, z) = \vec{\hat{E}}(\omega, k_x, k_y, 0) \exp \left[ik_0 z \sqrt{1 - \frac{k_x^2}{k_0^2} - \frac{k_y^2}{k_0^2}} \right] , \qquad (2.11)$$

where $\hat{E}(\omega, k_x, k_y, z)$ is the output field and $\hat{E}(\omega, k_x, k_y, 0)$ is the input field. Further on, when the temporal frequency ω will be fixed, we will not always include it into the argument of the field amplitude and simply write e.g. $\hat{E}(k_x, k_y, z)$. It is natural to define the spatial frequency response of the system as

$$H(k_x, k_y, z) = \frac{\vec{\hat{E}}(k_x, k_y, z)}{\vec{\hat{E}}(k_x, k_y, 0)} = \exp \left[ik_0 z \sqrt{1 - \frac{k_x^2}{k_0^2} - \frac{k_y^2}{k_0^2}} \right] . \qquad (2.12)$$

Here the ratio between vectors has to be interpreted component by component. H is the spatial frequency transfer function related with light propagation through a distance z in free space. If we assume that $k_x^2 + k_y^2 \ll k_0^2$, meaning that the bandwidth of the angular spectrum of the beam is small we have

$$\vec{\hat{E}}(k_x, k_y, z) = \vec{\hat{E}}(k_x, k_y, 0) \times H(k_x, k_y, z) ,$$
$$H(k_x, k_y, z) \simeq \exp[ik_0 z] \exp \left[-\frac{iz}{2k_0} (k_x^2 + k_y^2) \right] . \qquad (2.13)$$

In other words, we enforce the paraxial approximation. In order to obtain the output field distribution in the space-frequency domain $\vec{\hat{E}}(x, y, z)$ at the distance z away from the input position at $z = 0$, we simply take the inverse 2D Fourier transform of $\vec{\hat{E}}(k_x, k_y, z)$ with Eq. (2.9).

2.1.3 Gaussian beam optics

In order to present a convenient analytical representation of a wave optics calculation method it is convenient to specialize our discussion considering a model Gaussian beam. In order to simplify the notation, we will consider a monochromatic radiation at frequency ω in the space-frequency domain only. Let us consider a Gaussian intensity distribution with initially (at $z = 0$) plane wavefront in two transverse dimensions.

$$\bar{E}(x, y, 0) = A \exp\left[-\frac{x^2 + y^2}{w_0^2}\right] , \tag{2.14}$$

where w_0 is the transverse waist size of the Gaussian beam. The spatial Fourier transform of $\bar{E}$ is given by

$$\hat{E}(k_x, k_y, 0) = A\pi w_0^2 \exp\left[-\frac{w_0^2}{4}\left(k_x^2 + k_y^2\right)\right] . \tag{2.15}$$

Using Eq. (2.13), after propagation over a distance z one obtains

$$
\begin{aligned}
\hat{E}(k_x, k_y, z) &= \hat{E}(k_x, k_y, 0)H(k_x, k_y, z) \\
&= A\pi w_0^2 \exp[ik_0 z]\exp\left[-\frac{iz}{2k_0}\left(k_x^2 + k_y^2\right)\right]\exp\left[-\frac{w_0^2}{4}\left(k_x^2 + k_y^2\right)\right] \\
&= A\pi w_0^2 \exp[ik_0 z]\exp\left[-\frac{iq}{2k_0}(k_x^2 + k_y^2)\right] ,
\end{aligned}
\tag{2.16}
$$

where q is the so-called q-parameter of the Gaussian beam

$$q = z - iz_R , \tag{2.17}$$

where z_R defines the Rayleigh range of the Gaussian beam

$$z_R = k_0 w_0^2/2 . \tag{2.18}$$

The spatial profile of the beam after propagation through a distance z can be found by taking the inverse Fourier transform of Eq. (2.16):

$$\bar{E}(x, y, z) = -\frac{iAk_0 w_0^2}{2q}\exp[ik_0 z]\exp\left[i\frac{k_0}{2q}(x^2 + y^2)\right] , \tag{2.19}$$

which can also be written as

$$
\begin{aligned}
\bar{E}(x, y, z) = A\frac{w_0}{w(z)}&\exp[i\phi(z) + ik_0 z] \\
&\times \exp\left[-\frac{(x^2 + y^2)}{w^2(z)}\right]\exp\left[i\frac{k_0}{2R(z)}(x^2 + y^2)\right] ,
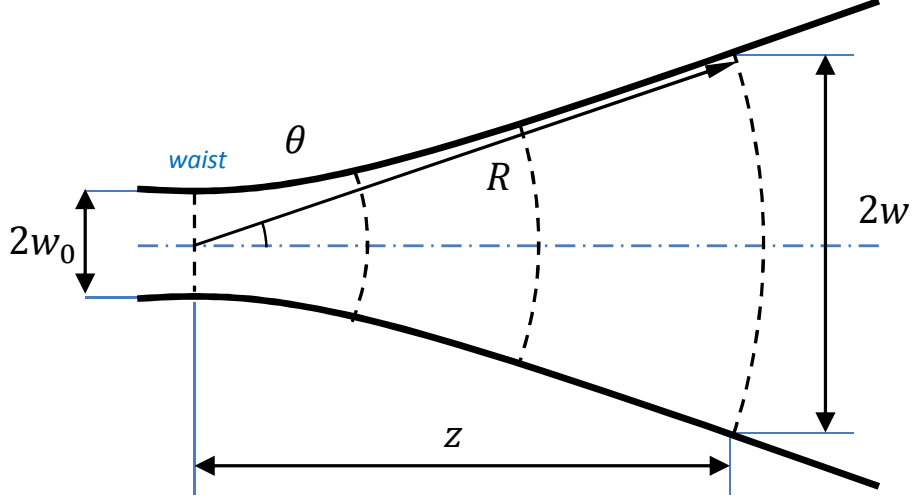\end{aligned}
\tag{2.20}
$$

Figure 2.1: Wavefront of the Gaussian beam in far zone becomes spherical with the center at the waist

where

$$w^2(z) = w_0^2 \left[1 + \left(\frac{z}{z_R} \right)^2 \right] \,, \tag{2.21}$$

$$R(z) = \frac{1}{z} \left(z^2 + z_R^2 \right) \,, \tag{2.22}$$

and

$$\phi(z) = -\arctan \left[\frac{z}{z_R} \right] \,, \tag{2.23}$$

with z_R defined in Eq. (2.18). Note that the width $w(z)$ of the Gaussian beam is a monotonically increasing function of the propagation distance z, and reaches $\sqrt{2}$ times its original width, w_0, at $z = z_R$. The radius of curvature $R(z)$ of the wavefront is initially infinite (see Fig. 2.1), corresponding to an initially plane wavefront, but it reaches a minimum value of $2z_R$ at $z = z_R$, before starting to increase again. The slowly varying phase $\phi(z)$, monotonically varies from 0 at $z = 0$ to $-\pi/2$ as $z \longrightarrow \infty$, assuming the value $\pi/4$ at $z = z_R$. At large z divergence angle θ is

$$\theta(z) = \frac{w(z)}{z} \simeq \frac{2}{k_0 w_0} \,. \tag{2.24}$$

Note that the q-parameter contains all information about the Gaussian, namely its curvature $R(z)$ and its waist $w(z)$. The knowledge of the transformation of q as a function of z fully characterizes the behavior of the Gaussian beam.

An optical system would usually comprise lenses or mirrors spaced apart from each other. While Gaussian beam propagation in between optical elements can be tracked using the translation law above, Eq. (2.19), we still need to discuss the law for the transformation of q by a lens. The transparency function for a thin converging lens is of the form
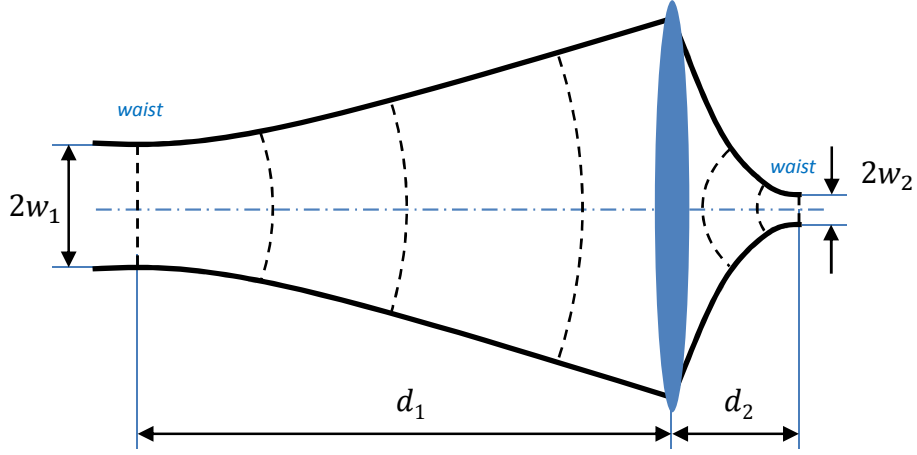
Figure 2.2: Gaussian beam transformation by a lens. A Gaussian beam with plane wavefront and waist w_1, located at a distance d_1 from the thin lens with focal length f is transformed to a Gaussian beam of plane wavefront and waist w_2, located at a distance d_2, according to Eq. (2.30).

$$T_f(x, y) = \exp\left[-\frac{ik_0}{2f}(x^2 + y^2)\right] . \tag{2.25}$$

The optical field immediately behind a thin lens at position z is related to that immediately before a lens by

$$
\begin{aligned}
\bar{E}_{\text{after\_lens}}(x, y, z) &= T_f(x, y)\bar{E}_{\text{before\_lens}}(x, y, z) \\
&= -\frac{iAk_0w_0^2}{2q}\exp[ik_0z]\exp\left[i\frac{k_0}{2q}(x^2 + y^2)\right]\exp\left[-\frac{ik_0}{2f}(x^2 + y^2)\right] \\
&= -\frac{iAk_0w_0^2}{2q}\exp[ik_0z]\exp\left[i\frac{k_0}{2q_l}(x^2 + y^2)\right] \tag{2.26}
\end{aligned}
$$

where $\bar{E}_{\text{before\_lens}}(x, y, z)$ is given by Eq. (2.16) and q_l, the transformed of q, is defined by

$$\frac{1}{q_l} = \frac{1}{q} - \frac{1}{f} . \tag{2.27}$$

As an example of an application we analyze the focusing of a Gaussian beam by a converging lens. We assume that a Gaussian beam with a plane wavefront and the waist w_1, is located at a distance d_1 from a thin lens with the focal length f. After the propagation through a distance d_2 behind the lens, it is transformed to a beam with a plane wavefront and the waist w_2, Fig. 2.2. Using Eq. (2.17) and Eq. (2.27) we can find the transformed q-parameter at a distance d_2. From Eq. (2.17), immediately in front of the lens we have

$$q(d_1) = q(0) + d_1 , \tag{2.28}$$

Immediately behind the lens, the q-parameter is transformed to q_l according to Eq. (2.17):

$$\frac{1}{q_l} = \frac{1}{q(0) + d_1} - \frac{1}{f} \ . \tag{2.29}$$

Finally, using again Eq. (2.17), we find the q-parameter after propagation through a distance d_2 behind the lens:

$$q(d_2 + d_1) = q_l + d_2 \ . \tag{2.30}$$

The Gaussian beam is said to be focused at the point $z = d_2 + d_1$ where $q(d_2 + d_1)$ becomes purely imaginary again, meaning that the Gaussian beam has a planar wavefront. Thus, calculating explicitly $q(d_2 + d_1)$, setting $q(d_2 + d_1) = ik_0 w_2^2/2$, and equating imaginary parts we obtain

$$w_2^2 = \frac{w_1^2 f^2}{[(d_1 - f)^2 + (k_0 w_1^2/2)^2]} \ . \tag{2.31}$$

Equating the real part of $q(d_2 + d_1)$ to zero one obtains instead

$$d_2 = f + f^2 \frac{(d_1 - f)}{[(d_1 - f)^2 + (k_0 w_1^2/2)^2]} \ . \tag{2.32}$$

Note that the Gaussian beam does not exactly focus at the geometrical back focus of the lens. Instead, the focus is shifted closer to the lens. In other words the "lensmaker" equation valid in geometrical optics

$$\frac{1}{d_1} + \frac{1}{d_2} = \frac{1}{f} \tag{2.33}$$

is modified to

$$\frac{1}{d_1 + z_R^2/(d_1 - f)} + \frac{1}{d_2} = \frac{1}{f} \ , \tag{2.34}$$

which is just another way of writing Eq. (2.32) and is well known from a long time (see e.g. [56]).

2.2 Beam propagation in inhomogeneous medium

In section 2.1, we considered the problem of wave propagation in a homogeneous medium, namely vacuum, characterized by constant permittivity, $\epsilon = 1$. We specialized our investigations to the case of a Gaussian beam and, additionally, we analyzed propagation of a Gaussian beam through a thin lens using the wave optics formalism. The description of wave propagation through a thin lenses does not require the use of wave propagation theory in inhomogeneous media. In fact, as we have seen, thin lenses contribute to the wave propagation via a phase multiplication. In other words, if we consider a wave field in front of and immediately behind a lens, we find that the phase of the wave has changed, while its amplitude has remained practically

the same. A mirror may be equivalently modeled by a similar phase transformation.

Of course, strictly speaking, the polarization of the light has an influence on its reflection properties from the lenses. However, if we are willing to disregard such reflection phenomena, we are justified to use the scalar wave equation to describe the wave optics of lenses, and to model a thin lens as described before. In this section we will study, at variance, wave propagation in a medium that is inhomogeneous. Therefore, we will be in position to numerically analyze such effects as reflection of X-rays from gratings or mirrors.

2.2.1   Wave equation for inhomogeneous medium

Let's consider Eq. (2.4) once again for the case of a dielectric medium.

$$\nabla^2 \vec{E} - \frac{1}{c^2}\frac{\partial^2 \vec{E}}{\partial t^2} = \frac{4\pi}{c^2}\frac{\partial \vec{j}}{\partial t} + 4\pi\vec{\nabla}\rho \; . \qquad (2.4 \text{ revisited})$$

Charge density ρ can be seperated into two terms $\rho = \rho_{bound} + \rho_{free}$, where ρ_{bound} represents charge density caused by polarization of medium, and ρ_{free} is free charges density. The latter term in our case equals zero. Polarization of dielectric is related to the electric field $\vec{E}$ according to $\vec{P} = \chi\vec{E}$, where χ is the electric susceptibility. It induces polarization currents (for time-dependent polarization) and bound charge density (for inhomogeneous polarization) within a medium in the following way:

$$\vec{\nabla}\vec{P} = -\rho_{bound} \; , \qquad (2.35a)$$

$$\frac{\partial \vec{P}}{\partial t} = \vec{j} \; . \qquad (2.35b)$$

Incorporating Eq. (2.35a) to the first Maxwell's equation (2.1a), we obtain

$$\vec{\nabla}(\vec{E} + 4\pi\vec{P}) = 4\pi\rho_{free} = 0 \; . \qquad (2.36)$$

Value in brackets is convenient to redefine as the electric displacement field

$$\vec{D} = \vec{E} + 4\pi\vec{P} = (1 + 4\pi\chi)\vec{E} = \epsilon\vec{E} \; , \qquad (2.37)$$

where ϵ denotes the permittivity of medium. This way source (right-hand side) terms in wave equation 2.4 can be rewritten via polarization induced in the medium:

$$\frac{4\pi}{c^2}\frac{\partial \vec{j}}{\partial t} = \frac{4\pi}{c^2}\frac{\partial^2 \vec{P}}{\partial t^2} = \frac{(\epsilon - 1)}{c^2}\frac{\partial^2 \vec{E}}{\partial t^2} \; , \qquad (2.38a)$$

$$4\pi\vec{\nabla}\rho = -4\pi\vec{\nabla}(\vec{\nabla}\vec{P}) = \vec{\nabla}\left[\vec{\nabla}\frac{\vec{D}}{\epsilon}\right] = \vec{\nabla}\left[\frac{\vec{\nabla}\vec{D}}{\epsilon} + \vec{D}\vec{\nabla}\frac{1}{\epsilon}\right] = -\nabla(\vec{D}\frac{\nabla\epsilon}{\epsilon^2}) = -\vec{\nabla}\left[\vec{E}\frac{\vec{\nabla}\epsilon}{\epsilon}\right] \; . \qquad (2.38b)$$

Consequently we obtain the wave equation

$$\nabla^2 \vec{E} - \frac{1}{c^2}\frac{\partial^2 \vec{E}}{\partial t^2} = \frac{(\epsilon - 1)}{c^2}\frac{\partial^2 \vec{E}}{\partial t^2} - \vec{\nabla}\left[\vec{E}\frac{\vec{\nabla}\epsilon}{\epsilon}\right] , \qquad (2.39)$$

By taking temporal Fourier transform of Eq. (2.39) we obtain

$$c^2\nabla^2 \vec{\vec{E}} + \omega^2 \vec{\vec{E}} = -(\epsilon - 1)\omega^2 \vec{\vec{E}} - c^2\vec{\nabla}\left[\vec{\vec{E}}\frac{\vec{\nabla}\epsilon}{\epsilon}\right] , \qquad (2.40)$$

where $\vec{\vec{E}} = \vec{\vec{E}}(\omega, x, y, z)$ is the temporal Fourier transform of an electric field.

In the special case that ϵ is constant in space, the gradient of ϵ vanishes, and Equation (2.40) assumes the form of the wave equation:

$$\nabla^2 \vec{\vec{E}} + k_0^2 \epsilon \vec{\vec{E}} = 0 , \qquad (2.41)$$

where $k_0 = \omega/c$. Qualitatively it is similar to the one for a free space (2.6). In our case we consider an inhomogeneous medium, so in order for this approximation to be applicable the gradient term must not introduce important changes to the part of the equation relative to propagation through the dielectric. In other words, the gradient term should be small compared with $\frac{(\epsilon-1)}{c^2}\frac{\partial^2 \vec{E}}{\partial t^2}$. The following analysis is very similar to the treatment in [57] and applies only to order of magnitude estimates and must not be taken to be precise. The first term is of the order of

$$\frac{(\epsilon - 1)}{c^2}\frac{\partial^2 \vec{E}}{\partial t^2} \sim (\epsilon - 1)\frac{\omega^2}{c^2}\vec{E} . \qquad (2.42)$$

Replacing gradient by a derivative with respect to some direction S we can write second term with order of magnitude

$$\vec{\nabla}\left[\vec{E}\frac{\vec{\nabla}\epsilon}{\epsilon}\right] \sim \frac{\partial}{\partial S}\left[\vec{E}\frac{\vec{\nabla}\epsilon}{\epsilon}\right] \sim \frac{2\pi}{\lambda}\vec{E}\frac{\nabla\epsilon}{\epsilon} + \vec{E}\frac{\partial}{\partial S}\frac{\vec{\nabla}\epsilon}{\epsilon} . \qquad (2.43)$$

Derivative of the $\nabla\epsilon$ is beyond our precision. Comparing of the two terms we obtain

$$R = \frac{\vec{\nabla}\left[\vec{E}\dfrac{\vec{\nabla}\epsilon}{\epsilon}\right]}{\dfrac{(\epsilon - 1)}{c^2}\dfrac{\partial^2 \vec{E}}{\partial t^2}} = \frac{\dfrac{2\pi}{\lambda}\vec{E}\dfrac{\nabla\epsilon}{\epsilon}}{(\epsilon - 1)\dfrac{\omega^2}{c^2}\vec{E}} = \frac{1}{2\pi}\frac{\lambda}{\Delta S}\frac{\epsilon_2 - \epsilon_1}{\epsilon - 1} \sim \frac{\epsilon_2 - \epsilon_1}{\epsilon - 1} , \qquad (2.44)$$

since it is convenient to consider ΔS to be comparable with the wavelength If we want to neglect the gradient term in Eq. (2.39), we must require $R \ll 1$.

For optical wavelengths and in general, in regimes where ϵ is sensibly larger than unity, condition (2.44) will not lead to much different regions of applicability compared to the condition

proposed in [57]:

$$R' \sim \frac{\epsilon_2 - \epsilon_1}{\epsilon} \tag{2.45}$$

An important difference arises when one considers the x-ray range, where ϵ is very close to unity. In that case, according to condition (2.44), the wave equation is not applicable in such situations. However, in that case we can limit ourselves to small angles of incidence. But this condition may be modified under the additional small angle approximation.

Applying Fourier transform to Eq. (2.4) we obtain the inhomogeneous Helmholtz equation.

$$c^2 \nabla^2 \vec{\tilde{E}} + \omega^2 \vec{\tilde{E}} = -4\pi \omega^2 \vec{\tilde{P}} - 4\pi c^2 \vec{\nabla} \left(\vec{\nabla} \cdot \vec{\tilde{P}} \right) \ . \tag{2.46}$$

Here $\vec{\tilde{E}}$ and $\vec{\tilde{P}}$ are temporal Fourier transforms of electric field $\vec{E}$ and polarization $\vec{P}$.

We now introduce a Green function for the Helmholtz wave equation, $G(\vec{r}, \vec{r'})$, defined as

$$\left(\nabla^2 + k_0^2 \right) G(\vec{r}, \vec{r'}) = -\delta \left(\vec{r} - \vec{r'} \right) \ . \tag{2.47}$$

For unbounded space, a Green function describing outgoing waves is given by [57, p. 33]:

$$G(\vec{r}, \vec{r'}) = \frac{1}{4\pi} \frac{\exp \left[ik_0 |\vec{r} - \vec{r'}| \right]}{|\vec{r} - \vec{r'}|} \ . \tag{2.48}$$

With the help of Eq. (2.48) we can write a formal solution for the field equation (2.46) as the convolution of the Green function with right-hand side of equation representing radiation sources:

$$\vec{\tilde{E}}_d = \frac{4\pi}{c^2} \int d\vec{r'} \, G(\vec{r}, \vec{r'}) \left[\omega^2 \vec{\tilde{P}}(\vec{r'}) + c^2 \vec{\nabla} \left(\vec{\nabla} \cdot \vec{\tilde{P}}(\vec{r'}) \right) \right] \ , \tag{2.49}$$

Eq. (2.49) is the integral equivalent of the differential equation (2.46). This integral form is convenient to overcome the difficulty of comparing the two terms on the right-hand side of Eq. (2.46). Integrating by parts the term in grad $\vec{\nabla} \left(\vec{\nabla} \cdot \vec{\tilde{P}}(\vec{r'}) \right)$ twice[2] we obtain

$$\vec{\tilde{E}}_d = 4\pi k_0^2 \int d\vec{r'} \, G(\vec{r}, \vec{r'}) \left[\vec{\tilde{P}}(\vec{r'}) - \vec{n}(\vec{n} \cdot \vec{\tilde{P}}(\vec{r'})) \right] \ , \tag{2.50}$$

where $\vec{n} = (\vec{r} - \vec{r'})/|\vec{r} - \vec{r'}|$ is the unit vector from the position of the "source" to the observer. We assume that the condition that observation distance is much larger than radiation wavelength

---

[2]Knowing that

$$\int_{-\infty}^{\infty} d\vec{r'} \, G \vec{\nabla} \vec{P} = \cancel{G \vec{P}}^{\ 0} - \int_{-\infty}^{\infty} d\vec{r'} \, \vec{P} \vec{\nabla} G$$

$$\vec{\nabla} G(\vec{r}, \vec{r'}) = G(\vec{r}, \vec{r'}) \frac{(\vec{r} - \vec{r'})}{|\vec{r} - \vec{r'}|} \left(ik_0 + \frac{1}{|\vec{r} - \vec{r'}|} \right)$$

$|\vec{r} - \vec{r'}| \gg k_0$ holds for all values of $\vec{r}$ occurring in the integral in Eq. (2.50). We thus account for the radiation field only. Moreover, the edge term in the integration by parts vanishes since $\vec{P} = 0$ at infinity. We note that the combination of the first and second term in the integrand obviously exhibits the property that the diffracted field $\vec{E}_d$ is directed transversely with respect to vector $\vec{n}$, as it must be for the radiation field. Furthermore, one can see that only the second term is responsible for the polarization dependence.

Returning to X-ray optics, we can easily obtain that the second term in the integrand of Eq. (2.50) includes, in this case, an additional small factor proportional to the the diffraction angle $\theta_d \sim (\vec{n} \cdot \vec{P})/|\vec{P}| \ll 1$, which can be neglected under the grazing incidence approximation. Finally, we conclude that for describing the reflection of a coherent X-ray beam from the interface between two dielectrics, one can use the wave equation Eq. (2.41) under the grazing incidence condition with accuracy

$$\theta_i^2 \ll 1 \, ,$$
$$\theta_d^2 \ll 1 \, . \tag{2.51}$$

It is important that, in order for Eq. (2.41) to apply, it is not sufficient that the paraxial approximation for X-ray propagation in vacuum or in a dielectric be satisfied. Additionally, incident and diffracted angles relative to the interface between dielectric and vacuum must be small compared to unity, according to condition (2.51).

2.2.2 The split-step beam propagation method

Let us return to the model for inhomogeneous media given by the wave equation, Eq. (2.41). As discussed in the previous section, it is valid for the X-ray beam reflection from the surface at a small angle.

$$\nabla^2 \vec{E} + k_0^2 \epsilon \vec{E} = 0 \, . \tag{2.41 revisited}$$

We can always write the radiation beam in the form of it's amplitude and phase

$$\vec{E}(x, y, z) = \vec{A}(x, y, z) \exp[ik_0 z] \, . \tag{2.52}$$

By substituting this expression into Eq. (2.41) we derive the following equation for the complex field envelope:

$$\nabla_\perp^2 \vec{A} + \frac{\partial^2 \vec{A}}{\partial z^2} + 2ik_0 \frac{\partial \vec{A}}{\partial z} + k_0^2 \delta\epsilon \vec{A} = 0 \, , \tag{2.53}$$

where $\nabla_\perp^2$ denotes the transverse Laplacian, and $\delta\epsilon(x, y, z) \equiv \epsilon(x, y, z) - 1$. If the electric field is predominantly propagating along z-direction with an envelope $\vec{A}$ which varies slowly with respect to the wavelength, Eq. (2.52) separates slow from fast varying factors. We actually assume that $\vec{A}$ is a slowly varying function of z in the sense that

$$\left| \frac{\partial \vec{A}}{\partial z} \right| \ll k_0 \vec{A} \,. \tag{2.54}$$

This assumption physically means that, within a propagation distance along z of the order of the wavelength, the change in $\vec{A}$ is much smaller than $\vec{A}$ itself. With this assumption, Eq. (2.53) becomes the paraxial Helmholtz equation for $\vec{A}$ in inhomogeneous media, which reads

$$\nabla_\perp^2 \vec{A} + 2ik_0 \frac{\partial \vec{A}}{\partial z} + k_0^2 \delta\epsilon \vec{A} = 0 \,, \tag{2.55}$$

A large number of numerical methods can be used for analyzing beam propagation in inhomogeneous media. The split-step beam propagation method is an example of such methods. To understand the idea of this method, we re-write Eq. (2.55) in the operator form [58, 59]

$$\frac{\partial \vec{A}}{\partial z} = (\mathcal{D} + \mathcal{S})\vec{A} \,, \tag{2.56}$$

where $\mathcal{D} = -(2ik_0)^{-1}\nabla_\perp^2$ is the linear differential operator accounting for diffraction, also called the diffraction operator, and $\mathcal{S} = (ik_0/2)\delta\epsilon$ is the space-dependent, or inhomogeneous operator. Both operators act on $\vec{A}$ simultaneously, and a solution of Eq. (2.56) in operator form is given by

$$\vec{A}(x, y, z + \delta z) = \exp\left[(\mathcal{D} + \mathcal{S})\,\delta z\right] \vec{A}(x, y, z) \,. \tag{2.57}$$

Note that, in general, $\mathcal{D}$ and $\mathcal{S}$ do not commute. In order to see this, it is sufficient to consider the dependence of $\mathcal{S}$ on z. As a result, $\exp\left[(\mathcal{D} + \mathcal{S})\,\delta z\right] \neq \exp[\mathcal{D}\delta z] \exp[\mathcal{S}\delta z]$. More precisely, for two non-commuting operators $\mathcal{D}$ and $\mathcal{S}$, we have

$$\exp[\mathcal{D}\delta z] \exp[\mathcal{S}\delta z] = \exp[(\mathcal{D} + \mathcal{S})\delta z] + [\mathcal{D}, \mathcal{S}]\frac{\delta z^2}{2} + \dots \,, \tag{2.58}$$

where $[\mathcal{D}, \mathcal{S}] = \mathcal{D}\mathcal{S} - \mathcal{S}\mathcal{D}$ is the commutator of $\mathcal{D}$ and $\mathcal{S}$. However, for an accuracy up to the first order in δz, we can *approximately* write:

$$\exp[(\mathcal{D} + \mathcal{S})\delta z] \simeq \exp[\mathcal{D}\delta z] \exp[\mathcal{S}\delta z] \,. \tag{2.59}$$

This means that, when the propagation step δz is sufficiently small, the diffraction and the inhomogeneous operators can be treated independently of each other in Eq. (2.57), and we obtain

$$\vec{A}(x, y, z + \delta z) = \exp[\mathcal{S}\delta z] \exp[\mathcal{D}\delta z] \vec{A}(x, y, z) \,. \tag{2.60}$$

The role of the operator acting first, $\exp[\mathcal{D}\delta z]$, is better understood in the spectral domain. This is the propagation operator that takes into account the effect of diffraction between the planes at position z and $z + \delta z$. Propagation is readily handled in the spatial-frequency domain using

transfer function for propagation given by

$$H_A(k_x, k_y, \delta z) = \frac{\hat{A}(k_x, k_y, \delta z)}{\hat{A}(k_x, k_y, 0)} = \exp[-i(k_x^2 + k_y^2)\delta z/(2k_0)] . \qquad (2.61)$$

This is nothing but Eq. (2.13), specialized for the slowly varying envelope of the field.

Hence, the action of the exponential operator $\exp[\mathcal{D}\delta z]$ is carried out in the Fourier domain using the prescription

$$\exp[\mathcal{D}\delta z]\vec{A}(x, y, z) = FT^{-1}\left\{\exp[-i(k_x^2 + k_y^2)\delta z/(2k_0)]\hat{A}(k_x, k_y, \delta z)\right\} , \qquad (2.62)$$

where "FT^{-1}" refers to the inverse spatial Fourier transform defined as in Eq. (2.9). The second operator, $\exp[\mathcal{S}\delta z]$, describes the effect of propagation in the absence of diffraction and in the presence of medium inhomogeneities, and is well-described in the spatial domain.

Summing up, a prescription for propagating $A(x, y, z)$ along a single step in δz can be written as

$$
\begin{aligned}
A(x, y, z + \delta z) = {} & \exp[ik_0\delta\epsilon\,\delta z/2] \\
& \times FT^{-1}\left\{\exp[-i(k_x^2 + k_y^2)\delta z/(2k_0)]\hat{A}(k_x, k_y, \delta z)\right\} .
\end{aligned}
\qquad (2.63)
$$

The algorithm repeats the above process until the field has traveled the desired distance. The usefulness of the Fourier transform lies in the fact that one can reduce a partial differential operator to a multiplication of the spectral amplitude $\hat{A}(k_x, k_y, z)$ with a phase transformation function. Since $\mathcal{D}$ is just a number in the spatial Fourier domain, the evaluation of Eq. (2.60) is straightforward.

2.3 Grating Theory

The derivation of the grating condition describing the geometry of light diffraction by gratings presented in textbooks usually relies on Huygens principle. At variance, there is another treatment of gratings theory is based on first principles, namely Maxwell equations, still retaining basic simplicity.

2.3.1 Plane grating

Ruled gratings are essentially two-dimensional structures. As such, their surface S can be described by a function, e.g. $x = f(y, z)$, which expresses one of the three coordinates (in this case, x) as a function of the other two, Fig. 2.3. Let the beam be incident from vacuum ($x > 0$) on the periodic cylindrical interface illustrated in Fig. 2.4.
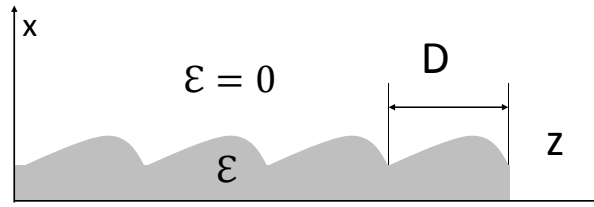
Figure 2.3: Grating geometry and notation.
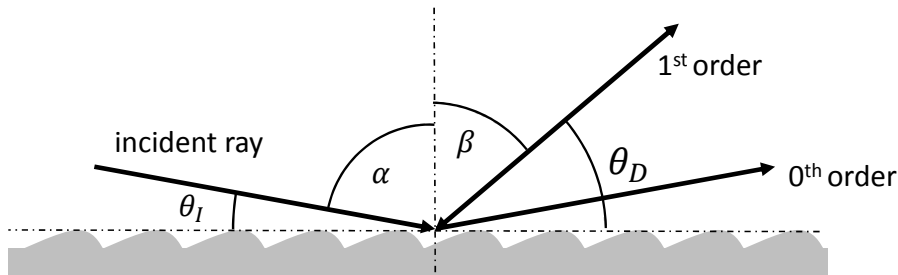
Figure 2.4: Scattering geometry for a diffraction grating. In this case angles have the following signs: $\alpha > 0$, $\beta < 0$.

In this case, since S is cylindrical, f can be considered as the only function of z independently on the value of y, and one has that $x = f(z)$ is a periodic function of period D (with spatial wave number $K = 2\pi/D$). Susceptibility is a periodic function of z and can be described by the Fourier series

$$\delta\epsilon = 4\pi\chi = \sum_{m=-\infty}^{\infty} u_m(x) \exp[imKz] \,. \tag{2.64}$$

We want to obtain a diffracted wave, which we express in its most general form as Eq. (2.50), from the knowledge of the field incident on the grating. Using the relation between $\vec{P}$ and $\vec{E}$,

and the explicit expression for G in Eq. (2.48) we can write the following integral equation for the electric field:

$$\vec{E}_d(\vec{r}) = \omega^2 \int d\vec{r'} \frac{\exp[ik_0|\vec{r} - \vec{r'}|]}{|\vec{r} - \vec{r'}|} \chi(x', z')$$
$$\times \left\{ \left[\vec{\bar{E}}_d(\vec{r'}) + \vec{\bar{E}}_i(\vec{r'}) \right] - \vec{n} \left[\vec{n} \cdot \left(\vec{\bar{E}}_d(\vec{r'}) + \vec{\bar{E}}_i(\vec{r'}) \right) \right] \right\} . \qquad (2.65)$$

In general case polarization of the medium is caused by both incident ($\vec{\bar{E}}_i$) and re diffracted ($\vec{\bar{E}}_d$) fields, which leads us to self-consistent problem. When we are interested in studying kinematic effects only, we can limit ourselves to the solution via perturbation theory ignoring dynamical effects. Assumption is that at all points within the dielectric medium the diffracted field $\vec{\bar{E}}_d$ is much smaller than the incident field $\vec{\bar{E}}_i$. This allows one to neglect the diffracted electric field on the right hand side of Eq. (2.65) with the incident field $\vec{\bar{E}}_i$, yielding

$$\vec{E}_d(\vec{r}) = k_0^2 \int d\vec{r'} \frac{\exp[ik_0|\vec{r} - \vec{r'}|]}{|\vec{r} - \vec{r'}|} \chi(x', z') \left[\vec{E}_i(\vec{r'}) - \vec{n} \left(\vec{n} \cdot \vec{E}_i(\vec{r'}) \right) \right] , \qquad (2.66)$$

where for simplicity we neglected the bar in the notation for the field in the space-frequency domain.

In order to compute $\vec{E}_d$ in Eq. (2.66) we need to specify the incident field distribution $\vec{E}_i(\vec{r'})$ within the dielectric medium. In fact, according to Eq. (2.66) the integration ranges over all coordinates $d\vec{r'}$, but χ is different from zero inside the dielectric. Consider Fig. 2.5, where we sketch the geometry for our problem. Monochromatic light from a point source $A(x_1, y_1, z_1)$ is incident on a point $P(x', y', z')$ located into the grating, i.e. into our dielectric medium. Point A is assumed, for simplicity, to lie in the xz plane, i.e. $A = A(x_1, 0, z_1)$. The plane xz is called the tangential plane (or the principal plane, or the dispersive plane). The plane yz is called the sagittal plane. As a first step we need to express the incident field $\vec{E}_i$, appearing in Eq. (2.66), at the generic point P inside the dielectric. In order to do so, since we deal with a point source, we can take advantage of the spatial impulse response of free-space. As we have seen, this is nothing but the expression for a spherical wave originating from A:

$$\vec{E}_i(x', y', z') = E_0 \frac{\exp[ik_0|\vec{r'} - \vec{r}_1|]}{|\vec{r'} - \vec{r}_1|} . \qquad (2.67)$$

After this, we consider that the beam is diffracted to the point $B = B(x_2, 0, z_2)$. Mathematically, diffraction is taken care of by the Green's function in Eq. (2.66), which represents a secondary source from point P. Finally, an explicit expression for χ is given in Eq. (2.64).

Even without explicit calculation of the integral in Eq. (2.66), a lot can be said analyzing the phase in the integrand. In fact, since integration in Eq. (2.66) involves an oscillatory integrand, the integrand does not contribute appreciably unless the arguments in the exponential functions vanishes. We therefore calculate the total phase in the integrand of Eq. (2.66), and analyze it.
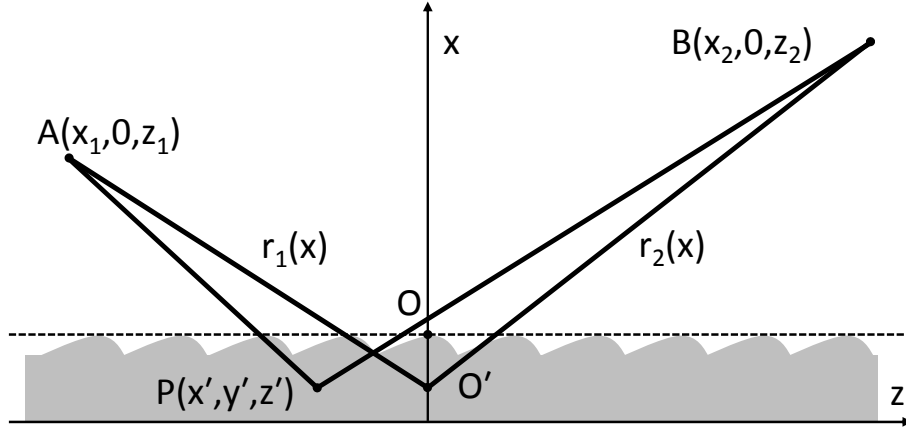
Figure 2.5: Schematic diagram of diffraction from a plane grating. The gray area represents the grating volume. A point source is located at A. Point P is an arbitrary point inside the grating volume. Grating can be divided into layers. Each layer is either homogeneous or modulated with refractive index that changes periodically as a function of z at any given height x.

Calculations can be simplified by applying the paraxial approximation. In fact, one can rely on it for writing expansions for $\overline{AP} = |\vec{r'} - \vec{r}_1|$ and $\overline{PB} = |\vec{r}_2 - \vec{r'}|$ entering into the expression for the phase. This can be done in terms of the distances $r_1(x) = \overline{AO'}$ and $r_2(x) = \overline{O'B}$, where $O' = (x', 0, 0)$, x' being the x-coordinate of point P. However, further simplifications apply by noting that, in paraxial approximation, light actually traverses a very small portion of material with susceptibility χ. The range of coordinates x', y', z' inside the grating is much smaller than the distances r_1 and r_2. In other words, the grating size and its thickness are much smaller than r_1 and r_2. Additionally, we assume that the grating thickness is much smaller than the relevant transverse size. Thus, we can neglect the dependence of distances r_1 and r_2 on x' in the expansion for the incident wave and in the Green function exponent, and use the approximations $r_1 \simeq \overline{AO}$ and $r_2 \simeq \overline{OB}$, where $O = (0, 0, 0)$ is a pole on the surface of grating, Fig. 2.5. Thus, the path AOB defines the optical axis of the beam, and the angle of incidence and of diffraction, α and β in Fig. 2.4, are simply following that optical axis. If points A and B lie on different sides of the xz plane, angles α and β have an opposite sign.

Starting from the expressions

$$
\begin{aligned}
\overline{AP}^2 &= [r_1 \sin\alpha + z']^2 + y'^2 + [r_1 \cos\alpha]^2 \ , \\
\overline{PB}^2 &= [r_2 \sin\beta + z']^2 + y'^2 + [r_2 \cos\beta]^2 \ ,
\end{aligned}
\tag{2.68}
$$

and using a binomial expansion we can write the incident wave phase as

27

$$\exp[ik_0|\vec{r'} - \vec{r_1}|] =$$
$$\exp\left[ik_0\left(r_1 + z'\sin\alpha + \frac{z'^2\cos^2\alpha}{2(r_1 + z'\sin\alpha)} + \frac{y'^2}{2(r_1 + z'\sin\alpha)}\right)\right] =$$
$$\exp\left[ik_0\left(r_1 + z'\sin\alpha + \frac{z'^2\cos^2\alpha}{2r_1} + \frac{y'^2}{2r_1} - \frac{z'^3\sin\alpha\cos^2\alpha}{2r_1^2} - \frac{z'y'^2\sin\alpha}{2r_1^2}\right)\right],$$

(2.69)

This exponent originates from Green function under the integral Eq. (2.66) as a function of the coordinates x', y' and z' of the point P on the grating. Similarly, one obtains

$$\exp[ik_0|\vec{r} - \vec{r'}|] =$$
$$\exp\left[ik_0\left(r_2 + z'\sin\beta + \frac{z'^2\cos^2\beta}{2(r_2 + z'\sin\beta)} + \frac{y'^2}{2(r_2 + z'\sin\beta)}\right)\right] =$$
$$\exp\left[ik_0\left(r_2 + z'\sin\beta + \frac{z'^2\cos^2\beta}{2r_2} + \frac{y'^2}{2r_2} - \frac{z'^3\sin\beta\cos^2\beta}{2r_2^2} - \frac{z'y'^2\sin\beta}{2r_2^2}\right)\right],$$

(2.70)

We will now show that the periodic structure of the gratings restricts the continuous angular distribution of the diffracted waves to a discrete set of waves only, which satisfy the well-known grating condition. In order to do so, we insert Eqs. (2.64, 2.69, and 2.70) into Eq. (2.66). As noticed above, the integrand does not contribute appreciably unless the arguments in the exponential functions vanishes. From Eqs. (2.64, 2.69, and 2.70) it follows that the total phase in Eq. (2.66) can be expressed as a power series

$$\phi = k_0[r_1 + r_2 + C_{10}z' + C_{20}z'^2 + C_{02}y'^2 + C_{30}z'^3 + C_{12}z'y'^2 + ...] .$$

(2.71)

Typically, third order aberration theory is applied to the analysis of grating monochromators. In that case, the power series needs to include third order terms. The explicit expressions for the coefficients C_{ij} are

$$C_{10} = \frac{nK}{k_0} + \sin\alpha + \sin\beta \ ,$$

$$C_{20} = \frac{1}{2}\left[\frac{1}{r_1}\cos^2\alpha + \frac{1}{r_2}\cos^2\beta\right] \ ,$$

$$C_{02} = \frac{1}{2}\left[\frac{1}{r_1} + \frac{1}{r_2}\right] \ ,$$

$$C_{30} = -\frac{1}{2r_1^2}\sin\alpha\cos^2\alpha - \frac{1}{2r_2^2}\sin\beta\cos^2\beta \ ,$$

$$C_{12} = -\frac{1}{2r_1^2}\sin\alpha - \frac{1}{2r_2^2}\sin\beta \ . \tag{2.72}$$

C_{20} and C_{02} are the coefficients describing defocusing. C_{30} describes the coma, and C_{12} the astigmatic coma aberration[3]. In practice, the most important ones are defocusing and coma. Ideal optics would require the phase ϕ to be independent of z' and y' coordinates along the grating

Note that the presence of the term nK/k_0 in the C_{10} coefficient directly follows from the insertion of Eq. (2.64) into Eq. (2.66). As said above, it is the periodic structure of the gratings which restricts the continuous angular distribution of the diffracted waves to a discrete set of waves. In order to find the direction of incident and diffracted beam, we impose the condition $C_{10} = 0$, yielding:

$$nK + k_0(\sin\alpha + \sin\beta) = 0 \ . \tag{2.73}$$

Eq. (2.73) is also valid for a plane mirror, if the grating period is taken equal to infinity. This fact can be seen inspecting Eq. (2.73), which yields $\alpha = -\beta$ for $D \longrightarrow \infty$, which is nothing but the law of mirror reflection.

Eq. (2.73) is known as the grating condition. This condition shows how directions of incident and diffracted waves are related. Both signs of the diffraction order n appearing into the equation are allowed. Assuming for simplicity diffraction into first order, i.e. $n = +1$, one has

$$\lambda = D(\cos\theta_i - \cos\theta_d) \ , \tag{2.74}$$

where θ_i and θ_d are the angles between the grating surface and, respectively, the incident and the diffracted directions. By differentiating this equation in the case of a monochromatic beam one obtains

$$b = \frac{d\theta_d}{d\theta_i} = \frac{\sin\theta_i}{\sin\theta_d} \tag{2.75}$$

Note that $b = W_i/W_d$ is the ratio between the width of the incident and of the diffracted beam. Fig. 2.6 shows the geometry of this transformation. As has been pointed out elsewhere this is

---

[3]Differences in sign for C_{10}, C_{30} and C_{12} with respect to literature are due to a different definition of the direction of the z-axis, which points towards B, and not towards A.
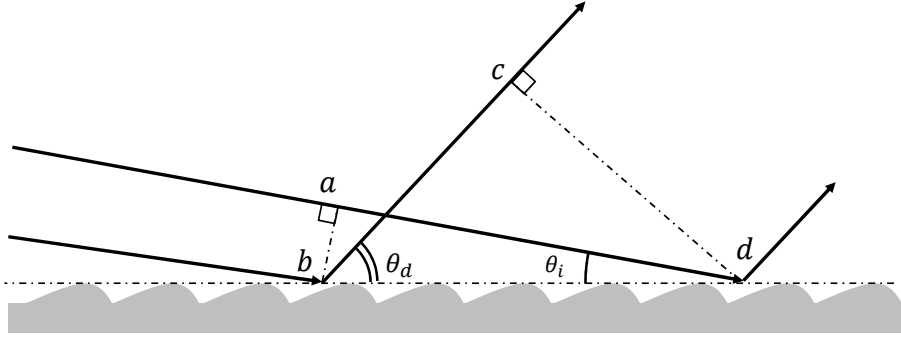
Figure 2.6: Geometry of the reflection. The properties of the grating are naturally described in terms of the asymmetry parameter $b = \sin(\theta_i)/\sin(\theta_d)$
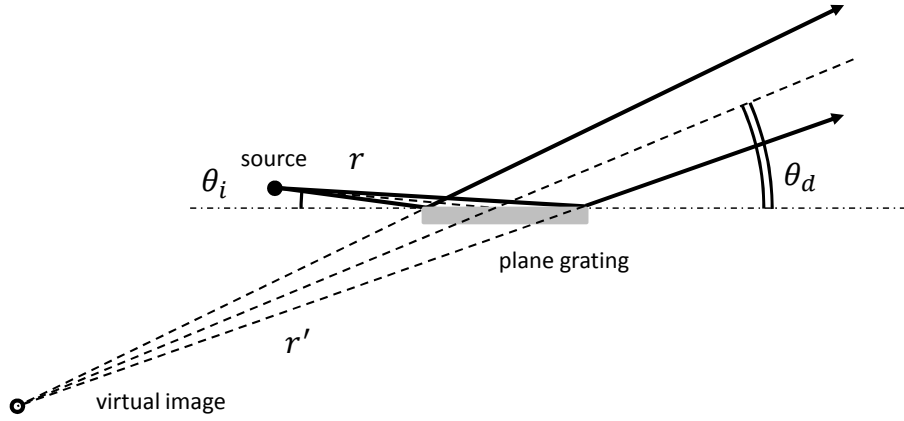
Figure 2.7: Plane grating in the case of a monochromatic point source. The virtual image of the real source is located at a distance $r' = r \cdot (\sin(\theta_d)/\sin(\theta_i))^2$ behind the grating.

just the consequence of Liouville's theorem.

The effect of the plane grating on the monochromatic beam is twofold: first, the source size is scaled by the asymmetry factor b defined in Eq. (2.75) and, second, the distance between grating and virtual source behind the grating is scaled by the square of the asymmetry factor b, Fig. 2.7. In order to illustrate this fact, we consider a 1D Gaussian beam with an initially plane wavefront, described by the field amplitude (along a given polarization component) $\psi(x,0) = exp[-x^2/w_0^2]$. Assuming that the plane grating is positioned at z, the spatial spectrum of the Gaussian beam immediately in front of the grating, i.e. after propagation in free-space by a distance z from the waist point, is given by

$$\psi(k_x, z) = \sqrt{\pi} w_0 \exp[ik_0 z] \exp\left[-\frac{k_x^2 w_0^2}{4}\right] \exp\left[-\frac{ik_x^2 z}{2k_0}\right] . \qquad (2.76)$$

However, according to Eq. (2.75), the transformation of the angular spectrum performed by grating can be described with the help of $k_x' = bk_x$, so that immediately after grating one obtains

$$\psi(k_x, z) = \sqrt{\pi} w_0 \exp[ik_0 z] \exp\left[-\frac{k_x'^2 w_0^2}{4b^2}\right] \exp\left[-\frac{ik_x'^2 z}{2k_0 b^2}\right] . \tag{2.77}$$

We can interpret Eq. (2.77) in the following way: the Gaussian beam diffracted by the grating is characterized by a new *virtual* beam waist $w_0' = w_0/b$ and by a new *virtual* propagation distance $z' = z/b^2$. Introducing the dimensionless distance through the relation z/L_R, where L_R is called the Rayleigh length, we can conclude that this dimensionless distance is invariant under the transformation induced by the plane grating.

The treatment of the diffraction grating given above yielded most of the important results needed for further analysis. In particular, it allowed one to derive the grating condition and it also makes it possible to study the theory of grating aberrations. Current theoretical approach reaches into the foundation of electrodynamics, as is based on the use of Maxwell equations. Note that the treatment considered so far was carried out under the assumption of the validity of the first order perturbation theory, i.e. we assumed that for all the points in the dielectric medium, the diffracted field is negligible with respect to the incident field. The properties of the field actually exploited amount to the fact that in the yz plane, the diffracted field has the same phase as the incident field plus an extra-phase contribution nKz'. If we go up to second and higher orders in the perturbation theory we can see that this property remains valid, and results derived above still hold independently of the application of a perturbation theory. Note that inside the grating the beam is attenuated with a characteristic length that is much shorter compared to the range of the grating surface coordinates, and can always be neglected in the phase expansion. We can immediately extend the range of validity of this analysis to arbitrary values of the dielectric constant. The general proofs of the grating condition and of the results of the theory of grating aberration are derived from first principles as follows [60].

First let us note that two-dimensional problems are essentially scalar in nature, and can be expressed in terms of only one single independent electromagnetic field variable, either E_y or H_y. Here we will work considering the TE polarization, i.e. we will focus on E_y. The action of the grating on the electromagnetic field can be modeled, mathematically, as an operator $\mathcal{G}$ that transforms an incident field into a diffracted field, i.e. $E_d(z,y) = \mathcal{G}[E_i(z,y)]$. Since the grating is periodic and extends to infinity, the action of the operator $\mathcal{G}$ is invariant under translation by a grating period: $E_d(z+D,y) = \mathcal{G}[E_i(z+D,y)]$. Since the incoming beam is incident at an angle θ_i, this translation adds an extra path distance $D\cos\theta_i$ to the incident wave E_i, for a phase change

$$E_i(z+D, y) = \exp(ik_0 D \cos\theta_i) E_i(z,y) . \tag{2.78}$$

Also, since the set of Maxwell partial differential equations is linear, any solution multiplied by a constant is still a solution and one obtains

$$\mathcal{G}[E_i(z+D,y)] = \mathcal{G}[\exp(i\delta\phi)E_i(z,y)] = \exp(i\delta\phi)\mathcal{G}[E_i(z,y)] = \exp(i\delta\phi)E_d(z,y) , \tag{2.79}$$

where $\delta\phi = k_0 D \cos\theta_i$. Now, since

$$\mathcal{G}[E_i(z + D, y)] = E_d(z + D, y) \tag{2.80}$$

we must have

$$\exp(i\delta\phi)E_d(z, y) = E_d(z + D, y) . \tag{2.81}$$

Now, since the product $E_d \exp[-ik_0 z \cos\theta_i]$ is a periodic function, it can be represented as a Fourier series expansion on the grating period D, and we can write the diffracted field as

$$E_d(z, y) = \sum_{m=-\infty}^{+\infty} E_m(y) \exp[imKz + ik_0 z \cos\theta_i] . \tag{2.82}$$

This result is fully general, and all that is required to prove it is that the grating is periodic. Eq. (2.82) is sufficient for describing the geometry of the beam diffraction by the grating. We can use Eq. (2.82) to derive the grating condition once again.

In order to illustrate this fact, we see that the phase of the integrand in the integral Eq. (2.65) consists of three terms: the first term is the phase in the Green function, the second is the phase in Eq. (2.64), and the third is the phase in $\vec{E}_d$. The first and the second terms are known, and have already been analyzed. Eq. (2.82) shows the structure of the phase for $\vec{E}_d$ in the case for a plane wave impinging on the grating with incident angle θ_i. In principle, the incident field $\vec{E}_i$ comes from a point source located in A, and consists of a diverging spherical wave. Such spherical wave can always be decomposed in plane waves and, due to the validity of the paraxial approximation, only those plane wave components with angle near to θ_i should be considered. Therefore, neglecting small corrections in $\Delta\theta_i$, one can take the phase in Eq. (2.82) as a good approximation for the phase of the diffracted field. Then, considering the expansion in Eq. (2.70) to the first order in z' one obtains, without using a perturbative approach, that the term in z' in the integrand in Eq. (2.65) is given by $(m + n)K + k_0(\cos\theta_i - \cos\theta_d)$. Imposing that this term be zero, and remembering that $\alpha = \pi/2 - \theta_i$, one gets back Eq. (2.73).

This result, albeit very general, still says nothing about the grating efficiency. We still do not know anything about the amplitudes of the diffracted waves. In order to determine these coefficients we need to model the grooves of the grating. At this point, we need to apply classical numerical integration techniques [61, 62].

2.3.2 VLS plane grating

A diffractive plane grating can focus a diffracted beam when the groove spacing properly varies with the groove position; such a grating is called a variable-line-spacing (VLS) grating. A VLS plane grating can be incorporated into the monochromator to act as both dispersive and spectrally focusing component. The working principle of such kind of grating can be understood by expressing the groove spacing $D(z)$ as a function of the coordinate z along the perpendicular

to the grooves. So it can be expanded as a polynomial series[4]:

$$D(z) = D_0 + D_1 z + D_2 z^2 + ... , \tag{2.83}$$

where the term D_0 is the spacing at the pole of the grating (located, by definition, at $z = 0$), while D_1 and D_2 are the parameters for the variation of the ruling with z. Now susceptibility is not a periodic function of z anymore, and can be described by the Fourier integral:

$$\delta\epsilon = 4\pi\chi = \int_{-\infty}^{\infty} B(K, x) \exp[iKz] dK . \tag{2.84}$$

Let us assume, for simplicity, that the distance between grooves varies according to the linear law: $D(z) = D_0 + D_1 z$. Now we also assume that $D_1 \ll 1$ and we apply the so-called adiabatic approximation imposing that the width of the peaks in the spectrum $B(K, x)$ is much narrower than the harmonic separation $K_0 = 2\pi/D_0$ between the peaks. In this case, Eq. (2.84) can be represented in the form

$$\delta\epsilon = \sum_{n=-\infty}^{+\infty} B_n(x, z) \exp[inK_0 z] , \tag{2.85}$$

where the complex amplitudes $B_n(x, z)$ are all slowly varying function of the z coordinate on the scale of the period D_0. This means that the terms in sum over n in Eq. (2.85) can be analyzed separately for each value of n. For the case of a linearly chirped grating considered here, the slowly varying amplitude of the nth harmonic is given by

$$B_n = A_n(x) \exp\left[i\frac{z^2}{2}\frac{dK}{dz}\right] , \tag{2.86}$$

where $dK/dz = 2\pi d(1/D)/dz = -(2\pi/D_0^2)D_1$ is the chirp parameter.

We now substitute Eq. (2.85) into Eq. (2.66) and, as before, we express the phase in the integrand as a power series. Only the C_{20} term differs, with respect to the expression in Eq. (2.72). In fact, for a linearly chirped grating we obtain [63]

$$C_{20} = -\frac{\lambda}{2D_0^2}D_1 + \frac{1}{2r_1}\cos^2\alpha + \frac{1}{2r_2}\cos^2\beta . \tag{2.87}$$

The condition $C_{20} = 0$ has to be verified in order to guarantee imaging in the tangential plane.

Here we used Maxwell equations for studying the imaging properties of VLS grating. However, certain aspects of this theory can be derived in a simple way using ray optics. For convenient use in the following discussions, it is necessary to make clear the reference coordinate systems and rays describing the optical system. Fig. 2.8 shows the VLS plane grating optical system with an object point A. The coordinate systems (x, y, z), (x_1, y_1, z_1) and (x_2, y_2, z_2) correspond, respectively, to the grating, to the incident beam, and to the diffracted beam; the

---

[4]Another choice of line-spacing parametrization found in literature is the expansion of the line density $n(z) = 1/D(z) = n_0 + n_1 z + n_2 z^2 + ...$. With these definitions, n_1 and n_2 are the same as in Tables 3.3 and 4.2.
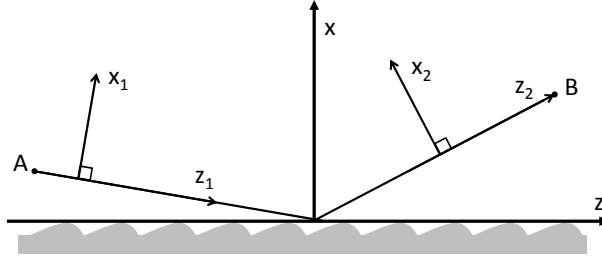
Figure 2.8: Coordinate notation. The coordinate systems (x, y, z), (x_1, y_1, z_1) and (x_2, y_2, z_2) correspond to grating, incoming beam and diffracted beam; the axes z, z_1 and z_2 are along grating surface, incident and exit principal rays respectively.

axes z, z_1 and z_2 are along the grating surface, the incident and the exit principal rays, respectively. As shown in Fig. 2.4, the input beam is incident on grating at angle θ_i. The diffracted angle θ_d is a function of the groove distances according to the grating equation

$$\lambda = D(\cos\theta_i - \cos\theta_d) . \tag{2.88}$$

By differentiating over z for the case of a monochromatic beam we obtain

$$\frac{dD}{dz}(\cos\theta_i - \cos\theta_d) = -\frac{d\theta_d}{dz}D\sin\theta_d , \tag{2.89}$$

yielding

$$[\lambda/D_0^2(\sin^2\theta_d)]D_1 = -\frac{d\theta_d}{dx_2} , \tag{2.90}$$

where we used the relations (2.83), $z\sin\theta_d = x_2$ and $D_1 \ll 1$.

Let us now define a thin lens as a device that deflects every light beam incident parallel to the optical axis in such a way that it crosses the optical axis at a fixed distance f after passing through the lens. In paraxial approximation, the thin lens equation assumes the familiar form $d\theta_d = -dx_2/f$. The physical meaning of Eq. (2.90) is that the VLS plane grating can be represented by a combination of a planar grating with fixed line spacing and a lens after the grating, with a focal length f equal to the focal length of the VLS grating

$$f = [\lambda D_1/D_0^2(\sin^2\theta_d)]^{-1} , \tag{2.91}$$

as shown in Fig. 2.9. It may seem surprising that the focal length depends on θ_d only. However, it is reasonable to expect an influence of the assumption that the lens is placed after the grating. One intuitively expects that full transfer matrix for the VLS grating should not depend on the choice of the lens position. It may be shown that indeed, the transfer matrix satisfies this invariance (See Appendix A).
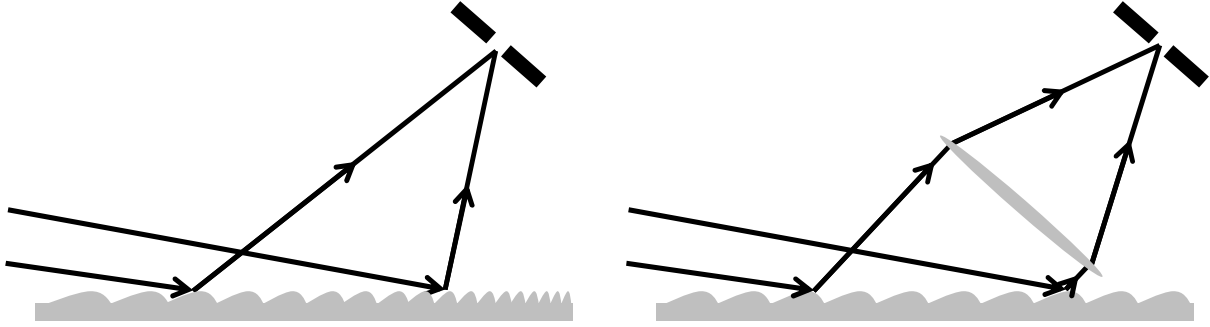
Figure 2.9: Schematic diagram of a VLS grating element used in theoretical analysis. The VLS grating is represented by a contribution of a planar grating with fixed line spacing and a thin lens.

2.3.3 Toroidal grating

A logical extension of the plane VLS grating concept described above follows from the idea to rule the VLS grooves on a toroidal surface, producing a toroidal VLS grating [64]. Additional design parameters, namely tangential and sagittal radius, are then available to control imaging aberrations and to optimize the grating monochromator performance [65]. We consider a curved VLS grating and we assume that the surface of the grating is toroidal with tangential and sagittal radius of curvature R and ρ respectively (see Fig. 2.10). Let us assume that the distance between the grooves varies according to quadratic law:
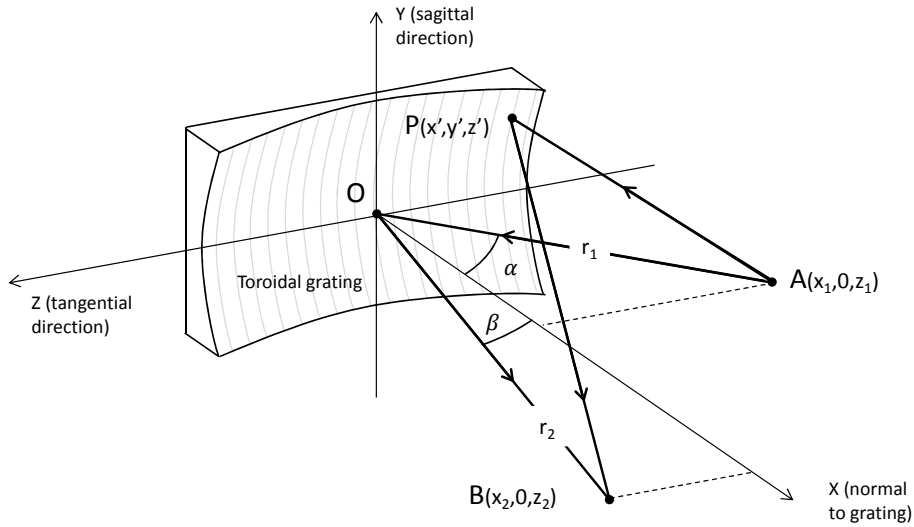
Figure 2.10: Schematic diagram of a toroidal grating. A point source is located at A. Point P is an arbitrary point of the grating.

$$D(z) = D_0 + D_1 z + D_2 z^2 \ . \tag{2.92}$$

As before, the susceptibility is not a periodic function with respect to z, and in adiabatic approximation can be represented in the form

35

$$\delta\epsilon = \sum_{-\infty}^{+\infty} B_n(x,z) \exp[inK_0 z] \, , \tag{2.93}$$

which is identical to Eq. (2.85), where complex amplitudes B_n are slowly varying functions of the z coordinate on the scale of the period D_0. In the case of quadratically chirped grating, the nth amplitude is given by

$$B_n = A_n(x) \exp[iK'z^2/2 + iK''z^3/6] \, , \tag{2.94}$$

where

$$\begin{aligned}
K' &= 2\pi(1/D)' = -2\pi D_1/D_0^2 = 2\pi n_1 \, , \\
K'' &= 2\pi(1/D)'' = -4\pi[D_2/D_0^2 - D_1^2/D_0^3] = 4\pi n_2 \, ,
\end{aligned} \tag{2.95}$$

are the linear and quadratic chirp parameters.

From the geometry (see Fig. 2.10), and similarly as done before we can write

$$\begin{aligned}
\overline{AP}^2 &= [r_1 \sin\alpha + z]^2 + y^2 + [r_1 \cos\alpha - x]^2 \, , \\
\overline{PB}^2 &= [r_2 \sin\beta + z]^2 + y^2 + [r_2 \cos\beta - x]^2 \, ,
\end{aligned} \tag{2.96}$$

where the coordinate x on the toroidal surface is related to z and y by the equation of the torus

$$x = R - R\left[1 - \frac{z^2+y^2}{R^2} + 2\frac{\rho}{R}\left(\frac{\rho}{R}-1\right)\left(1 - \left(1 - \frac{y^2}{\rho^2}\right)^{1/2}\right)\right]^{1/2} \, . \tag{2.97}$$

The integrand in Eq. (2.66) is oscillatory, and does not contribute appreciably to the total integral unless the arguments of the exponential function vanishes. Using Eqs. (2.66, 2.69 and 2.70), together with Eqs. (2.93, 2.94, 2.96 and 2.97), it is then possible to expand the phase as a power series such as

$$\phi = k_0(r_1 + r_2 + C_{10}z + C_{20}z^2 + C_{02}y^2 + C_{30}z^3 + C_{12}zy^2 + ...) \, . \tag{2.98}$$

The explicit expressions for coefficients C_{ij} are [66]

$$C_{10} = \frac{n\lambda}{D_0} + (\sin\alpha + \sin\beta) \, ,$$

$$C_{20} = \frac{n\lambda n_1}{2} + \frac{1}{2}\left[\frac{\cos^2\alpha}{r_1} + \frac{\cos^2\beta}{r_2} - \frac{\cos\alpha}{R} - \frac{\cos\beta}{R}\right] \, ,$$

$$C_{30} = \frac{n\lambda n_2}{3} - \frac{1}{2}\left[\left(\frac{\cos^2\alpha}{r_1} - \frac{\cos\alpha}{R}\right)\frac{\sin\alpha}{r_1} + \left(\frac{\cos^2\beta}{r_2} - \frac{\cos\beta}{R}\right)\frac{\sin\beta}{r_2}\right] \, ,$$

$$C_{02} = \frac{1}{2}\left[\frac{1}{r_1} - \frac{\cos\alpha}{\rho} + \frac{1}{r_2} - \frac{\cos\beta}{\rho}\right] \, ,$$

$$C_{12} = -\frac{1}{2}\left[\left(\frac{1}{r_1} - \frac{\cos\alpha}{\rho}\right)\frac{\sin\alpha}{r_1} + \left(\frac{1}{r_2} - \frac{\cos\beta}{\rho}\right)\frac{\sin\beta}{r_2}\right] \, , \tag{2.99}$$

where the condition $C_{10} = 0$ yields back the grating condition, $C_{20} = 0$ yields the position of the tangential focus, $C_{02} = 0$ that of the sagittal focus, and the relation $C_{30} = 0$ minimizes the coma aberration.

In Appendix B it is shown that toroidal grating aberrations can be modeled very straightforwardly using a geometrical approach. This derivation is very different from the analytical method used in literature and it relies on geometrical considerations giving an intuitive understanding of Equations (2.99).

2.3.4 Concluding remarks for wave optics simulations

As we mentioned before, the radiation distribution that is modified by an optical component may be modeled by a phase-shifter in the following way:

$$\vec{E}(\omega, x, y) = \vec{E}_0(\omega, x, y)\exp\left[i\Delta\Phi(x, y, ...)\right] \, . \tag{2.100}$$

It is convenient to modify convention of coordinate notation, swapping y and z coordinates, so that coordinate z becomes the principle axis of an optical system, x, y become the axes of a phase shifter, perpendicular to z. Here the phase shift $\Delta\Phi$ is determined by various parameters, depending on the effect we want to model.

For example, a lens introduces a quadratic phase shift:

$$\Delta\Phi(x, y) = -\frac{k}{2}\left(\frac{x^2}{f_x} + \frac{y^2}{f_y}\right) . \tag{2.101}$$

Here the shift in both transverse dimensions x and y is introduced, representing focusing with different focal distances f_x and f_y.

Tangential and sagittal curvatures of a toroidal grating act as independent cylindrical lenses

with the focal lengths in case of a first order diffraction are given by

$$f_{sag} = \left[\frac{\sin\theta_i}{2\rho} + \frac{\sin\theta_d}{2\rho} \right]^{-1} \qquad (2.102)$$

for sagittal plane and

$$f_{tang} = \left[\frac{\lambda D_1}{D_0^2 \sin^2\theta_d} + \frac{\sin\theta_i}{2R\sin^2\theta_d} + \frac{1}{2R\sin\theta_d} \right]^{-1} \qquad (2.103)$$

for tangential. The latter is composed of curvature and VLS components.

Here R and ρ are tangential and sagittal radii of curvature, θ_i and θ_d are incidence and diffraction angles respectively. Eqs. 2.102 and 2.103 show that focal lengths are wavelength-dependent, since $\theta_d = \arccos(\cos\theta_i - \lambda D_0)$, according to the grating equation.

While the D_0 coefficient defines the dispersive properties of the grating, coefficients D_1 and D_2 are responsible of VLS focusing and aberration compensation correspondingly. They are optimized to eliminate wavelength dependence of an image position at a slit and the coma aberration effect. It is worth mentioning that an effective source position of radiation at the end of SASE undulator is wavelength-dependent (see Section 4.2.2).

The resulting phase shift from focusing contribution can be expressed as

$$\Delta\Phi(\omega, x, y) = -\frac{k_0}{2} \left(\frac{x^2}{f_{tang}} + \frac{y^2}{f_{sag}} \right). \qquad (2.104)$$

Both C_{30} and C_{12} coefficients can be expressed in angles with respect to the surface

$$C_{30} = \frac{n\lambda n_2}{3} + \left(\frac{\sin^2\theta_i}{r_1} - \frac{\sin\theta_i}{R} \right) \frac{\cos\theta_i}{2r_1} - \left(\frac{\sin^2\theta_d}{r_2} - \frac{\sin\theta_d}{R} \right) \frac{\cos\theta_d}{2r_2},$$

$$C_{12} = -\frac{1}{2} \left(-\frac{\sin\theta_i \cos\theta_i}{\rho r_1} + \frac{\cos\theta_i}{r_1^2} + \frac{\sin\theta_d \cos\theta_d}{\rho r_2} - \frac{\cos\theta_d}{r_2^2} \right), \qquad (2.105)$$

resulting in a following phase shift

$$\Delta\Phi(\omega, x, y) = k \left(\frac{C'_{30} x^3}{\theta_d^3} + \frac{C_{12} xy^2}{\theta_d} \right). \qquad (2.106)$$

In order to simulate time-dependent phenomena caused by grating one needs to take into account grating dispersion. We propose to introduce a wavefront tilt, according to an angular dispersion of the grating. Each wavelength is reflected from the grating at a different angle. Having an ensemble of wavelengths we can choose a principle ray wavelength λ that will propagate downstream with no wavefront tilt. Each other wavelength will propagate from the grating at a certain angle from the principle ray, determined by grating angular dispersion, e.g. $\lambda_0 + \Delta\lambda$

will be tilted by:

$$\Delta\theta = \frac{\Delta\lambda D_0}{\theta_d} \ .$$

(2.107)

In this case a linear phase tilt should be applied with respect to the principal ray frequency ω_0:

$$\Delta\Phi(\omega_0, \Delta\omega, x, y) = -\frac{2\pi x \Delta\theta}{\lambda_0} = \frac{2\pi x \Delta\omega D_0}{\omega_0\theta_d} \ .$$

(2.108)

Finally, the cumulative effect of the grating modeling may be written as

$$\vec{E}(\omega, x, y) = \vec{E}_0(\omega, x, y) \exp\left[i\Delta\Phi\right] \ ,$$
$$\Delta\Phi = k \left(-\frac{x^2}{2f_{tang}} - \frac{y^2}{2f_{sag}} + \frac{C'_{30}x^3}{\theta_d^3} + \frac{C_{12}xy^2}{\theta_d} + \frac{2\pi x \Delta\omega D_0}{k\omega\theta_d} \right) \ .$$

(2.109)

In case of the non-dispersive optical component, phase shift is similar to the grating, but D_0, D_1 and D_2 VLS coefficients are equal to zero, $\theta_i = \theta_d$, and no field resizing should be applied.

The total phase shift by such a mirror is given by the following:

$$\vec{E}(\omega, x, y) = \vec{E}_0(\omega, x, y) \exp\left[i\Delta\Phi\right] \ ,$$
$$\Delta\Phi = k \left(-\frac{x^2}{2f_{tang}} - -\frac{y^2}{2f_{sag}} + \frac{C_{30}x^3}{\theta_d^3} + \frac{C_{12}xy^2}{\theta_d} \right) \ ,$$
$$f_{tang} = \frac{R_{tang}\theta_i}{2} \ ,$$
$$f_{sag} = \frac{2\theta_i}{\rho} \ ,$$
$$C_{12} = -\frac{\cos\theta_i}{2} \left[\frac{\sin\theta_i}{R_{sag}} \left(-\frac{1}{z_1} + \frac{1}{z_2} \right) + \frac{1}{z_1^2} - \frac{1}{z_2^2} \right] \ ,$$
$$C_{30} = -\frac{\sin\theta_i\cos\theta_i}{2} \left[\sin\theta_i \left(\frac{1}{z_1^2} - \frac{1}{z_2^2} \right) - \frac{1}{R_{tang}} \left(\frac{1}{z_1} - \frac{1}{z_2} \right) \right] \ .$$

(2.110)

Here θ_i is M_2 incidence angle, z_1 and z_2 are distances the mirror to an object and an image, respectively.

2.4 Resolution

A preliminary resolution study of the toroidal grating can be performed using Gaussian optics calculations. The reason for first modeling the source as a Gaussian beam was to obtain

a completely analytical, albeit approximated description of the self-seeding monochromator operation. In fact, such approach gives the upper estimate of the grating resolving power.

2.4.1 Analytical description

Let us consider the toroidal VLS grating described in the previous section, and the incident radiation beam, characterized by a Gaussian distribution. Gaussian beam transformation due to mirrors, and translation in between mirrors can be tracked using the law for the transformation of q in Eq. (2.30). The relevant geometry is shown in Fig. 2.10. The grating has a local groove spacing $D(z) = D_0 + D_1 z$ at a position z on the grating surface, a radius of curvature of the substrate R in the tangential plane, and ρ in the sagittal plane. In the tangential plane, a toroidal VLS grating is represented by combination of a planar grating with fixed line spacing and lens after the grating, Fig. 2.9, with a focal length equal to the focal length of the toroidal VLS grating (Equations 2.102 and 2.103)

In current analysis we calculate the propagation of the input signal to the slit plane of the monochromator. We start by writing the input field in object plane, that is the source plane, as

$$\tilde{E}(x, y) = \exp\left[-\frac{x^2}{w_0^2} - \frac{y^2}{w_0^2}\right] . \tag{2.111}$$

As shown in Fig. 2.4, the input beam is incident on the grating at the angle θ_i. The diffracted beam emerges at an angle θ_d, and is a function of the wavelength according to grating equation. Assuming diffraction into $n = +1$ order, one has

$$\lambda = D_0(\cos\theta_i - \cos\theta_d) . \tag{2.112}$$

By differentiating this equation one obtains

$$\frac{d\theta_d}{d\lambda} = \frac{1}{D_0\theta_d} , \tag{2.113}$$

where we assume grazing incidence geometry, $\theta_i \ll 1$ and $\theta_d \ll 1$. The physical meaning of this equation is that different spectral components of the outgoing beam travel in different directions. As aforementioned, in the tangential plane the toroidal VLS grating is represented as a combination of plane grating and convergent lens. We are interested in determining the intensity distribution in the image plane, i.e. at the slit position. The grating introduces an angular dispersion, which is transformed into the spatial dispersion in the slit plane bu the lens. The spatial dispersion parameter, which describes the proportionality between spatial displacement and optical wavelength is given by

$$\eta = \lambda\frac{dx}{d\lambda} = \frac{d_2\lambda}{D_0\theta_d} , \tag{2.114}$$

where d_2 is the distance between grating and image plane. In our case study, the relative difference between focal length and image distance is about 1%. As a result one may approximately

write $d_2 = f_1$. The spectral resolution of the monochromator equipped with an exit slit depends on the spot size in the slit plane, is related with the individual wavelengths composing the beam, and with the rate of spatial dispersion with respect to the wavelength. For a Gaussian input beam, the intensity distribution in the waist plane, that is the slit plane, is given by $I = \exp(-2x^2/w_s^2)$, where w_s is the waist size on the slit. A properly defined merit function is indispensable for the design of a grating monochromator. A merit function based on the spread of the radiation spots is a suitable choice in our case of interest. Let us consider the limiting case of a slit with much narrower opening than the spot size of the beam for a fixed individual wavelength centered at $x = 0$. In this case, the Gaussian instrumental function (i.e. the spectral line profile of the beam after monochromatization) is given by

$$I = \exp\left[-2\left(\frac{f_1\lambda}{w_s D_0\theta_d}\right)^2\left(\frac{\Delta\lambda}{\lambda}\right)^2\right] . \tag{2.115}$$

The resolving power is often associated to the FWHM $\Delta\lambda$ of the instrumental function through the relation $R = \lambda/(\Delta\lambda)$. In our case of interest the resolving power is consequently given by

$$R = \frac{f_1\lambda}{1.18 w_s D_0\theta_d} . \tag{2.116}$$

The effect of a plane grating on the monochromatic beam is, as previously discussed, twofold: first, the source size is scaled by the asymmetry factor $b = \theta_i/\theta_d$ and, second, the distance between grating and virtual source before the grating is scaled by the square of the asymmetry factor. In our case, the waist of the virtual source w_0' and the distance d_1' are thus given by

$$w_0' = w_0\theta_d/\theta_i ,$$
$$d_1' = d_1(\theta_d/\theta_i)^2 . \tag{2.117}$$

After propagation through a distance d_2 behind the lens, the Gaussian beam is said to be focused at the point where it has a plane wavefront. Using Eq. (2.32), we obtain

$$w_s = \frac{w_0' f_1}{[(d_1' - f_1)^2 + z_R'^2]^{1/2}} , \tag{2.118}$$

where $z_R' = z_R(\theta_d/\theta_i)^2$ is the Rayleigh range associated with the virtual source. In our case of interest, $f_1/d_1' \sim 10^{-2}$, and the waist transforms as

$$w_s = w_0\frac{\theta_i}{\theta_d}\frac{f_1}{[d_1^2 + z_R^2]^{1/2}} . \tag{2.119}$$

Using this relation we can recast the expression for the resolving power in the form

$$R = \frac{\lambda z_R(1 + d_1^2/z_R^2)^{1/2}}{1.18 w_0\theta_i D_0} = \frac{\pi w_0(1 + d_1^2/z_R^2)^{1/2}}{1.18\theta_i D_0} , \tag{2.120}$$

41

and with the help of Eq. (2.31), we finally obtain

$$R = \frac{\pi w_g}{1.18\theta_i D_0} \,,$$ (2.121)

where w_g is the actual waist size of the Gaussian beam after propagation through a distance d_1, i.e in the plane immediately in front of the grating. In that plane beam has finite radius of curvature and its intensity is given by

$$I = I_0 \exp\left[-2\frac{x^2}{w_g^2}\right].$$ (2.122)

2.4.2 Self-seeding requirements

As mentioned before, the goal of a self-seeding scheme is to create the longitudinally coherent pulse. This pulse power should be high enough to overcome the shot noise in the electron beam and create the electron density modulation (bunching) at a given frequency. Let's consider an unchirped transform-limited pulse with a Gaussian shape in time domain:

$$E(t) = A \exp\left[-\frac{t^2}{2\sigma_t^2}\right].$$ (2.123)

We can define a pulse length as a FWHM of the temporal pulse intensity $\delta t \simeq 2.35\sigma_t^{intensity} \simeq 1.17\sigma_t$. In this case the FWHM of the pulse spectrum $\delta\omega$ is related to the pulse duration with the following relation [67]:

$$\delta t \delta\omega = 4\ln 2 \simeq 2.77,$$ (2.124)

which is more convenient to use in other form:

$$\delta s = 0.44\lambda R\,, \frac{4\ln 2}{\omega}\frac{\omega}{\delta\omega},$$ (2.125)

where δs is the pulse length intensity FWHM, λ is the radiation wavelength and $R = \frac{\omega}{\delta\omega}$.

This relation is visualized on the Fig. 2.11. We are interested to obtain a narrow-bandwidth transform-limited pulse after the monochromator that has the length close to the length of the electron beam. Longer pulse will lead to an energy loss, since radiation power distributed beyond the electron beam will not interact with electrons in an FEL process. Shorter pulse would not provide a coherent density modulation over an entire electron bunch, leading to the creation of more than one mode in both time and frequency domains.

2.5 Effects of mirror surface height errors

A very important issue of the radiation transport is the preservation of the wavefront from the source to the entrance of the second undulator. Estimates of the requirements on the mirror for
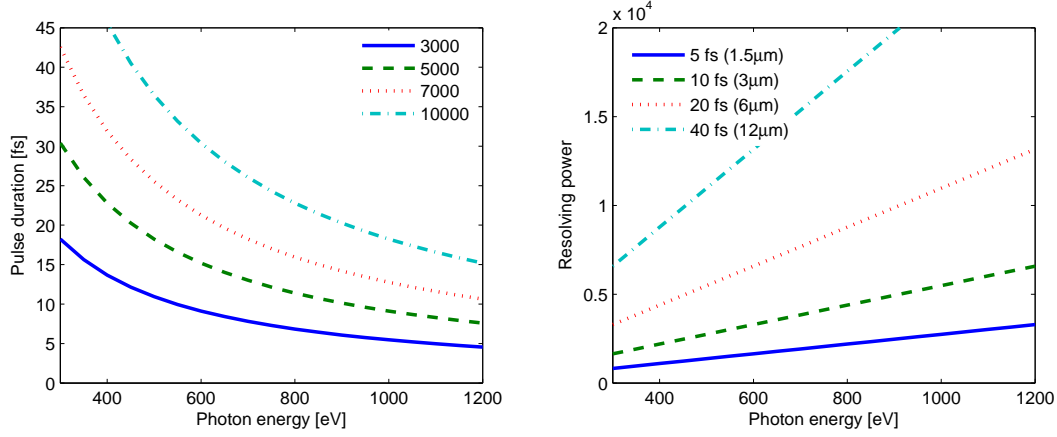
Figure 2.11: Monochromator resolving power required to create the bandwidth-limited pulse with a given FWHM duration for a certain photon energy.

grating monochromators are usually based on ray-tracing codes for incoherent light sources. Since the XFEL beam is almost transform-limited, one needs to perform simulations of the effect of the mirror imperfections by wavefront propagation codes. In the wave optical model, the height error contribution to the scattered field can be expressed as a perturbation of the wavefront according to an optical path difference (OPD) [68]. It is easy to demonstrate that an error δh on the optical surface will perturb the wavefront of a phase ϕ, according to

$$\phi = \frac{4\pi\delta h}{\lambda} \sin\theta_i \,, \tag{2.126}$$

where θ_i is the angle of incidence with respect to the surface. In the case of a grating, the phase shift can be expressed in terms of incidence and diffracted angles:

$$\phi = 2\pi(\sin\theta_i + \sin\theta_d)\frac{\delta h}{\lambda} \,. \tag{2.127}$$

In practice, ϕ represents the deformation of the wavefront in the propagation direction divided by the wavelength. For the shifter model to be applicable, the phase change must be small, i.e. $|\phi| \ll 1$.

A reflection from the mirror becomes similar to the propagation through a transparency at the mirror position, which just changes the phase of the reflected beam without changing its amplitude, (see Fig. 2.12).
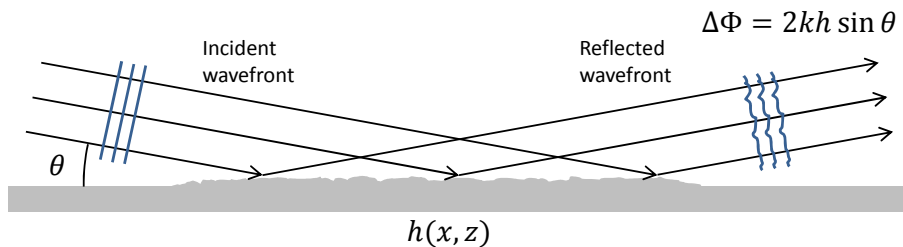
Figure 2.12: Thin-shifter-like behavior of surface roughness for small mean square of surface displacement. Adapted from [69].

On Figure 2.13 this model is compared with a split-step propagation method, described in Section 2.2.2.

This comparison shows a very good agreement between the two methods. Unlike a split-step method, the phase-shifter model allows a quick numerical evaluation of the disturbed wavefront and is used to model effects caused by height errors of the optical elements later in this work.
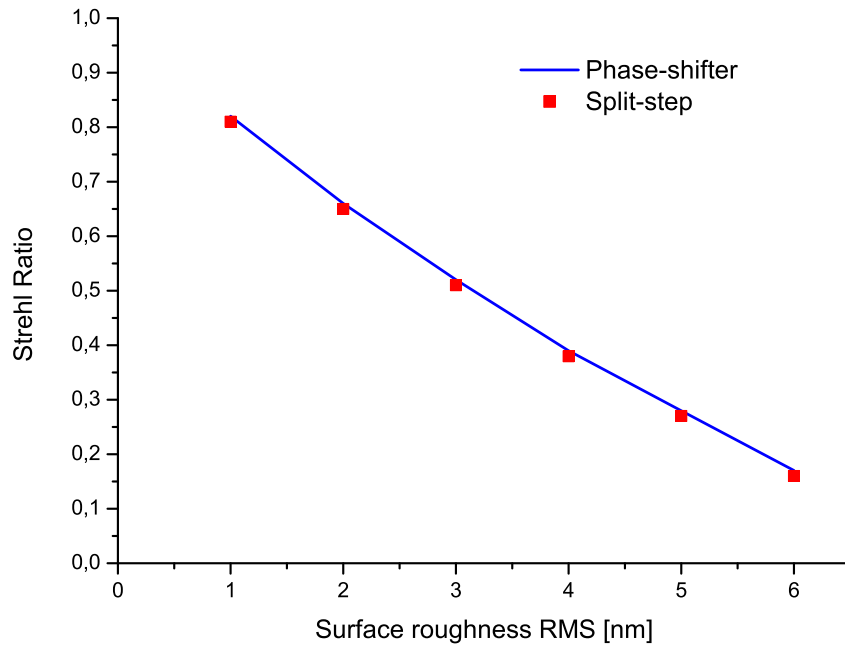
Figure 2.13: Comparison of a phase-shifter model with a split-step propagation method. Strehl ratio after reflection simulation from a bulk platinum mirror with various height errors. Here $\hbar\omega = 500\ eV$, angle of incidence $\theta = 1°$. Unpublished. Courtesy of Vitaly Kocharyan.

Chapter 3

Monochromator study for the LCLS

The Linac Coherent Light Source (LCLS) is the XFEL based at SLAC National Accelerator Laboratory, California (see Fig. 3.1). The first lasing at this facility was reported in 2009 [70] making LCLS the world's first hard X-ray laser in operation. At present, it delivers the radiation to 6 experimental stations. The typical pulse energy of the LCLS is around 2-3 mJ, the radiation photon energy ranges from 270 eV up to about 11.2 keV.
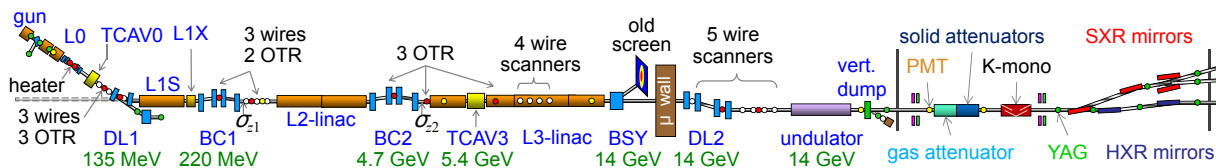
Figure 3.1: Schematic layout of the LCLS accelerator, undulators, and photon distribution lines. Reprinted from [71].

During the last five years, significant efforts were dedicated to both theoretical investigation and $R\&D$ at the LCLS, leading to the pioneering design of a compact self-seeding setup in the soft X-ray range, based on a grating monochromator. The evolution of the design can be reconstructed from [72–74], striving at the same time for the needed resolution and compactness. Below the latest and current design is discussed.

3.1   Self-seeding setup description

The overall soft X-ray self-seeding FEL operation scheme consists of three parts: the SASE undulator, the monochromator set-up and the output seeded undulator in which the monochromatic seed signal is being amplified. The SASE undulator consists of 8 modules. It is followed by the SXRSS monochromator setup, designed to occupy the space of the 9-th module. The seeded undulator consists of the last 22 modules. Parameters of the LCLS undulator modules are listed in Table 3.1

The LCLS SXRSS set-up was introduced in [74], and includes an electron chicane, and a grating-based monochromator. The electron chicane (see Fig. 3.3) is composed of 4 dipole magnets and performs 4 tasks:
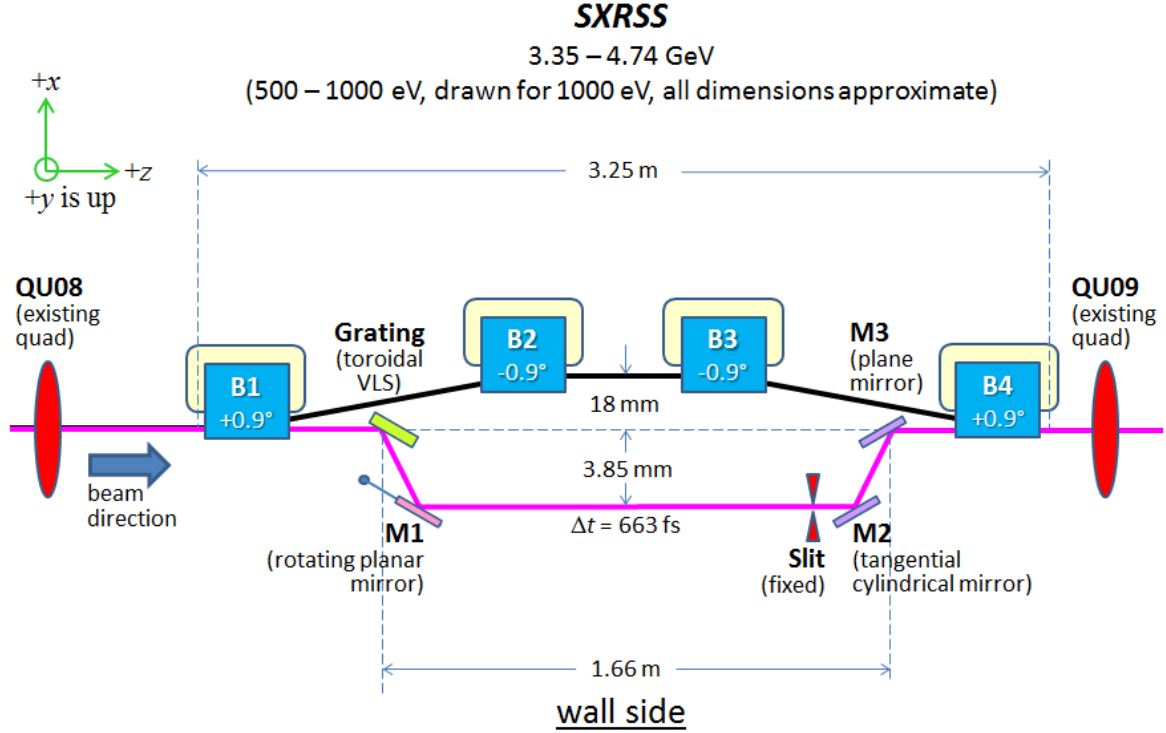
Figure 3.2: The compact soft x-ray self-seeding system, located in U9. The grating is a toroidal VLS grating, M1 is a rotating plane mirror, M2 a tangential cylindrical mirror, and M3 a plane mirror used to steer the beam. Reprinted from [74].

- creates the transverse offset of the electron beam to introduce the monochromator optics;

- delays the electron beam accordingly to the temporal delay caused by the optical scheme;

- smears out an electron density microbunching of a beam created in the SASE undulator;

- compensates the electron beam phase mismatch due to the absence of the undulator, replaced by this chicane during a conventional non-seeded undulator maintenance;

The monochromator consists of reflective optical components: the toroidal variable-line-spacing (VLS) grating, the steering plane mirror, the spherical mirror, another plane mirror and a slit (Figs. 3.2 and 3.4), ending up in a qualitatively symmetrical design.

Parameter	Value	Units
Undulator period	30	mm
K parameter (RMS)	2.475	-
Section length	3.3	m
Intersection length	0.6 & 0.9	m

Table 3.1: Parameters for the LCLS undulator modules used for simulations. Adapted from [75, 76].

Parameter	Value	Unit
e^- beam delay	633-930	fs
Delay precision	0.1	fs
R_{56}	477-397	μm
Dipole bend angle	14.91-13.59	mrad
e^- beam displ.	19.2-15.9	mm
H. separation	4.3-3.4	mm

Table 3.2: Main parameters of the electron beam chicane. Adapted from [74].
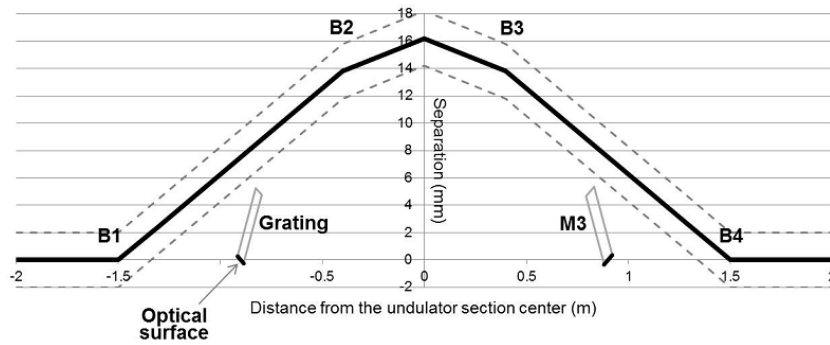
Figure 3.3: Stretched sketch of the separation between electrons and the two closest optics, the grating and M3. The electrons trajectory is represented by the black fat line. A 22 mm free area around is emphasized by the dashed lines. Reprinted from [77].
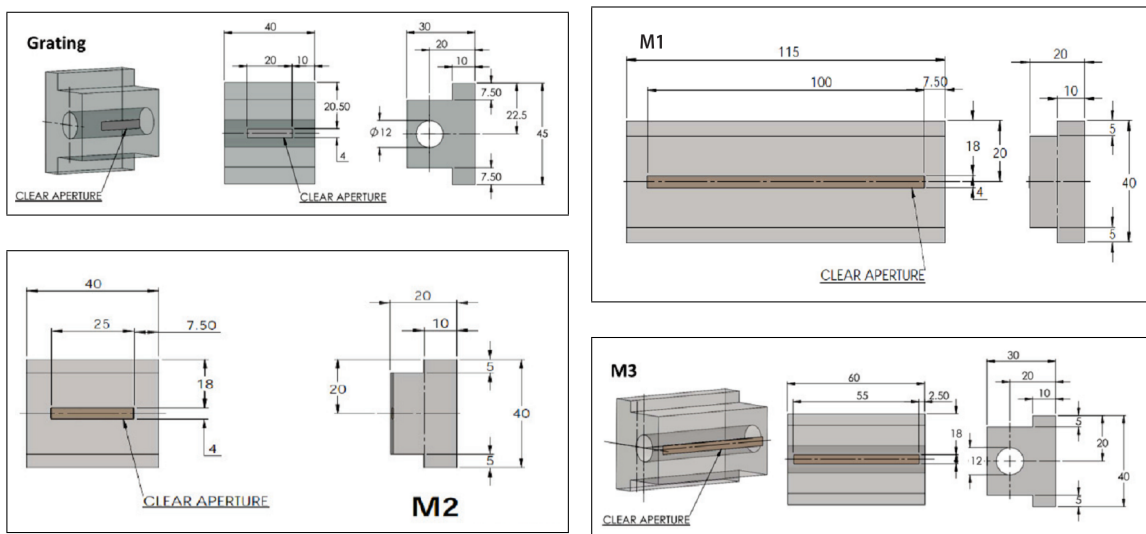
Figure 3.4: LCLS SXRSS monochromator optics dimensions. The holes in grating and M3 mirror are designed to transport the electron beam through. All values are given in [mm]. Reprinted from the [78] talk slides.

The dispersive **grating** is illuminated by the SASE FEL radiation produced in the SASE undulator with the source position inside undulator sections U7 or U8.

Usually, a grating monochromator consists of an entrance slit, a grating, an exit slit and focusing system. The grating equation, which describes how the monochromator works, relies on the principle of interference applied to the light coming from the illuminated grooves. Such principle though, can only be applied when phase and amplitude variations in the electromagnetic field are well-defined across the grating, that is when the field is perfectly transversely coherent. The purpose of the entrance slit is to supply a transversely coherent radiation spot at the grating, in order to allow the monochromator to work with an incoherent source and with a given resolution. However, an FEL source is highly transversely coherent and no entrance slit is required in this case [79, 80]. The dispersive grating has a toroidal shape with a variable line spacing (VLS). It is platinum coated, which allows it to cover the 300-1200 eV range with a satisfactory efficiency (12-15% [81]). The grating is fixed with and incidence angle of 1 degree with respect to the surface. This allows one to reflect high photon energies thanks to total in-

Parameter	Value	Unit
grating		
Line density (n)	1123	l/mm
Linear coeff. (n_1)	1.6	l/mm^2
Quad coeff. (n_2)	0.002	l/mm^2
Groove profile	blazed 1.2°	-
Tangential radius	195	m
Sagittal radius	0.18	m
Diffraction order	+1	-
Incident angle	1	°
Exit angle	3.18-4.39	°
exit slit		
Location	1.35	m
Width	variable	-
mirror M2		
Location	1.53	m
Radius	23.2	m
Incident angle	0.86	°
mirror M3		
Location	1.66	m
total		
Optical delay	797.9-662.8	fs

Table 3.3: Parameters of the LCLS SXRSS monochromator optical elements within 500 eV - 1000 eV nominal photon energy range. Adapted from [74].

ternal reflection phenomenon, to increase the irradiated spot area avoiding single shot damage from an intense FEL radiation and to make it less sensitive to the souse point position within the seeded undulator. Tangential focal distance of the grating is composed of two components: surface curvature (tangential radius) and the variable line spacing linear coefficient D_1 (more in subsection 2.3.2). The curvature component gives a wavenength-independent focal distance of the grating while the VLS contribution depends on a photon energy. This way grating carries out focusing of the different wavelengths at different directions but almost at the same focal distance. Sagittal focal distance of the grating is defined only by the sagittal component of the grating curvature and carries out focusing of the source radiation to the re-imaging point within the seeded undulator (see Fig 3.7).

The rotating plane mirror **M1** is used to steer a certain wavelength of the angularly dispersed radiation to the slit. It's pivot point position is optimized to keep the constant transverse offset of the monochromatized beam (see Fig. 3.5)

The **Slit** stops the undesired radiation wavelengths from further propagation (see Fig. 3.6). Slit width may be tuned with discrete steps or fully removed. It was found that slit-less operation of FEL is possible giving satisfactory results [82], see Section 3.4 for further details.

The spherical mirror **M2** is positioned downstream the slit and re-images the radiation from the slit position to the re-imaging point at the entrance of the seeded undulator. Focusing is
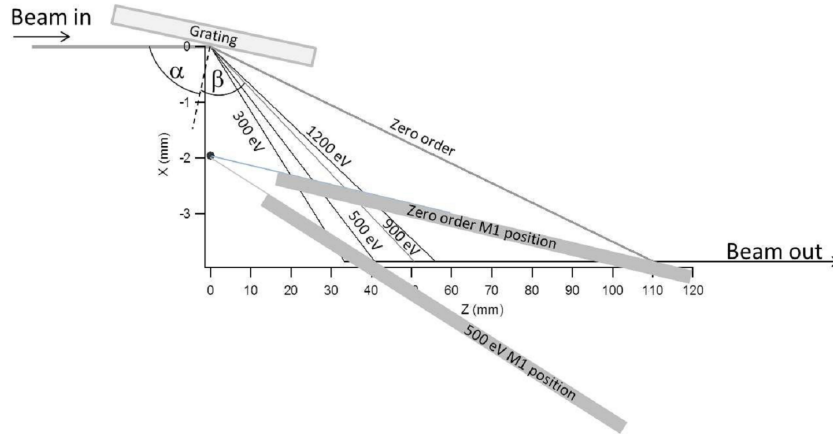
Figure 3.5: Relative position of the grating and M1 mirror with diffracted beams at different wavelengths and in zero order mode. The M1 mirror rotation allows one to "steer" the radiation with desired wavelength onto the slit. Rotation pivot point is optimized to keep deflected beam offset dependency in the "x" direction close to constant with respect to the monochromator wavelength setting. Reprinted from [77].
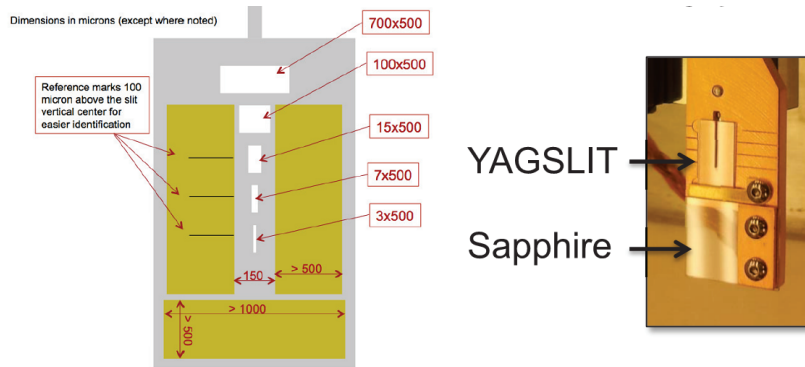
Figure 3.6: The design and the photograth of the slit with YAG screens to monitor the dispersed radiation. Reprinted from [78].

carried out in tangential plane. Due to the small incidence angle, a sagittal focusing distance of the M2 mirror is very large and therefore can be neglected.

The plane mirror **M3** reflects the radiation to the seeded undulator. It introduces two additional degrees of freedom for an overlap of the electron beam and the monochromatic radiation inside of the undulator section U10.

Detailed parameters of the monochromator optical system may be found in Table 3.3

3.2 Gaussian beam optics calculations

Understanding principles of the LCLS design was essential in order to implement it for the European XFEL undulator. We started with the Gaussian beam optics approach knowing the FEL source parameters within SASE undulator. We found it to be a very useful analytical method for the monochromator performance characterization. Source properties, such as its size and distance to the grating were obtained from the LCLS SXRSS PRD [unpublished]. Here we calculate the waists of the model Gaussian beam, focused by the grating and M2 mirror (See
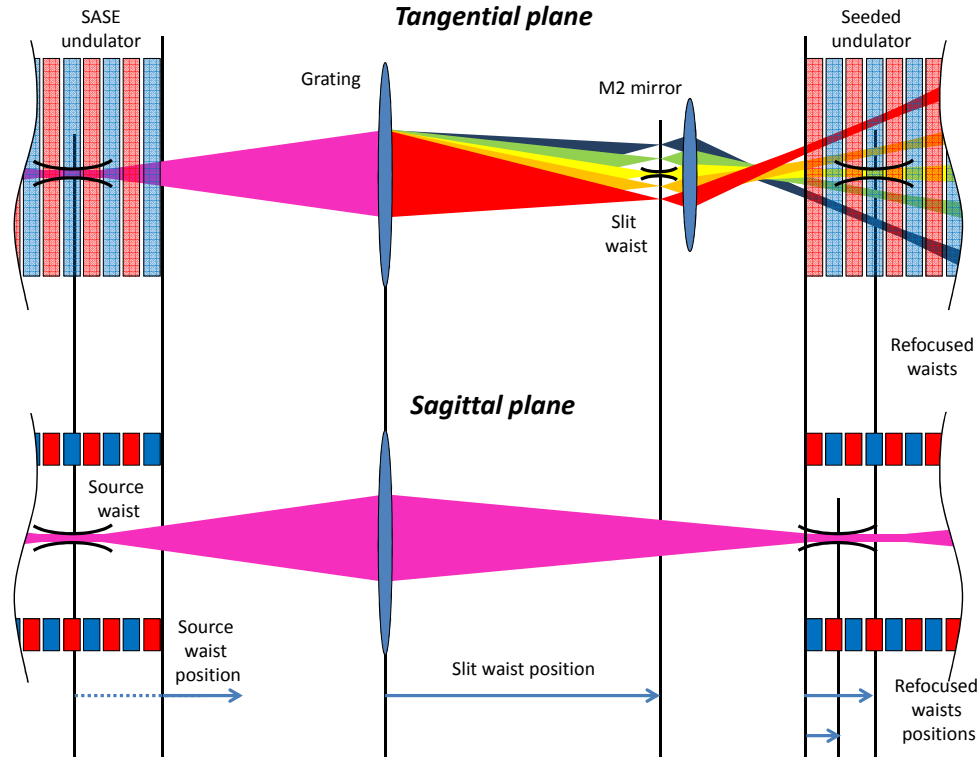
Figure 3.7: Tangential (top) and sagittal (side) views of the principal optical components, and radiation propagation paths and waists. Waist positions arrows reveal the conventions used further in Figures 3.8-3.12.

Fig. 3.7). Initially we ignore aberrations and an effect of the rest optical components of the monochromator. Exit slit is assumed to be retracted. Let us revisit the following relations:

$$z_R = k_0 w_0^2/2 \; . \tag{2.18 revisited}$$

for Rayleigh length of the waist,

$$w^2(z) = w_0^2 \left[1 + \left(\frac{z}{z_R} \right)^2 \right] , \tag{2.21 revisited}$$

for beam spot size at a given distance from the waist,

$$w_2^2 = \frac{w_1^2 f^2}{[(d_1 - f)^2 + (k_0 w_1^2/2)^2]} \; . \tag{2.31 revisited}$$

For the image waist size obtained with a lens with focal distance f, and

$$d_2 = f + f^2 \frac{(d_1 - f)}{[(d_1 - f)^2 + (k_0 w_1^2/2)^2]} \; . \tag{2.32 revisited}$$

for the position of the reimaged waist.

Radiation spot and waist sizes presented on the figures below are defined as RMS of the transverse intensity profile of the radiation at the point of interest. FWHM and RMS of a
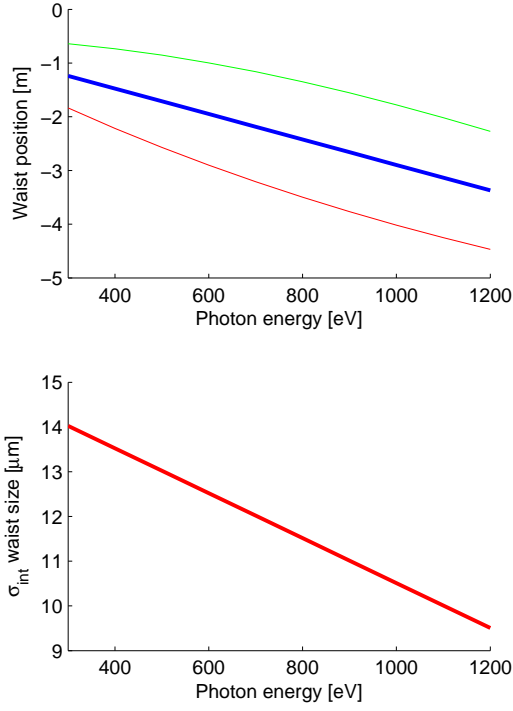
Figure 3.8: SASE undulator source waist size and position.
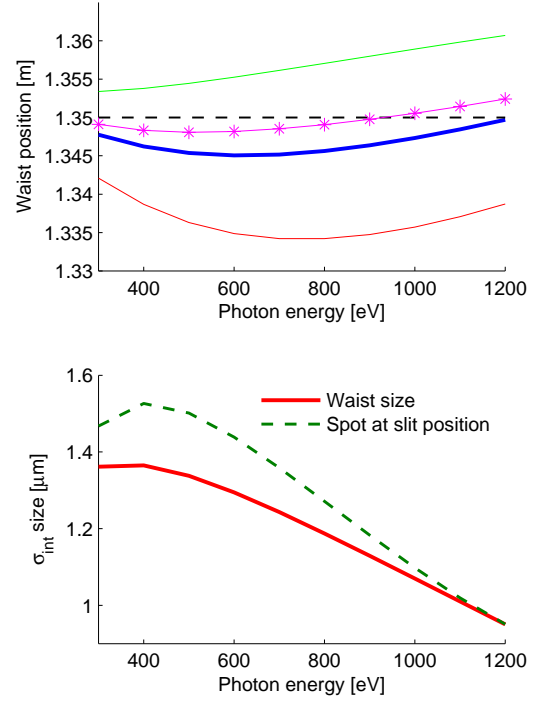
Figure 3.9: Slit tangential waist size and position. Dashed line depicts the slit position

Gaussian beam intensity profile are related to the laser community definition w presented in Eq. (2.14) as

$$\sigma^{int} = w/2 \ ,$$
$$FWHM^{int} = 2\sqrt{2\log 2}\sigma^{int} = \sqrt{2\log 2}w \simeq 1.18w \ .$$

Hereinafter green and red lines along the waist position depict the Rayleigh range, pink diamonds - position of the geometrical optics images, and black diamonds - size of the SASE undulator source for comparison. Source properties are shown on Figure 3.8. Position and size of the source waist are wavelength-dependent, which makes it more complicated to obtain a wavelength-independent image position on the slit. Effectively, it is done with a D_1 VLS parameter of the grating [77]. Grating carries out reimaging of the waist in tangential plane onto the slit position located 1.35 m downstream the grating. Reimaged waist size and position are presented on Figure 3.9.

At the entrance to the seeded undulator the radiation has to be efficiently overlapped with an electron beam. On Figures 3.10 and 3.11 we present calculations for the sagittal and tangential planes respectively. Reimaged waist size is compared with the size of the source. In fact, according to Eq. 2.18, waist size is connected with the divergence of the radiation. If the waist is too small, the light would diverge within the undulator before effectively interacting with the
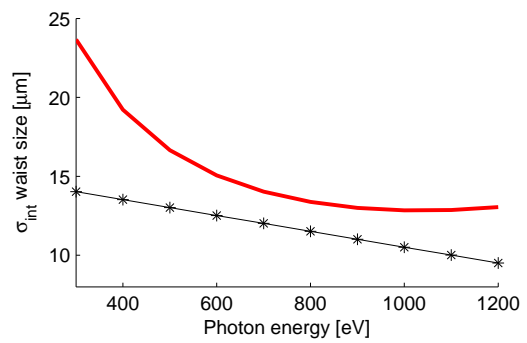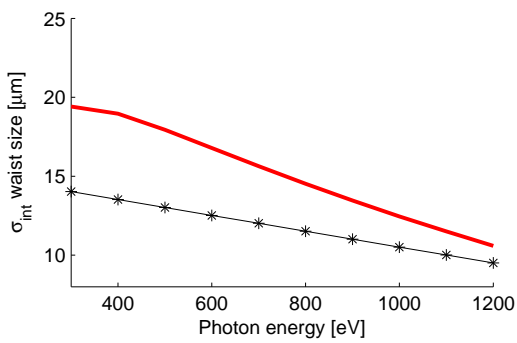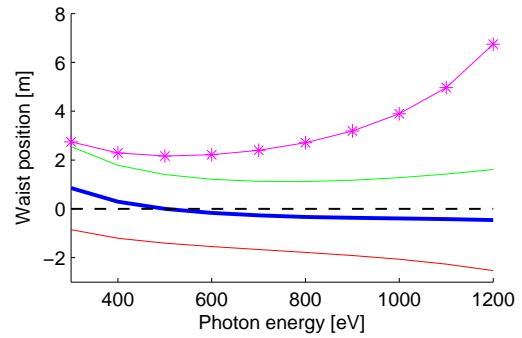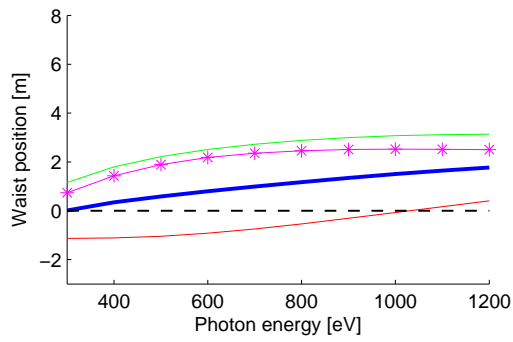
Figure 3.10: Seeded undulator sagittal waist size and position. Dashed line depicts the seeded undulator entrance.

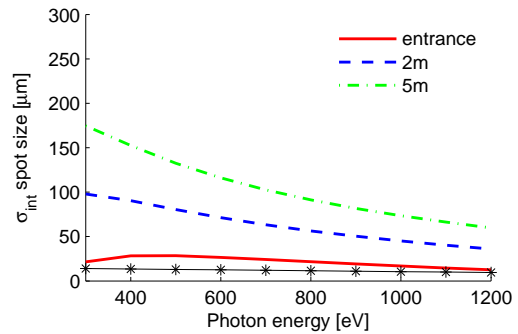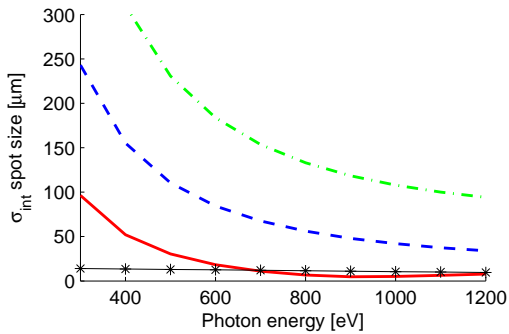Figure 3.11: Seeded undulator tangential waist size and position.
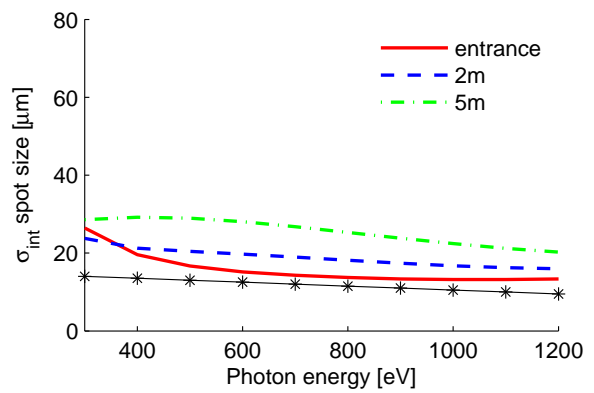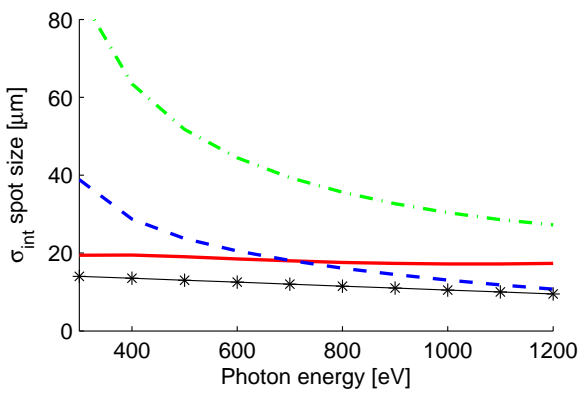
Figure 3.12: Seeded undulator waist evolution for sagittal (left subfigure) and tangential (right subfigure) planes.
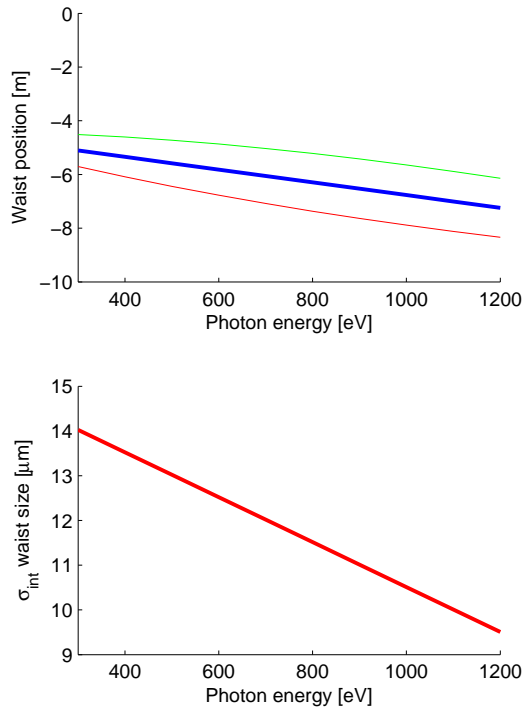
Figure 3.13: SASE undulator source waist size and position.
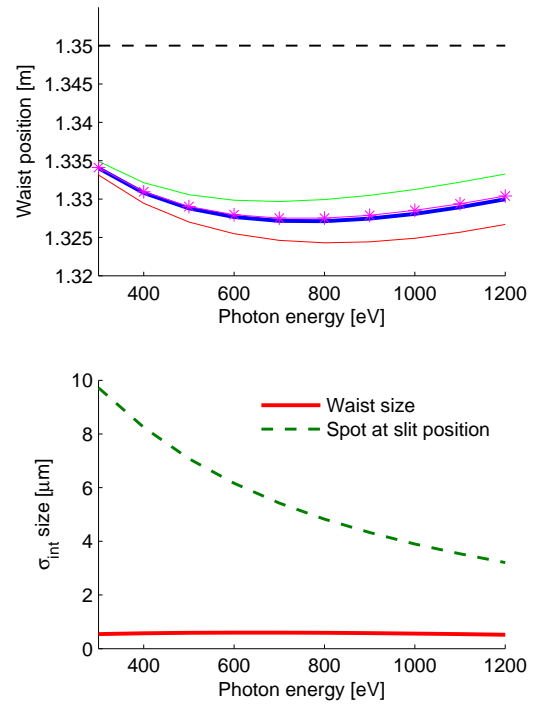
Figure 3.14: Slit tangential waist size and position. Dashed line depicts the slit position

electron beam. If the waist is too large - input coupling factor along with resolving power will degrade. We can see that the waist position dramatically differs from the geometrical optics - based calculations.

It is also interesting to track the size of the spots at different distances downstream the undulator (Fig. 3.12).

Although Gaussian beam optics is a very simple method, it can be applied to the FEL source as an estimation. It requires characterization of the FEL source inside the SASE undulator as a Gaussian beam with certain parameters, that in general does not apply for the FEL source.

3.2.1   Effect of the source position change by one section upstream

In order to ensure the safe operation of the monochromator with respect to the damage of the grating, it was chosen to operate the self-seeding set-up with the undulator U8 removed. This leads to a smaller energy density on the grating due to an increase of the footprint area. Energy within the pulse is kept the same. From geometrical consideration, the FEL source point is moved by one section upstream by 3.87 m. Below we present the results of the Gaussian beam optics for this case. Figures 3.13 and 3.14 show parameters of waists at the source and at the slit. Waist at the slit position is far off the Rayleigh length, leading to a large spot at the slit in case of its presence.

Figures 3.15 and 3.16 show that reimaged waists are at the undulator entrance, but their
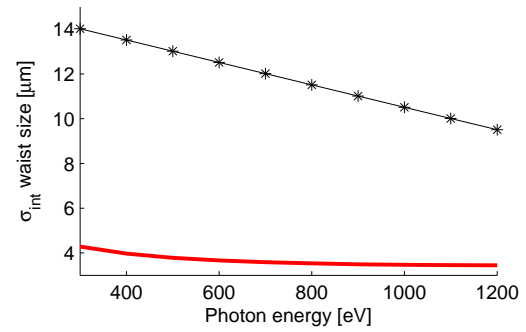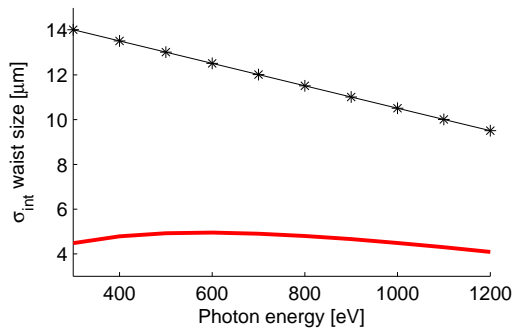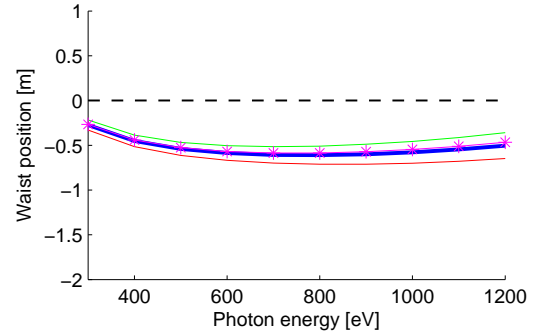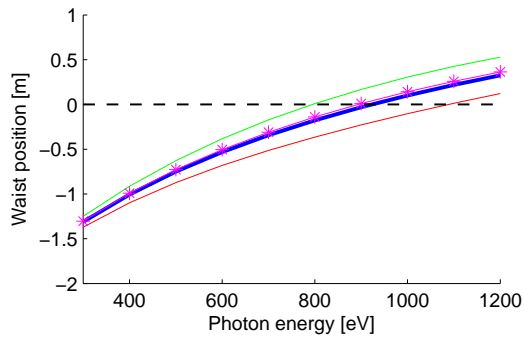
Figure 3.15: Seeded undulator sagittal waist size and position. Dashed line depicts the seeded undulator entrance.

Figure 3.16: Seeded undulator tangential waist size and position.

Figure 3.17: Seeded undulator waist evolution for sagittal (left subfigure) and tangential (right subfigure) planes.

Rayleigh lengths are considerably smaller in this case. This leads to a very large divergence and worse coupling with an electron beam.

3.3 Start-to-end self-seeding simulation: details and approaches

As mentioned before, Gaussian beam optics allows one to calculate the monochromator performance based on a certain assumptions, such as a Gaussian profile of the FEL source, no height errors on mirrors, no aberrations. Also it is very important to calculate the effective resolving power of the monochromator when no exit slit is inserted.

In the simulations of the current monochromator design, an effect of two slits needs to be taken into account (see Fig. 3.18). The first slit is physical, which makes it possible to calculate its effect on the monochromator instrumental function analytically. Another slit is a virtual one: the electron beam being placed in the spatially dispersed radiation acts as a slit. The latter case can be barely analyzed analytically since the FEL process is involved in both coupling and amplification.
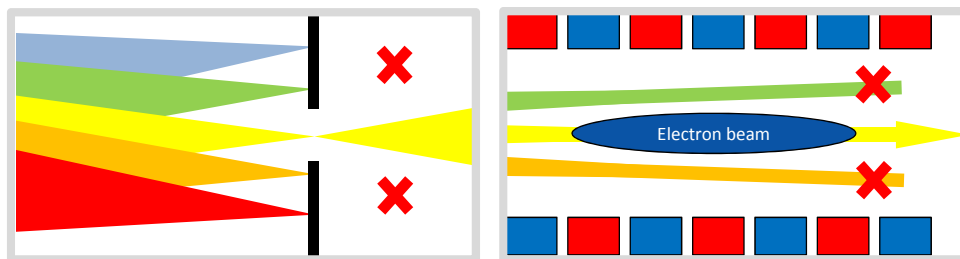
Figure 3.18: Physical slit (left figure) blocks undesired wavelengths, passing through only certain bandwidth. It is easily controlled and may be moved out.
Since radiation amplification in an undulator takes place via interaction with accelerated electrons, only a radiation overlapped over the electron beam will be amplified. It can be expressed as a virtual slit (right figure). This process is not directly controlled.
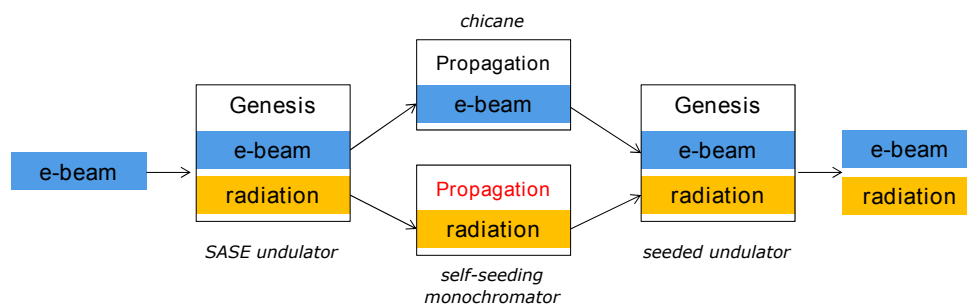
Figure 3.19: Wave optics propagation algorithm allows us to fill the gap in start-to-end time-dependent simulations of FEL performance with the SXRSS monochromator.

FEL pulses have a specific temporal and spectral structure, therefore a time-dependent start-to-end study should be done in order to fully characterize the SXRSS monochromator perfor-

mance and compare simulation with an experiment. (see Fig. 3.19) The simulation methods described below allow one to answer all these questions.

We use the "GENESIS 1.3" FEL simulation code [83, 84] to obtain an electric field distribution in space and time at the end of the SASE undulator. The temporal Fourier transform (Eq. 2.7) allows one to represent this distribution in a frequency domain.

Let us consider a transverse radiation distribution at the end of the SASE undulator at a frequency ω_i. To simulate the transverse distribution of this beam at the grating position, we apply the Fresnel propagator from Eq. (2.13) with z equal to a distance between the end of the undulator and the beam's footprint at the grating. The phase shifter, described in Eq. (2.109) and the height error phase shifter (Eq. 2.127) are used to simulate focusing of the beam by the toroidal VLS grating with a certain height error profile. The phase-shifter includes both aberrations, height error effect and the beam tilt. The tilt is introduced according to a difference $\Delta\omega$ between the frequency of a beam being currently propagated and the frequency of a beam that is chosen to be a principle ray of the dispersed radiation (Eq. 2.108).

In our case, the principle ray direction is assumed to pass through an optical centre of all monochromator components. Physically it is done via M1 pitch angle optimization. The transformations of the radiation discussed above compute the transverse radiation distribution (perpendicular to the principle ray *after* reflection from the optical element), based on optical element properties and the initial transverse radiation distribution (perpendicular to the principle ray *before* reflection from the optical element). We model height error effects associated with each optical element by applying phase shifters at the position of every optical component, taking into account the incident angles of the radiation.

After the grating, the beam is propagated to the M1 mirror and, as discussed above, the height error - related phase shifter is applied. Then after propagation to the slit one may choose either to model its presence with given width by applying a transparency mask to the field distribution, or to ignore the slit within the algorithm, effectively modeling slit-less monochromator performance. After modeling M2 (refocusing) and M3 (flat) mirrors and including intermediate drift spaces one obtains the radiation distribution at the frequency ω_i at the entrance of the seeded undulator. This distribution may be used as an input radiation field for the following GENESIS application.

Below we present two approaches for an FEL pulse propagation through the monochromator. Both of them are based on the single frequency beam propagation method, described above and propagate the same pulse, generated in the SASE undulator. Start-to-end simulated electron beam was used. Its parameters at the entrance of the SASE undualator are presented at the Fig. 3.20.

3.3.1 Direct propagation approach

In this straightforward approach the SASE pulse at the end of SASE undulator is decomposed into monochromatic beams using temporal Fourier transform (Eq. 2.7). As it has already been
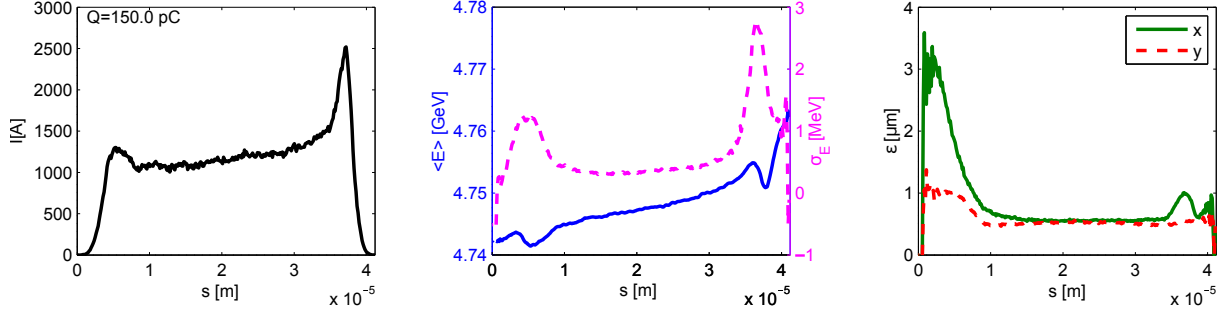
Figure 3.20: Results from electron beam start-to-end simulations at the entrance of SASE undulator. From left to right: electron beam current, energy and energy spread, emittance along the beam.

mentioned at the beginning of Section 4, every beam is propagated independently through the monochromator so that every beam obtains a certain tilt with respect to the principal ray at the grating. At the entrance to the seeded undulator those propagated beams are transformed back to the time domain. This dispersed 3D SASE radiation distribution is used as a seed for a time dependent FEL simulations i.e. directly as in real setup without extra approximations.

An example of a propagation algorithm for a pulse at 1000 eV central photon energy is given below. Monochromator model with no exit slit inserted is used for simulation. First, the pulse is obtained at the end of SASE undulator in time domain (see Fig. 3.21). Afterwards, it is transformed to frequency domain (Fig. 3.22). Then the monochromatic beams are propagated downstream to the grating (Fig. 3.23). At the grating frequency-dependent phase shifters are applied for simulating focusing and height error (Eqs. 2.109, 2.127). Then the field is propagated to the mirror M1, where the height error phase shifter is applied (Eq. 2.126), to the mirror M2 (Eqs. 2.110, 2.126), M3 (Eq. 2.126), and then to seeded undulator entrance. In Figure 3.24 we can see the spatial dispersion of our radiation: beams at different wavelengths have different transverse offsets. Note that due to the spatial dispersion the spectrum is imprinted into the transverse profile of the radiation (second row, first and second figures from the left). Due to the limited resolving power of the monochromator individual spikes are not resolved. After the inverse transformation of the radiation into the time domain we can see all 3 spatial projections of the spatially dispersed pulse, that, at this point is being overlapped with the electron beam (Fig. 3.25). In our case the transverse size of the electron beam is typically around $25\mu m$ RMS and is much smaller than the transverse size of the spatially dispersed radiation in the horizontal dimension. Since the radiation will continue to diverge when propagated downstream the seeded undulator, due to angular dispersion, only a relatively small fraction of the dispersed beam will interact with the electron beam. Therefore, although an entire spectrum was used in Figures 9-11 to illustrate the process, during practical simulations we can use fractional spectrum to save computing time.
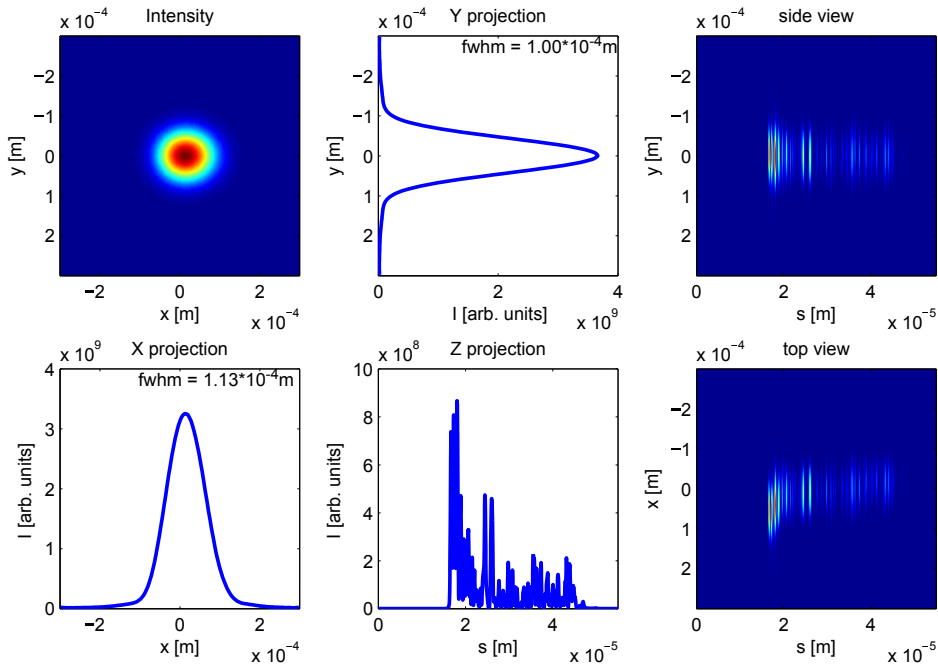
Figure 3.21: Radiation distribution at the end of SASE undulator in time domain. The average photon energy is 1000 eV.

Left figure in first row is the transverse intensity distribution. Right figures represent projections of intensity distributions. Here and below spatial-time domain is represented in spatial coordinates x, y, and $s = ct$.
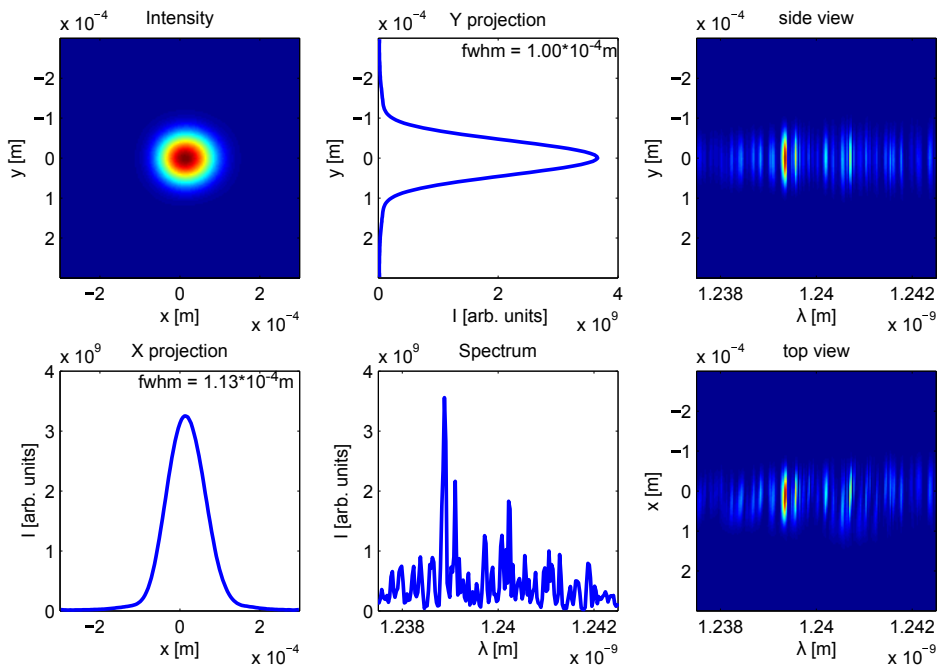
Figure 3.22: Radiation distribution at the end of SASE undulator in frequency domain.

Left figure in first row is the transverse intensity distribution. Right figures represent projections of beam distributions at different wavelengths. Note that at this point all wavelengths are transversely overlapped. Here and below spatial-frequency domain is represented in transverse coordinates x, y, and $\lambda = c/\omega$.

58
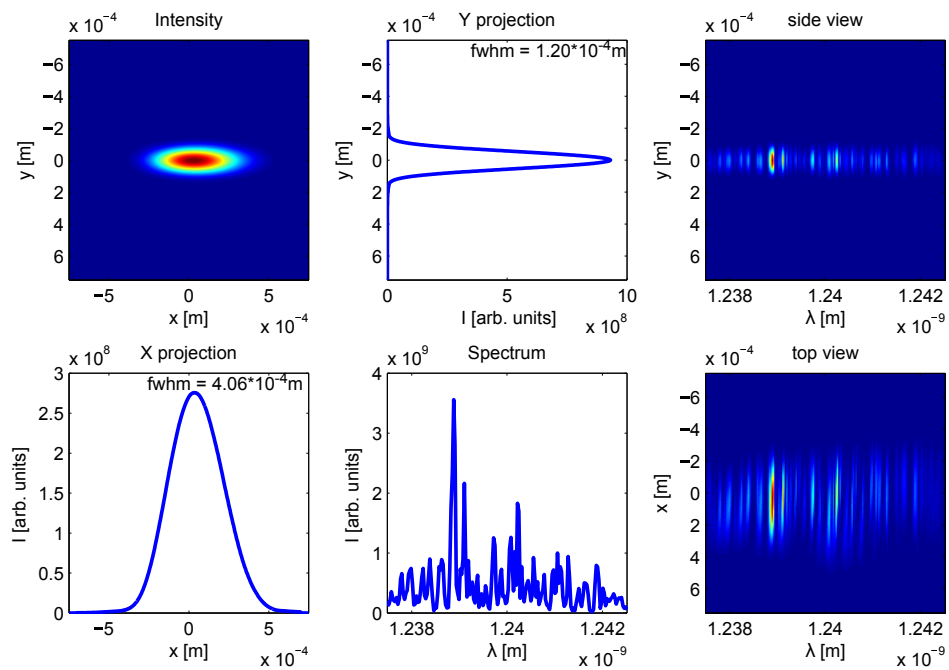
Figure 3.23: Radiation distribution immediately after the grating in frequency domain.
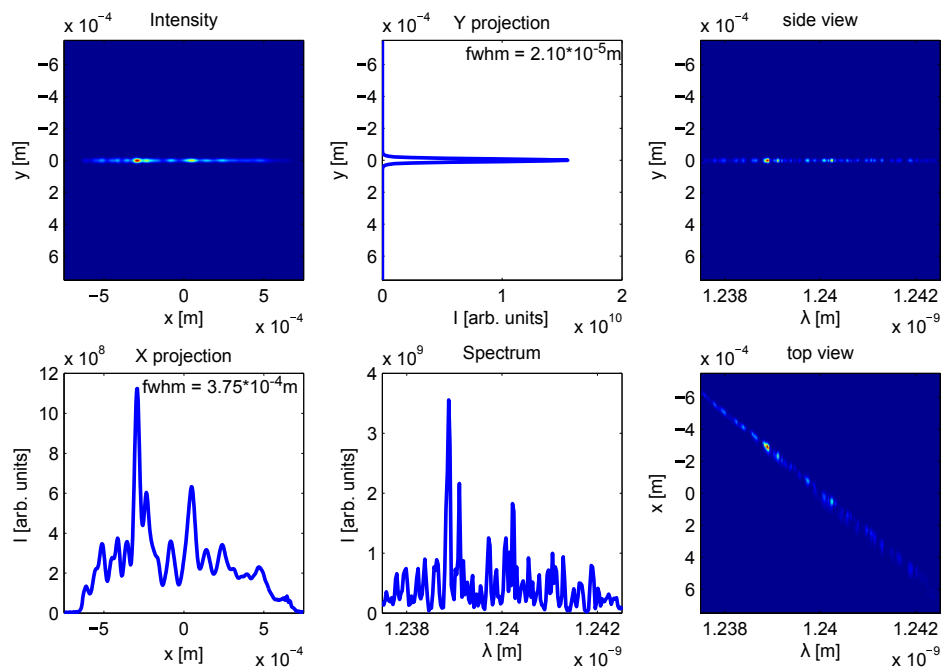
Figure 3.24: Radiation distribution at the entrance of seeded undulator in frequency domain.
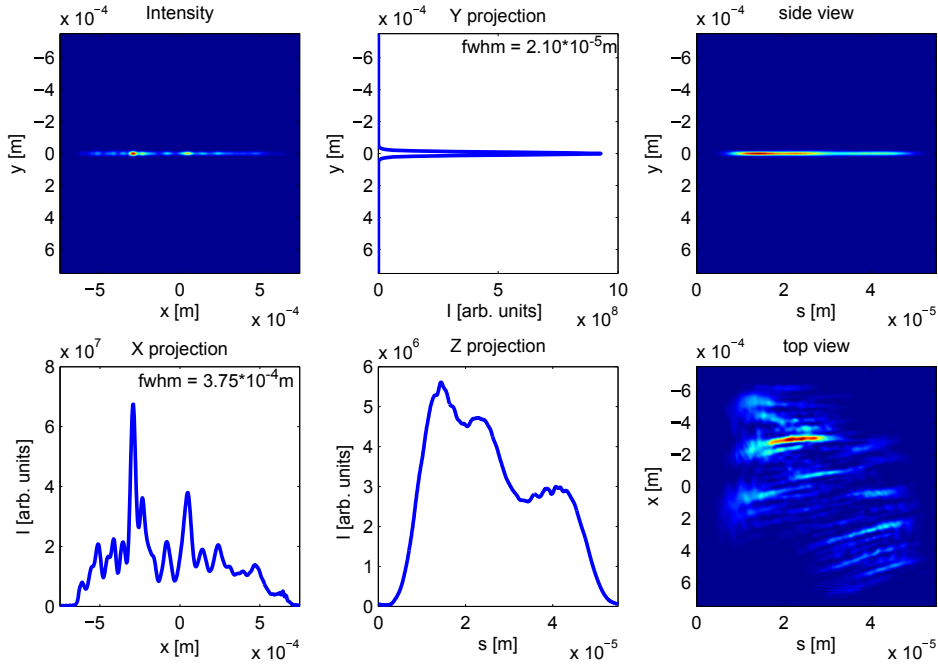
Figure 3.25: Radiation distribution at the entrance of seeded undulator in time domain.

3.3.2 Phenomenological propagation approach

This method is very similar to the one used in the hard X-ray self-seeding (HXRSS) simulations (e.g. [52, 85, 86]).

In this approach, we first simulate the SASE FEL with GENESIS code to obtain a radiation distribution at the end of the SASE undulator, then apply a temporal Fourier transform which switches from time to frequency domain (see Figs. 3.26, 3.27). Afterwards, the obtained radiation spectrum is multiplied by a monochromator instrumental function that characterizes the monochromator performance based on both monochromator geometry and FEL amplification in the seeded undulator downstream the monochromator. In this way the FEL spectrum is filtered (only a certain spectral bandwidth defined by an instrumental function passes through the monochromator, while other frequencies are effectively blocked). After applying an inverse temporal Fourier transform, one obtains the FEL radiation in the time domain that can be used as a seed for the next undulator section in GENESIS simulations.

In the HXRSS case, the monochromator instrumental function is a transmittance function of the diamond crystal itself at a given geometry. This function can be either calculated or measured. In the SXRSS case in order to obtain an effective transmission function one can make use of a beam propagation method. In the phenomenological approach we use a response of FEL power amplification of the seed pulse within the seeded undulator section (in other words - input coupling factor - ICF) from the spatial dispersion effect. Since different frequencies are spatially separated at the entrance of the seeded undulator, some of them will be overlapped with the electron beam and some will not. In this way one can measure the mismatching of

(a) Power at U8

(b) Spectrum at U8

(c) Power at U10

(d) Spectrum at U10
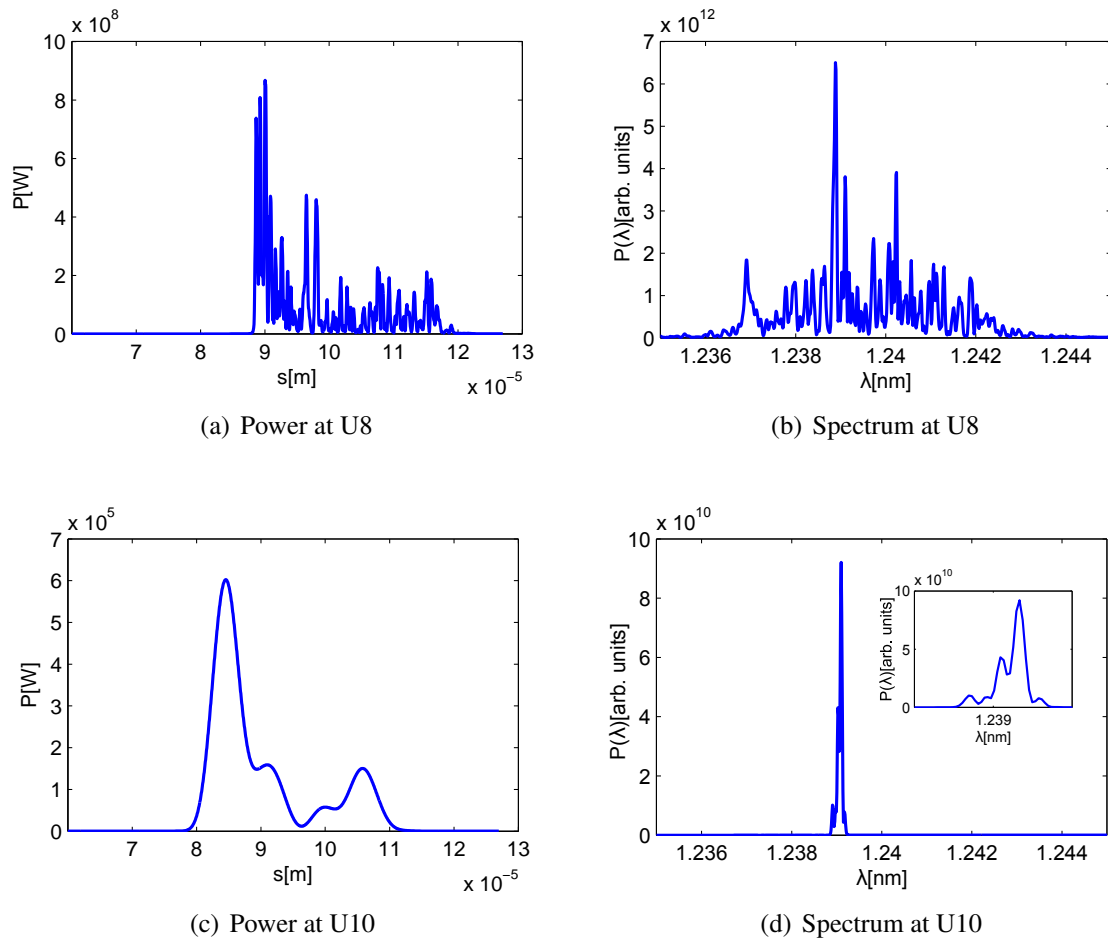
Figure 3.26: 1000eV FEL pulse at the end of the SASE undulator in time domain (a) was transformed to frequency domain (b). Spectrum was filtered (d) after being multiplied by the monochromator instrumental function (Fig. 3.28-f). Afterwards it was transformed back to time domain (c), representing effective power distribution at the entrance of the seeded undulator.

(a) Power at U8

(b) Spectrum at U8

(c) Power at U10

(d) Spectrum at U10
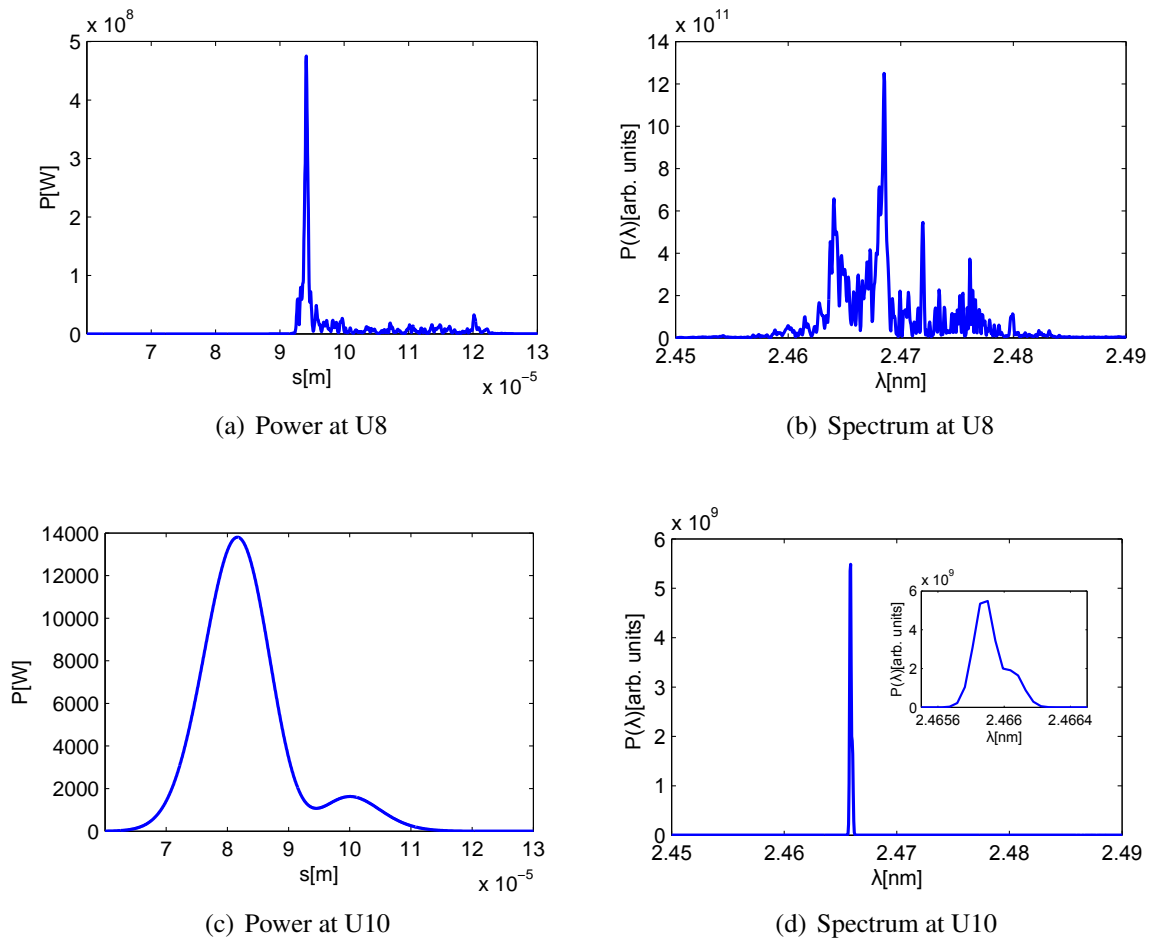
Figure 3.27: 500eV FEL pulse at the end of the SASE undulator in time domain (a) was transformed to frequency domain (b). Spectrum was filtered (d) after being multiplied by the monochromator instrumental function (Fig. 3.28-d). Afterwards it was transformed back to time domain (c), representing effective power distribution at the entrance of the seeded undulator.
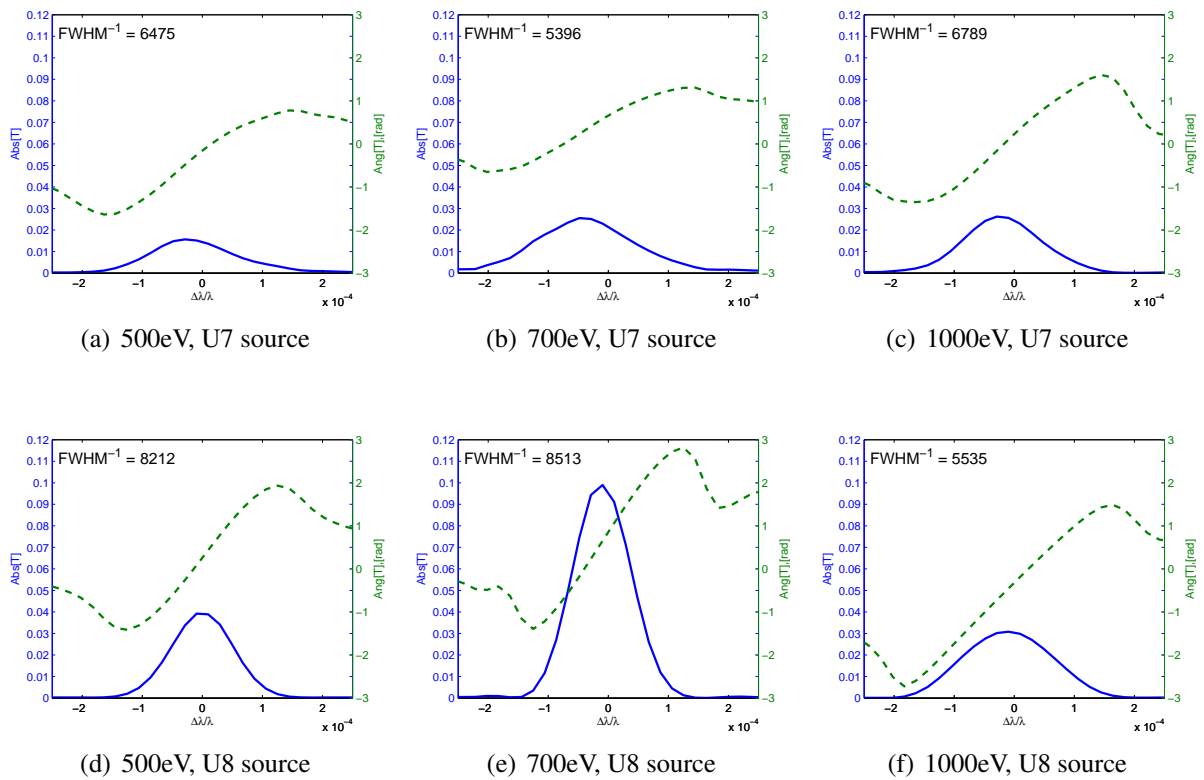
Figure 3.28: Monochromator instrumental functions for different photon energies and source positions (undulator U8 "in", leading to source position in this undulator, or undulator U8 "out", resulting in the source within undulator U7). Physical slit is not inserted. Inverse Full width at half maximum is interpreted as an effective resolving power of the monochromator.

the radiation and the electron beam as a function of the wavelength. It allows one to obtain an effective monochromator transmission function.

We calculated the instrumental function of the monochromator in the following way. First, a single wavelength λ_0 (or frequency ω_0) of a radiation distribution at the end of the SASE undulator was simulated with the GENESIS code in the steady-state mode. This radiation can be propagated through all of the optical components of the monochromator to the entrance of the seeded undulator, used as an input for the GENESIS code that simulates the seeded undulator. This field is amplified within the seeded undulator in a linear mode of operation for a fixed distance. At the end the obtained amplified power is recorded. This procedure was repeated for other frequencies with different wavefront tilts introduced at the grating (Eq. 2.108).

This allows one to simulate an angular dispersion during the radiation propagation with different wavelengths through the monochromator. At the entrance of the seeded undulator the radiation distributions with different $\Delta\lambda$ with respect to the principal ray will obtain different offsets in the dispersive direction: the result of the spatial dispersion of the monochromator. These radiation distributions can be used as an input radiation field for the GENESIS simulation within the seeded undulator. Due to the transverse mismatching between the electron beam and the radiation at different wavelengths, the amplification process will depend on the particular wavelength offset $\Delta\lambda$ from the principal ray wavelength λ_0. If the undulator length is properly chosen to satisfy the FEL amplification in the linear mode of operation, one may measure the amplified power as a function of $\Delta\lambda$. It effectively represents how different frequencies are amplified within the seeded undulator after the propagation through the monochromator. In order to obtain the effective instrumental function of the monochromator, the power distribution must be properly normalized. Since the radiation propagated through the monochromator is not only spatially dispersed but also undergoes focusing as well as an aberration and mirror surface error effects, the amplified power must be normalized by the power obtained with one-to-one imaging of the radiation at the end of the SASE undulator to the entrance of the seeded undulator. Also the normalized power dependence should be multiplied by the monochromator transmittance for a given wavelength, calculated by [81]. In this way the instrumental functions for different wavelengths and geometries of the LCLS self-seeding monochromator were obtained (see Fig. 3.28). If multiplied by the radiation distribution in frequency domain before the monochromator, it gives an effective radiation distribution after the monochromator at the entrance of the seeded undulator. Nevertheless, in order to maintain causality of the transported radiation in the time domain, a phase information was introduced into the monochromator instrumental function. The phases were obtained with Kramers-Kronig relations (this approach was also used for the HXRSS setup simulation in e.g. [85, 86]). It is worth mentioning that unlike the HXRSS monochromator simulations, the causality effect is not critical for the SXRSS and is used rather for purity of the simulation.

What is important is the fact that those instrumental functions are effective ones and are based on: the source position from which the radiation propagates to the monochromator, the optical elements properties, the distance to seeded undulator, the FEL amplifier properties,

etc. The instrumental function curve shows only the spectral bandwidth that will be amplified downstream of the undulator, but not the bandwidth that is actually transmitted through the monochromator: while the slit is fully opened, the electron beam filters out a certain spectral bandwidth to be amplified further (Fig. 3.18). In fact, without the exit slit the entire radiation spectrum passes through the monochromator.

Consequently, this approach allows one to characterize the self-seeding monochromator that operates without both entrance and exit slits with an instrumental function. Once it was done, every propagated pulse is just transformed to the frequency domain, multiplied by the instrumental function, transformed back to the time domain and amplified further in the seeded undulator.

3.3.3   Comparison of approaches

Both the direct and the phenomenological approaches used to simulate the slit-less monochromator performance show similar results when comparing the radiation after amplification in the seeded undulator. In Figures 3.29 and 3.30 one may see that despite an initial difference in the power and the structure of spectra, the results show a very good correspondence to each other after amplification in the seeded undulator. The spectrum is shifted due to the electron energy chirp evolution, induced by wakefields. Initial spectra are different: phenomenological approach should provide spectrum with a lower spectral density and narrower spectrum since it includes additional filtering associated with the gain process of the downstream FEL.

The phenomenological approach provides an effective radiation distribution that will be amplified in the seeded undulator. It is much faster than the direct one in terms of the computational time and is more applicable for batch processing of numerous FEL shots with once calculated single monochromator instrumental function. This method uses extra assumptions, since steady-state FEL simulation is used to obtain the instrumental function. Also this method is not applicable if one wants to perform simulations with a different monochromator or amplification parameters, since the monochromator instrumental function depends not only on the monochromator set-up but also on gain lengths in the SASE and in the seeded undulator as well as the electron beam parameters. Therefore one must keep in mind that a simulated FEL gain length during the instrumental function calculation should be similar to the one at which this instrumental function would be used for the pulse monochromatization via the phenomenological approach. Therefore, in general one needs to re-calculate the transmission function for different setups of FEL.

Unlike the phenomenological method, the direct approach needs significantly more computational power and time to simulate the single SASE radiation pulse propagation through the monochromator. It does not need a preliminary measurement of the instrumental function, since dispersion of the radiation is simulated for every run. Also this method is more universal. It gives a possibility of reusing simulated, monochromatized radiation for simulating the effect of different configurations of the seeded undulator. Since the radiation after the monochromator
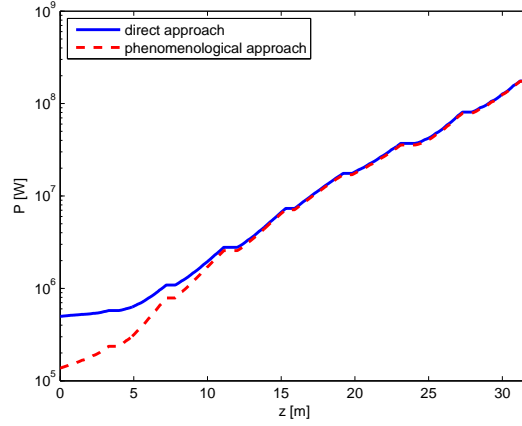
Figure 3.29: Power of the radiation in seeded undulator. The radiation was propagated through the seeded undulator with the direct (solid line) and the phenomenological (dashed line) approaches. Photon energy is $1000\ eV$.
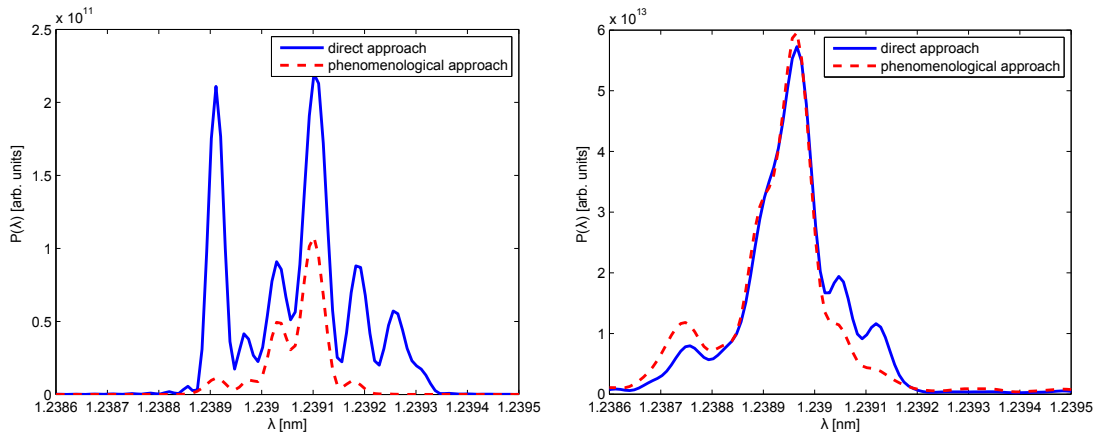

Figure 3.30: Spectra of the radiation at the seeded undulator entrance (left figure) and exit (right figure). The radiation was propagated through the seeded undulator with the direct (solid line) and the phenomenological (dashed line) approaches. Photon energy is $1000\ eV$.

is divergent and transversely large, it becomes important to control the interactions between the propagated radiation and the transverse mesh borders of an FEL simulation software. If non-absorbing boundary conditions are used (like in the GENESIS code), then after propagation downstream the seeded undulator, the radiation will be eventually "reflected" from the borders before the central part starts being amplified. The direct method allows one to obtain the actual pulse properties after the monochromatization, that makes it very useful for in-depth research of a monochromator performance. It may be used to cross-check the phenomenological approach simulations.

66

3.4 Comparison with an experiment

The SXRSS monochromator setup commissioning in the LCLS started in November 2013. In December 19-th the first seeding was achieved at 800 eV photon energy. More systematic study of the monochromator performance was done during 2014. Results were presented at the FEL conference in August the same year [78] and published in February 2015 [54]. During that time an extensive study of the monochromator simulation possibilities was done in parallel to the commissioning in order to understand the SXRSS setup performance. Self-seeding has been observed across the nominal photon energy range of 500-1000 eV. Here comparison of an experiment and start-to-end simulation is presented on the example of seeding at 930 eV energy.

During the **experiment** the electron beam with a phase space modified with a slotted foil [87] was used (see Fig. 3.31). It was found that the non-linear energy chirp within the nominal, e.g. not modified with a slotted foil or collimator, electron beam (particularly, one of the horns) causes higher heat load on the grating with a little effect on the seeding performance.

(a) nominal electron beam   (b) electron beam spoiled with a slotted foil
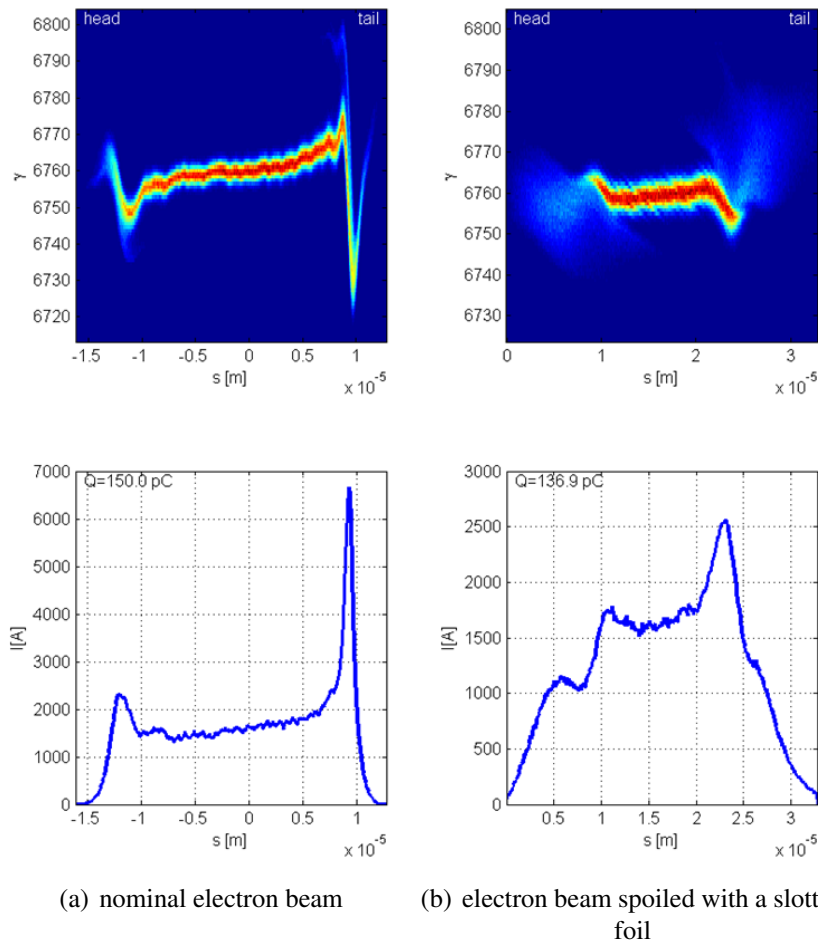
Figure 3.31: LCLS electron beams simulation. Phase space (top plots) and current profiles (bottom plots). Simulation data obtained from [88].

The gas detector [89] and the grating spectrometer [90] located downstream the LCLS undulator modules measure the FEL energy and spectra. By retracting undulators or introducing

a transverse "kick" of the electron beam it is possible to measure the FEL radiation parameters between any undulator sections via stopping the FEL process downstream [91]. Exit slit was retracted during the experiment.

Simulation parameters were reproducing the ones used in the experimental setup. The electron bunch 6D distribution file was simulated [88] with the "ELEGANT" code [92] up to the entrance of the LCLS undulator. Initially 150 pC, 10 Million particles bunch with 4 GeV energy was spoiled with a slotted foil. The simulated foil slit width was 1.3 mm. The electron bunch was used to provide SASE radiation within the first 7 sections of the undulator. During the experiment the K value of the first undulator segment U1 was detuned in order to keep the pulse energy at the grating below 5 μJ. U8 segment of the undulator was retracted to minimize the incident energy density (fluence) on the grating surface. Evolution of the power and energy within the SASE undulator is shown on Figure 3.32.
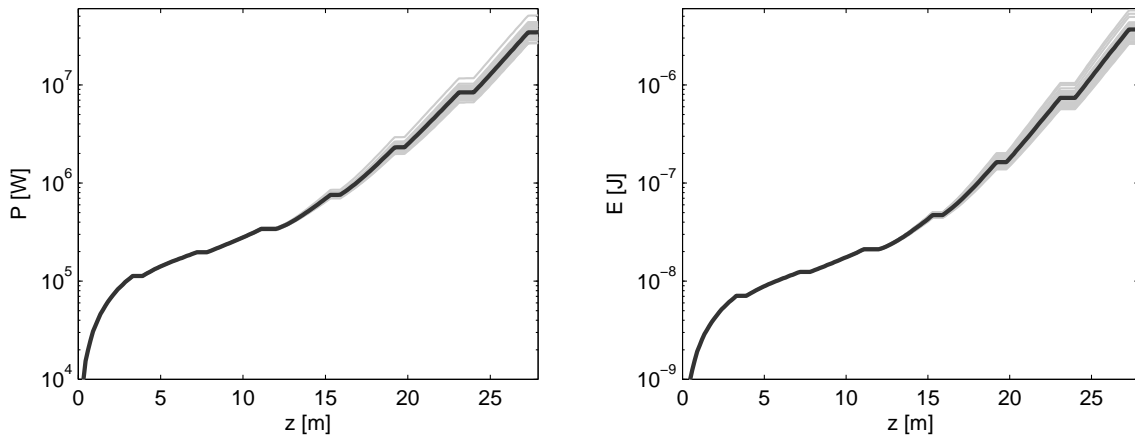
Figure 3.32: Power and energy evolution within the SASE undulator

After dumping the radiation field and electron beam distributions they were treated separately and combined as an input to the seeded undulator simulation. Radiation was propagated within the monochromator with a direct propagation approach. Electron beam distribution shot noise in the seeded undulator was automatically arranged by the GENESIS code. This method is justified by the fact that hromatic dispersion effects in the bypass chicane smear out the microbunching in the electron bunch produced by SASE lasing in the SASE undulator. But the chicane dispersion is not strong enough to affect macroscopic parameters of the longitudinal bunch profile, such as current, emittance, energy spread, etc.

Similarly to the experiment, only fifteen of 23 undulator sections downstream the monochromator were used within the simulation, including drift space at the HXRSS setup which occupies the U16 undulator section. Monochromatized pulse is overlapped with an electron beam and amplified with improved longitudinal coherence and narrower spectral width compared to the SASE undulator (see Fig. 3.34). The seeded undulator was tapered [20], and tapering profile used in simulation was adopted from the experiment (Fig. 3.33). Power and energy evolutions in the seeded undulator are presented in Figure 3.35.
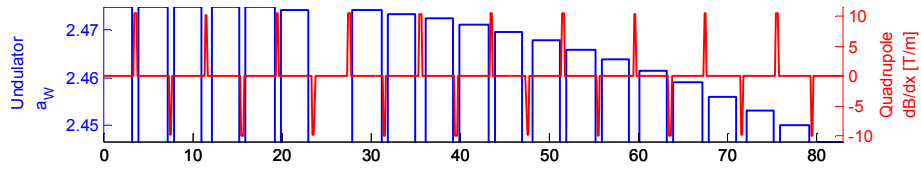
Figure 3.33: Undulator tapering profile and quadrupole fields used for simulation and based on corresponding values measured during the commissioning study

The input coupling factor (ICF) in the seeded undulator obtained with the simulation was found to be inconsistent with the experiment by the factor of 5. It may be explained by a misalignment of optical components. An appropriate power compensation of the seeding radiation was made to match the simulated power with the experimental values. This compensation resulted in a good agreement of the simulated and measured pulse energy evolutions, presented on Figure 3.36. Comparison of spectral bandwidth on Figure 3.37 proves a good agreement as well. It was shown that the self-seeding technique allows one to bring down the LCLS radiation spectral bandwidth by the factor of 20. Note that the averaged SASE spectrum is additionally broadened due to an electron energy jitter.

Difference in ICF between the experiment and the simulation shows that seeding quality may be improved and further study is needed.
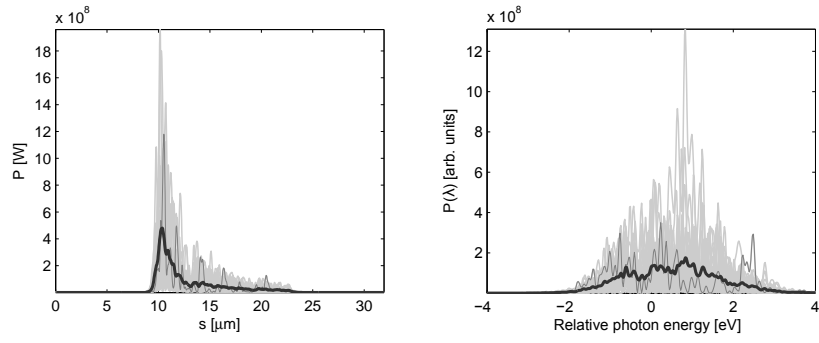
(a) SASE undulator end
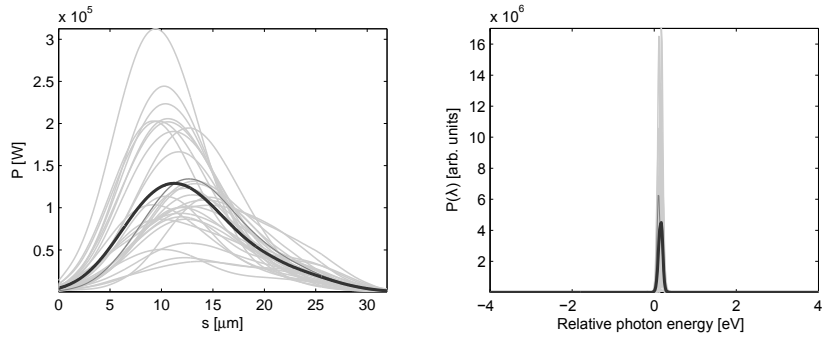
(b) seeded undulator entrance (0m)
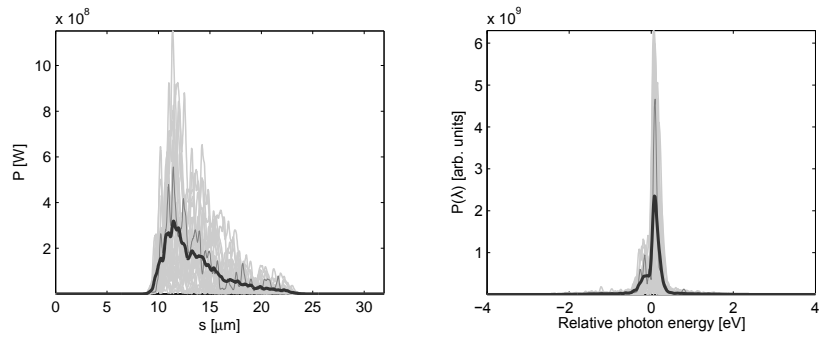
(c) seeded undulator 20 m
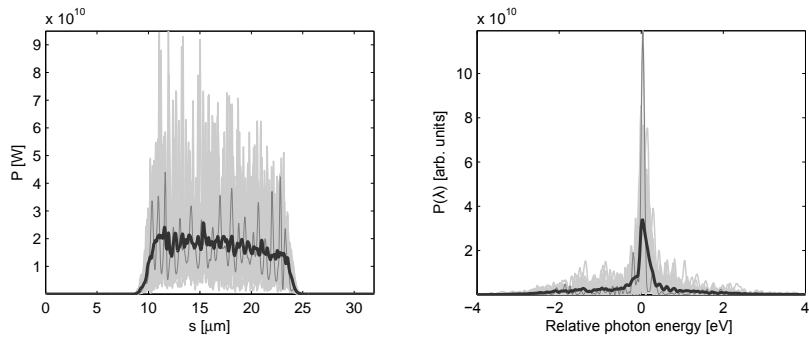
(d) seeded undulator end (60m)

Figure 3.34: The results of the FEL pulse power (left plots) and corresponding on-axis spectra (right plots) at different positions inside the undulator.
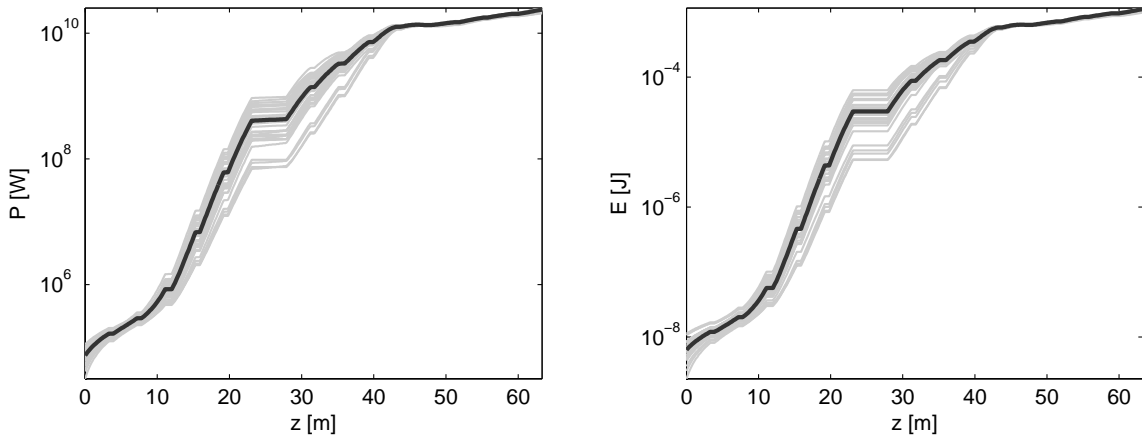
Figure 3.35: Power and energy evolution within the seeded undulator
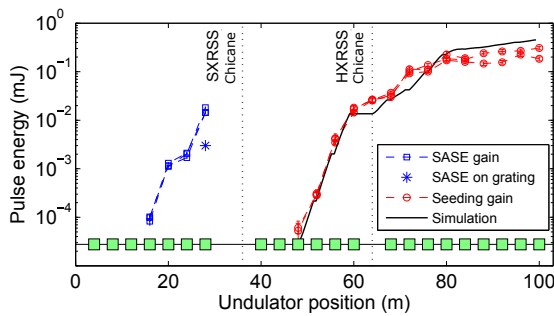
Figure 3.36: Gain length scans showing SASE growth before the seeding monochromator (blue squares, three scans) and seeding growth afterwards (red circles, three scans). During seeded operation, undulator U1 is detuned to keep pulse energy on the grating below 5 J (blue star). Black line shows simulated seeding. Green boxes show undulators inserted during seeding; undulator U8 is removed to protect the grating, and undulators U9 and U16 were replaced by the self-seeding chicanes. Measured gain lengths for SASE ($\sim 2 \pm 0.2m$) and seeding ($\sim 1.7 \pm 0.2m$) match simulations. All measurements taken with the gas detector. Reprinted from [54].
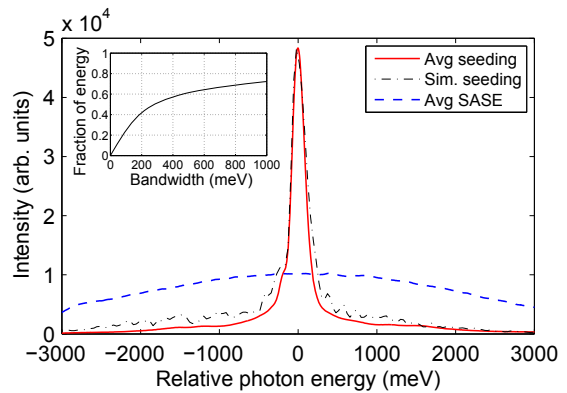
Figure 3.37: Comparison of seeded (solid red line) and SASE (dashed blue line) spectra at 930 eV for 10 000 shot averages, and seeded simulation (sim.) averaged over 30 shots (dotted-dashed black line). Both seeded and SASE spectra use the slotted foil to produce a 50 fs beam [87]. Seeded spectra are taken after undulator U25 and with the slit retracted. SASE spectra use an optimized configuration with all undulators. Inset shows the fraction of FEL energy contained within an integrated bandwidth when seeding. Reprinted from [54].

3.5 Commissioning details

During commissioning of the SXRSS monochromator numerous challenges were faced. Below the main ones are outlined.

3.5.1 Electron beam energy jitter effects

A very important issue of the SXRSS setup operation is an effect of the electron beam energy jitter. First of all, according to the FEL resonance condition (Eq. 1.1) shot-to-shot fluctuations in electron beam energy (jitter) cause doubled fluctuations of the FEL amplifier gain curve. On Figure 3.38 it is illustrated that jitter may be large enough to stop the seed. In case of the current LCLS operation parameters it is larger than the FEL gain curve.

If the electron beam has an energy chirp, it will affect the properties of the amplified seed signal. In case of a linear energy chirp, the wavelength of the monochromatic seed will be shifted. If the chirp is non-linear, then broadening of spectrum will occur. During the commissioning a non-linear chirp effect was compensated with a slotted foil. More details were presented in [78] FEL conference talk.
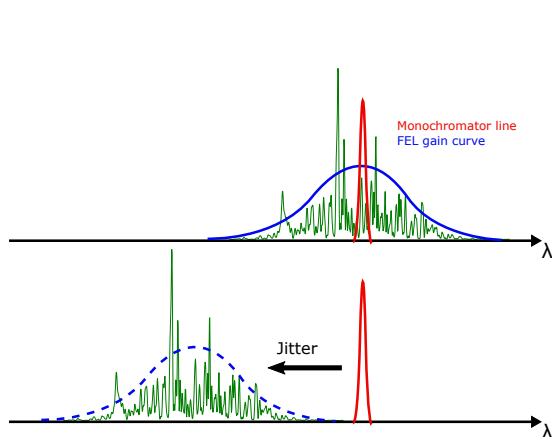
Figure 3.38: An illustration of the effect of an electron energy jitter. The seeded wavelength is fixed after the monochromator, so the electron energy must be set in the way that FEL gain curve matches it. There will be no seeding when FEL gain curve due to jitter drifts away.
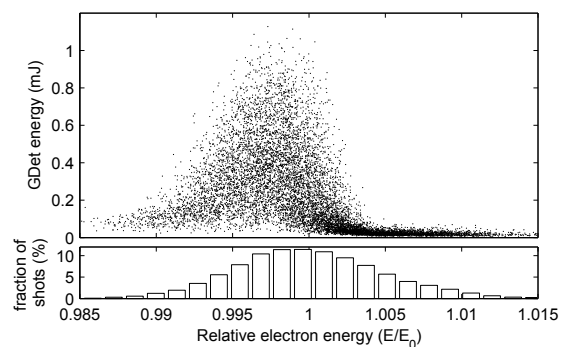
Figure 3.39: A scatter plot shows the FEL pulse energy from the gas detector vs measured electron bunch energy for individual shots at 930 eV. Histogram at bottom shows the jitter of the central electron beam energy. The seeding monochromator was set slightly below the average electron energy to match the best lasing condition. 45% of the shots fall outside the FWHM of FEL seeded region. Reprinted from [54].

Both effects were measured during the SXRSS commissioning and are presented in a correlation plot of the seeded FEL power and electron beam energy on Figure 3.39.

Another possible causes of the wavelength jitter are instability of the M1 mirror pitch angle and electron beam orbit fluctuations [93]. There are ongoing efforts to reduce the electron energy jitter and potentially increase the average seeded power by the factor of 2, and there is always a possibility to overcome the jitter problem by sorting shots with a certain electron beam
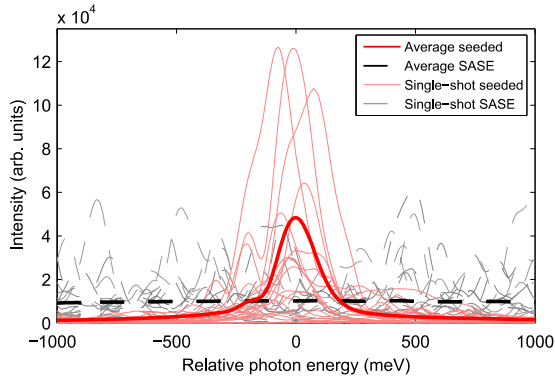
Figure 3.40: A comparison of 20 single-shot seeded (solid light red lines) and SASE (dashed grey lines) spectra shows fluctuations in both peak brightness and central seeded wavelength. Bold lines show average performance for both seeding and SASE. Reprinted from [54].
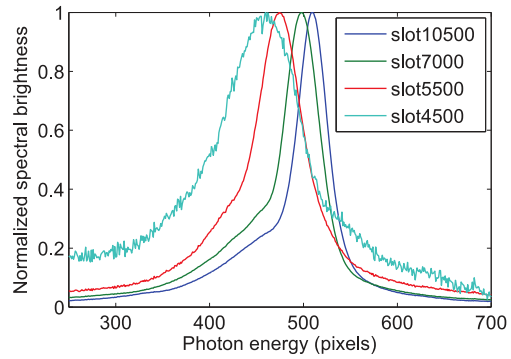

Figure 3.41: Slotted foil selects part of the beam. Seeded spectrum bandwidth is brought down when a non-linear chirp is eliminated. Reprinted from [78].

parameters [54]. This way, the self-seeding setup causes extra demands on the electron beam energy stability.

3.5.2 Overlap diagnostics

An important aspect of the SXRSS scheme compared to the HXRSS is the need to realign the seeded radiation after the monochromator with an initial radiation path in order to overlap it with the electron beam transversely (Fig. 3.42).
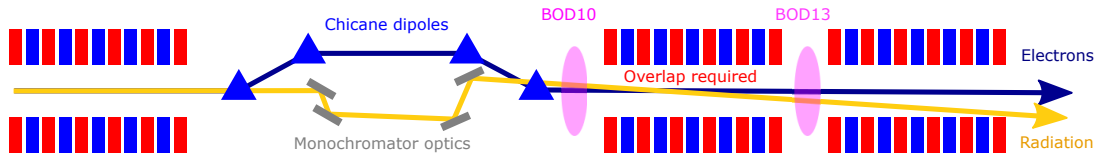
Figure 3.42: Overlap diagnostics at the LCLS SXRSS. Adapted from [94]

The beam overlap diagnostics (BOD) is used to measure the transverse positions of both photon and electron beams [94]. Each BOD unit consists of crossed wires and a YAG screen (see Fig. 3.43). The electron beam transverse position is determined by scanning the crossed wires positions while measuring a current loss downstream. When transverse kick of the electron beam is applied, seed radiation transverse position is detected on the YAG screen fluorescence (Fig. 3.44). The spontaneous emission stripe from the electrons in the final chicane bend magnet can be used for the vertical alignment of the x-rays and electrons.

Aligning radiation and electrons is achieved by matching 4 degrees of freedom: radiation offsets and tilts in both "x" and "y" dimensions. Mechanically it is provided by tuning grating "y" position (sagittal curvature contribution), and M3 "x" position along with pitch and roll angles. Alignment of the optics is proceeded sequentially from the grating to the M3 mirror. Worth mentioning that a strong CSR background causes additional difficulties in the seed radiation detection on BODs. The exit slit insertion was found to be useful for the alignment. Therefore
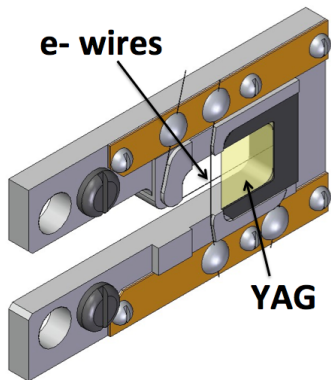
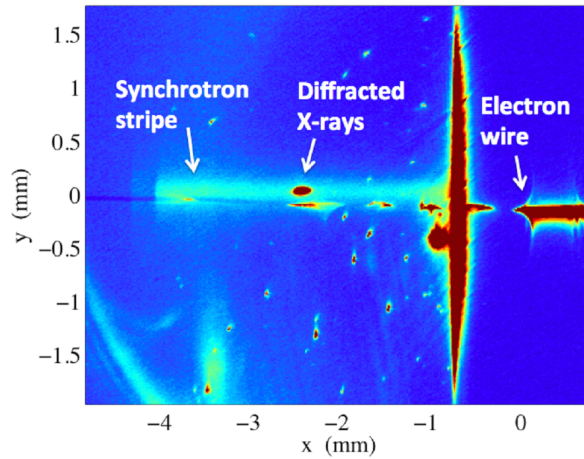Figure 3.43: Diagram of beam overlap diagnostics design. Reprinted from [95]

Figure 3.44: Image of the BOD10 YAG fluorescence. Diffracted X-rays are seen on top of the synchrotron radiation stripe. 15 μm exit slit is inserted limiting the dispersed radiation in "x" dimension. Reprinted from [95]

slit inclusion into monochromator design is desirable, albeit it was found that monochromator works well in slit-less regime.

3.5.3 Grating damage concerns

Due to a high power of the LCLS FEL, damage of the platinum-coated grating was found to be a matter of a major concern for the SXRSS operation. As mentioned before, the grating was chosen to be platinum coated. It is expected that a B_4C coated grating would have a higher damage threshold than the platinum coated. However, in X-ray regime mirrors suffer from carbon contamination effect [96], and platinum coating allows one to perform oxygen cleaning of the surface [97]. On the other hand, platinum coating is more sensitive to the radiation damage. The damage of platinum coatings in the soft X-ray at grazing incidences was studied exclusively [98] in order to determine safe power levels.

An important value for the damage threshold estimation is the energy absorption dose per atom [98–100] and [101, p. 233]:

$$D_A = \frac{F(1-R)\sin\theta_i}{l_{\text{att}}\, n_A} = \frac{E_{\text{pulse}}(1-R)\sin\theta_i}{2\pi\sigma^2 l_{\text{att}} n_A} \, , \tag{3.1}$$

where F is the fluence, E_{pulse} - the energy in one radiation pulse, R - reflection coefficient, θ_i is a grazing incidence angle, n_A is a material-specific density of atoms and σ is the RMS of the Gaussian beam intensity distribution immediately in front of the grating. Here l_{att} is the extinction length. Multi-shot damage on the platinum-coated silicon substrate at 2 degrees incidence angle[1] was observed at $0.75\ J/cm^2$ average fluence. Based on the experimental conditions, $6 - 9\ eV$ absorption dose per atom was estimated. It exceeds the dose, required to bring a solid to the melt temperature $D_{melt} \simeq 0.47\ eV/atom$ by approx. 14 times. As mentioned in [98], this inconsistency can be explained with the so called "two temperature model" [102] (different heat diffusion within electron and ion systems) and the ballistic transport of electrons [103]. The same effect was reported in [104]. This way the energy deposition length was introduced extending the depth at which the pulse energy is distributed up to 24 nm (by the factor of 14 with respect to the extinction length d of 1.7 nm). Based on this study, the SASE undulator pulse energy was chosen not to exceed $5\ \mu J$, or 25 times lower than the measured threshold.

Energy per pulse at the grating can be measured straightforwardly during the commissioning by retracting the entire monochromator optics along with the undulators downstream. It allows one to measure the FEL energy produced by the SASE undulators with the gas detectors [89]. The incident energy can be lowered by detuning or removing the frontmost SASE undulator sections without affecting the FEL source properties. Heat from an absorbed energy is removed from the grating via a copper heat sink. Another safety measure is the protection of the grating from a spontaneous radiation from the SASE undulator. This way a boron carbide "chin guard" is placed at the front side of the grating.

A minimum fluence for seeding was found by start-to end direct method propagation. 9 FEL runs for four photon energies were studied with the start-to-end simulation using the slotted foil - treated electron beam. An FEL radiation was propagated though the monochromator with a

---

[1]Incidence angle was set to two degrees to mimic 1° blaze angle of the grating and 1° radiation grazing incidence angle on the grating, designed for SXRSS monochromator.
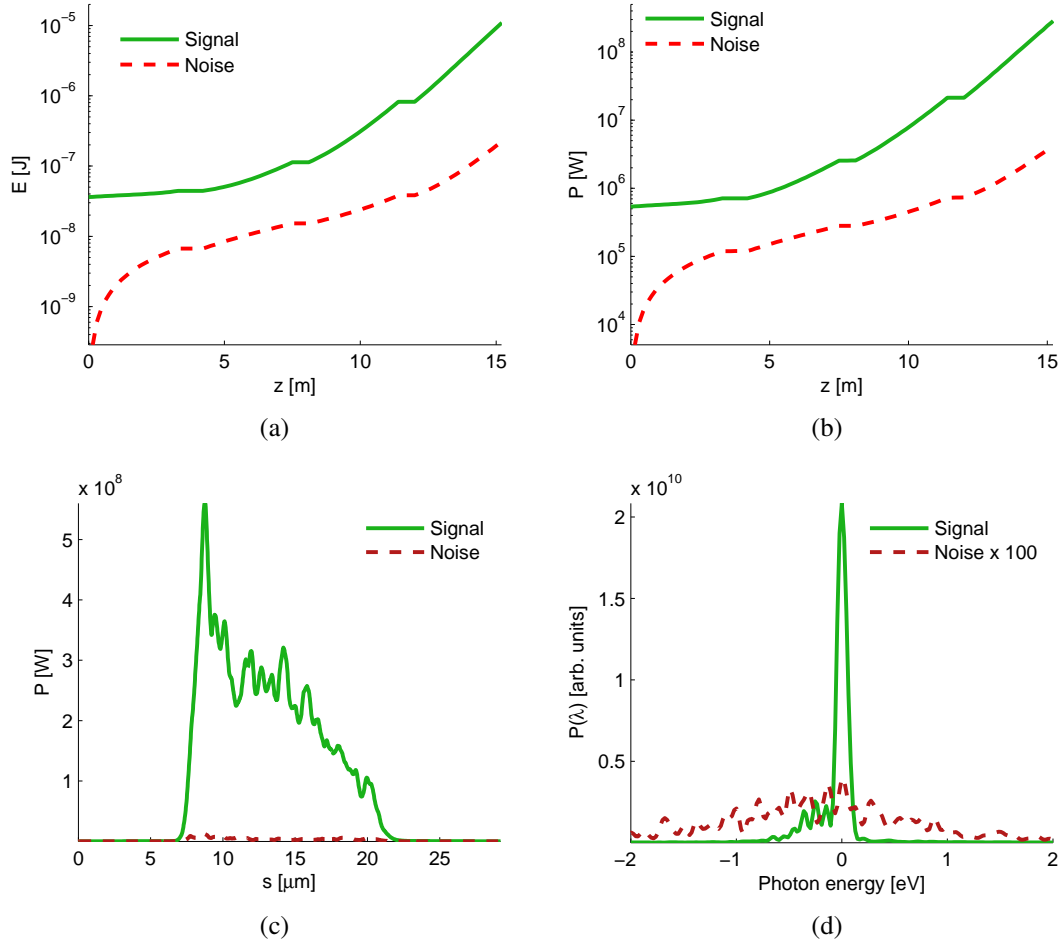
Figure 3.45: Pulse energy (subfigure (a)) and peak power (subfigure (b)) evolution of 700 eV FEL pulses in the seeded undulator. Red dashed curves depicts amplification of noise, while green solid curves represent amplification of the seed signal along with noise. In deep linear regime at 15.2 m position pulse power values are compared and pulse energy SNR ratio 50 is found. Power profiles and spectra of pulses are compared in subfigures (c) and (d) respectively. Note the large difference of a peak spectral brightness.

direct approach and an electron microbunching was assumed to be smeared with the chicane. For an every run, simulation in the seeded undulator was done with a seed signal (providing FEL amplification of both signal and noise) and without (only noise, e.g. SASE radiation was amplified). This way it became possible to distinguish the contributions of the seeded and SASE radiation after an FEL amplification and define a signal-to-noise ratio (SNR) for a seeding. The following definition was accepted: SNR is the ratio of mean pulse energy of a signal (seed) over a SASE mean pulse energy (noise in the absence of a signal).

$$\text{SNR} = \frac{\langle E_{signal+noise} \rangle - \langle E_{noise} \rangle}{\langle E_{noise} \rangle} \tag{3.2}$$

The seeding requirement for SNR value was chosen to be 3, e.g. 75% of the pulse energy is amplified seed signal and the rest 25% is the noise. Since a spectral bandwidth of a seed signal is considerably smaller than the one of noise, spectral brightness of noise is low. An example
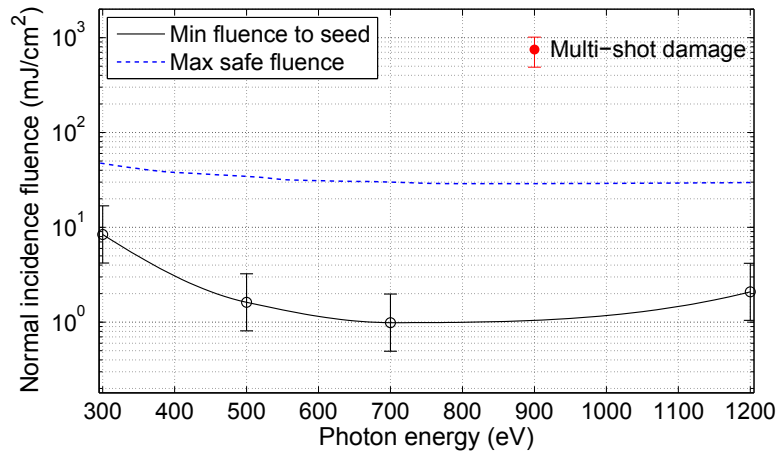
Figure 3.46: Black line - minimum fluence to obtain a reasonable signal-to-noise ratio. Dotted blue line - maximum fluence guaranteed to avoid multi-shot damage. (it is equivalent to 1.25 μJ with undulator U8 inserted or 5 μJ with undulator U8 removed). Reprinted from [95]

of the FEL signal and noise amplification is presented on Figure 3.45

Both upper and lower limits of the fluence on the grating are depicted on Figure 3.46.

Chapter 4

Monochromator design for the European XFEL

In this chapter we present a study of the soft X-ray self-seeding opportunities for the European XFEL, based on start-to-end simulations for an electron beam with 0.5 nC charge [105]. Simulations show that the FEL power of the transform-limited soft X-ray pulses may be increased up to 1 TW by tapering the baseline (SASE3) undulator.

4.1 European XFEL

The European XFEL is an international X-ray research laser facility currently under construction in Hamburg, Germany. It is based on TESLA (Tera-Electronvolt Superconducting Linear Accelerator) technology, allowing to reach nominal electron energies up to 17.5 GeV
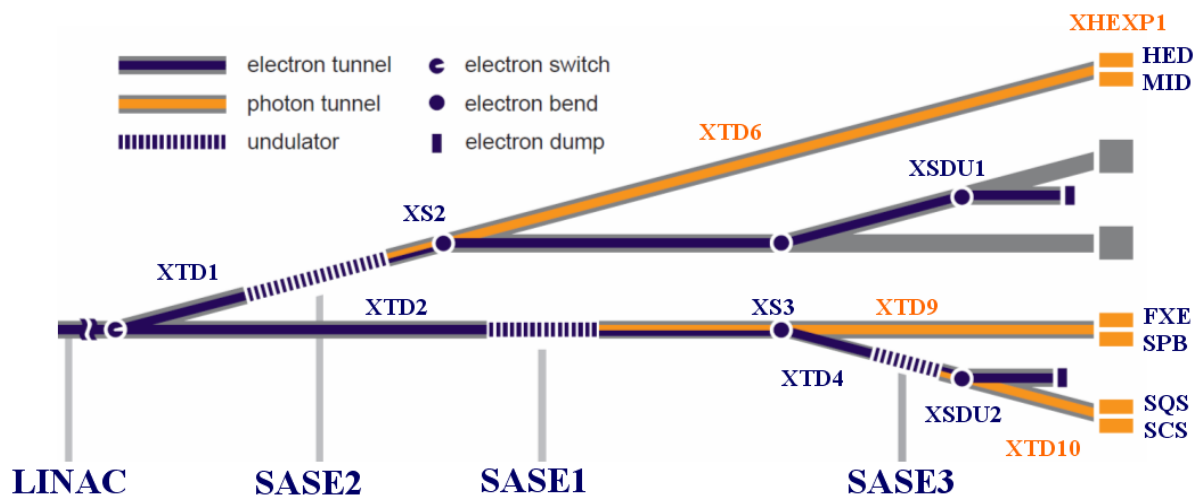
Figure 4.1: Schematic overview of the electron beam and the radiation distribution between accelerator and experimental hall. Two electron beamlines include the three undulator systems for SASE FEL. The distance between the electron switch and the experimental hall is ∼1300 m. Reprinted from [106]
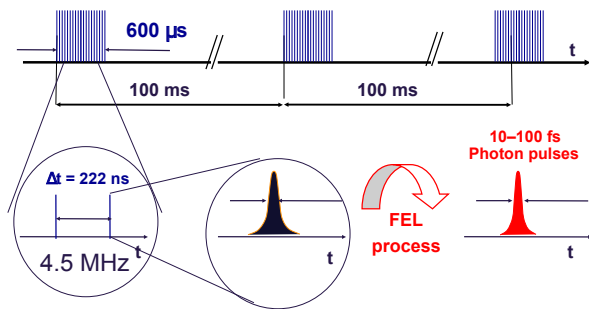
Figure 4.2: Time structure of European XFEL radiation pulses generated by electron bunch trains with up to 2700 bunches in each. Bunch charge is $20 - 1000$ pC. Reprinted from [107]
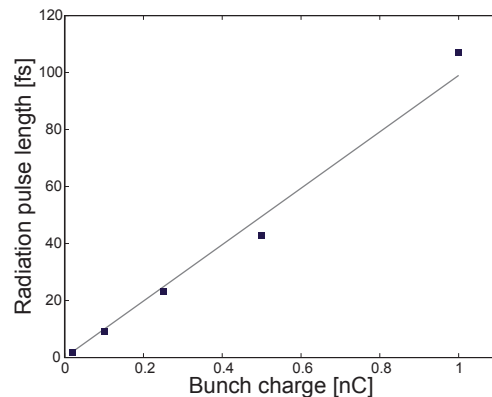
Figure 4.3: Radiation pulse length (FWHM) grows proportionally to the bunch charge in the SASE saturation. Reprinted from [108]

Three undulator lines (Hard X-ray specialized SASE1 and SASE2 along with soft X-ray dedicated SASE3) will deliver FEL radiation to the experimental hall (Fig. 4.1) at certain range of photon energy each.

SASE3 undulator line is designed mainly for soft X-ray photon energies and provides radiation from ranging from 260 eV to 1.5 KeV within a single electron beam energy of 8.5 GeV changing only undulator gap (see Fig. 4.4). Switching among nominal electron energies allows to reach higher photon energies.

Radiation will be delivered to the experimental stations in pulse trains carrying up to 2700 pulses within train that allows to fulfill photon-hungry experiments needs (see Fig. 4.2).

European XFEL single pulse length depends mostly on the electron bunch length. With five nominal bunch parameters, one can find a linear dependence (see Fig. 4.3).

4.2 SASE3 undulator line

4.2.1 Description

SASE3 undulator is located in the European XFEL tunnel downstream SASE1 undulator. [101, 110, 111] It has a cell structure (see Fig. 4.5) and consists of 21 cells. Undulator gap is variable and its main parameters are outlined in Table 4.1.

The "fresh-bunch" technique [115] makes it possible to deliver an unspoiled electron beams to the entrance of the SASE3 undulator. It is achieved by "kicking" the bunch out of the lasing orbit e.g. in SASE1 and "kicking" it back later to lase in SASE3.

Downstream the undulator the SASE3 photon beamline is located [113, 114], carrying out distribution and refocusing of the FEL radiation to the instrumental stations. Its layout is presented on Figure 4.6. The beamline includes VLS monochromator, which allows operation with 10 mJ pulse energies and higher, depending on the FEL beam divergence [113, p. 43].
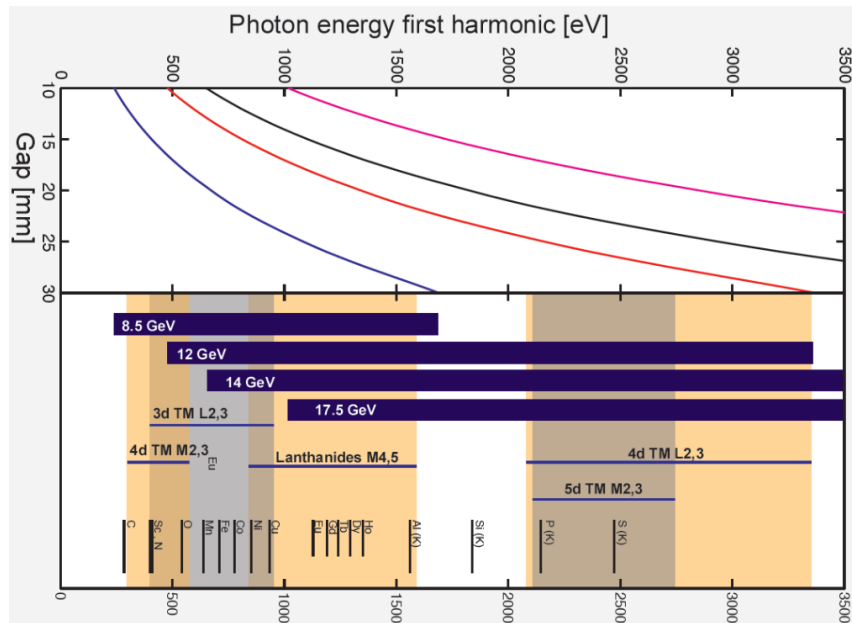
Figure 4.4: Combination of European XFEL nominal electron energy working points and undulator variable gap allows to reach wide range of photon energies at SASE3 beamline. Reprinted from [109].
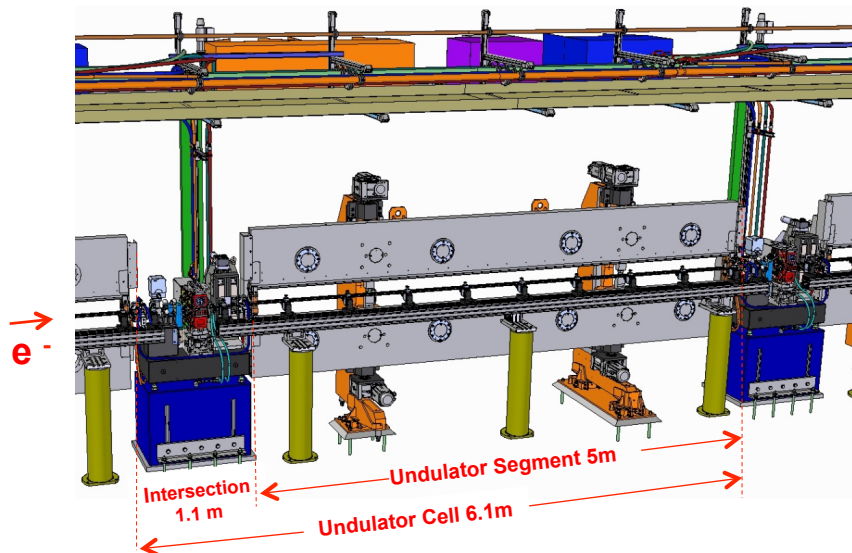

Figure 4.5: Cell structure of European XFEL undulators. 5 meter undulator section alternate with 1.1 meter intersections, accommodating phase shifters, electron beam optics and diagnostics. Reprinted from [112].

		Units
Undulator period	68	mm
Operation gap range	10-25	mm
K-range	9.0-4	-
Radiation wavelength range		
@17.5 GeV	1.22-0.27	nm
@14.0 GeV	1.90-0.42	nm
@12.0 GeV	2.59-0.57	nm
@8.5 GeV	5.17-1.15	nm
Periods per cell	73	-
Total number of cells	21	-
Segment length	5	m
Intersection length	1.1	m
Physical length	128.1	m
Magnetic length	105	m

Table 4.1: Parameters for the SASE3 undulator. Adapted from [101, 110, 111].

Two scientific instruments utilize SASE3 radiation: *Small Quantum System (SQS)* [116, 117] and *Spectroscopy and Coherent Scattering (SCS)* [108].

4.2.2 Source study

In order to perform calculations of the grating beamline performance, one needs the effective source size and position through the operating photon energy range. In our case of reimaging the monochromatized FEL radiation, its source is at a same time an object for the focusing system. In FELs radiation is emitted by the electron beam at an every undulator period with intensity increasing exponentially with undulator length. This results in development of a complicated non-Gaussian shape of the self-reproducing mode. Properties of the latter depend on the electron beam parameters. In this section it is described how FEL source was modelled as a Gaussian distribution with certain parameters, as size of the waist and its position within an undulator module.

The properties of the effective source are found from the steady-state (single frequency) simulations with the help of the GENESIS 1.3 code [83, 84]. The simulations include electron beam parameters (emittance, energy spread, current) correspondent to the nominal 0.1 nC electron bunch. Beam parameters for the steady-state simulations have to be chosen to match the ones of the bunch slice with the maximum peak current. The properties of the effective source can be found from the simulated transverse radiation distribution at the SASE undulator exit. Position of the model source is obtained by propagating the simulated field backwards from the undulator exit in order to find the maximum on-axis intensity. Propagation is performed with the Fresnel propagator algorithm described in Sec. 2.1.2. The RMS size of the model Gaussian source is calculated based on RMS of the radiation divergence angle. These parameters are
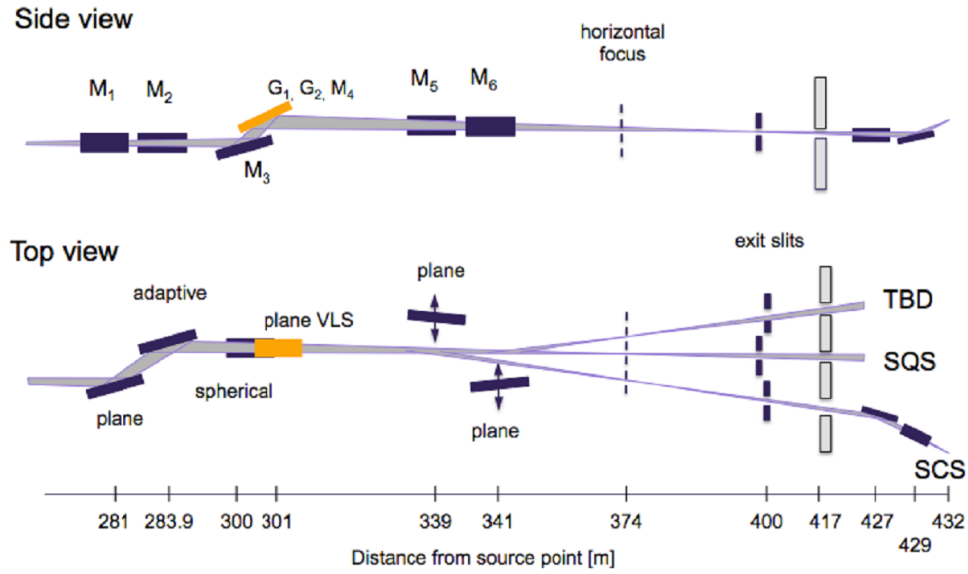
Figure 4.6: Optical layout of SASE3 beamline. Location of optical elements is given as a distance from the FEL source point that is assumed to be fixed and located in the middle of the second to last undulator. Reprinted from [113, 114].
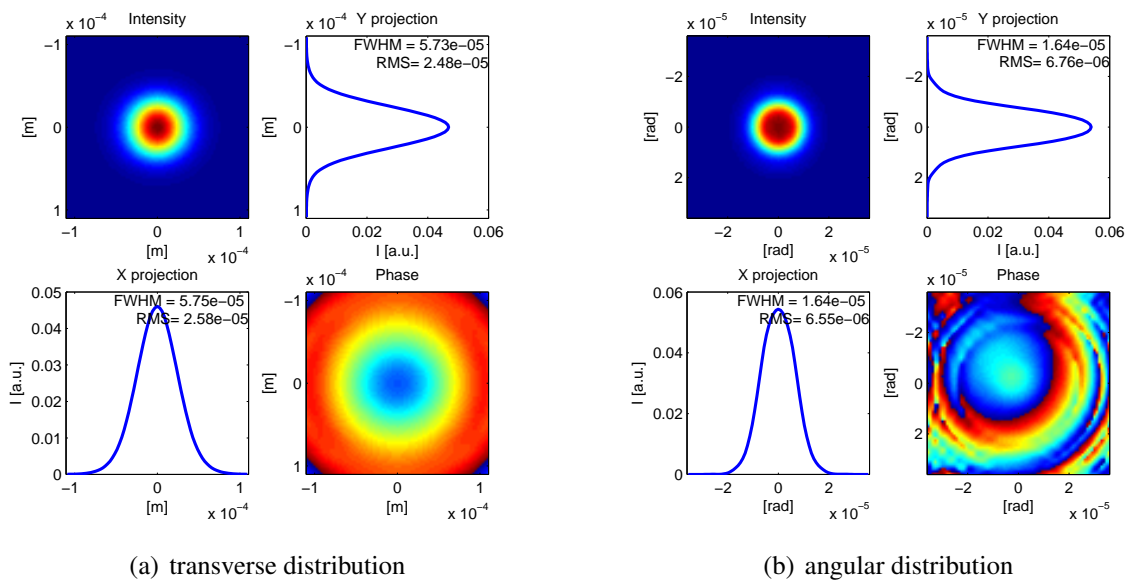

(a) transverse distribution

(b) angular distribution

Figure 4.7: Transverse and angular distributions of the FEL radiation at the end of a SASE3 undulator section. Here $\hbar\omega = 1 \, keV$.
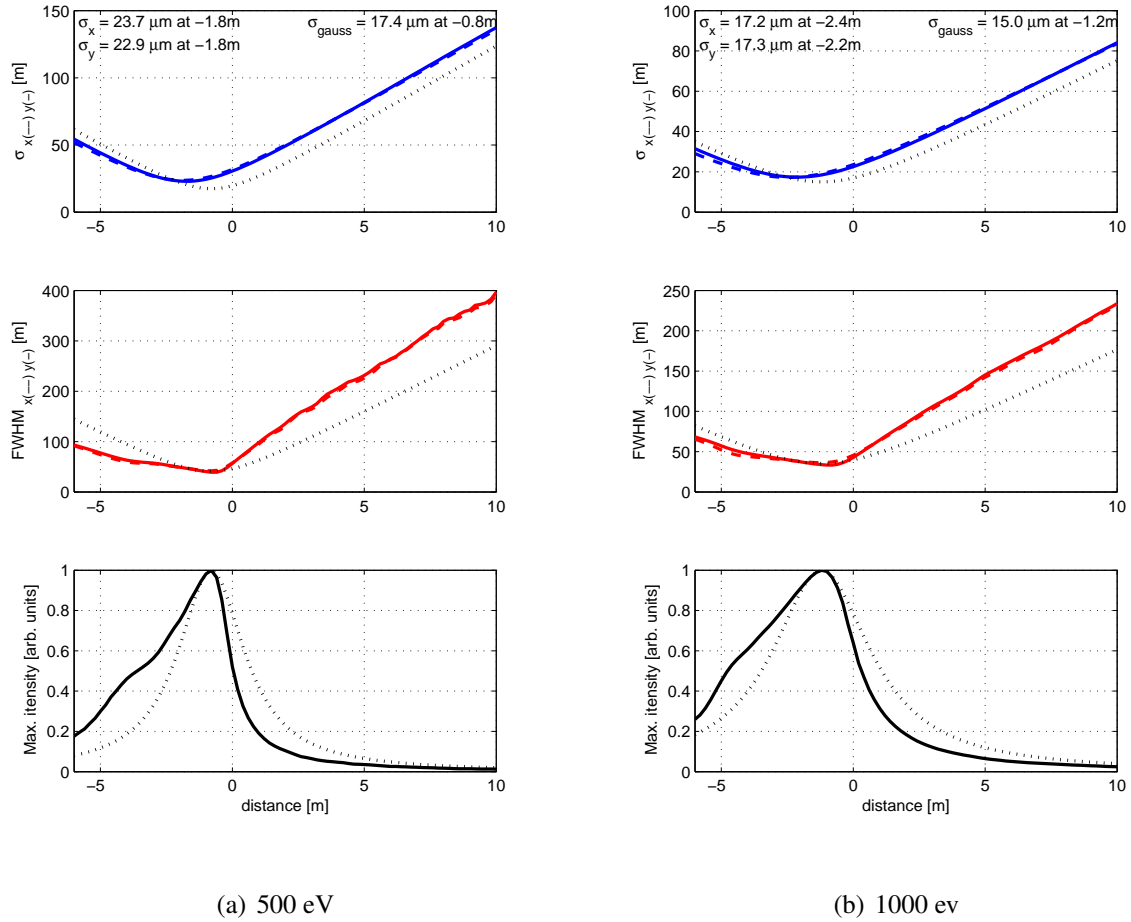
(a) 500 eV   (b) 1000 ev

Figure 4.8: Variation of the radiation distribution parameters as a function of the position from the end of the SASE3 undulator section in linear operation mode with nominal 0.1 nC electron bunch. Two energies of 500 eV (subfigure 'a') and 1000 eV (subfigure 'b') presented. Top plots depict standard deviation of the radiation intensity distribution. Middle plots - measured FWHMs of distributions. Solid lines represent tangential direction "y" and dashed - sagittal one "x". Bottom plot - maximum of the distribution dependence. Dotted lines show corresponding parameters for model beams.

related by

$$\epsilon = \sigma'\sigma = \lambda/4\pi \, , \tag{4.1}$$

where the product of the RMS divergence angle by the RMS source size is the emittance ϵ of the photon beam. For a two-dimensional distribution the definition of the Gaussian beam emittance applies to each direction.

A transverse radiation distributions were obtained at the end of the undulator section U5. The 1000 eV photon energy distribution is presented on Figure 4.7 along with its angular distribution (directivity diagram).

RMS and FWHM of the transverse radiation distribution and its maximum intensity as a function of position of the propagated radiation distribution are presented on Figure 4.8. Note symmetrical and asymmetrical behavior for RMS and FWHM dependences correspondingly. RMS size of the transverse radiation distribution is a convenient way to characterize size of

(a) Source position   (b) Source size
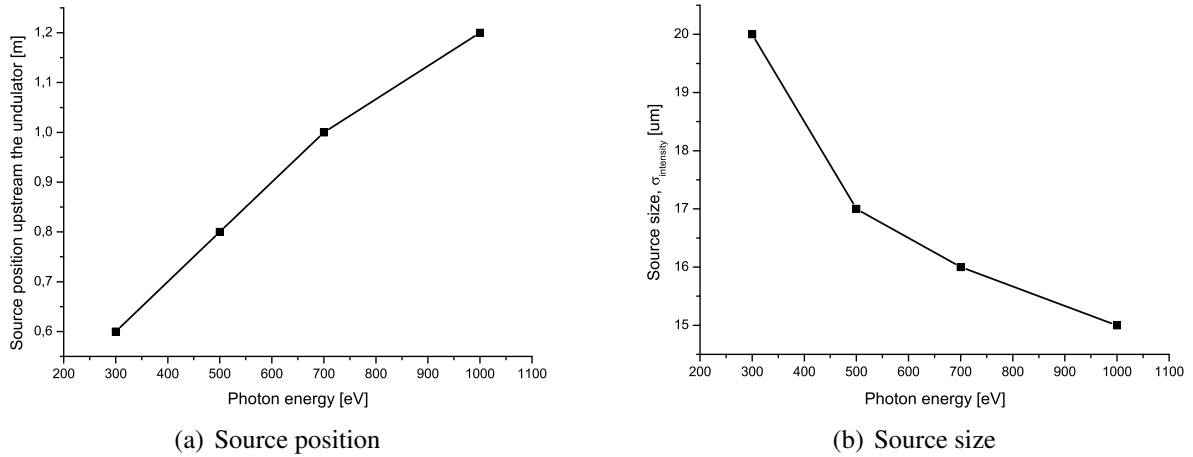
Figure 4.9: Position and size of the model Gaussian source, in the SASE undulator for different photon energies

its waist and evolves symmetrically when propagated through the waist for any arbitrary non-Gaussian beam [118]. In fact, an FEL source transverse distribution is not Gaussian. Nevertheless, Gaussian beam was found to be a convenient way to simulate the FEL radiation propagation analytically.

A resulting dependence of the model source parameters from the photon energy is presented on Figure 4.9. This correlation of the source properties with photon energy is accounted for in the current monochromator design.

Transverse coherence properties of an FEL radiation allow to avoid the entrance slit installation: grating grooves are illuminated coherently [79, 80, 119].

4.2.3 Reimaging study
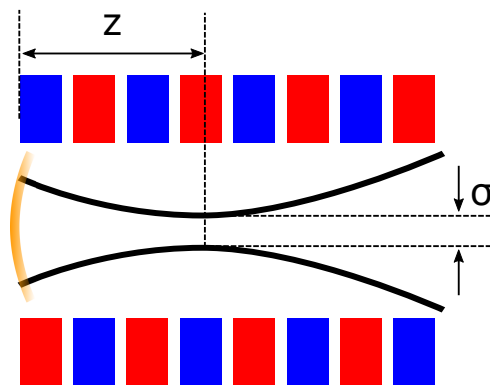
Figure 4.10: The illustration of the spherical wavefront of the Gaussian beam used as an input for the second undulator. Transverse distribution is generated in a way to converge to the waist of size RMS σ, at a distance z downstream the undulator.

Another very important aspect of SXRSS monochromator performance is to overlap a monochromatized radiation (image) with an electron beam in the most effective way along the undulator. In our case reimaging does not imply focusing to the minimal spot with maximum
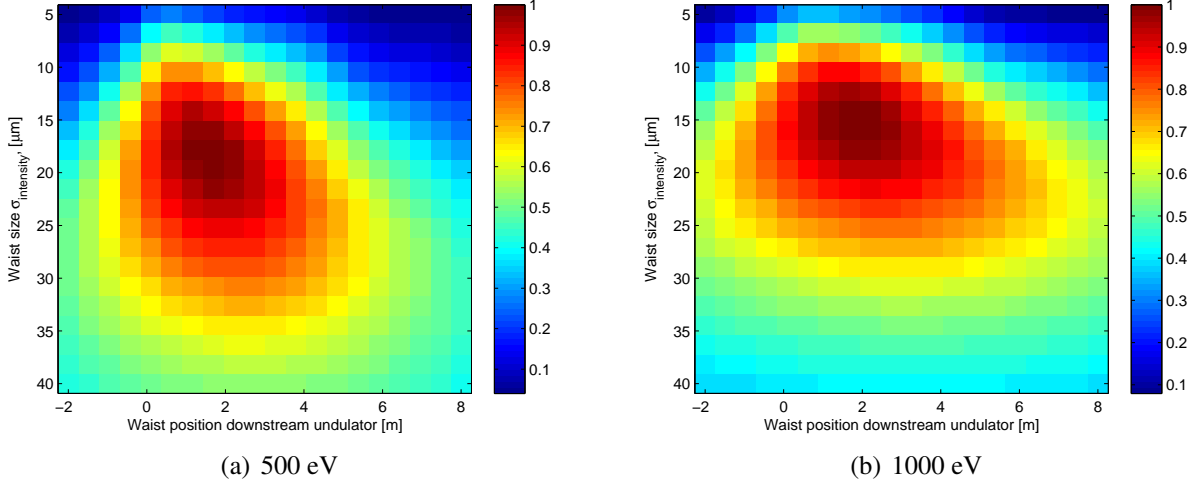
Figure 4.11: Input coupling factor [arb. units] in the seeded undulator as a function of the Gaussian waist size and it's position at reimaging. Zero in length scale indicates an undulator entrance.

intensity at certain position, but overlapping the radiation with the electron beam along the maximum path in order to let them interact more efficiently. Large image waist will cause small energy density overlapped with electron beam, too small image will diverge way before electron beam would be able to interact with it. Optimal position of the image along the seeded undulator is also important. We can model this dependence numerically with GENESIS steady-state simulation. A Gaussian beam transverse distribution is used as an input radiation field. It is generated in the way that it converges at certain distance z downstream the undulator to the waist of a certain size s (see Fig. 4.10). This way we have two parameters of the model image to optimize: Gaussian waist size and its position downstream the undulator. We can optimize both size and position of the reimaged waist for the maximum ICF. On Figure 4.11 the parameter space of ICF is simulated for two energies: 500 and 1000 eV.

We can see that optimal parameters for both energies are approximately the same, but tolerances for the lower energy are more restrictive. Also it is technically more desirable to reimage with slightly larger waists in order to relax requirements for waist position parameter. Here based of FEL theory we assume that obtained optimum parameters apply for both horizontal and vertical dimensions for FEL.

4.3 Monochromator setup description

4.3.1 Optics layout and parameters

Soft X-ray self-seeding (SXRSS) monochromator setup for the European XFEL was initially designed in 2012 [120], has been noticed in the TDR revision [121]. Since that time a sufficient progress has been made by the LCLS $R\&D$, ending up with a new improved design [74, 77]. This new monochromator design has been adapted and optimized for the European XFEL undulator system and its performance has been studied in 2013 [82]. In 2015 successful commissioning in LCLS proved feasibility of SXRSS of FELs with current design [54] and provided more information to take into account during SXRSS design for the European XFEL.

The next design iteration that takes into account the LCLS commissioning experience is presented in this work.

The overall self-seeding setup proposed here consists of three parts: a SASE undulator, a self-seeding grating monochromator and an output undulator in which the monochromtic seed signal is amplified up to the TW power level.

A layout of the self-seeding setup based on the SASE3 undulator system for the European XFEL baseline is sketched in Fig. 4.12. SXRSS monochromator replaces undulator section U7 without disturbing the "FODO" electron beam focusing system. Calculations show that in order not to spoil the electron beam quality and to simultaneously reach signal dominance over shot noise, the number of cells in the first (SASE) undulator should be equal to 4. This way, SASE radiation is produced in undulator sections U2-U5. Undulator section U6 is always opened, since monochromator in the current design is optimized for the source position in undulator section #5: nearly 10 meters from the grating. Doing so allows to decrease the energy density on the grating footprint, that is crucial for the high repetition FEL operation. Section U1 is reserved for FEL study and low current operation. Undulator sections U8-U22, defined as "seeded undulator", amplify monochromati radiation, delivered to the user experimental stations. Taking advantage of the SASE3 undulator line length and tunable undulator gap it is convenient to apply undulator tapering technique as way to extract more FEL power than that at saturation. High monochromaticity of the pulses generated with the self-seeding technique make the tapering very efficient.

Fig. 4.13 shows the optical configuration of the self-seeding monochromator. Table 4.2 summarizes the optical parameters of the setup.
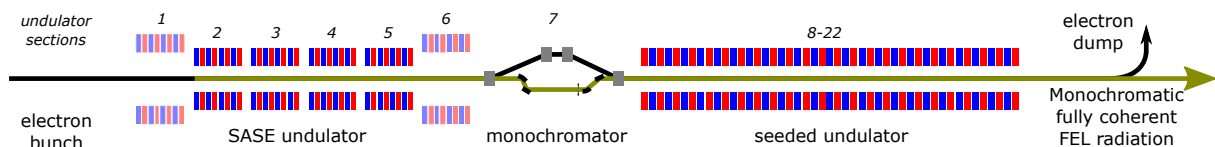

Figure 4.12: Design of the SASE3 undulator system for TW mode of operation in the soft X-ray range. SXRSS monochromator. Undulator sections U1 and U6 are retracted.

Element	Parameter	Value at photon energy			Required precision	Unit
		300 eV	700 eV	1200 eV		
G	Line density (n)		500		0.2%	l/mm
G	Linear coeff (n_1)		0.615		0.5%	l/mm^2
G	Quad coeff (n_2)		0.001		50%	l/mm^3
G	Groove profile		Blazed 0.8°		-	-
G,M1	Roughness (RMS)		-		1	nm
G	Tangential radius		195		1%	m
G	Sagittal radius		0.32		10%	m
G	Diffraction order		+1			-
G	Incident angle		1		-	deg
G	Exit angle	3.82	2.61	2.09	-	deg
	SASE undulator distance[1]		8870		-	mm
	Source distance[1]	9640	9810	11500	-	mm
	Source size ($\sigma_{intensity}$)	20.0	16.3	14.8	-	μm
	Image distance[1]	1507	1501	1513	-	mm
	Image size ($\sigma_{intensity}$)	0.83	0.87	0.93	-	μm
	Seeded undulator distance[1]		4430		-	mm
M1	Location[12]	47.4	63.4	73.9	-	mm
M1	Incident angle	2.41	1.80	1.55	-	deg
S	Slit location[1]		1505		1	mm
S	Slit width		variable		-	-
M2	Location[1]		1818		1	mm
M2	Incident angle		0.859		-	deg
M2	Tangential radius		39.4		1%	m
M3	Location[1]		1948		-	mm
M3	Incident angle		0.859		-	deg
	Optical delay	740	605	547	-	fs

Table 4.2: Parameters for the SXRSS monochromator x-ray optical elements
[1]Distance to the grating.
[2] Principal ray hit point.
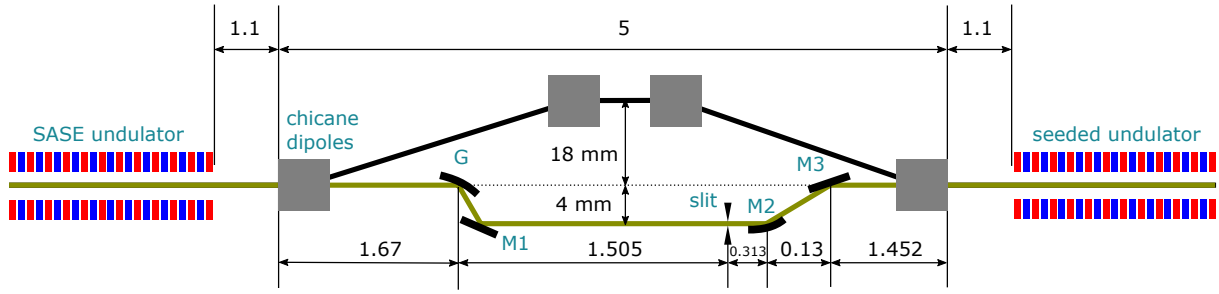
Figure 4.13: Layout of the SASE3 self-seeding system, to be located in the space freed after removing the undulator segment U5. G is a toroidal VLS grating. $M1$ is a rotating plane mirror, $M2$ is a tangential cylindrical mirror, $M3$ is a plane mirror used to steer the beam. The deflection of both electron and photon beams is in the horizontal "x" direction that matches a dispersive dimension

The design of the monochromator was optimized with respect to the resolving power, seeding efficiency, spatial constraints in the undulator and grating damage concerns. The design energy range of the monochromator is in the 0.3 keV - 1 keV interval with a resolving power exceeding 7000. It is only equipped with an exit slit. A toroidal grating with a variable line spacing (VLS) is used for imaging the FEL source to the exit slit of the monochromator. The grating has a groove density of 500 lines/mm. The grating will operate in fixed incident angle mode in the +1 order. The incident X-ray beam is imaged at the exit slit and re-imaged at the entrance of the seed undulator by a cylindrical mirror $M2$. In the sagittal plane, the source is imaged at the entrance of the seeded undulator directly by the grating. The monochromator scanning is performed by rotating the post-grating plane mirror. The scanning results in a wavelength-dependent optical path length. Therefore, a tenability of the electron bunch path length in the magnetic chicane in the range of 0.03 mm is required to compensate for the change in the optical path.

Unlike the initial European XFEL SXRSS monochromator setup [82], in this work it is proposed to retract the undulator segment U6 and to use a U5 segment as the last undulator module in which FEL source is located. This choice has couple of reasons:

1. When the source is located in the segment U6, its reimaging with grating in the sagittal plane into the seeded undulator cannot be done efficiently due to a significantly larger undulator section length

2. Larger distance from the source to the grating ~ 10 m vs ~ 4 m leads to a larger radiation footprint on the grating, allowing to relax the grating damage - related requirements.

3. Geometrically it becomes possible to reach higher resolving power of the monochromator, seeding the entire electron beam with longitudinally coherent pulse.

Compared to the previous design for the European XFEL [82], the slit position is changed from $\sim 1.35\ m$ from the grating to $\sim 1.5\ m$ distance. Focusing properties of the grating were modified accordingly. It leads to the higher angular dispersion in the reimaged waist in the

seeded undulator, eliminating PFT effects downstream the undulator. In fact, referring to [54], slit itself may not be used during the self-seeding operation. Instead it be used for an alignment of optical components of the monochromator and for possible FEL study.

4.3.2   Dispersive grating

Similar to the LCLS SXRSS monochromator design, the first optical component is the grating. It has a fixed incidence angle of 1 degree, that allows one to distribute radiation over a large area and minimize a radiation damage.
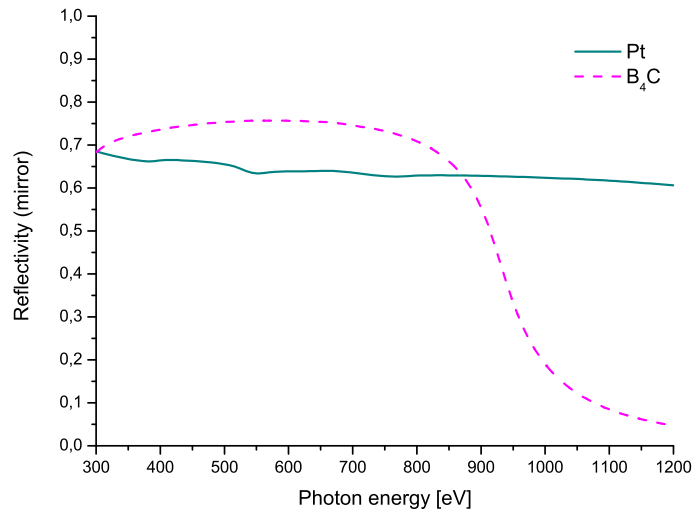
Figure 4.14: Reflectivity of thick mirrors of platinum and B_4C. $2°$ incidence angle is used to simulate $1°$ incidence angle on the grating with $\sim 1°$ blaze angle.

It has a toroidal shape, allowing it to carry out focusing of the incident radiation. The toroidal shape exhibits two radii of curvature: tangential (in plane with incident radiation) and sagittal (in plane, perpendicular to the incident radiation). Source in a tangential plane is reimaged onto the slit, where according to the initial LCLS design wavelength filtering should take place. In a sagittal plane source is reimaged directly into the seeded undulator.

Dispersion takes place in the tangential plane. Line spacing of the grating is variable (VLS). If decomposed polynomially, constant component is responsible for the dispersion. The linear component compensates the wavelength dependence of the FEL source position, discussed in section 4.2.2. This component of a VLS grating acts as a lens with a wavelength-dependent focal distance. The quadratic component allows one to eliminate a coma aberration caused by a non-elliptical shape of the grating.

The grating is coated with a layer of platinum, since is has both a good reflectivity along the entire photon energy range (see Fig.4.14) and can be cleaned from a carbon contamination with the oxygen-discharge method [97].

The efficiency of the grating should be optimized over the range of photon energies where

(a) First order efficiency (b) Total reflectivity
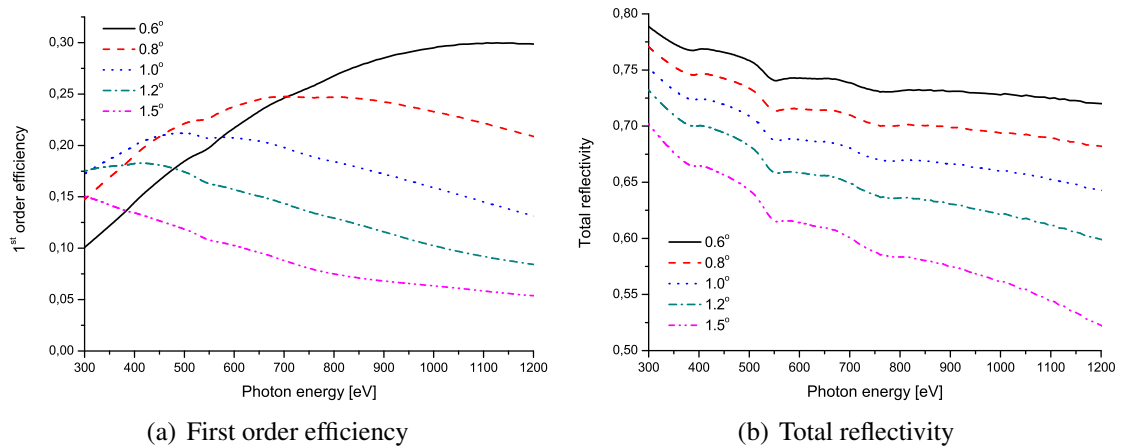
Figure 4.15: Efficiency and reflectivity of the Platinum-coated grating as a function of photon energy at different blaze angles. These plots assume a constant incident angle of 1 degree. The optimal blaze angle was found to be 0.8 degrees

the grating will be used. It was done by adjusting the blaze angle. The blazed profile is substantially superior to laminar alternative. For the specified operating photon energy range, the optimal blaze angle is 0.8 degree in means of optimal efficiency and overall reflectivity (Fig. 4.15). These dependencies were calculated using the code "GSolver 5.2" [122].

Compared to the previous monochromator design [82], better grating grooves illumination along with higher demagnification ratio caused rise in resolving power, that allowed one to decrease line density. Latter resulted in 1-st order efficiency growth by up to 30% in 500eV region (see Fig. 4.16)
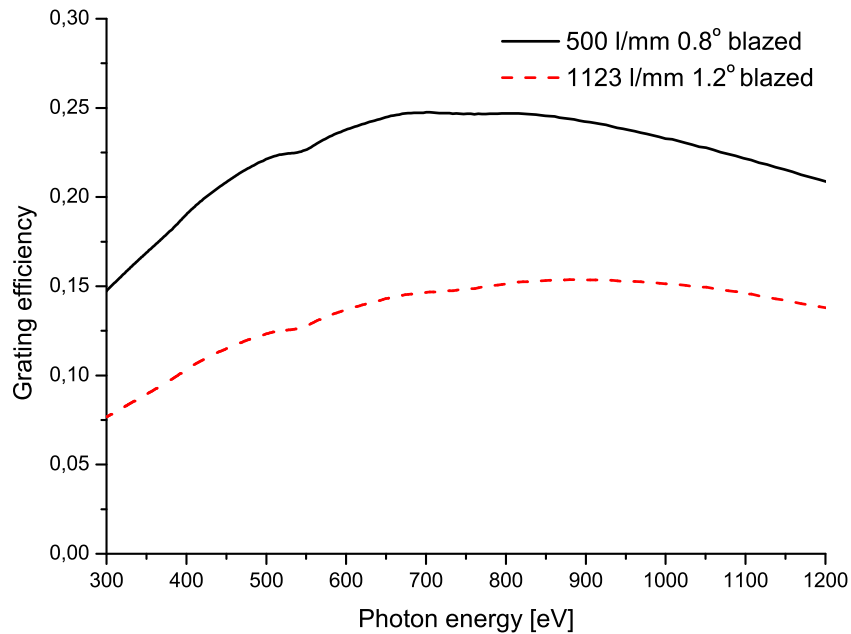
Figure 4.16: Comparison of the grating efficiency at two line densities of 1123 and 500 lines per millimeter with an optimized blazed angles for each.

4.3.3 Radiation transport efficiency

It is important to calculate the expected total transmission of the monochromator beamline. The reflectivity of the mirrors was calculated using the code CXRO [123]. Mirrors are assumed to be platinum-coated.

The combining effect of two fixed angle mirrors $M2$ and $M3$ cannot be neglected. In the soft X-ray range, platinum has reflectivity of about 83 % at 0.86 degree grazing angle. The compound loss over two last reflections is thus appreciable. The most significant factor in the post grating efficiency is the low reflectivity of the rotating plane mirror $M1$. This is because the first post-grating mirror operates at a relatively large incident angle of about 2 degrees. Overall and element-wise efficiency of the monochromator beam transport is presented on Figure 4.17 for the π-polarization component. Values for the σ-polarization component do not differ significantly.
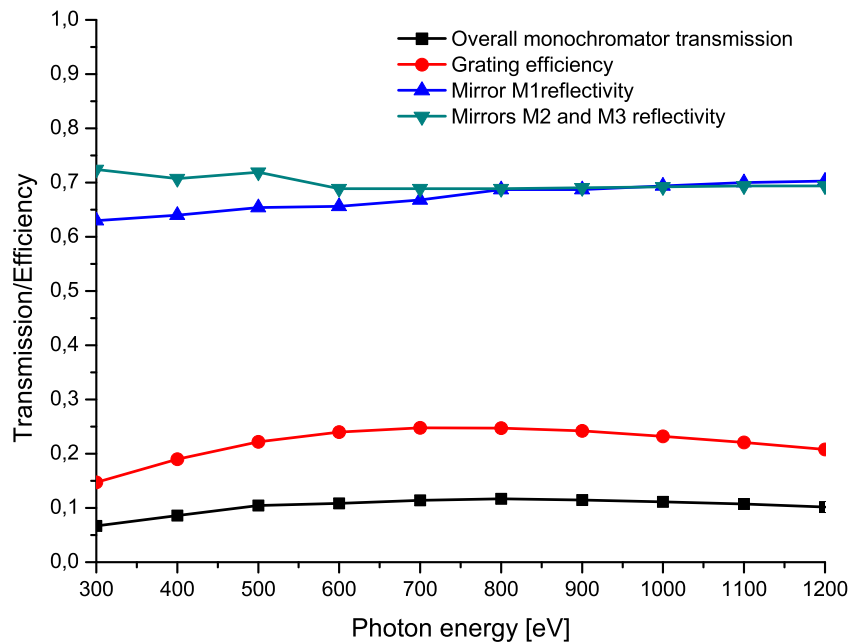
Figure 4.17: Grating efficiency, reflectivity of the post-grating optical components (rotational $M1$ mirror and combined effect of $M2$ and $M3$ mirrors) of the monochromator and overall efficiency of the monochromator beam transport without the exit slit. The grating and the three mirrors are platinum-coated.

4.3.4 Energy tuning and optical delay

In order to maintain a constant direction of the exit beam, a scanning post grating mirror is placed in the diffracted beam, and rotated to direct the beam towards the exit slit. Thus, with a fixed grating and exit slit one can maintain a good focus over a wide photon energy range by simply translating and rotating a plane mirror to aim the diffracted light at the exit slit. Translating the mirror during rotation scanning can be achieved by pivoting the mirror at a point above the center of the mirror. During the energy tuning the beam "walks" along the surface of $M1$, as shown in Fig. 4.18.
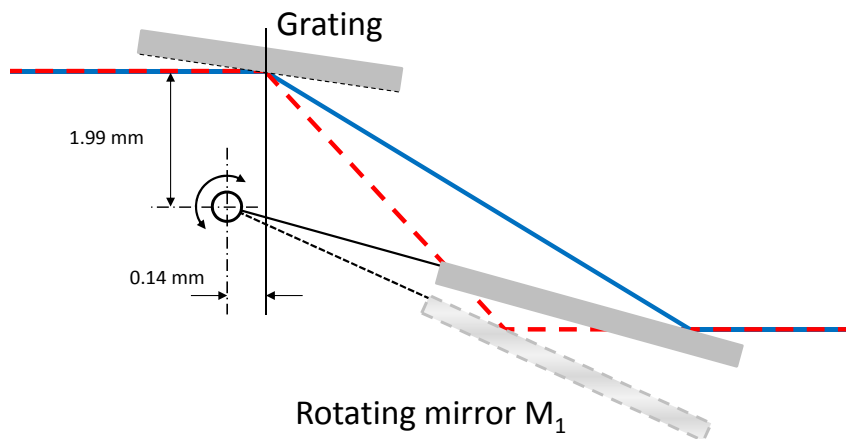
Figure 4.18: Principle of photon energy tuning. A plane scanning mirror, M_1, is rotated to maintain a fixed exit beam direction and focal spot at the exit slit. The mirror M_1 and grating are schematically shown for two photon energies: 1 keV (solid) and 0.5 keV (dashed line).

The optical delay caused by the use of the grating monochromator is about 0.7 ps and its energy-dependence is shown in Fig. 4.19.

The delay is not constant, but varies with the energy due to the fact that X-rays reflect off the post-grating mirror $M1$ at different points, and take different optical paths as the energy is tuned. The image on the slit plane is also found to vary by $1~\mu$m in the dispersion direction, amounting to a change of $1~\mu$rad in the angle of incidence, which is small compared to the divergence of the beam at the slit plane. As such, the impact of this effect on the monochromator performance is negligible.

4.3.5 Electron chicane

The electron beam chicane contains four identical dipole magnets, each of them 0.5 m-long. The choice of the strength of the magnetic chicane only depends on the maximum delay that we want to introduce. Parameters discussed below fit with a short, 5 m-long magnetic chicane to be installed in place of a single undulator module. Such chicane, albeit very compact, is however strong enough to create a sufficiently large transverse offset for the installation of the optical elements of the monochromator.
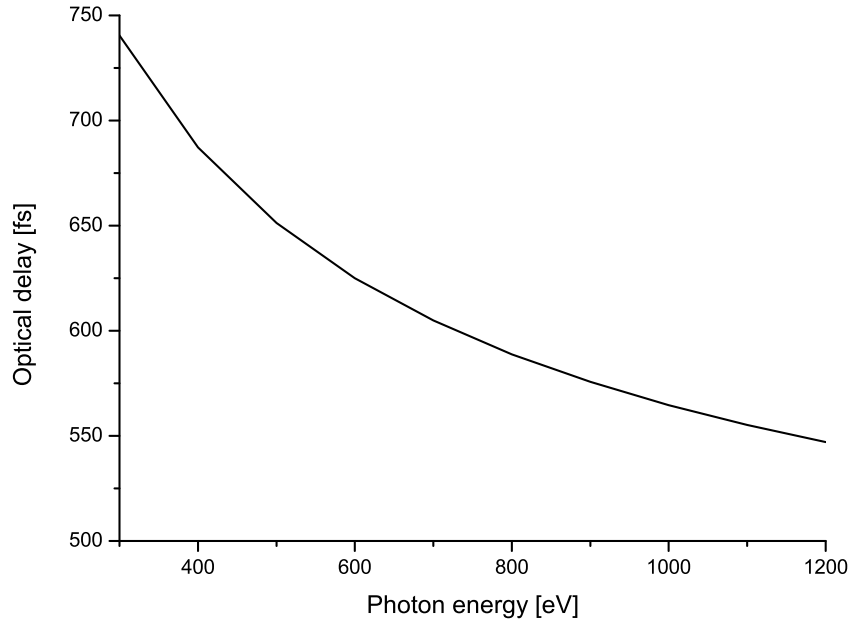
Figure 4.19: Optical delay caused by the use of monochromator as a function of photon energy.

Contrary to [82], at the current monochromator design proposal, due to reduction of line density in the grating down to 500 l/mm , maximum optical delay was also reduced down to 740 fs , as presented on Figure 4.19. It allows one to operate SXRSS setup freely with beam energy 8.5 GeV and 12 GeV along entire working photon energy range in case of an average magnetic field of 0.82 T along each dipole magnet (see Fig.4.20). Each electron beam energy has a certain range of photon energies that it can radiate with inside the undulator due to a limited gap values. At 12 GeV undulator gap limits FEL the resonance photon energies lower than $500\ eV$. Higher electron beam energies are more beneficial for the FEL process. Electron beam energies of 14 and $17.5\ GeV$ are already beyond the limits of the chicane performance. In this way current design satisfies the European XFEL operation with 2 of 4 current nominal electron energies, allowing relatively flexible interaction with other beamlines in terms of common electron beam utilization.

4.4   Monochromator performance study

4.4.1   Gaussian beam optics

In general, as discussed in section 4.2.2, FEL source is not Gaussian, but it allows one to optimize monochromator parameters for optimal FEL performance. Further calculations are based on Gaussian beam optics method described in section 2.1.3. Focusing scheme for both tangential and sagittal dimensions along with waist positions convention is shown on Figure 4.21.

Dependence of a distance from the grating to the object and the size of the latter from the photon energy are shown on Figure 4.22. These values are used for analytical calculations. In tangential plane FEL source is reimaged into the slit position. Location and size of the waist
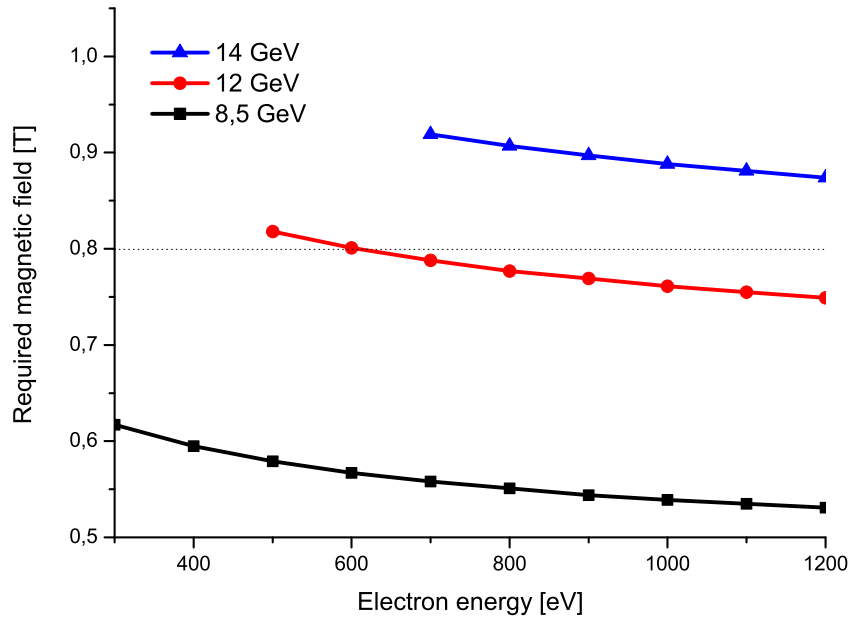
Figure 4.20: The dipole magnetic field, required to compensate the optical delay caused by the monochromator as a function of photon energy.

are presented on Figure 4.23. One can see that drift of the waist with respect to the wavelength is within its Rayleigh range. M2 mirror carries out reimaging of the waist at the slit into the seeded undulator in tangential plane (Figure 4.25), while grating reimages it in the sagittal plane from the undulator source.

Monochromator was optimized to reach an optimal input coupling factor in the seeded undulator along the entire energy range. Waist position of the sagittal plane is off the optimal one for 1 keV, but as mentioned in section 4.2.3, higher photon energies as well as large waists greatly relax reimaging requirements. Coupling in the tangential plane was achieved much better, because more degrees of freedom among monochromator parameters were available for this purpose. Also, since dispersion takes place in a tangential plane, improper reimaging in this plane would affect monochromator's resolving power. Beam focusing quality in a sagittal plane affects ICF only. Footprint on the grating is presented on Figure 4.27.
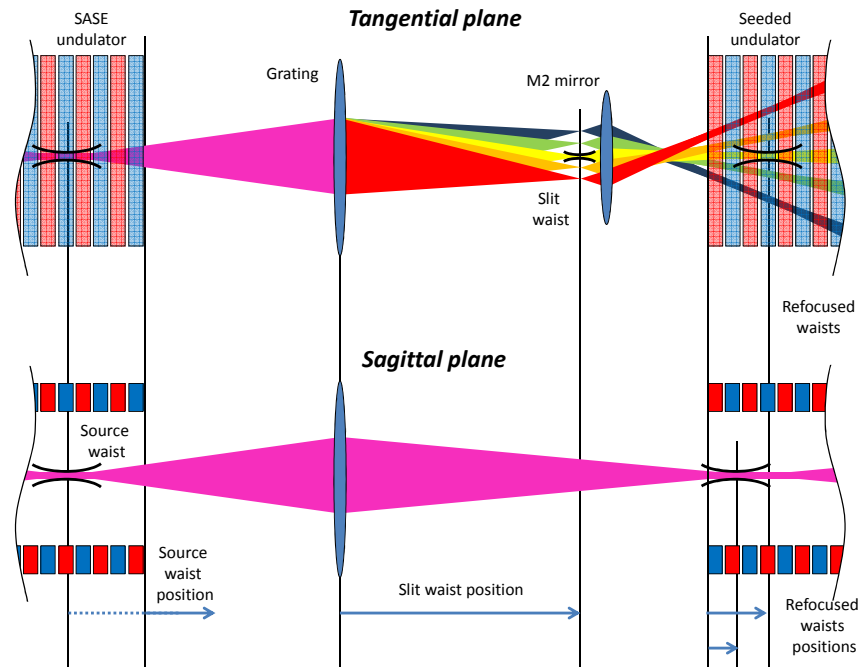
Figure 4.21: Tangential (top) and sagittal (side) views of the principal optical components, and radiation propagation paths and waists. Waist positions arrows reveal the conventions used further in Figures 4.22-4.26.
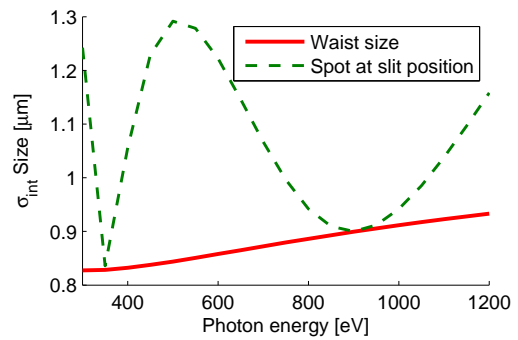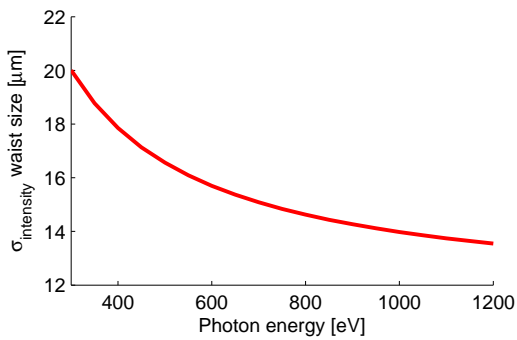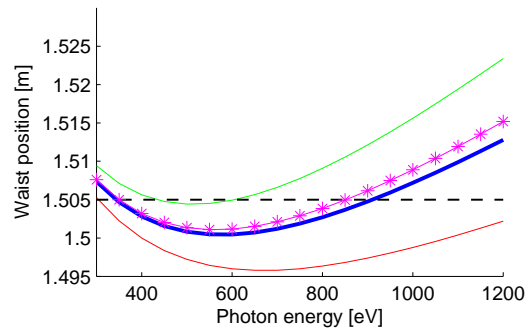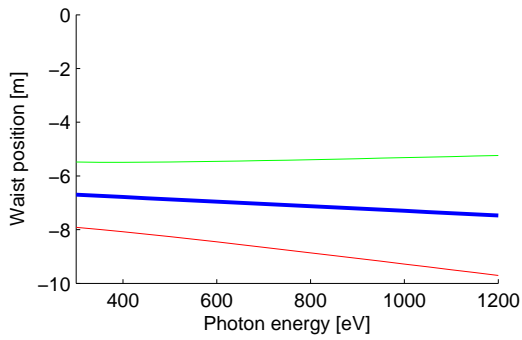
Figure 4.22: SASE undulator source waist size and position.

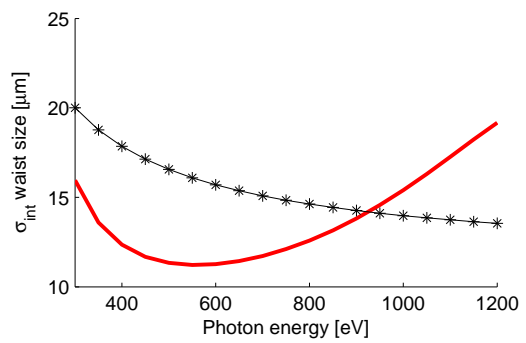Figure 4.23: Slit tangential waist size and position. Dashed line depicts the slit position
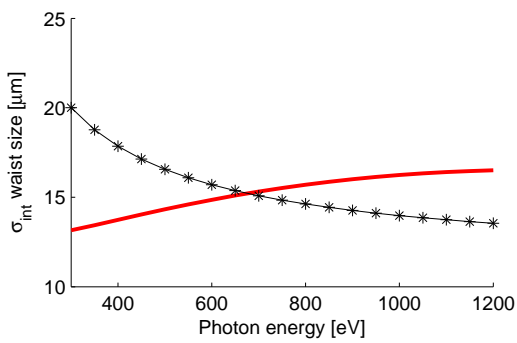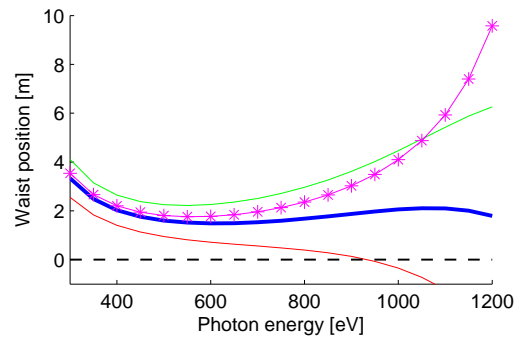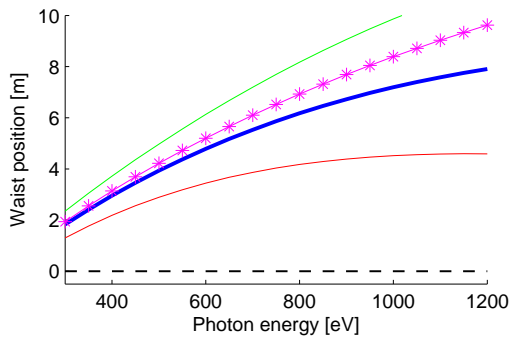
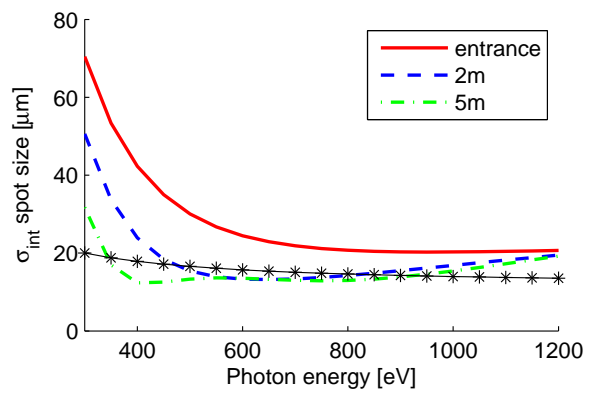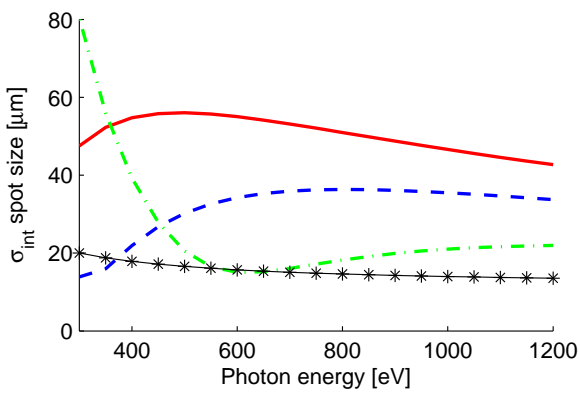Figure 4.24: Seeded undulator sagittal waist size and position. Dashed line depicts the seeded undulator entrance.

Figure 4.25: Seeded undulator tangential waist size and position.

Figure 4.26: Seeded undulator waist evolution for sagittal (left subfigure) and tangential (right subfigure) planes.
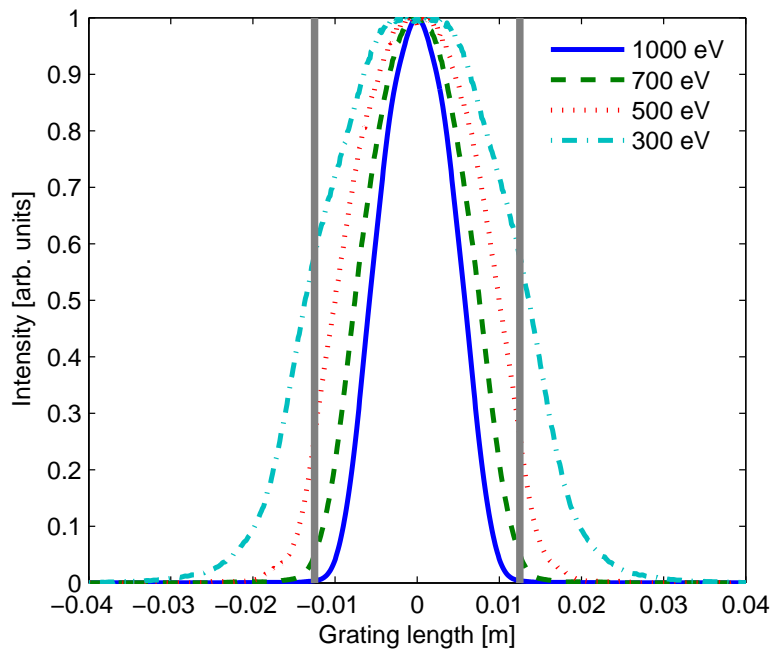
Figure 4.27: Radiation intensity footprint on the grating. Grating limits are represented with solid vertical lines. The grating length of 2.5 cm is assumed in simulations.

4.4.2 Ray-tracing

The optical system was simulated using the ray-tracing code SHADOW [124] in order to evaluate the performance of the monochromator. The reason for modeling the monochromator using ray-tracing is the need to check the results found by wave optics calculations, especially minimization of aberrations. The source has been modeled as a Gaussian-shaped beam with a Gaussian divergence distribution as a function of wavelength, since the XFEL source is nearly transform-limited. We performed ray-tracing simulations for 500 and 1000 eV cases at three different photon energies for each. We assumed the RMS values of 17.4 μm for the source size, and 11.3 μrad for the beam divergence for 500 eV and 15 μm with 6.56 μrad respectfully for 1000 eV case.
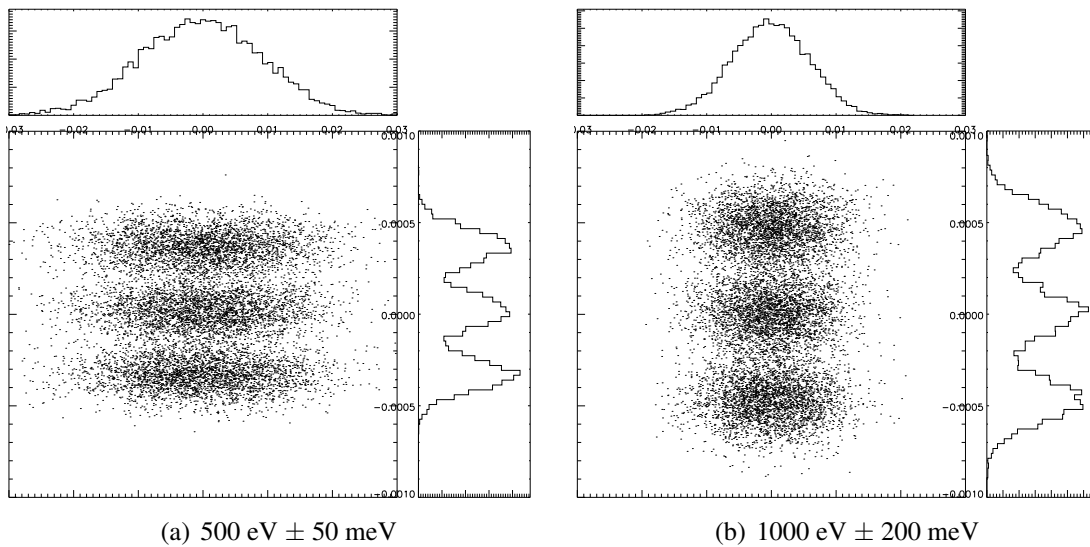

(a) 500 eV ± 50 meV   (b) 1000 eV ± 200 meV

Figure 4.28: Results from ray tracing simulations at the **slit position** for 500 eV (a) and 1000 eV (b) photon energies, 3 lines each, obtained from the ray-tracing program SHADOW. Dispersive axis "x" is oriented vertically on the plot.

No mirror height errors were accounted for. In this way, the FEL source has been propagated over the grating and the exit slit plane, and then over the refocusing mirror. Infinite dimensions of optical elements assumed. Ray-tracing results at the plane of the exit slit for photons of 500 eV and 1000.0 eV are shown in Fig. 4.28. The histograms show that in the dispersive (tangential) and non-dispersive (sagittal) directions the distributions are almost Gaussian. As it can be seen from the figure, the focusing properties of the monochromator at these photon energies are satisfactory, and resolution is larger than 5000. Fig. 4.29 displays results of ray-tracing simulations 1.5 meters downstream the entrance of the second undulator.

The location of the beam focus, shown in Fig. 4.30, was found to vary with the energy around the slit. Fig. 4.30 also shows a comparison between results found with ray tracing and wave optics calculations. Fig. 4.31 summarizes the energy resolution obtained from the linear dispersion and the FWHM of the spot size at the exit slit plane as a function of the photon energy. Comparing the waist position to the one found by wave optics calculations, one can see that
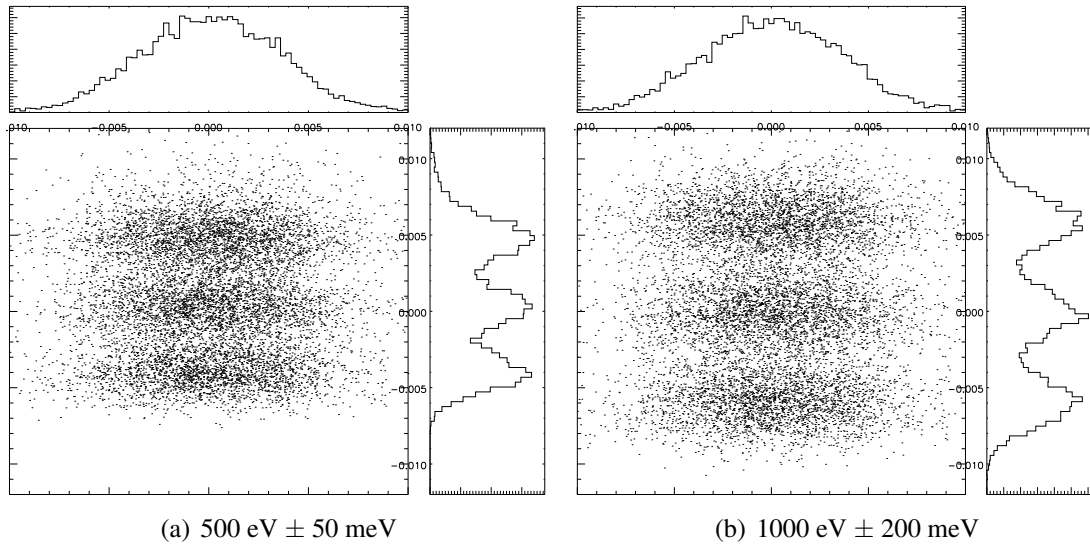
(a) 500 eV ± 50 meV   (b) 1000 eV ± 200 meV

Figure 4.29: Results from ray tracing simulations at **1.5 m downstream the entrance of the second undulator** for 500 eV (a) and 1000 eV (b) photon energies, 3 lines each, obtained from the ray-tracing program SHADOW. Dispersive axis "x" is oriented vertically on the plot.

there is a very good agreement between coherent and incoherent models. However a complete, straightforward analysis of the full self-seeding monochromator setup can be performed in terms of wave optics only.
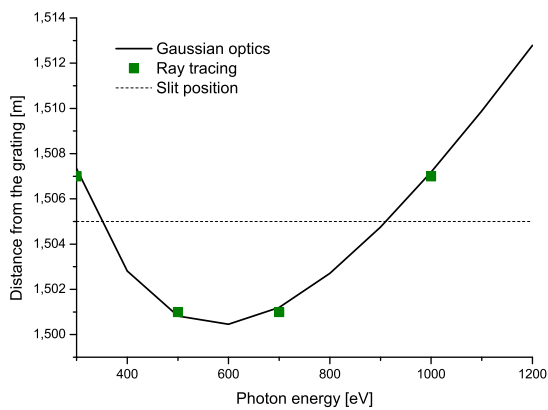

Figure 4.30: Focusing at the slit position. Variation of the focus location as a function photon energy.
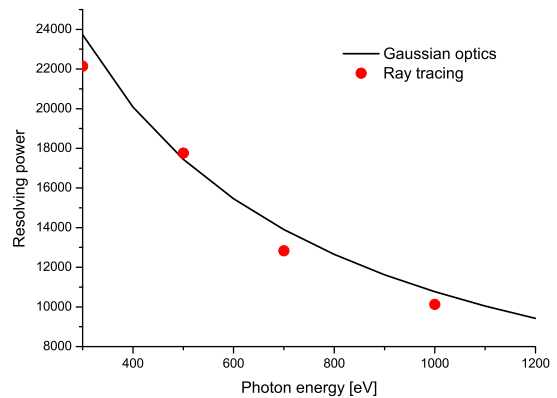

Figure 4.31: Resolving power of the monochromator at the waist position around the slit. Gaussian optics calculation and ray-tracing simulation results provide similar results.

4.4.3 FEL simulations

Instrumental function and resolving power calculation

The analytical calculation of the ultimate grating performance works well only when 4σ beam footprint is not larger than the grating length (see Figure 4.35). The spectral resolution of the monochromator depends on the spot size in the dispersive plane. The FWHM of this spot size multiplied by a spatial dispersion in this plane is interpreted as a spectral resolution. Interaction of this dispersed and focused radiation with an electron beam in an FEL can be simulated numerically.

The effective resolving power of the monochromator with the exit slit retracted was simulated with an approach, outlined in Section 3.3.2. The FEL radiation wavefront was simulated at the end of the SASE undulator with the GENESIS simulation code. Than it was propagated through the monochromator to the entrance of the seeded undulator. Transverse distributions of the radiation at the slit position and 1.5 m downstream the seeded undulator are presented at Figures 4.32 and 4.33.
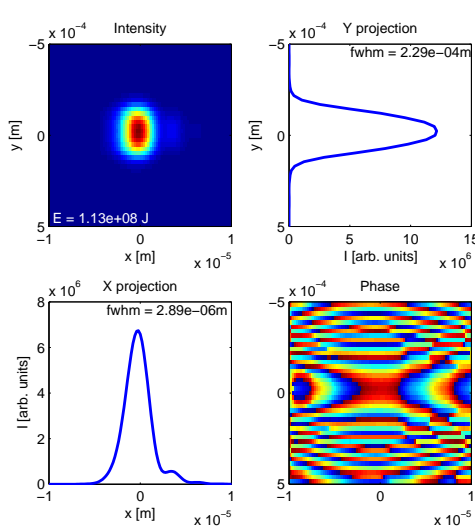

Figure 4.32: Transverse radiation distribution at the slit position. Here $\hbar\omega = 700$ eV.
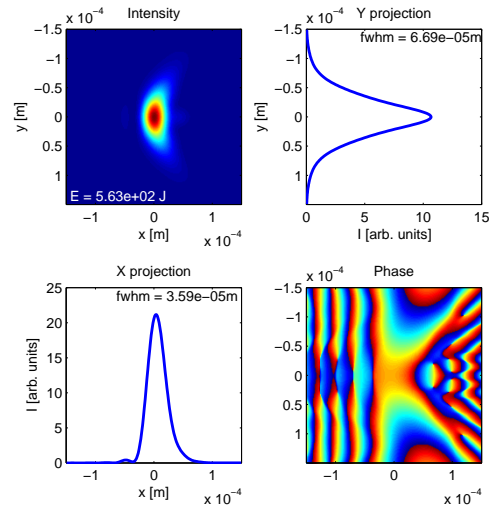

Figure 4.33: Transverse radiation distribution at 1.5 m downstream the seeded undulator entrance. Here $\hbar\omega = 700$ eV.

Monochromator instrumental functions along the range of photon energies were calculated and effectively represent the performance of the monochromator. Results are presented on Figure 4.34.

Finally, comparison of the monochromator resolving power is presented on the Fig. 4.35. An effective resolving power stays relatively constant at the level of about 8000. The main reason of this is an overfill of the grating at the lower photon energies. Nevertheless, this value is high enough to produce a transform-limited seed pulses with length FWHM from 4 μm at 1000 eV to 17 μm at 300 eV. This seed is to be amplified in the second undulator. When an instrumental function of the monochromator was calculated, we assumed that the electron beam
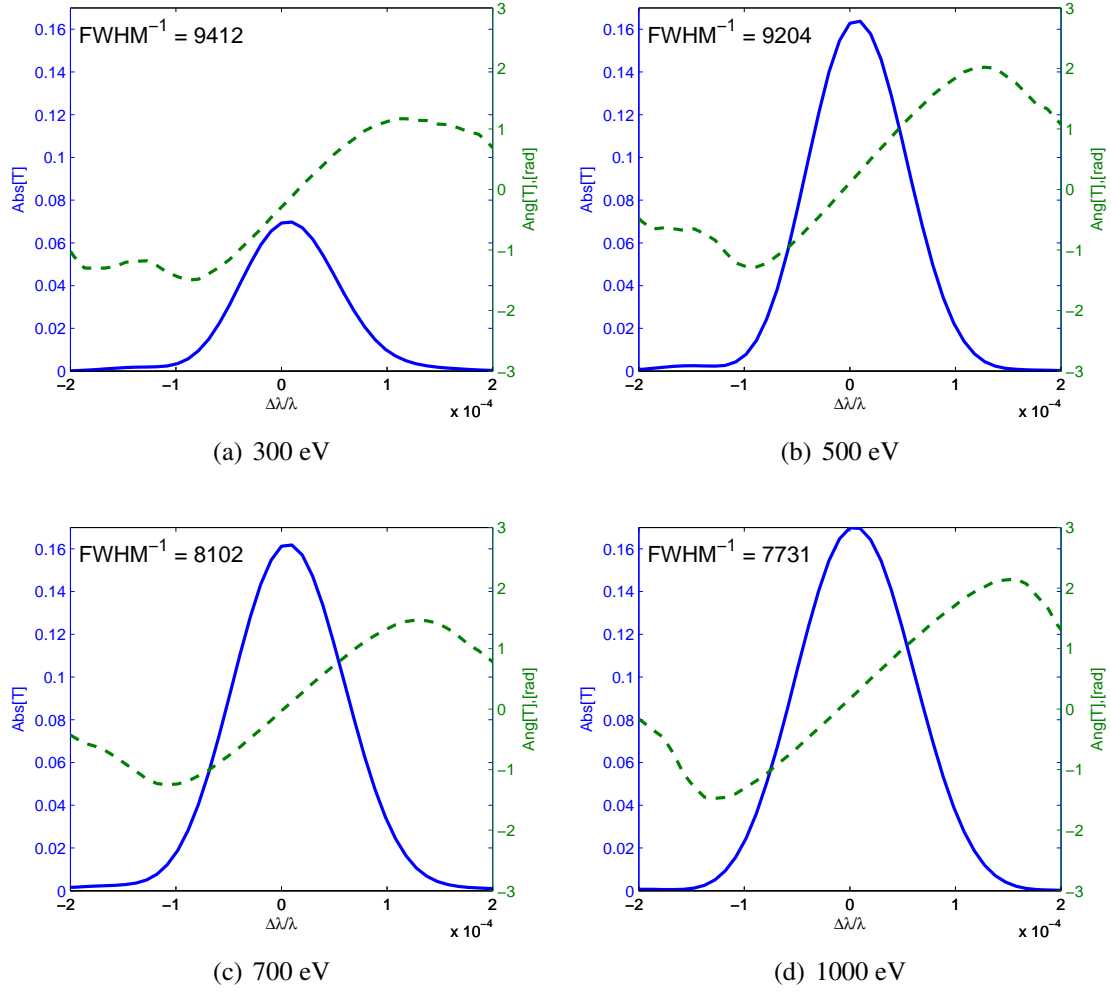
Figure 4.34: Monochromator instrumental functions for different photon energies. Inverse full width at half maximum is interpreted as an effective resolving power of the monochromator.

has the same properties in the longitudinal dimension, namely - the electron energy. Below it will be shown that this is not the case with the simulated electron beam for a European XFEL.

Start-to-end simulations

Start-to-end self-seeding simulation techniques are described in Section 3.3. They have proved their efficiency during the LCLS commissioning: simulation results showed a good correspondence with an experiment. Therefore it is possible to simulate the performance of the proposed SXRSS setup for the European XFEL. Below a feasibility study for the SASE3 FEL line of the European XFEL is presented. It is based on a direct simulation approach and statistical analysis; 50 independent runs are presented.

The expected electron bunch parameters at the entrance of the SASE3 undulator are shown in Fig. 4.36, [105].

The SASE pulse power and spectrum after the first (SASE) undulator are shown in Fig. 4.37, and the evolution of the energy and peak power per pulse along this undulator are presented in
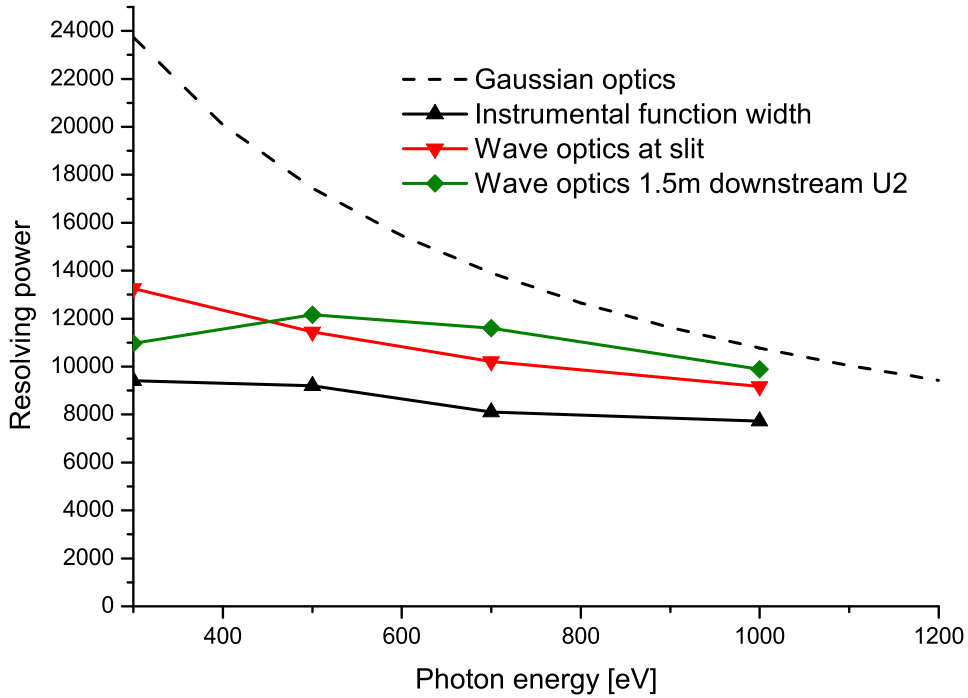
Figure 4.35: Comparison of monochromator resolving power calculations: with Gaussian optics analytically; from the size of the waist in image planes and from the monochromator instrumental function FWHM

Fig. 4.38.

This pulse goes through the grating monochromator. The monochromator instrumental function is presented in Fig. 4.34 (700 eV case). At the exit of the monochromator, one obtains the seed pulse, Fig. 4.39. The direct propagation method through the monochromator was used, the exit slit was assumed to be retracted. Linear amplification of the spatially dispersed radiation in the seeded undulator proved that propagated bandwidth is large enough (Fig. 4.40).

As explained before, the monochromator introduces only a short optical delay of about 0.7 ps, which can be easily compensated by the electron chicane. The chicane also "washes out" the electron beam microbunching. As a result, at the entrance to the seeded undulator the electron beam and the radiation pulse can be recombined.

The most promising way to increase the FEL output power is a post-saturation tapering. Tapering is a slow reduction of the field strength of the undulator in order to preserve the resonance wavelength, while the kinetic energy of the electrons decreases due to the FEL process. The undulator taper could be simply implemented as a step taper from one undulator segment to the next, as shown in Fig. 4.41. Using that tapering configuration one obtains the output characteristics, in terms of power and spectrum, shown in Fig. 4.42. The output power is increased by about a factor ten after the saturation, allowing one to reach nearly one TW when averaged over runs. The evolution of the radiation properties as a function of the undulator length is shown in Fig. 3.26 The spectral width increases after a tapering, but still remains acceptable with an average inverse relative bandwidth (FWHM) higher than 4000. The most significant source of a spectrum broadening is a non-linear electron energy chirp.
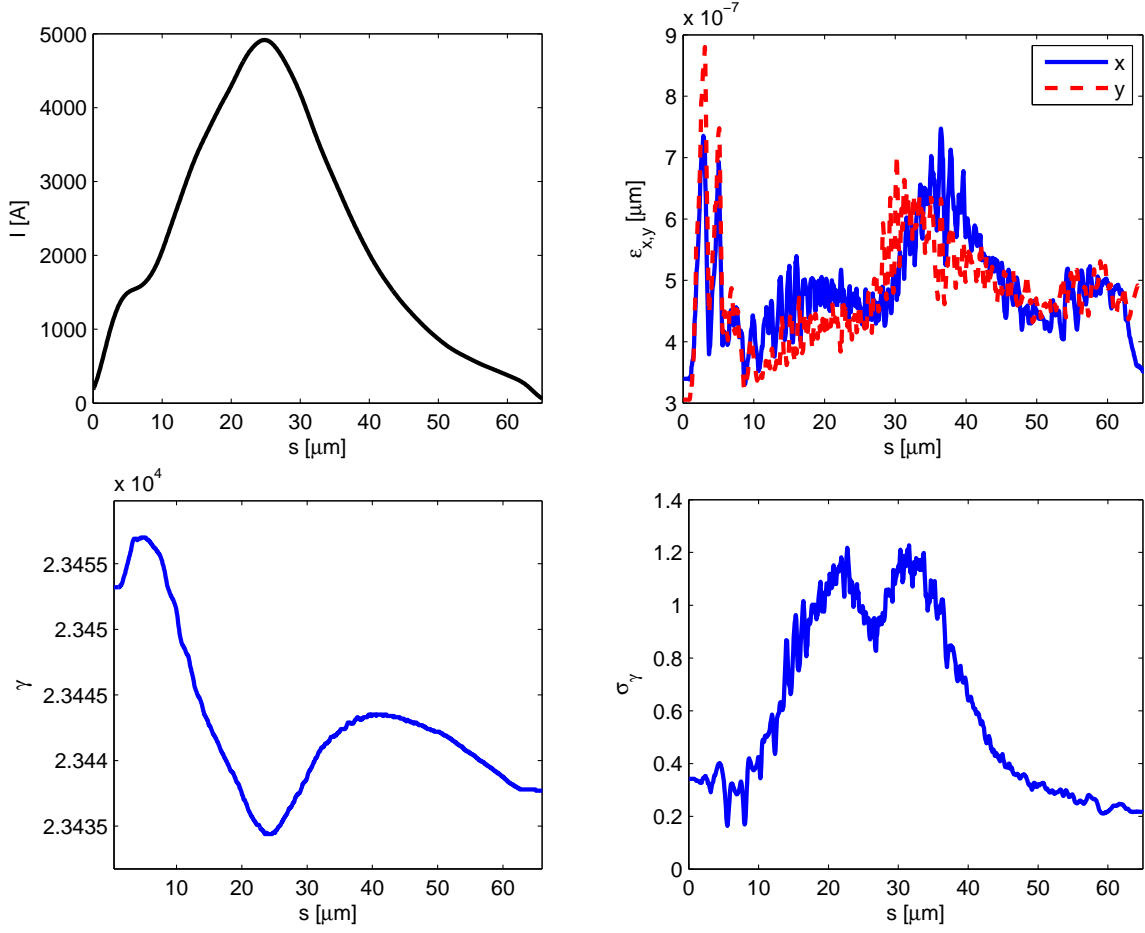
Figure 4.36: Results from electron beam start-to-end simulations at the entrance of SASE3. (First Row, Left) Current profile. (First Row, Right) Normalized emittance as a function of the position inside the electron beam. (Second Row, Left) Energy profile along the beam. (Second Row, Right) Electron beam energy spread profile. Bunch charge $q = 500\ pC$.

After the SXRSS monochromator, the monochromatic seed induces an electron density modulation in the electron bunch at a given frequency. In the presence of an energy chirp within a bunch, regions locating electrons with higher energy will move faster within an undulator than those with a lower energy because undulator has a non-zero R_{56} compression factor. If the chirp is linear, the electron beam will either spread out longitudinally, or shrink, and so will an electron density modulation. FEL radiation will inherit the phase of the bunching, this way the electron energy chirp causes a phase chirp of the FEL radiation. Linear electron energy chirp will result in a radiation wavelength shift. Non-linear chirp will cause a broadening of the FEL spectrum.

The evolution of the energy per pulse in the seeded undulator and of the energy fluctuations as a function of the undulator length are shown in Fig. 4.44. The transverse radiation distribution and divergence at the end of the output undulator are presented in Fig. 4.43. Worth mentioning that due to high computational demands of the start-to-end simulation the chosen tapering profile is suspected to be not the most efficient one.

It is necessary to compare the results for the self-seeded beam with the characteristics of the baseline SASE pulse generated with the same electron beam. The best compromise between
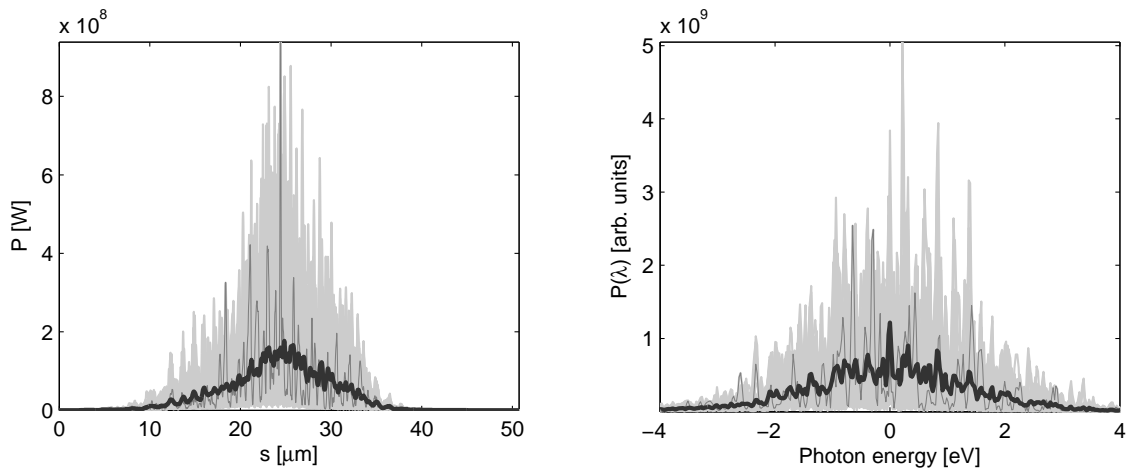
Figure 4.37: Power distribution and spectrum of the X-ray radiation pulse after the first (SASE) undulator. Grey lines refer to single shot realizations, the black line refers to the average over a fifty realizations.
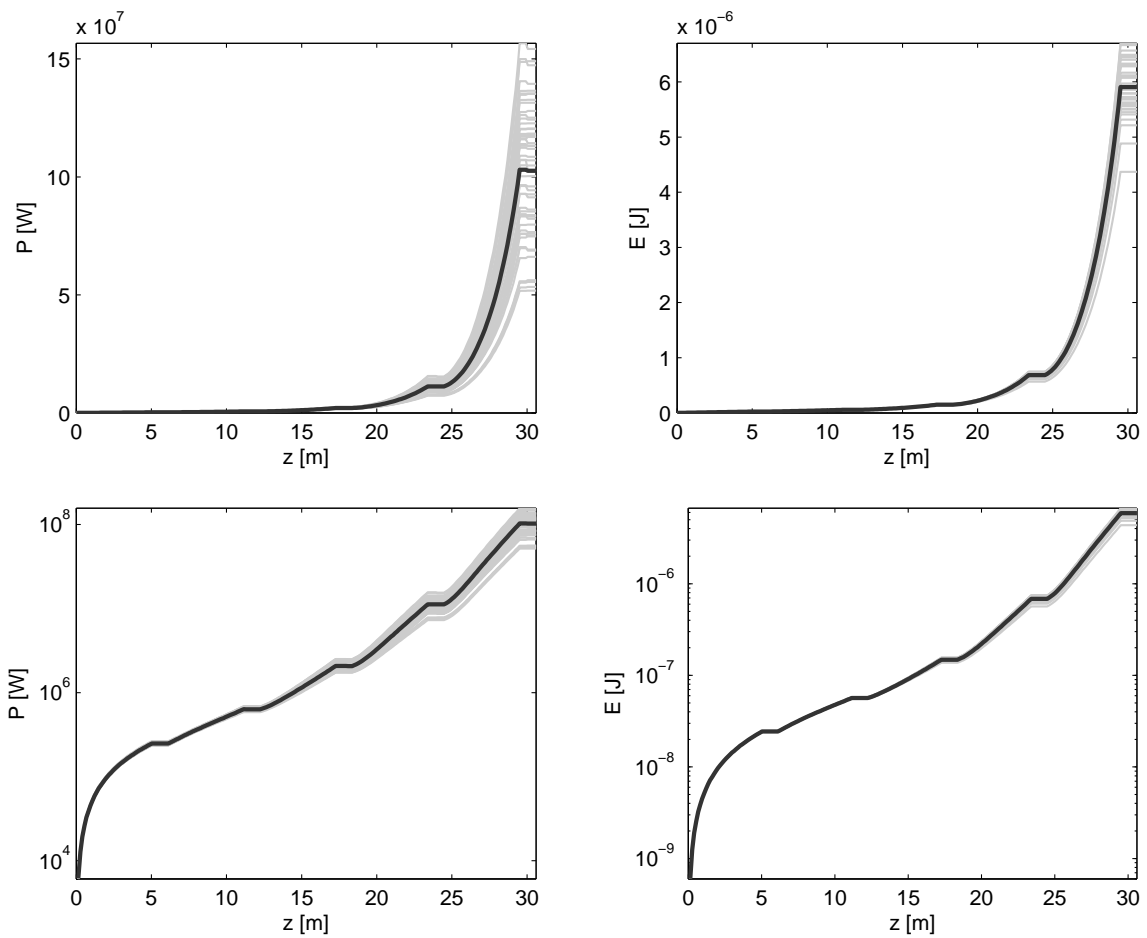

Figure 4.38: Evolution of the energy and peak power per pulse as a function of the first (SASE) undulator length.
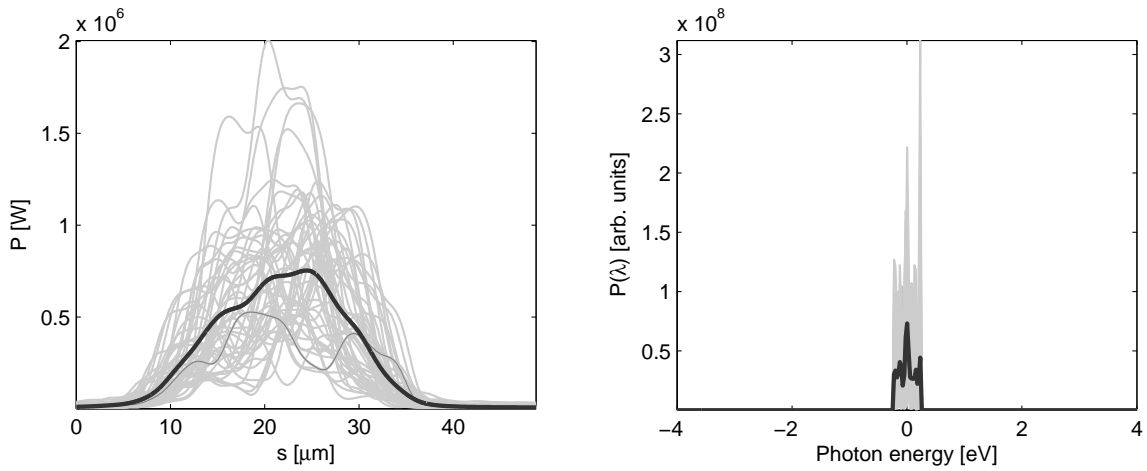
Figure 4.39: Power distribution and spectrum of the X-ray radiation pulse after the monochromator. During operation mode without exit slit the entire spectrum of both spatially and angularly dispersed pulse passes through the monochromator. In the simulation only a part of the spectrum lager than the monochromator instrumental function is used as a seed. Grey lines refer to single shot realizations, the black line refers to the average over a fifty realizations.
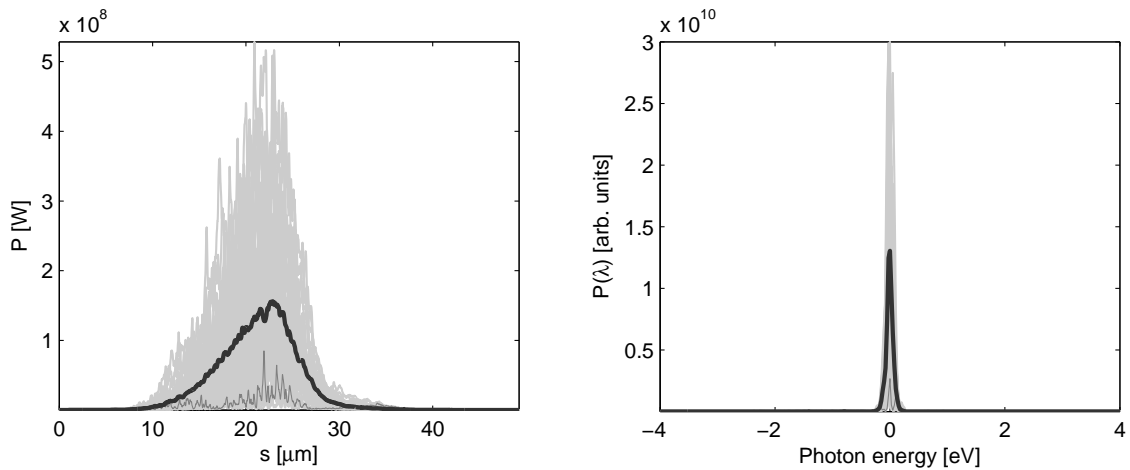

Figure 4.40: Power distribution and spectrum of the X-ray radiation pulse after the monochromator 17 m downstream the seeded undulator. Grey lines refer to single shot realizations, the black line refers to the average over a fifty realizations.
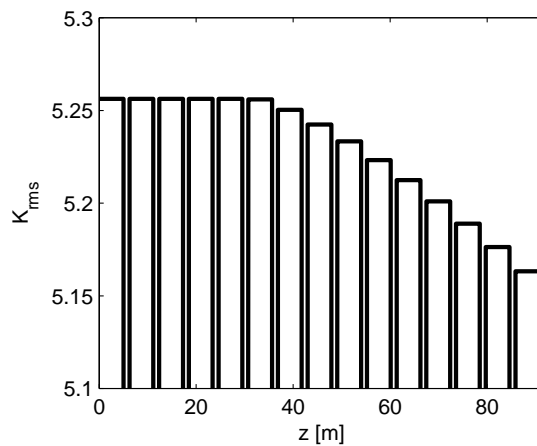

Figure 4.41: Taper configuration for high-power mode of operation at 700 eV.
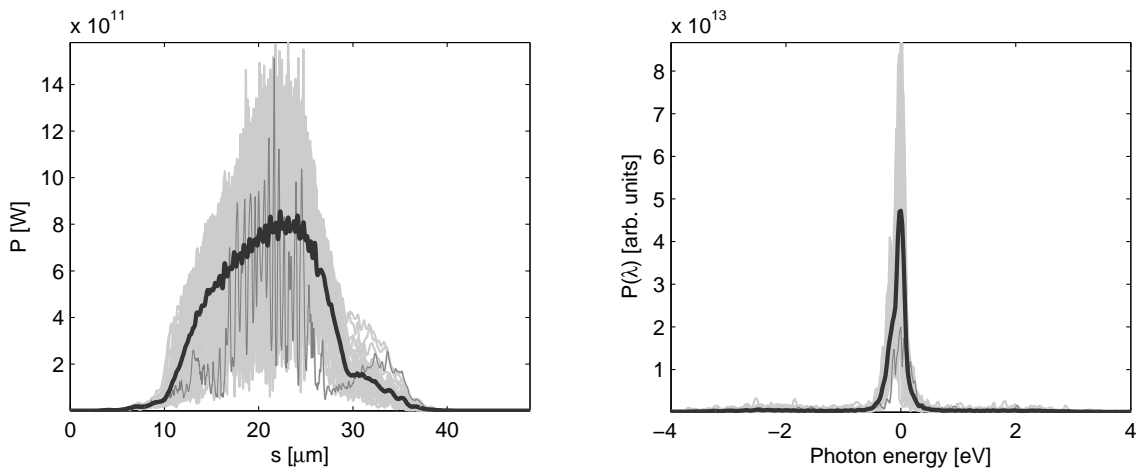
Figure 4.42: Power distribution and spectrum of the X-ray radiation pulse after the second undulator in the tapered case. Grey lines refer to single shot realizations, the black line refers to the average over a fifty realizations.

Figure 4.43: (Left plot) Transverse radiation distribution in the case of tapering at the exit of the output undulator. (Right plot) Directivity diagram of the radiation distribution in the case of tapering at the exit of the output undulator.

Figure 4.44: Evolution of the energy, energy fluctuations and peak power per pulse as a function of the undulator length in the tapered case. Grey lines refer to single shot realizations, the black line refers to the average over a fifty realizations.
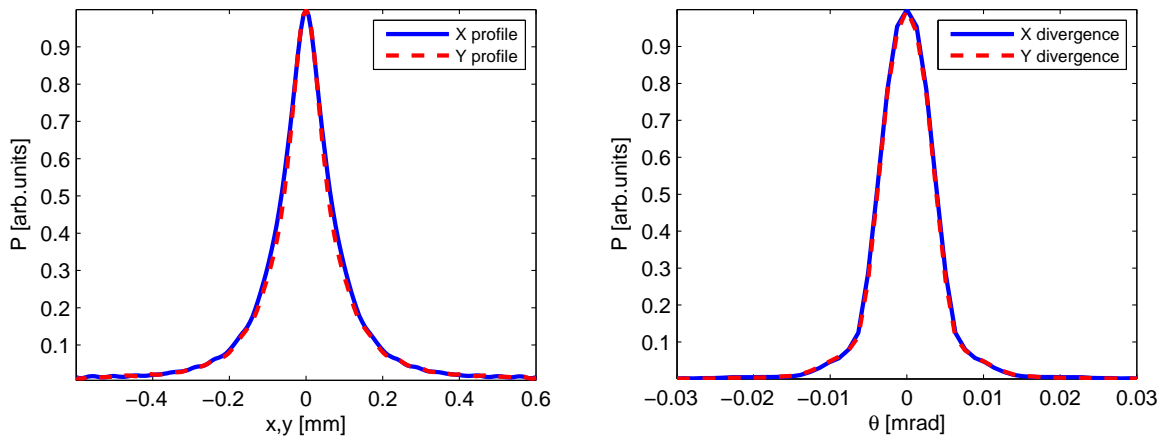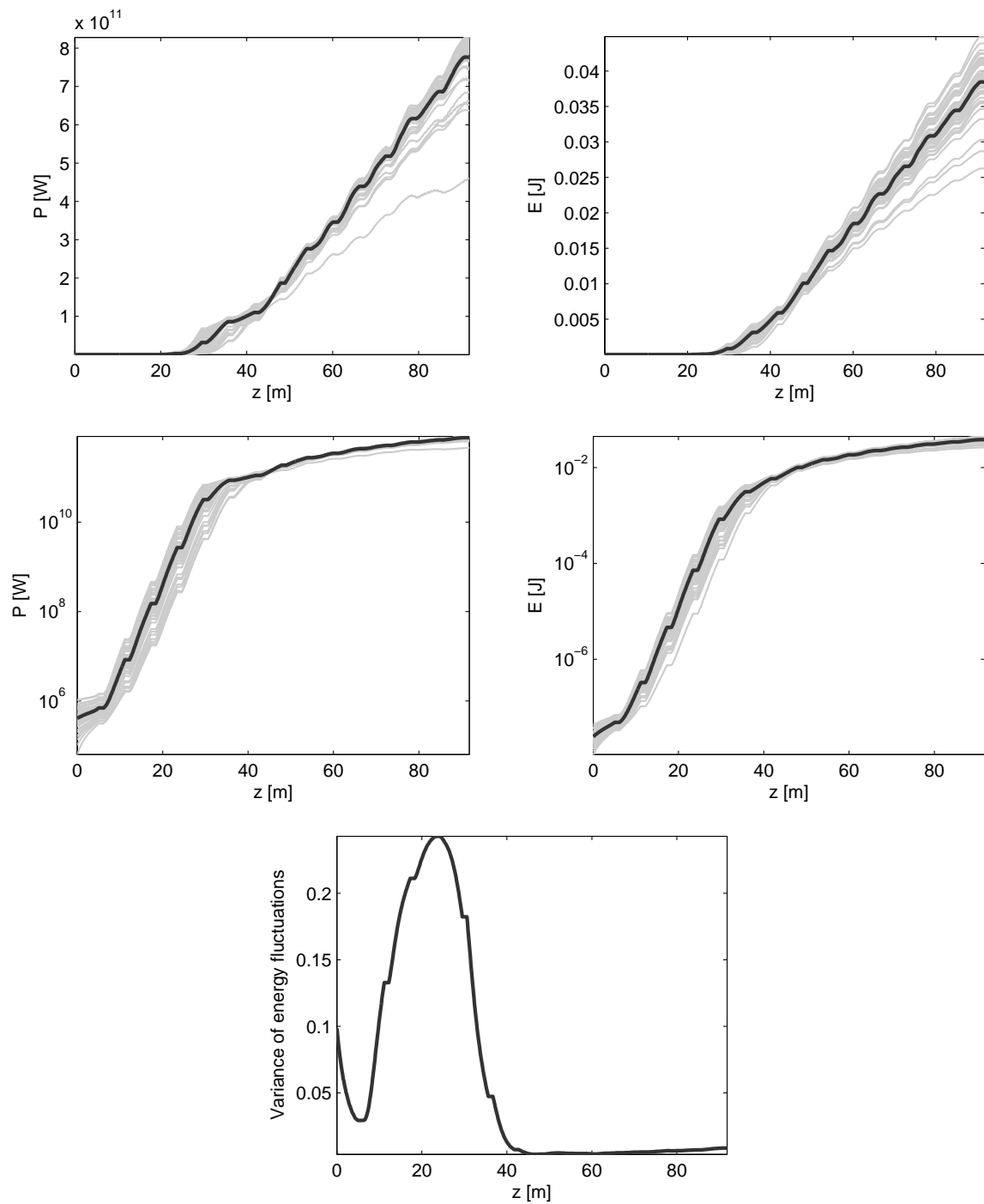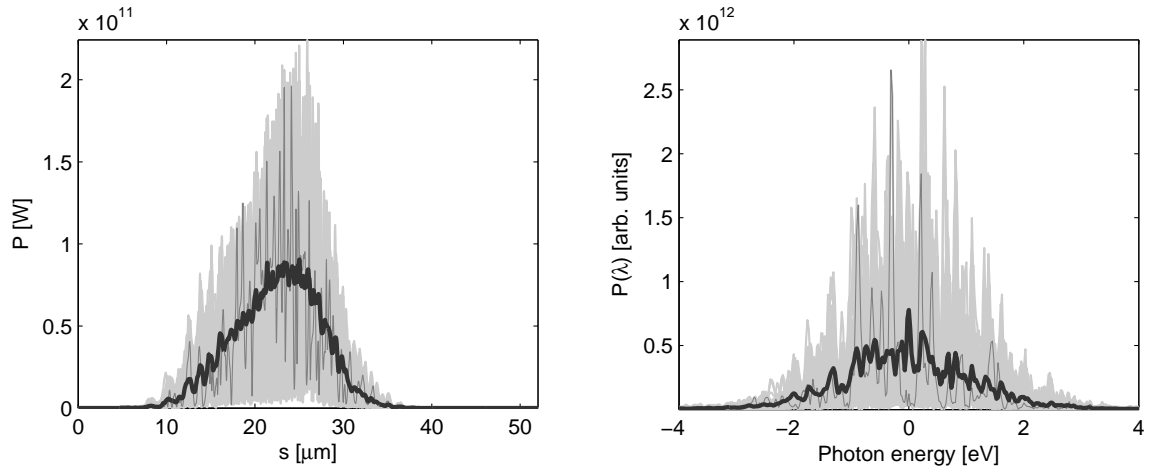
Figure 4.45: Power distribution and spectrum of the baseline SASE X-ray radiation pulse at saturation. Grey lines refer to single shot realizations, the black line refers to the average over a fifty realizations.
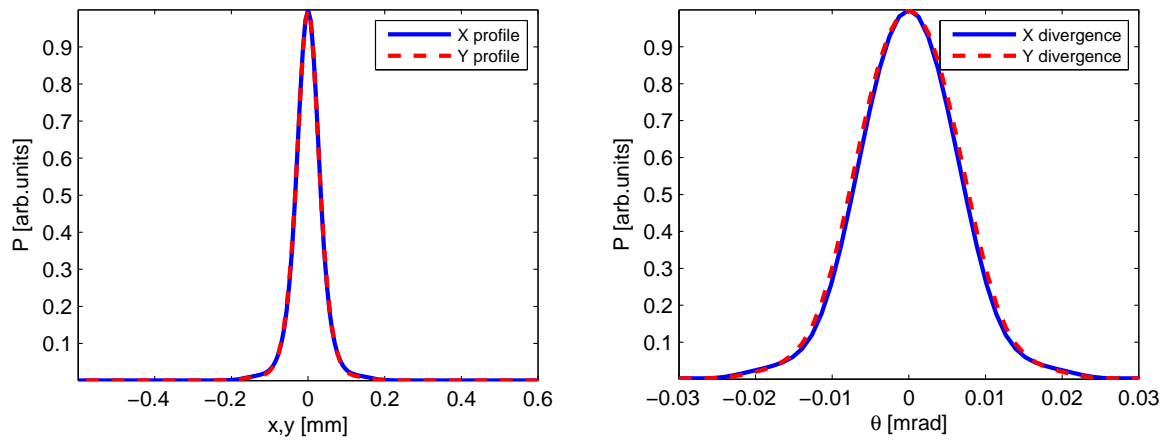

Figure 4.46: (Left plot) Transverse radiation distribution in the case of the baseline SASE pulse. (Right plot) Directivity diagram of the radiation distribution in the case of tapering at the exit of the output undulator.

power and spectral bandwidth of the SASE operation mode was reached after 8 sections: right before the saturation point. The output SASE characteristics in terms of power and spectrum are shown in Fig. 4.45. The evolution of the energy in the SASE pulse and of the energy fluctuations as a function of the undulator length are shown in Fig. 4.47. The transverse radiation distribution and divergence at saturation are shown in Fig. 4.46. By comparison with Fig. 4.44 one can see that in case of tapering the divergence reduction is accompanied by an increase in the transverse size of the radiation spot at the exit of the undulator.

Finally, power and spectrum of the self-seeded European XFEL are compared with those of the SASE radiation at saturation. The comparison is presented on Figure 4.48. Numerical simulations proved a hundredfold rise of a radiation spectral density, compared to the SASE at saturation ($1.8 \cdot 10^{14}$ photons/0.02% b/w per pulse compared with $8.2 \cdot 10^{12}$ photons/0.1% b/w per pulse). According to [125], the ultimate XFEL performance with a SASE operation regime and optimal tapering provides $8 \cdot 10^{13}$ photons/0.1% b/w per pulse. According to simulation results, a spectral bandwidth of the seeded radiation is $0.16 \, eV$ compared to $1.8 \, eV$ for a SASE
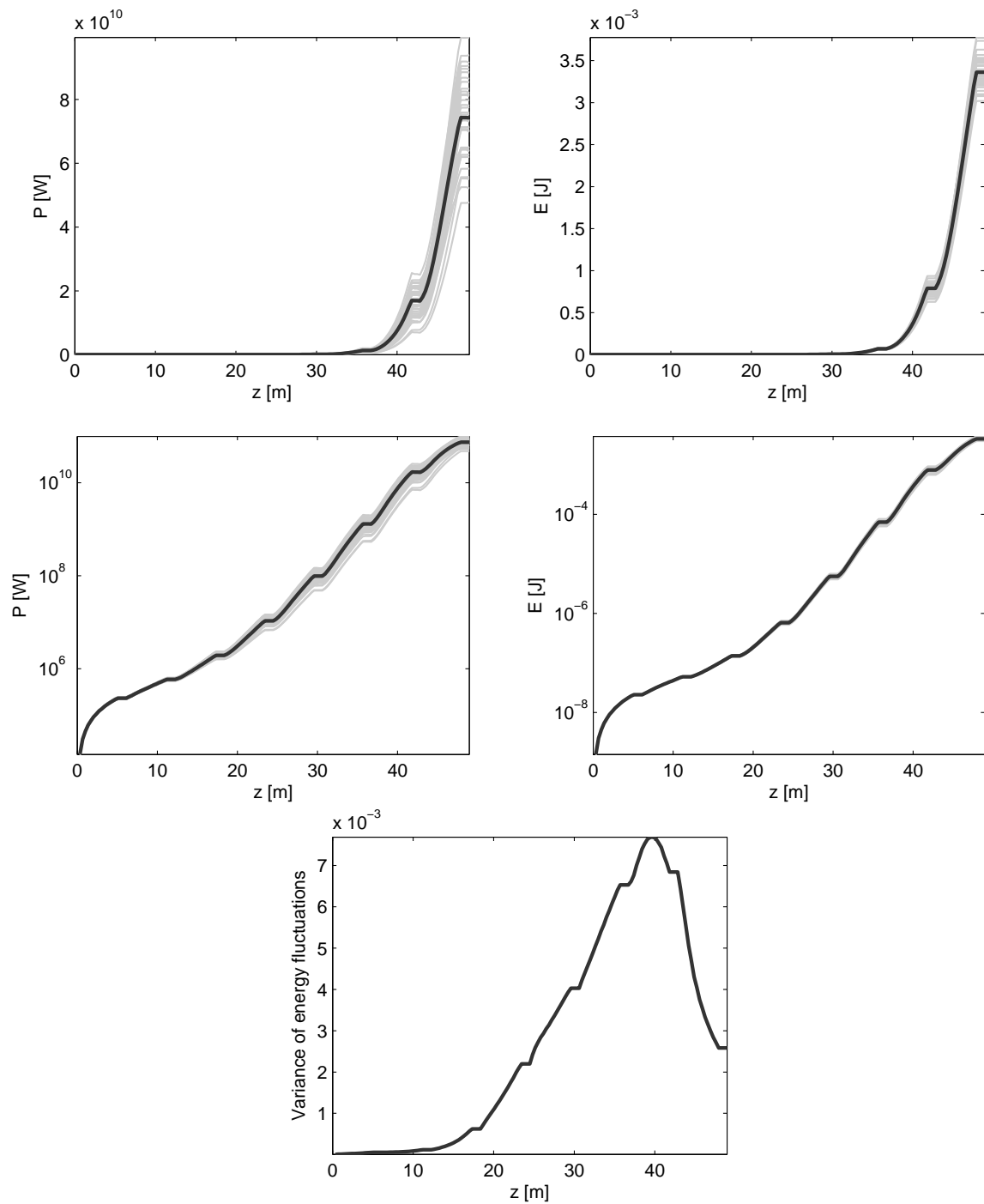
Figure 4.47: Evolution of a maximum power, an energy per pulse and of the energy fluctuations as a function of the undulator length in the case of the baseline SASE pulse. Grey lines refer to single shot realizations, the black line refers to the average over a fifty realizations.
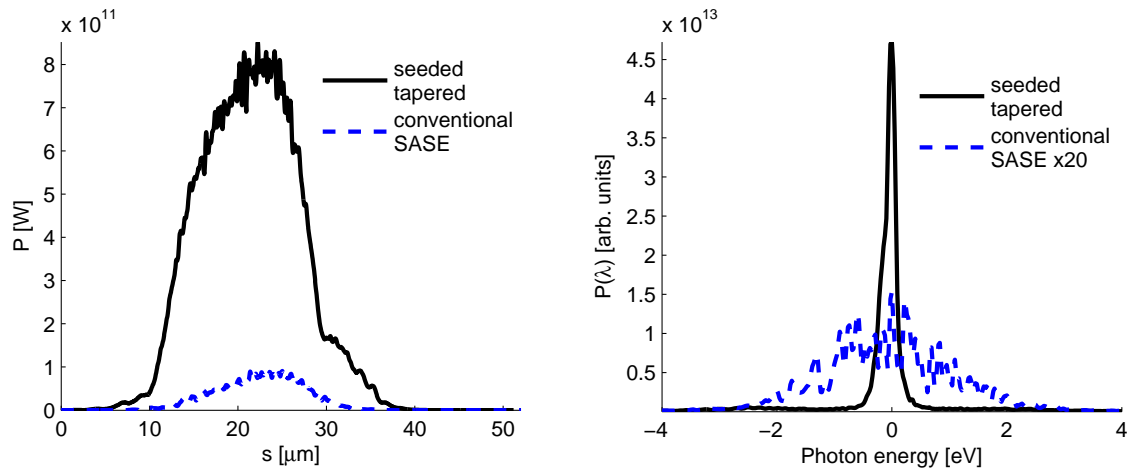
Figure 4.48: Comparison of the FEL pulse power distribution and spectrum for the SASE operation and seeded operation with a tapering technique. An average over a fifty realizations is presented.
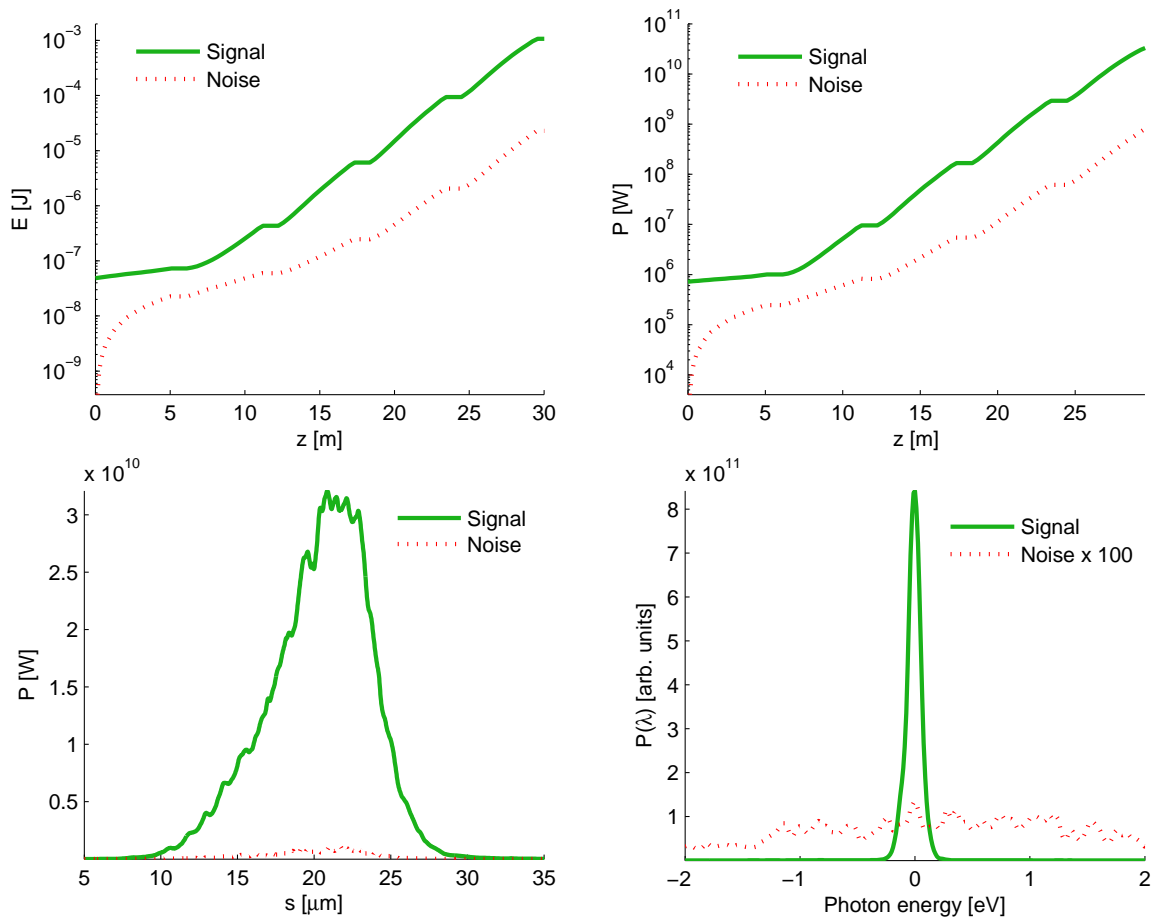
Figure 4.49: Comparison of the FEL pulse power distribution, evolution and on-axis spectrum for the second undulator with seed (signal) and without it (noise). Signal and noise comparison is valid before the saturation only; this way the first 30 meters of the linear amplification regime are presented with radiation properties at the end of this range. An average for over a 50 (signal) and 25 (noise) realizations is presented.

pulse. The reason of the seeded pulse resolving power bandwidth broadening compared to the instrumental function width by a factor of two is a presence of the non-linear energy chirp within the electron beam. This problem may be solved with a slotted foil, which selects the optimal part of an electron beam to lase.

The signal-to-noise ratio in the seeded undulator was calculated for the case of a 6 μJ energy per pulse at the grating. Simulation results are presented on Figure 4.49. SNR of a pulse energy is 45, SNR of a power is 40 and about 800 of a spectral density.

4.5 Effects of mirror height errors

Monochromator optical elements were modeled as a phase shifters, this way the simulation problem was reduced to the proper description of the phase shifters and to the propagation of the wavefront in vacuum between these phase shifters. The main wavefront distortion at the slit position and at the entrance of the second undulator originates from the grating and the plane mirror $M1$. Applying the Marechal criterion, i.e. requiring a Strehl ratio larger than 0.8, and treating the errors from the different optics independently, we obtain the following condition for the RMS height error h_{rms} [90]:

$$2h_{\mathrm{rms}}\theta_i\sqrt{N} < \lambda/14 \ , \tag{4.2}$$

where θ_i is the grazing angle of incidence and N is the number of optical elements. The most tight requirements corresponds to shortest wavelength. The grating operates at a fixed incidence angle $\theta_i = 1$ degree, and at 1 keV photon energy, the diffraction angle is about 2.1 degree. This corresponds to an incidence angle $(\theta_i + \theta_d)/2 = 1.5$ degree for the mirror $M1$. From Marechal criterion we conclude that a height error $h_{\mathrm{rms}} = 1$ nm should be sufficient for a diffraction-limited monochromatization at the photon energy of 1 keV. This is a realistic requirement given short length of an optical components (below 12 cm) compared with 60 cm optical element specifications provided in [113, pp. 54-56].
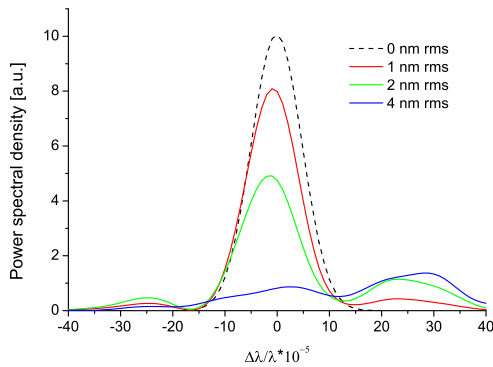
Figure 4.50: Effect of surface roughness on the monochromator performance. Simulations of the monochromator instrumental function for different root-mean-square of surface displacements. Here $\hbar\omega = 1$ keV.
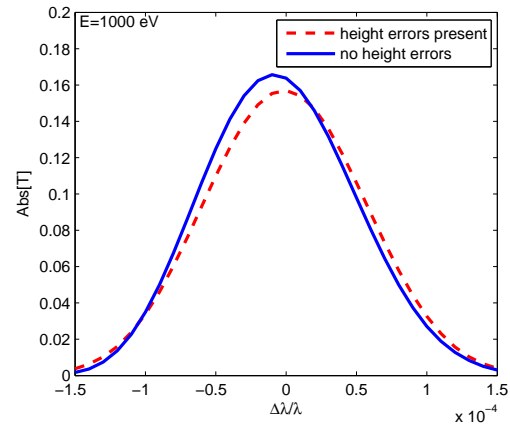
Figure 4.51: Effect of surface height errors on the monochromator instrumental function for European XFEL based on the measured height profiles of the LCLS SXRSS monochromator optical elements. Here $\hbar\omega = 1$ keV.

The surface errors were generated from power spectral density (PSD) functions described in mirrors specifications. The part of the PSD, which makes the most significant contribution to the overall RMS height error is the low spatial-frequency part. Due to the very small incident angle, the beam footprint is much larger in the tangential direction than in the sagittal direction. The lowest spatial frequency that contributes is in order of $\theta_i/w \sim 1/$cm in the tangential direction. Here w is the beam size at the optical element. It follows that the grating and the mirrors will

disturb the wavefront mainly in the tangential direction. Simulations were performed using a BPM code. The surface figure can be directly mapped onto the optical field coordinate system using the geometrical transformation described above. Examples of the simulated focus at the exit slit for 1 nm, 2 nm and 4 nm RMS quality optics are presented in Fig. 4.50 (left plot). These simulations were carried out for the previous XFEL SXRSS monochromator design [82], nevertheless, results apply for the current design as well. Non Gaussian tails are seen on the sides of the instrumental function. The influence of surface errors on the resolution in the case when the slit is absent is shown in Fig. 4.50 (right plot). An RMS roughness of order of 1 nm is acceptable for the self-seeding setup.

Another simulation of the surface error effect was carried out with a measured height profiles of the optical components manufactured and installed in the LCLS SXRSS monochromator (unpublished). Straightforward adoption of these height profiles (with residual peak-to-valley height errors of below 1 nm for grating and below 10 nm) for the rest of optical components to the European XFEL monochromator optics shows that this effect becomes negligible (see Fig. 4.51) .

4.6 Grating heat load and single shot damage issues

The energy deposited onto the optical element is of a great importance, especially for the high repetition facility. While SXRSS monochromator was adapted from the LCLS design, there is a difference in a maximum FEL pulse repetition rate between LCLS (100 Hz) and the European XFEL (2700 pulses per 0.6 ms pulse train or 27000 pulses per second average). Below study on the subject is presented.

There are two contributions of the energy deposited on the grating: SASE radiation and spontaneous emission (SE) radiation. The difference between them is in power and wavelength. The latter determines radiation penetration depth and its reflectivity by the grating. A SASE radiation has a narrow spectrum in the 300-1200 eV operation range, therefore it is mainly reflected by the grating (approx. 70%), and its attenuation length (penetration depth into material at given incidence angle) stays relatively constant with its value around 2 nm (see Figs. 4.52 and 4.53). SE, on the other hand, has a broad spectrum (Fig. 4.54) with its maximum in the range of a poor reflectivity of the grating but deep penetration into its volume. Here we model the grating as a bulk mirror at a 2 degrees grazing incidence. We assume that the grating incident angle is 1 degree, and that the blaze angle is about 1 degree too.
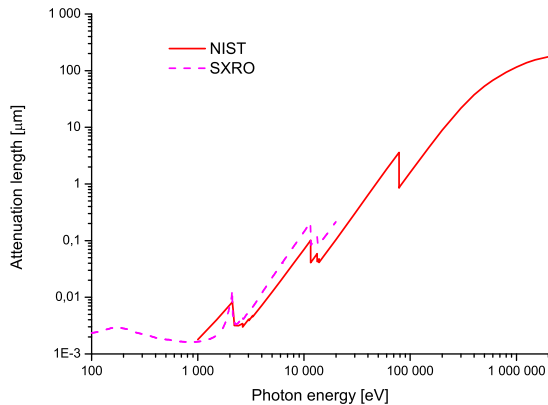
Figure 4.52: Attenuation depth in the bulk platinum mirror. Incidence angle is 2 degrees. Presented values are based on the X-ray database "SXRO" [123] and The National Institute of Standards and Technology database (NIST) [126].
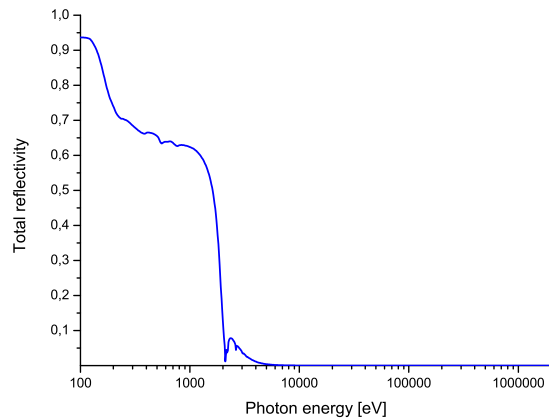
Figure 4.53: Reflectivity of the bulk platinum mirror. Incidence angle is 2 degrees. It corresponds well to the grating reflectivity presented at Fig. 4.15. Given values are based on the X-ray database "SXRO" [123].

FEL SE radiation grows linearly with an undulator length in contrast to the exponential growth of SASE. The interest in the latter is usually at the saturation point, where it is dominant over SE. In our case the undulator length is much smaller and SE radiation should not be neglected.

Pulse energies and power absorbed by the grating are presented in Table 4.3 and apply for the start-to-end simulation conditions (Section 4.4.3). The results presented refer to the case of an impinging pulse train composed by 2700 FEL pulses. The power is averaged over the 0.6 ms of the pulse train, which is the most extreme approximation ("mean over pulse train" values)
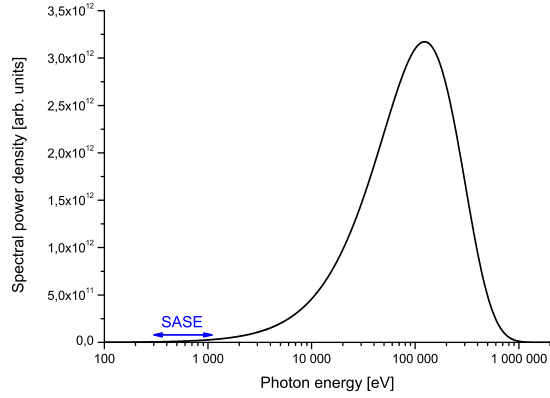
Figure 4.54: Power spectral density of the SE radiation calculated with [127] for the 12 GeV electron beam with undulator tuned 700 eV fundamental. The SASE3 operation range of SASE radiation is given for comparison.

Figure 4.55: Transverse distribution of the SE energy density per surface area at the position of the grating. Grating aperture in "x" dimension is 0.7 mm, therefore only a fraction of the radiation will hit the grating.

and over 0.1 s of the repetition rate period ("integrated" values). Results are presented for the 700 eV FEL photon energy.
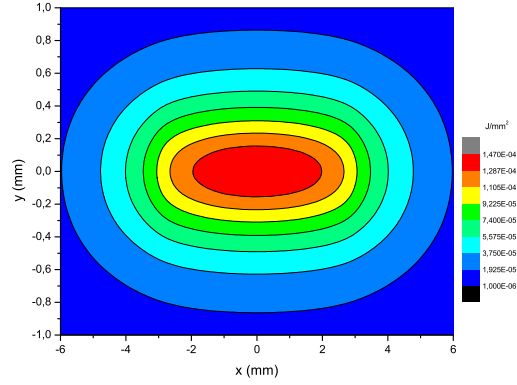
	SASE	SE	Units
Photon energy	0.7	10-500	keV
Mean pulse energy	6	1250	μJ
Energy deposited onto the grating	6	110	μJ
Incident power (peak)	1×10^9	2×10^{11}	W
Incident power (integrated)	0.16	33	W
Incident power (mean over pulse train)	27	5600	W
Absorbed power (integrated)	0.05 [30% for 700 eV]	3	W
Absorbed power (mean over pulse train)	8.1	500	W
Footprint surface on the grating	4 (0.26×15 mm)	80 (1×40 mm)	mm^2
Attenuation length	2	>800	nm
Peak power density (integrated)	0.012	0.067	W/mm^2
Peak power density (mean over pulse train)	2	11.2	W/mm^2
Dose	73	<2	meV/atom

Table 4.3: Thermal power and power density absorbed by the grating for an incidence angle of 2 degrees grazing incidence.

Heat load The heat load can be evaluated by considering the average power deposited on the grating. Main contribution comes from the SE. At 700 eV FEL photon energy only a fraction ($\sim 8\%$) of a divergent SE radiation is deposited onto a grating optical surface. Installation of an obstruction on the tip of the grating may cut-off half of the rest thermal power. In terms of a combined integrated power density peak value on the grating, it reaches 11 W/mm^2 at full repetition rate of 2700 pulses per train and 0.067 W/mm^2 on average. An 0.5 nC bunch charge is assumed with 4 undulators active. It is of the same order with values reported in [113, p. 61] at the SASE3 beamline soft X-ray monochromator located downstream. This power density value may be considered as a reference point and may be rescaled for lower repetition rates and

lower bunch charges proportionally.

Heat load contribution of the SASE radiation is much smaller. Despite the smaller footprint, which fully covers the grating, the mean pulse energy of the FEL is 6 μJ within a narrow spectrum bandwidth. Peak power density on the grating surface is 2 W/mm^2 and 0.012 W/mm^2 for an average over a pulse train and integrated respectively.

Due to a difference in the amplification behavior, the energy deposited onto the grating cannot be decreased simply by removing or detuning the SASE undulator sections: SNR will fall dramatically with a very little decrease of a heat load.

Worth mentioning that 2700 pulses per train is the most extreme estimation and each train will most likely be distributed between 3 beamlines, bringing the heat load down by the factor of 3.4 [113, p. 23]

Also, stability with respect to heat load effects becomes less important for optical element of a small footprint size, which is the case of the grating in the proposed monochromator design.

Single-shot damage   The peak power within the single pulse from the first SASE undulator will be in the range of a GW and is even higher for SE. At these power levels the possibility of ablation of the grating surface, which would result in permanent damage becomes important. Ablation depends on the radiation dose per pulse, which can be quantified as the energy absorbed in the volume defined by the projected beam area on the optical element and by one attenuation length, which is the depth into the material, measured along the surface normal, where the radiation intensity falls by $e \simeq 2.7$ times of its value at the surface. Normalized to one atom this energy corresponds to the atomic dose near the surface [101]

$$D = \frac{E_{\text{pulse}}(1 - R)\sin\theta_i}{2\pi\sigma^2 l_{\text{att}} n_A} , \qquad\qquad (3.1 \text{ revisited})$$

where E_{pulse} is the energy in one radiation pulse, R is the reflectivity, l_{att} is the attenuation length, σ is the RMS of the Gaussian beam intensity distribution immediately in front of the grating, and n_A denotes the element-specific density of atoms. For the SASE radiation and Pt coating we find $n_A \sim 6.4 \cdot 10^{22}$ cm^{-3}, $R \sim 0.7$, $l_{\text{att}} \sim 2$ nm, $\sigma \sim 0.05$ mm, and $E_{\text{pulse}} \sim 6\mu J$. The calculated dose reaches 73 meV/atom, which is still significantly below a $(6 - 9$ eV/atom) multi-shot damage threshold observed in the experiment [98].

In case of the SE radiation, an amount of energy deposited onto the grating is significantly higher (110 μJ), nevertheless, this energy is being distributed over much larger volume within the grating. Attenuation length of a radiation in a matter grows with a photon energy, and reaches values above 0.5 μm for a SE at the photon energy at its peak spectral power density of 100 keV (compared with 2 nm for SASE). This way the atomic dose per atom from the SE is less than 2 meV/atom, therefore negligible.

Both single shot damage contributions combined are below the melting threshold for Pt, therefore safe from damage. Worth mentioning that effects of "two temperature model" [102] (different heat diffusion within electron and ion systems) and ballistic transport of elec-

trons [103] that relax damage limits further by factor of 14 [98] were not taken into account.

Successful commissioning of the SXRSS monochromator at the LCLS with a smaller radiation footprint on the grating provides another argument for its safety in the proposed design.

Chapter 5

Summary and conclusions

The X-ray Free Electron Laser emerged as a revolutionary radiation source with unprecedented properties. The radiation generated by FELs has much higher spectral brightness and coherence, compared to synchrotron sources. Self-Amplified Spontaneous Emission is the baseline operation regime of Free Electron Lasers: an electron bunch after being accelerated enters an undulator, where it radiates starting from shot noise in that bunch (spontaneous emission takes place). The X-rays produced in the SASE process are transversely coherent, but the start-up from noise leads to poor temporal coherence with a broad and noisy spectrum. There are several methods to improve this parameter, but the most promising in X-ray region is a self-seeding. It implies a presence of a spectral filter (monochromator) in the middle of an amplification process. Overlap of the monochromatic "seed" with an electron beam in an undulator allows to enforce the growth of a single longitudinal mode in FEL radiation, considerably raising its spectral brightness.

In order to avoid perturbation of the undulator focusing system, self-seeding implies substitution of a single undulator segment with a weak chicane and the monochromator, which is a challenging problem. However, a very compact soft X-ray self-seeding setup design fulfilling these requirements was proposed in SLAC. It is very simple, includes only four optical elements and it does not include an entrance slit. It was shown [82] that this design may operate without an exit slit as well.

Simulation of the self-seeding scheme performing with the grating monochromator was of a great interest. Usually, soft X-ray monochromators operate with incoherent sources and their design is based on the use of ray-tracing codes. However, XFEL radiation is almost completely transversely coherent, and in this case the optical system had to be studied using a wave optics method in combination with FEL simulations. Consequently, two methods to simulate the self-seeding setup operation were developed and published in [128]. Wave optics analysis takes into account the actual FEL beam wavefront, third order aberrations and surface errors from each optical element.

In order to simulate surface imperfections of optical elements, we studied the split-step propagation method and show its applicability for small angle reflections in the soft X-ray

photon range. Results of the split-step propagation agreed well with a numerically much simpler phase-shifter method, proving usefulness of the latter in wave optics simulations.

The SXRSS concept was demonstrated experimentally in LCLS. Numerical simulations based on developed methods showed a very good agreement with the experimental results [54]. While the SASE radiation bandwidth was 6 eV FWHM (broadened by the electron energy jitter), the measured bandwidth of the seeded radiation was narrowed down to 0.18 eV at 930 eV photon energy.

In current work it is shown that the LCLS monochromator design can be adapted for the European XFEL SASE3 undulator. This optical layout of the monochromator was optimized in order to satisfy the high pulse repetition rate. The last segment's gap of the undulator upstream the monochromator is assumed to be fully opened during the self seeding operation. Reallocation of the source one cell upstream increases the radiation footprint on the grating. This leads to a significantly smaller energy density on the grating and allows one to improve its efficiency considerably compared with previously proposed design [82]. Relatively constant effective resolving power of the monochromator of 7700-9400 is high enough to produce transform-limited seed pulses with length from 4 μm at 1000 eV to 17 μm at 300 eV photon energies.

The overall performance of the SXRSS setup is studied with the help of FEL numerical simulations using the GENESIS code [83, 84]. The start-to-end simulations based on nominal parameters of 0.5 pC electron beam show the technical feasibility of the 700 eV self-seeded European XFEL operation. In combination with post-saturation tapering the SASE3 baseline could deliver a TW-class pulses with a hundredfold benefit in a peak spectral density compared to the SASE saturation ($1.8 \cdot 10^{14}$ photons /0.02% b/w per pulse versus $8.2 \cdot 10^{12}$ photons /0.1% b/w per pulse). Radiation bandwidth of the amplified seed is $0.16\,eV$ compared with $1.8\,eV$ for a SASE at a saturation.

The LCLS SXRSS commissioning experience and European XFEL start-to-end simulations show that spectral bandwidth of the seeded European XFEL can be improved with an emittance spoiler technique [87]. Even with a non-linear energy chirp present in the electron beam, the spectral density is one order of magnitude higher than in optimized SASE configuration, presented in [125].

European XFEL is a high-repetition rate facility, therefore it was important to estimate the grating performance in such conditions. It was found that the main heat load contribution comes from the spontaneous emission, while a single-shot damage source is the SASE radiation. The grating will operate with an incident radiation power densities comparable with the ones at the soft X-ray monochromator at SASE3 beamline. Therefore the same FEL beam operation modes are expected to be applicable.

Downstream the SASE3 undulator, the FEL radiation will be distributed between two scientific instruments:

The SQS instrument makes preferential use of the direct non-monochromatized FEL beam, i.e. focuses on applications requiring the highest intensity and/or highest available temporal resolution. Nevertheless, benefit from the high spectral resolution is possible during specific

experiments [116, 117].

The SCS instrument will greatly benefit from the self-seeding scheme. Citing [108], "Most of the techniques [of soft X-ray spectroscopy and coherent scattering, provided by the SCS instrument] will require using the soft X-ray monochromator, which induces pulse stretching and caps the peak intensities. High peak intensities are important to drive nonlinear X-ray-matter interactions, and NLXS [Nonlinear X-ray Spectroscopy] will require short pulses. Here, the self-seeding soft X-ray scheme could provide a wavelength-controllable tool to generate femtosecond-short pulses near the transform limit".

Before reaching SQS and SCS instruments, radiation spectra can be filtered with a soft X-ray monochromator. Its resolving power with a baseline 50 l/mm grating in 1000 eV region is comparable with that of the SXRSS monochromator instrumental function, but spectral efficiency is in order of 0.6. In certain conditions implementation of the emittance spoiler may provide experimental stations with comparable radiation bandwidth without additional loss of spectral density caused by the monochromator optics.

Among other facilities, Swiss-FEL at Paul Sherer Institute [129], PAL-XFEL at Pohang Accelerator Laboratory [130, 131] and LCLS-II at SLAC [132, 133] can effectively implement the SXRSS technique and benefit from the simulation methods presented in this thesis.

XFEL is a beautiful scientific instrument, whole potential of which is yet to be discovered. One of the ways to do so is a self-seeding technique. A tremendous effort of many people made it possible to seed the LCLS in the both soft and hard X-ray regimes. There is always a room for an improvement in both technology and understanding of physical processes. I believe that the work presented in this thesis will make a worthy contribution to the progress in the field and will help to raise the efficiency of the future designs.

Chapter 6

List of Abbreviations

BOD   Beam Overlap Diagnostics

CSR   Coherent Synchrotron Radiation

e/m   electromagnetic

EEHG   Echo-Enabled Harmonic Generation

FEL   Free-Electron Laser

FLASH   Freie-elektronen-LASer in Hamburg

FWHM   Full Width at Half Maximum

HGHG   High-Gain Harmonic Generation

HHG   High-order Harmonic Generation

HXRSS   Hard X-Ray Self-Seeding

LCLS   Linac Coherent Light Source

NLCTA   Next Linear Collider Test Accelerator

PRD   Physics Requirements Document

RF   Radio Frequency

RMS   Root Mean Squared

SCSS   SPring-8 Compact SASE Source

SDUV-FEL   Shanghai Deep Ultraviolet Free Electron Laser

SE   Spontaneous Emission

SLAC   Stanford Linear Acceleratir Center

SNR   Signal-to-Noise Ratio

STD   Standard Deviation

SXRSS   Soft X-Ray Self Seeding

TESLA   Tera-Electronvolt Superconducting Linear Accelerator

TTF   Tesla Test Facility

XFEL   X-ray Free Electron Laser

YAG   Yttrium Aluminium Garnet

Chapter 7

Own publications

Publications directly related to the thesis

1. <u>S. Serkez</u>, G. Geloni, V. Kocharyan, and E. Saldin, "Grating monochromator for soft X-ray self-seeding the European XFEL," arXiv.org, March, 2013.

2. D. Ratner, R. Abela, J. Amann, C. Behrens, D. Bohler, G. Bouchard, C. Bostedt, M. Boyes, K. Chow, D. Cocco, F. J. Decker, Y. Ding, C. Eckman, P. Emma, D. Fairley, Y. Feng, C. Field, U. Flechsig, G. Gassner, J. Hastings, P. Heimann, Z. Huang, N. Kelez, J. Krzywinski, H. Loos, A. Lutman, A. Marinelli, G. Marcus, T. Maxwell, P. Montanez, S. Moeller, D. Morton, H. D. Nuhn, N. Rodes, W. Schlotter, <u>S. Serkez</u>, T. Stevens, J. Turner, D. Walz, J. Welch, and J. Wu, "Experimental Demonstration of a Soft X-Ray Self-Seeded Free-Electron Laser," Phys. Rev. Lett., vol. 114, no. 5, pp. 15, 2015.

3. <u>S. Serkez</u>, J. Krzywinski, Y. Ding, and Z. Huang, "Soft x-ray self-seeding simulation methods and their application for the Linac Coherent Light Source," Phys. Rev. Spec. Top. - Accel. Beams, vol. 18, no. 3, p. 030708, Mar. 2015.

Publications not directly related to the thesis

1. G. Geloni, V. Kocharyan, E. Saldin, S. Serkez, and M. Tolkiehn, "Wake monochromator in asymmetric and symmetric Bragg and Laue geometry for self-seeding the European X-ray FEL," arXiv.org, January, 2013.

2. S. Serkez, V. Kocharyan, E. Saldin, I. Zagorodnov, G. Geloni, and O. Yefanov, "Proposal for a scheme to generate 10 TW-level femtosecond x-ray pulses for imaging single protein molecules at the European XFEL," arXiv.org, June, 2013.

3. S. Serkez, V. Kocharyan, E. Saldin, I. Zagorodnov, G. Geloni, and O. Yefanov, "Extension of SASE Bandwidth Up To 2 % As a Way To Increase Number of Indexed Images for Protein Structure Determination By Femtosecond X-Ray Nanocrystallography At the European XFEL," arXiv.org, June, 2013.

4. S. Serkez, V. Kocharyan, E. Saldin, I. Zagorodnov, and G. Geloni, "Purified SASE undulator configuration to enhance the performance of the soft x-ray beamline at the European XFEL," arXiv.org, July, 2013.

5. S. Serkez, V. Kocharyan, E. Saldin, I. Zagorodnov, and G. Geloni, "Proposal to generate 10 TW level femtosecond x-ray pulses from a baseline undulator in conventional SASE regime at the European XFEL," arXiv.org, August, 2013.

6. S. Serkez, V. Kocharyan, and E. Saldin, "Nonlinear undulator tapering in conventional SASE regime at baseline electron beam parameters as a way to optimize the radiation characteristics of the European XFEL," arXiv.org, September, 2013.

7. I. Agapov, G. Geloni, G. Feng, V. Kocharyan, E. Saldin, S. Serkez, and I. Zagorodnov, "The Full Potential of the Baseline SASE Undulators of the European XFEL," arXiv.org, 2014.

8. K. Ayyer, G. Geloni, V. Kocharyan, E. Saldin, S. Serkez, O. Yefanov, I. Zagorodnov, "Perspectives for imaging single protein molecules with the present design of the European XFEL," Struct. Dyn., vol. 2, no. 4, p. 041702, July, 2015.

9. O. Chubar, G. Geloni, V. Kocharyan, A. Madsen, E. Saldin, S. Serkez and J. Sutter, "Novel opportunities for sub-meV inelastic X-ray scattering at high-repetition rate self-seeded X-ray free-electron lasers," arXiv.org, August, 2015, *submitted to JSR*.

Appendix A

ABCD matrix formalism for the VLS grating

An ABCD matrix is intended to represent any arbitrary paraxial element, or optical system located between an input plane and an output plane. It relates initial ray parameters (transverse position and direction) with final ones in the following form:

$$\begin{pmatrix} x_2 \\ \theta_2 \end{pmatrix} = \begin{pmatrix} A & B \\ C & D \end{pmatrix} \begin{pmatrix} x_1 \\ \theta_1 \end{pmatrix},$$

(A.1)

where

$$A = \left.\frac{x_2}{x_1}\right|_{\theta_1=0} \qquad B = \left.\frac{x_2}{\theta_1}\right|_{x_1=0}$$
$$C = \left.\frac{\theta_2}{x_1}\right|_{\theta_1=0} \qquad D = \left.\frac{\theta_2}{\theta_1}\right|_{x_1=0}.$$

In the present case, the optical element is the VLS plane grating with the input plane corresponding to the plane perpendicular to the incident beam and with the output plane the plane perpendicular to the diffracted beam. The most usual application for ray matrices is the determination of the image of the object located at the input plane. In this case, some important properties of optical system are obtained when any of the ABCD parameters vanish [134].

The total optical system from the object plane to the image plane is represented by the matrix:

$$\begin{pmatrix} A_{\text{tot}} & B_{\text{tot}} \\ C_{\text{tot}} & D_{\text{tot}} \end{pmatrix} = \begin{pmatrix} 1 & r_2 \\ 0 & 1 \end{pmatrix} \begin{pmatrix} 1 & 0 \\ -1/f & 1 \end{pmatrix} \begin{pmatrix} 1/b & 0 \\ 0 & b \end{pmatrix} \begin{pmatrix} 1 & r_1 \\ 0 & 1 \end{pmatrix},$$

(A.2)

where b is the asymmetric parameter $\sin\theta_i/\sin\theta_d$, see [135]. The explicit expression for the total matrix elements are

$$A_{\text{tot}} = 1/b - r_2/fb \,,$$

$$B_{\text{tot}} = r_1/b - r_1 r_2/fb + r_2 b \,,$$

$$C_{\text{tot}} = -1/fb \,,$$

$$D_{\text{tot}} = -r_1/fb + b \,. \qquad \text{(A.3)}$$

The condition $B_{\text{tot}} = 0$ has to be verified in order to guarantee imaging of the object at the output plane. In fact, when $B_{\text{tot}} = 0$, any point source at the input plane focuses at the corresponding point in the output plane, regardless of the input angle. Therefore, the output plane is the image plane. Dividing the equation $B_{\text{tot}} = 0$ by $r_1 r_2$ on the left hand side we find the imaging equation [136]

$$\frac{b}{r_1} + \frac{1}{br_2} = \frac{D_1 \lambda}{D_0^2 \sin\theta_i \sin\theta_d} \,, \qquad \text{(A.4)}$$

which is identical to the imaging condition $C_{20} = 0$ which we derived above from first principles, because $\sin\theta_i = \cos\alpha$ and $\sin\theta_d = \cos\beta$. It thus follows that the ABCD matrix for the VLS plane grating in the tangential plane has the general form

$$\begin{pmatrix} A_{\text{tot}} & B_{\text{tot}} \\ C_{\text{tot}} & D_{\text{tot}} \end{pmatrix} = \begin{pmatrix} A_{\text{tot}} & 0 \\ -1/f_{\text{tot}} & D_{\text{tot}} \end{pmatrix} \qquad \text{(A.5)}$$

with the effective focal length of the entire resizing-focusing system (grating) given by [136]

$$\frac{1}{f_{\text{tot}}} = \frac{\lambda D_1}{D_0^2 \sin\theta_i \sin\theta_d} \,, \qquad \text{(A.6)}$$

which is symmetric in θ_i and θ_d as it must be. The ABCD matrix elements can be used to characterize width and wavefront curvature of the Gaussian beam after its propagation through the VLS grating.

Appendix B

Method for computing third order aberrations for a toroidal grating

In this appendix an intuitive geometrical method of computation of aberrations is presented. It is first necessary to clearly define the reference coordinate systems used to describe the optical system. Figs. B.1 shows the toroidal grating, the object point A and the image point B. The three coordinate systems (x, y, z), (x_1, y_1, z_1), and (x_2, y_2, z_2) are used to describe the position of the wave on the optical surface, the incoming wavefront and the diffracted wavefront, respectively. The ray AOB is referred to as the principal ray. In the following, the wavefront aberrations, the positions of the object and image plane are specified with respect to this ray. The wavefront aberration W for a spherical wave passing through a point P in the system is defined as the path difference between the principal and auxiliary ray: $W = \overline{APB} - \overline{AOB}$. Here we take advantage of the paraxial approximation obtained by ignoring all terms but the first quadratic terms in x_1 and y_1. Let us assume that point A is in the tangential plane and $P(x_1, y_1, z_1)$ is any point on the grating surface. The equation for the path $\overline{AP}$ is

$$\overline{AP} = z_1 + \frac{x_1^2}{2z_1} + \frac{y_1^2}{2z_1} = \overline{AF} + \frac{\overline{PF}^2 + \overline{PP'}^2}{2\overline{AF}} \, , \tag{B.1}$$

where $\overline{AF} = \overline{AO} - \overline{OD} - \overline{FD}$, $\overline{OD} = |z| \sin \alpha$, $\overline{FD} = \overline{PE} = x \cos \alpha$, $\overline{PF} = \overline{CD} - \overline{CE} = |z| \cos \alpha - x \sin \alpha$. Here (x, y, z) are the coordinates of the point P in the grating coordinate system. The latter is chosen in such a way that $x > 0$. Neglecting all terms of order higher than the second in x and y, the form of a toroidal surface can be expressed by the equation

$$x = \frac{z^2}{2R} + \frac{y^2}{2\rho} \, , \tag{B.2}$$

where R and ρ are tangential and sagittal radius of curvature. Thus, the distance $PC = x$. Finally, we have

$$\overline{AP} - \overline{AO} = -\overline{OD} - \overline{FD} + \frac{\overline{PF}^2 + \overline{PP'}^2}{2\left(\overline{AO} - \overline{OD} - \overline{FD}\right)}$$

$$= z\sin\alpha - \frac{z^2}{2R}\cos\alpha - \frac{y^2}{2\rho}\cos\alpha + \frac{\left[z\cos\alpha + z^2\sin\alpha/(2R) + y^2\sin\alpha/(2\rho)\right]^2 + y^2}{2\left[r_1 + z\sin\alpha - z^2\cos\alpha/(2R)\right]}, \quad \text{(B.3)}$$

where we used the notation $\overline{AO} = r_1$. Knowing that $r_1 \gg z$, denominator may be expanded with $1/(1+x) \simeq 1 - x$, when $x \ll 1$. During multiplication we limit ourselves to third order terms, e.g. ignore $z^4, y^2 z^2, \ldots$ Finally,

$$\begin{aligned}
\overline{AP} - r_1 &= z\sin\alpha \\
&+ \frac{z^2}{2r_1}\cos^2\alpha - \frac{z^2}{2R}\cos\alpha \\
&- \frac{z^3}{2r_1^2}\cos^2\alpha\sin\alpha + \frac{z^3}{2Rr_1}\cos\alpha\sin\alpha \\
&+ \frac{y^2}{2r_1} - \frac{y^2}{2\rho}\cos\alpha \\
&+ \frac{zy^2}{2r_1\rho}\sin\alpha\cos\alpha - \frac{zy^2}{2r_1^2}\sin\alpha.
\end{aligned} \quad \text{(B.4)}$$

The difference $\overline{BP} - \overline{BO}$ can be obtained following the same procedure described above, simply replacing the incidence angle α with the diffraction angle β. Summing up the optical path difference $\left(\overline{AP} - \overline{AO}\right) + \left(\overline{BP} - \overline{BO}\right)$ and grouping the coefficients we obtain

$$\begin{aligned}
C_{10} &= \left(\sin\alpha + \sin\beta\right), \\
C_{20} &= \frac{1}{2}\left[\frac{\cos^2\alpha}{r_1} + \frac{\cos^2\beta}{r_2} - \frac{\cos\alpha}{R} - \frac{\cos\beta}{R}\right], \\
C_{30} &= -\frac{1}{2}\left[\left(\frac{\cos^2\alpha}{r_1} - \frac{\cos\alpha}{R}\right)\frac{\sin\alpha}{r_1} + \left(\frac{\cos^2\beta}{r_2} - \frac{\cos\beta}{R}\right)\frac{\sin\beta}{r_2}\right], \\
C_{02} &= \frac{1}{2}\left[\frac{1}{r_1} - \frac{\cos\alpha}{\rho}\right] + \frac{1}{2}\left[\frac{1}{r_2} - \frac{\cos\beta}{\rho}\right], \\
C_{12} &= -\frac{1}{2}\left[\left(\frac{1}{r_1} - \frac{\cos\alpha}{\rho}\right)\frac{\sin\alpha}{r_1} + \left(\frac{1}{r_2} - \frac{\cos\beta}{\rho}\right)\frac{\sin\beta}{r_2}\right], \quad \text{(B.5)}
\end{aligned}$$

proving that geometry-determined power series of z and y are identical to (2.99).
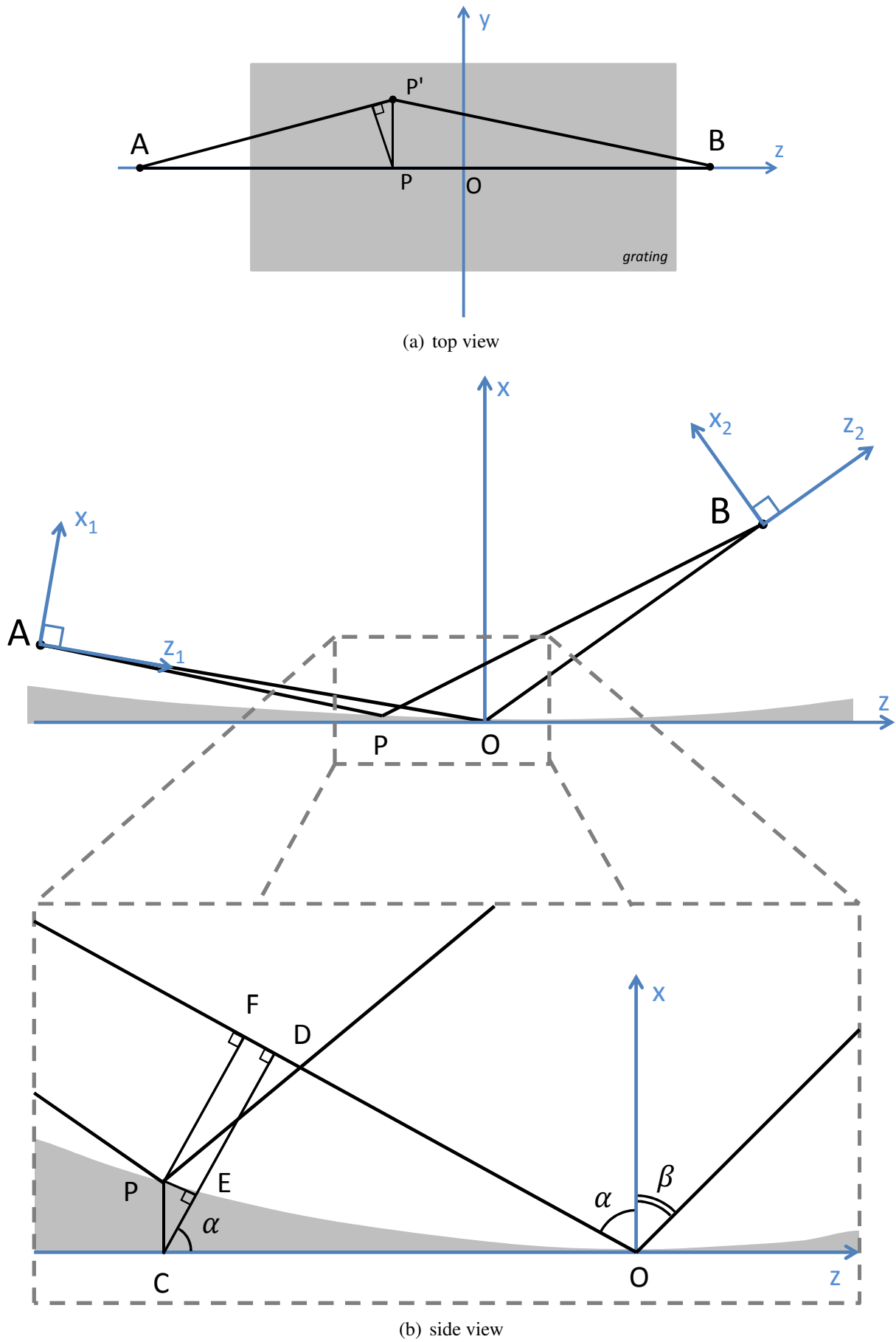
(a) top view

(b) side view

Figure B.1: Optical scheme and coordinate systems for a toroidal grating system.

Appendix C

Pulse Front Tilt

The grating in the SXRSS monochromator introduces an angular dispersion of the radiation. It yields to a pulse-front tilt (PFT) effect, which becomes important when dealing with ultrashort pulses. The geometrical interpretation of the PFT is that due to different incidence and reflection angles, pulse front immediately after the grating should be tilted in order to keep an optical path difference along the reflection area the same (AD=BC on Fig. C.1). Since SASE FEL pulse consists of numerous longitudinal modes, they may be geometrically interpreted as sequential pulses, and each of them will be tilted after the grating. When operated without the exit slit, the pulse-front tilt may affect an input coupling factor of the FEL at the entrance of the seeded undulator. The pulse propagation approach allows us to simulate the SASE pulse front tilt effect in the SXRSS monochromator. The propagation algorithm simulates an effect of the PFT on the input coupling factor automatically.

Following simulations were done for the LCLS. In Figure C.2 the 1000 eV SASE pulse (subfigure - a) is propagated after the grating (b) and through the slit position (c-e). We can see, that the PFT is present in the time domain when multiple angularly dispersed frequencies overlap in the frequency domain. At the slit position the PFT is absent. In the frequency domain wavelengths are focused and well-resolved. Out of the slit position numerous wavelengths overlap again, resulting in the PFT in the time domain. Situation will be similar at the entrance to the seeded undulator, but due to an image magnification and the higher angular dispersion, this effect will differ from the PFT around the slit position. The design of the SXRSS monochromator implies re-imaging of the radiation at the slit position to the entrance of the seeded undulator via mirror M2 with the magnification factor 10. Source point position at the end of the SASE undulator defines focusing parameters of the optical system of the monochromator. It affects the size and the position of the waist around the slit area, leading to changes in the structure of the re-imaged radiation at the entrance of the seeded undulator. It is shown in Figure C.3 that the optimal source position is located in the section 8 of the SASE undulator. It allows one to decrease the effect of the PFT.
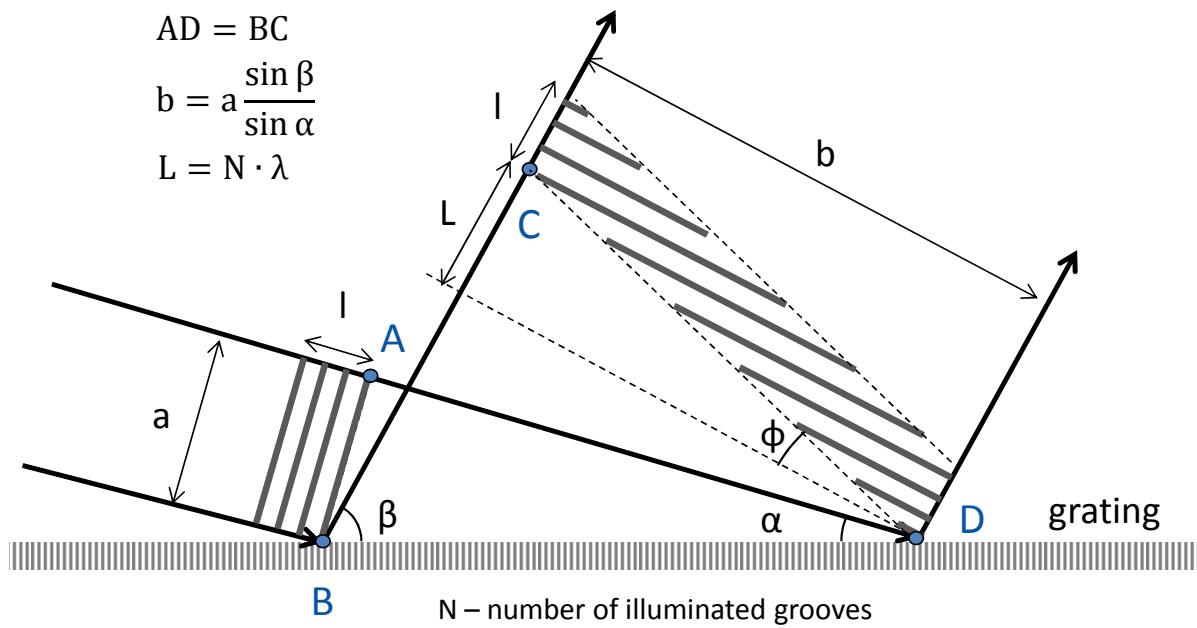
Figure C.1: Geometrical illustration of pulse front tilt created by an optical element with angular dispersion (grating)

(a) before G (b) after G, 0% to slit (c) 75% to slit (d) 100% to slit (e) 125% to slit
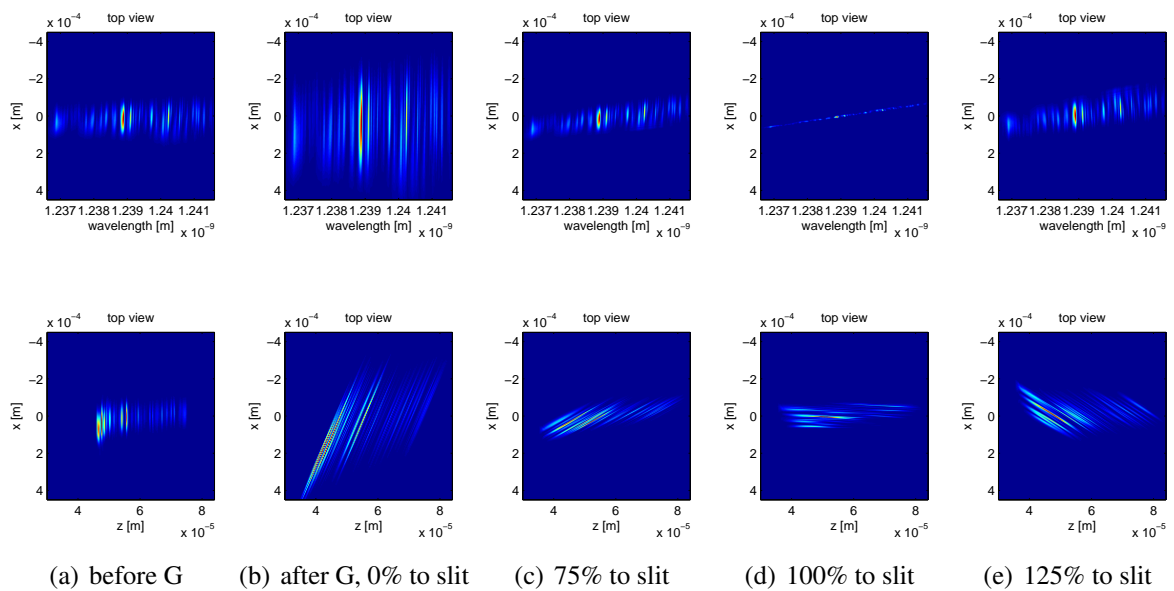
Figure C.2: Frequency (first row) and time (second row) domains of the vertical dispersive projection of 1000eV radiation pulse propagated after the grating through the slit position.
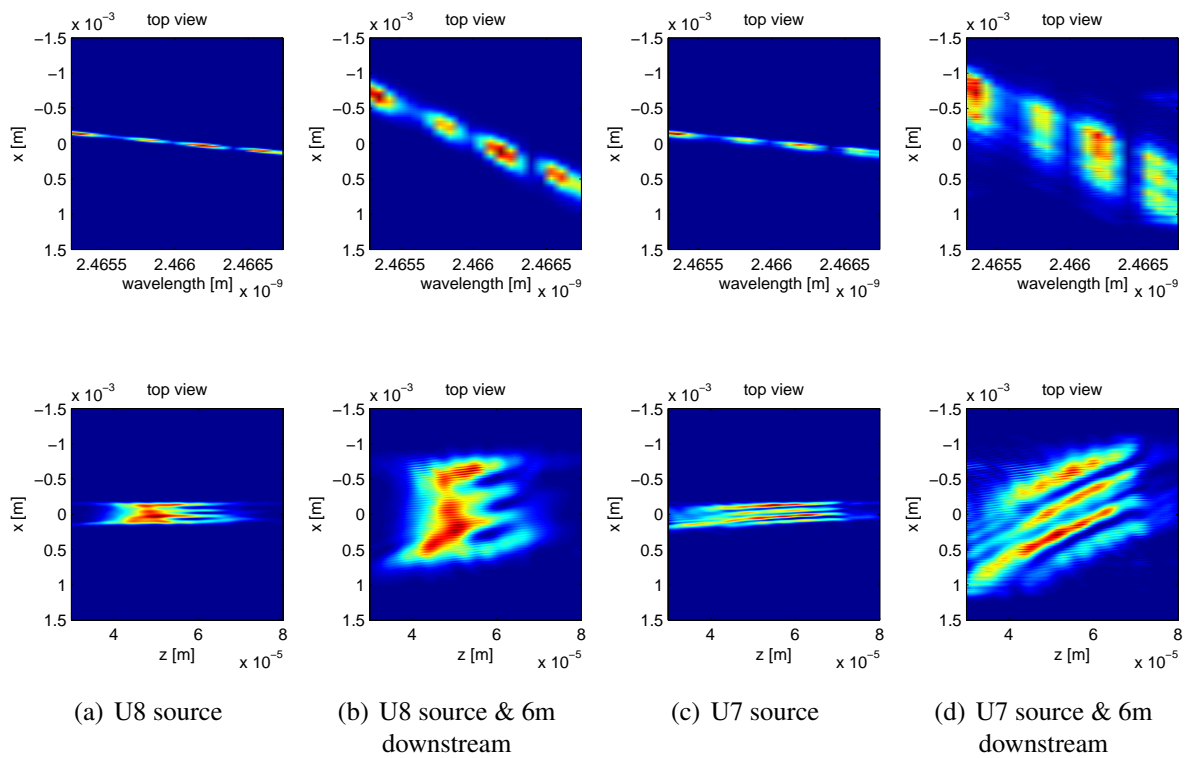
Figure C.3: Frequency (first row) and time domains (second row) of propagated radiation pulse through the monochromator. The direct approach with a limited spectral bandwidth was used for propagation. The radiation source position was simulated in undulator 8 (figs. a-b) and in undulator 7 (figs. c-d). In order to illustrate further evolution of the pulse, it was additionally propagated 6m downstream seeded undulator (figs. b,d). The radiation energy is 500 eV. At higher energies this effect is smaller.

Bibliography

[1] J. M. J. Madey. "Stimulated emission of bremsstrahlung in a periodic magnetic field". In: *Journal of Applied Physics* 42.5 (1971), pp. 1906–1913. ISSN: 00218979. DOI: 10.1063/1.1660466.

[2] D. a. G. Deacon et al. "First operation of a free-electron laser". In: *Physical Review Letters* 38.16 (1977), pp. 892–894. ISSN: 00319007. DOI: 10.1103/PhysRevLett.38.892.

[3] N. Kroll and W. McMullin. "Stimulated emission from relativistic electrons passing through a spatially periodic transverse magnetic field". In: *Physical Review A* 17.1 (1978), pp. 300–308. ISSN: 0556-2791. DOI: 10.1103/PhysRevA.17.300.

[4] A. Kondratenko and E. Saldin. "Generation of coherent radiation by a relativistic electron beam in an undulator". In: *Sov. Phys. Dokl.* 24.12 (1979).

[5] A. Kondratenko and E. Saldin. "Generation of coherent radiation by a relativistic electron beam in an ondulator". In: *Particle Accelerators* 10 (1980), pp. 207–216. DOI: 1003-0207.

[6] Y. Derbenev, A. Kondratenko, and E. Saldin. "On the possibility of using a free electron laser for polarization of electrons in storage rings". In: *Nuclear Instruments and Methods in Physics Research* 193.3 (1982), pp. 415–421. ISSN: 01675087. DOI: 10.1016/0029-554X(82)90233-6.

[7] R. Bonifacio, F. Casagrande, and L. De Salvo Souza. "Collective variable description of a free-electron laser". In: *Physical Review A* 33.4 (1986), pp. 2836–2839. ISSN: 10502947. DOI: 10.1103/PhysRevA.33.2836.

[8] M. Hogan et al. "Measurements of Gain Larger than 100000 at 12 um in a Self-Amplified Spontaneous-Emission Free-Electron Laser". In: *Physical Review Letters* 81.22 (1998), pp. 4867–4870. ISSN: 0031-9007. DOI: 10.1103/PhysRevLett.81.4867.

[9] E. Saldin, E. Schneidmiller, and M. Yurkov. "Statistical properties of radiation from VUV and X-ray free electron laser". In: *Optics Communications* 148.4-6 (1998), pp. 383–403. ISSN: 00304018. DOI: 10.1016/S0030-4018(97)00670-6.

[10] S. V. Milton et al. "Exponential gain and saturation of a self-amplified spontaneous emission free-electron laser." In: *Science (New York, N.Y.)* 292.5524 (2001), pp. 2037–2041. ISSN: 00368075. DOI: 10.1126/science.1059955.

[11] V Ayvazyan et al. "Generation of GW radiation pulses from a VUV free-electron laser operating in the femtosecond regime." In: *Physical review letters* 88.10 (2002), p. 104802. ISSN: 0031-9007. DOI: 10.1103/PhysRevLett.88.104802.

[12] B. Mcneil. "First light from hard x-ray laser". In: *Nature Photonics* 3.7 (2009), pp. 375–377. ISSN: 1749-4885. DOI: 10.1038/nphoton.2009.110.

[13] P. Emma et al. "First lasing and operation of an ångstrom-wavelength free-electron laser". In: *Nature Photonics* 4.9 (2010), pp. 641–647. ISSN: 1749-4885. DOI: 10.1038/nphoton.2010.176.

[14] T. Ishikawa et al. "A compact X-ray free-electron laser emitting in the sub-ångström region". In: *Nature Photonics* 6.8 (June 2012), pp. 540–544. ISSN: 1749-4885. DOI: 10.1038/nphoton.2012.141.

[15] H. Motz. "Applications of the radiation from fast electron beams". In: *Journal of Applied Physics* 22.5 (1951), pp. 527–535. ISSN: 00218979. DOI: 10.1063/1.1700002.

[16] B. W. J. McNeil and N. R. Thompson. "X-ray free-electron lasers". In: *Nature Photonics* 4.12 (2010), pp. 814–821. ISSN: 1749-4885. DOI: 10.1038/nphoton.2010.239.

[17] *Photon science web site*. URL: http://photon-science.desy.de/facilities/flash/the_free_electron_laser/how_it_works/energy_transfer/index_eng.html.

[18] J. Pierce. "Theory of the Beam-Type Traveling-Wave Tube". In: *Proceedings of the IRE* 35.2 (1947). ISSN: 0096-8390. DOI: 10.1109/JRPROC.1947.226217.

[19] N Kroll, P Morton, and M Rosenbluth. "Free-electron lasers with variable parameter wigglers". In: *IEEE Journal of Quantum Electronics* 17.8 (1981), pp. 1436–1468. ISSN: 0018-9197. DOI: 10.1109/JQE.1981.1071285.

[20] W. M. Fawley et al. "Tapered undulators for SASE FELs". In: *Nuclear Instruments and Methods in Physics Research, Section A: Accelerators, Spectrometers, Detectors and Associated Equipment* 483.1-2 (2002), pp. 537–541. ISSN: 01689002. DOI: 10.1016/S0168-9002(02)00377-7.

[21] G. Geloni, V. Kocharyan, and E. Saldin. "Scheme for generation of fully-coherent, TW power level hard X-ray pulses from baseline undulators at the European X-ray FEL". In: *arXiv.org* (2010), p. 23. arXiv: 1007.2743.

[22] R. Bonifacio, B. W. J. McNeil, and P Pierini. "Superradiance in the high-gain free-electron laser". In: *Physical Review A* 40.8 (1989), pp. 4467–4475. ISSN: 10502947. DOI: 10.1103/PhysRevA.40.4467.

[23] S. Reiche. "Overview of Seeding Methods for FELs". In: *Proceedings of International Particle Accelerator Conference*. 2013, pp. 2063–2067. ISBN: 9783954501229. URL: https://accelconf.web.cern.ch/accelconf/IPAC2013/papers/wezb102.pdf.

[24] L. Giannessi. "Harmonic Generation and Linewidth Narrowing in Seeded Fels". In: *Proceedings of International FEL Conference*. Trieste, 2004, pp. 37–40. URL: http://accelconf.web.cern.ch/AccelConf/f04/papers/MOPOS26/MOPOS26.PDF.

[25] M Cornacchia et al. "Future possibilities of the linac coherent light source". In: *Journal of Synchrotron Radiation* 11.3 (2004), pp. 227–238. ISSN: 09090495. DOI: 10.1107/S090904950400370X.

[26] X. J. Wang et al. "Efficiency and spectrum enhancement in a tapered free-electron laser amplifier". In: *Physical Review Letters* 103.15 (2009), p. 154801. ISSN: 00319007. DOI: 10.1103/PhysRevLett.103.154801.

[27] G. Geloni, V. Kocharyan, and E. Saldin. "Production of transform-limited X-ray pulses through self-seeding at the European X-ray FEL". In: *arXiv.org* (2011). arXiv: 1109.5112.

[28] W. M. Fawley and Others. "Toward TW-level LCLS radiation pulses". In: *Talk at International FEL Conference, Shanghai, China*. 2011. URL: http://accelconf.web.cern.ch/AccelConf/FEL2011/talks/tuoa4_talk.pdf.

[29] J Wu and Others. "Simulation of the Hard X-ray Self-seeding FEL at LCLS". In: *Poster at International FEL Conference, Shanghai, China*. 2011.

[30] Y Jiao et al. "Modeling and multidimensional optimization of a tapered free electron laser". In: *Physical Review Special Topics - Accelerators and Beams* 15.5 (2012), p. 50704. ISSN: 10984402. DOI: 10.1103/PhysRevSTAB.15.050704.

[31] J Wu, C Pellegrini, and A Marinelli. "Generation of Longitudinally Coherent Ultra High Power X-Ray FEL Pulses by Phase and Amplitude Mixing". In: *Proceedings of International FEL Conference, Nara, Japan* (2012), p. 237. URL: https://accelconf.web.cern.ch/accelconf/FEL2012/papers/tupd07.pdf.

[32] B. W. J. McNeil, N. R. Thompson, and D. J. Dunning. "Transform-limited x-ray pulse generation from a high-brightness self-amplified spontaneous-emission free-electron laser". In: *Physical Review Letters* 110.13 (2013), pp. 1–5. ISSN: 00319007. DOI: 10.1103/PhysRevLett.110.134802.

[33] D. Xiang et al. "Purified self-amplified spontaneous emission free-electron lasers with slippage-boosted filtering". In: *Physical Review Special Topics - Accelerators and Beams* 16.1 (2013), pp. 1–7. ISSN: 10984402. DOI: 10.1103/PhysRevSTAB.16.010703.

[34] S. Reiche. "Overview of Seeding Methods for FELs". In: *Talk slides at International Particle Accelerator Conference*. Shanghai, China, 2013. URL: http://accelconf.web.cern.ch/AccelConf/IPAC2013/talks/wezb102_talk.pdf.

[35] Q. Marksteiner. "FEL Seeding Techniques". In: *United States Particles Accelerator School, FEL class notes*. 2014. URL: https://uspas.fnal.gov/materials/14UNM/4_Seeding_SASE_\&_HGHG.pdf.

[36] D. Garzella et al. "Using VUV high-order harmonics generated in gas as a seed for single pass FEL". In: *Nuclear Instruments and Methods in Physics Research, Section A: Accelerators, Spectrometers, Detectors and Associated Equipment*. Vol. 528. 1-2. 2004, pp. 502–505. DOI: 10.1016/j.nima.2004.04.089.

[37] J Seres et al. "Laser technology: source of coherent kiloelectronvolt X-rays." In: *Nature* 433.7026 (2005), p. 596. ISSN: 0028-0836. DOI: 10.1038/433596a.

[38] G. Lambert et al. "Injection of harmonics generated in gas in a free-electron laser providing intense and coherent extreme-ultraviolet light". In: *Nature Physics* 4.4 (2008), pp. 296–300. ISSN: 1745-2473. DOI: 10.1038/nphys889.

[39] S. Ackermann et al. "Generation of coherent 19- and 38-nm radiation at a free-electron laser directly seeded at 38 nm". In: *Physical Review Letters* 111.11 (2013), pp. 1–5. ISSN: 00319007. DOI: 10.1103/PhysRevLett.111.114801.

[40] L. H. Yu. "Generation of intense uv radiation by subharmonically seeded single-pass free-electron lasers". In: *Physical Review A* 44.8 (1991), pp. 5178–5193. ISSN: 10502947. DOI: 10.1103/PhysRevA.44.5178.

[41] L. Yu. "High-Gain Harmonic-Generation Free-Electron Laser". In: *Science* 289.5481 (Aug. 2000), pp. 932–934. ISSN: 00368075. DOI: 10.1126/science.289.5481.932.

[42] L. Yu et al. "First Ultraviolet High-Gain Harmonic-Generation Free-Electron Laser". In: *Physical Review Letters* 91.7 (2003), pp. 89–92. ISSN: 0031-9007. DOI: 10.1103/PhysRevLett.91.074801.

[43] L. DiMauro et al. "First SASE and seeded FEL lasing of the NSLS DUV FEL at 266 and 400 nm". In: *Nuclear Instruments and Methods in Physics Research, Section A: Accelerators, Spectrometers, Detectors and Associated Equipment*. Vol. 507. 1-2. 2003, pp. 15–18. DOI: 10.1016/S0168-9002(03)00825-8.

[44] E. Allaria et al. "Highly coherent and stable pulses from the FERMI seeded free-electron laser in the extreme ultraviolet". In: *Nature Photonics* 6.10 (Sept. 2012), pp. 699–704. ISSN: 1749-4885. DOI: 10.1038/nphoton.2012.233.

[45] G. Stupakov. "Using the beam-echo effect for generation of short-wavelength radiation". In: *Physical Review Letters* 102.7 (2009), pp. 1–4. ISSN: 00319007. DOI: 10.1103/PhysRevLett.102.074801.

[46] D. Xiang and G. Stupakov. "Echo-enabled harmonic generation free electron laser". In: *Physical Review Special Topics - Accelerators and Beams* 12.3 (2009), pp. 1–10. ISSN: 10984402. DOI: 10.1103/PhysRevSTAB.12.030702.

[47] Z. T. Zhao and D Wang. "Progress in the Sduv-Fel and Development of X-Ray Fels in Shanghai". In: *Proceedings of International FEL Conference, Malmo, Sweden* (2010), pp. 15–19. URL: http://accelconf.web.cern.ch/AccelConf/FEL2010/papers/moobi1.pdf.

[48] D. Xiang et al. "Demonstration of the echo-enabled harmonic generation technique for short-wavelength seeded free electron lasers". In: *Physical Review Letters* 105.11 (2010), pp. 8–11. ISSN: 00319007. DOI: 10.1103/PhysRevLett.105.114801.

[49] J. Feldbaus et al. "Possible application of X-ray optical elements for reducing the spectral bandwidth of an X-ray SASE FEL". In: *Nuclear Instruments and Methods in Physics Research, Section A: Accelerators, Spectrometers, Detectors and Associated Equipment* 393.1-3 (1997), pp. 162–166. ISSN: 01689002. DOI: 10.1016/S0168-9002(97)00451-8.

[50] E. L. Saldin et al. "X-ray FEL with a meV bandwidth". In: *Nuclear Instruments and Methods in Physics Research, Section A: Accelerators, Spectrometers, Detectors and Associated Equipment* 475.1-3 (2001), pp. 357–362. ISSN: 01689002. DOI: 10.1016/S0168-9002(01)01539-X.

[51] G. Geloni, V. Kocharyan, and E. Saldin. "Self-seeded operation of the LCLS hard X-ray FEL in the long-bunch mode". In: *arXiv.org* December (2010). arXiv: 1012.3617.

[52] G. Geloni, V. Kocharyan, and E. Saldin. "A novel self-seeding scheme for hard X-ray FELs". In: *Journal of Modern Optics* 58.16 (Sept. 2011), pp. 1391–1403. ISSN: 0950-0340. DOI: 10.1080/09500340.2011.586473.

[53] J. Amann et al. "Demonstration of self-seeding in a hard-X-ray free-electron laser". In: *Nature Photonics* 6.10 (2012), pp. 693–698. ISSN: 1749-4885. DOI: 10.1038/nphoton.2012.180.

[54] D. Ratner et al. "Experimental Demonstration of a Soft X-Ray Self-Seeded Free-Electron Laser". In: *Physical Review Letters* 114.5 (2015), pp. 1–5. ISSN: 0031-9007. DOI: 10.1103/PhysRevLett.114.054801.

[55] X. Yang and Y. Shvydko. "Maximizing spectral flux from self-seeding hard x-ray free electron lasers". In: *Physical Review Special Topics - Accelerators and Beams* 16.12 (Dec. 2013), p. 120701. ISSN: 1098-4402. DOI: 10.1103/PhysRevSTAB.16.120701.

[56] S. A. Self. "Focusing of spherical Gaussian beams." In: *Applied optics* 22.5 (1983), pp. 658–661. ISSN: 0003-6935. DOI: 10.1364/AO.22.000658.

[57] D Marcuse. *Light Transmission Optics*. Van Nostrand Reinhold Company, 1972. ISBN: 9780442251574. URL: http://amazon.com/o/ASIN/0442251572/.

[58] V. Vysloukh. *Nonlinear fiber optics*. Vol. 160. 5. Academic Press, 1990, p. 151. ISBN: 0120451433. DOI: 10.3367/UFNr.0160.199005k.0151.

[59] T. Poon and T. Kim. *Engineering optics with Matlab*. World Scientific Company, Paperback(2006), 2006, p. 260. ISBN: 9812568727. URL: http://cds.cern.ch/record/1490072.

[60] G. W. Stroke. *An Introduction to Coherent Optics and Holography*. Academic Press, 1966. URL: http://amazon.com/o/ASIN/B006RLKJF2/.

[61] R Petit and L. C. Botten. *Electromagnetic theory of gratings*. Springer-Verlag Berlin ; New York, 1980. ISBN: 3540101934 0387101934.

[62] M. Boots, D. Muir, and A. Moewes. "Optimizing and characterizing grating efficiency for a soft X-ray emission spectrometer". In: *Journal of Synchrotron Radiation* 20.2 (2013), pp. 272–285. ISSN: 09090495. DOI: 10.1107/S0909049512051266.

[63] M. Itou, T. Harada, and T. Kita. "Soft x-ray monochromator with a varied-space plane grating for synchrotron radiation: design and evaluation." In: *Applied optics* 28.1 (1989), pp. 146–153. ISSN: 0003-6935. DOI: 10.1364/AO.28.000146.

[64] R. J. Thomas. *Toroidal varied-line space (TVLS) gratings*. 2003. DOI: 10.1117/12.460375.

[65] H. Haber. "The Torus Grating". In: *Journal of the Optical Society of America* 40.3 (1950), p. 153. ISSN: 0030-3941. DOI: 10.1364/JOSA.40.000153.

[66] T. Harada et al. "Design of a high-resolution extreme-ultraviolet imaging spectrometer with aberration-corrected concave gratings." In: *Applied optics* 37.28 (1998), pp. 6803–6810. ISSN: 0003-6935. DOI: 10.1364/AO.37.006803.

[67] J.-C. Diels and W. Rudolph. *Ultrashort Laser Pulse Phenomena*. Elsevier, 2006, p. 676. ISBN: 9780080466408. DOI: 10.1016/B978-012215493-5/50006-9.

[68] C. M. Kewish et al. "Wave-optical simulation of hard-x-ray nanofocusing by precisely figured elliptical mirrors". In: *Applied Optics* 46.11 (2007), p. 2010. ISSN: 0003-6935. DOI: 10.1364/AO.46.002010.

[69] A. Barty et al. "Predicting the coherent X-ray wavefront focal properties at the Linac Coherent Light Source (LCLS) X-ray free electron laser." In: *Optics express* 17.18 (2009), pp. 15508–15519. ISSN: 1094-4087. DOI: 10.1364/OE.17.015508.

[70] P Emma. "First Lasing of the Lcls X-Ray Fel At 1.5 Å". In: *Proceedings of Particle Accelerator Conference*. Vancouver, BC, Canada, 2009. URL: https://accelconf.web.cern.ch/accelconf/PAC2009/papers/th3pbi01.pdf.

[71]   H. Loos. "LCLS accelerator operation and measurement of electron beam parameters relevant for the X-ray beam". In: *SLAC-PUB-15422* (2013). URL: http://slac.stanford.edu/pubs/slacpubs/15250/slac-pub-15422.pdf.

[72]   Y Feng et al. "X-ray Optics for soft X-ray self-seeding the LCLS-II". In: *Proceedings of International FEL Conference, Malmo, Sweden*. 2010, pp. 270–273. URL: http://accelconf.web.cern.ch/AccelConf/FEL2010/papers/tupb10.pdf.

[73]   Y Feng et al. *Compact Grating Monochromator Design for LCLS-I Soft X-ray Self-Seeding*. 2012. URL: https://sites.google.com/a/lbl.gov/realizing-the-potential-of-seeded-fels-in-the-soft-x-ray-regime-workshop/talks.

[74]   Y Feng et al. "System design for self-seeding the LCLS at soft X-ray energies". In: *Proceedings of International FEL Conference, Nara, Japan*. 2012. URL: https://accelconf.web.cern.ch/accelconf/FEL2012/papers/tuobi01.pdf.

[75]   H. D. Nuhn. "LCLS Undulator commissioning, alignment, and performance". In: *Proceedings of International FEL Conference, Liverpool, UK*. 2009. URL: http://accelconf.web.cern.ch/AccelConf/FEL2009/papers/thoa02.pdf.

[76]   J Arthur et al. *Linac Coherent Light Source (LCLS) Conceptual Design Report*. Tech. rep. April. 2002. URL: http://www-ssrl.slac.stanford.edu/lcls/cdr/.

[77]   D. Cocco et al. "The optical design of the soft x-ray self seeding at LCLS". In: *Proceedings SPIE, X-Ray Lasers and Coherent X-Ray Sources: Development and Applications*. Vol. 8849. 2013, 88490A. DOI: 10.1117/12.2024402.

[78]   D. Ratner and Others. "Soft X-ray Self-seeding Setup and Results at LCLS". In: *Talk at International FEL Conference, Basel, Switzerland*. 2014. URL: http://accelconf.web.cern.ch/AccelConf/FEL2014/talks/tuc02_talk.pdf.

[79]   C. Svetina et al. "A fixed included angle monochromator for the 4th generation light source at FERMI@Elettra". In: *Proceedings of SPIE*. Vol. 7448. 2009, 74480O–74480O–11. ISBN: 9780819477385. DOI: 10.1117/12.824445.

[80]   M. D. Roper. "Matching a variable-included-angle grating monochromator to the properties of a soft X-ray FEL source to achieve a controlled temporal stretch". In: *Nuclear Instruments and Methods in Physics Research Section A: Accelerators, Spectrometers, Detectors and Associated Equipment* 635.1 (Apr. 2011), S80–S87. ISSN: 01689002. DOI: 10.1016/j.nima.2010.09.017.

[81]   D. Cocco. *Private communication*. 2013.

[82] S. Serkez et al. "Grating monochromator for soft X-ray self-seeding the European XFEL". In: *arXiv.org* March (2013). arXiv: 1303.1392v1.

[83] S. Reiche. "GENESIS 1.3: A fully 3D time-dependent FEL simulation code". In: *Nuclear Instruments and Methods in Physics Research, Section A: Accelerators, Spectrometers, Detectors and Associated Equipment* 429.1 (1999), pp. 243–248. ISSN: 01689002. DOI: 10.1016/S0168-9002(99)00114-X.

[84] S. Reiche. "Numerical studies for a single pass high gain free-electron laser". PhD thesis. 2000, p. 182. URL: http://pbpl.physics.ucla.edu/Research/Simulations/_genesis/download/documentation/genesis_thesis.pdf.

[85] G. Geloni, V. Kocharyan, and E. Saldin. "A simple method for controlling the line width of SASE X-ray FELs". In: (2010). arXiv: 1004.4067.

[86] G. Geloni, V. Kocharyan, and E. Saldin. "Cost-effective way to enhance the capabilities of the LCLS baseline". In: *arXiv.org* (2010). arXiv: 1008.3036.

[87] P Emma et al. "Femtosecond and subfemtosecond x-ray pulses from a self-amplified spontaneous-emission-based free-electron laser." In: *Physical review letters* 92.7 (2004), p. 074801. ISSN: 0031-9007. DOI: 10.1103/PhysRevLett.92.074801.

[88] Y. Ding. *Private communication*. 2013.

[89] S. P. Hau-Riege et al. "Measurement of x-ray free-electron-laser pulse energies by photoluminescence in nitrogen gas". In: *Journal of Applied Physics* 103.5 (2008). ISSN: 00218979. DOI: 10.1063/1.2844478.

[90] P. Heimann et al. "Linac coherent light source soft x-ray materials science instrument optical design and monochromator commissioning". In: *Review of Scientific Instruments* 82.9 (2011), p. 93104. ISSN: 00346748. DOI: 10.1063/1.3617420.

[91] D. F. Ratner et al. "FEL gain length and taper measurements at LCLS". In: *Proceedings of International FEL Conference*. Liverpool, 2009, pp. 221–224. URL: https://accelconf.web.cern.ch/accelconf/FEL2009/papers/tuoa03.pdf.

[92] M Borland. *Elegant: A flexible SDDS-compliant code for accelerator simulation*. Tech. rep. Argonne National Lab., IL (US), 2000. DOI: 10.2172/761286.

[93] A. Marinelli et al. "Comparative study of nonideal beam effects in high gain harmonic generation and self-seeded free electron lasers". In: *Physical Review Special Topics - Accelerators and Beams* 13.7 (2010), pp. 1–11. ISSN: 10984402. DOI: 10.1103/PhysRevSTAB.13.070701.

[94] H. Loos et al. *LCLS Physics Specifications for the SXRSS Beam Overlap Diagnostics*. Tech. rep. 2575 Sand Hill Road, Menlo Park, CA 94025: SLAC National Accelerator Laboratory, 2013. URL: http://slac.stanford.edu/pubs/slacpubs/16000/slac-pub-16073.pdf.

[95] D Ratner et al. *Supplementary Materials : Experimental Demonstration of a Soft X-Ray Self-Seeded Free-Electron Laser*. URL: http://journals.aps.org/prl/supplemental/10.1103/PhysRevLett.114.054801/SXRSS_supp.pdf.

[96] D. Denley et al. "Carbon K-edge fine structure in graphite foils and in thin-film contaminants on metal surfaces". In: *Physical Review B* 21.6 (1980), pp. 2267–2273. ISSN: 01631829. DOI: 10.1103/PhysRevB.21.2267.

[97] T Koide et al. "Resuscitation of carbon-contaminated mirrors and gratings by oxygen-discharge cleaning. 2: Efficiency recovery in the 100-1000-eV range." In: *Applied optics* 27.20 (1988), pp. 4305–4313. ISSN: 0003-6935. DOI: 10.1364/AO.27.004305.

[98] J. Krzywinski et al. "Damage threshold of platinum coating used for optics for self-seeding of soft x-ray free electron laser". In: *Optics Express* 23.5 (2015), p. 5397. ISSN: 1094-4087. DOI: 10.1364/OE.23.005397.

[99] M. Yabashi et al. "Optics development for Japanese XFEL project". In: *Damage to VUV, EUV, and X-ray Optics, Proceedings of SPIE*. Vol. 6586. 2007. Prague, 2007, pp. 658605–658605–9. ISBN: 0819467146. DOI: 10.1117/12.724318.

[100] R. A. London et al. "Computational Simulations of High Intensity X-Ray Matter Interaction". In: vol. 4500. 925. 2001, pp. 51–62. ISBN: 0277-786X. DOI: 10.1117/12.452958.

[101] M. Altarelli and Others. *The European X-Ray Free-Electron Laser*. Tech. rep. XFEL EU, 2007, July. URL: http://xfel.desy.de/tdr/tdr.

[102] S. Anisimov, B. Kapeliovich, and T. Perelman. "Electron emission from metal surfaces exposed to ultrashort laser pulses". In: *Sov. Phys.-JETP* 39.2 (1974), pp. 375–377.

[103] J. Hohlfeld et al. *Electron and lattice dynamics following optical excitation of metals*. 2000. DOI: 10.1016/S0301-0104(99)00330-4.

[104] T. Koyama et al. "Damage threshold investigation using grazing incidence irradiation by hard x-ray free electron laser". In: *Proceedings of SPIE*. Vol. 8848. 2013, 88480T. ISBN: 9780819496980. DOI: 10.1117/12.2025377.

[105] I Zagorodnov. *Beam Dynamics simulations for XFEL*. 2011. URL: http://www.dedy.de/sfel-beam/s2e.

[106] H. Sinn. "X-ray Beamline Optics and Photon Diagnostics". In: *Talk at European XFEL Users' Meeting*. Hamburg, 2015. URL: http://www.xfel.eu/sites/site_xfel-gmbh/content/e63594/e65073/e243602/e249144/Sinn_UM2015_eng.pdf.

[107] M. Altarelli. "The European X-Ray Free-Electron Laser: General Status of the Project". In: *Talk at European XFEL Users' Meeting*. Hamburg, 2015. URL: http://www.xfel.eu/sites/site_xfel-gmbh/content/e63594/e65073/e243602/e249143/Altarelli_UM2015_eng.pdf.

[108] A Scherz et al. "Scientific Instrument Spectroscopy and Coherent Scattering (SCS)". In: *Conceptual Design Report* (2013). DOI: 10.3204/XFEL.EU/TR-2013-006.

[109] A. Scherz. "Coherent Scattering (SCS) Scientific Instrument". In: *Talk at European XFEL Users' Meeting*. Hamburg, 2015. URL: http://www.xfel.eu/sites/site_xfel-gmbh/content/e63594/e65073/e243602/e249115/2015-01-28-UM15-scherzV2_eng.pdf.

[110] A. Beckmann, S. Karabekyan, and J. Pflüger. *Undulator Control Systems*. Tech. rep. January. 2013. DOI: 10.3204/XFEL.EU/TR-2013-004.

[111] J Pflueger et al. "Status of the undulator systems for the European X-ray Free Electron Laser". In: *Proceedings of International FEL Conference, New York, USA*. New York, 2013. ISBN: 9783954501267. URL: http://accelconf.web.cern.ch/Accelconf/FEL2013/papers/tupso60.pdf.

[112] J. Pflüger. *Status of the XFEL.EU Undulator Systems*. 2013. URL: http://cbp.lbl.gov/seminar/archive/Pfluger_3Sept_2013.pdf.

[113] H. Sinn et al. *Optics and Beam Transport*. Tech. rep. December. 2012. DOI: 10.3204/XFEL.EU/TR-2012-006.

[114] D. La Civita et al. "SASE3: soft x-ray beamline at European XFEL". In: *Proceedings SPIE 9210, X-Ray Free-Electron Lasers: Beam Diagnostics, Beamline Instrumentation, and Applications II*. Vol. 9210. 2014, p. 921002. DOI: 10.1117/12.2061693.

[115] R. Brinkmann, E. Schneidmiller, and M. Yurkov. "Possible operation of the European XFEL with ultra-low emittance beams". In: *Nuclear Instruments and Methods in Physics Research Section A: Accelerators, Spectrometers, Detectors and Associated Equipment* 616.1 (Apr. 2010), pp. 81–87. ISSN: 01689002. DOI: 10.1016/j.nima.2010.02.121. arXiv: 1001.3801.

[116] M. Meyer. "Scientific Instrument SQS". In: *Conceptual Design Report* April (2011). DOI: 10.3204/XFEL.EU/TR-2011-003.

[117] T Mazza, H Zhang, and M Meyer. "Scientific Instrument SQS". In: *Technical Design Report* December (2012). DOI: 10.3204/XFEL.EU/TR-2012-007.

[118] A. E. Siegman. "Defining, measuring, and optimizing laser beam quality". In: *Proc. SPIE 1868, Laser Resonators and Coherent Optics: Modeling, Technology, and Applications*. Ed. by A. Bhowmik. Vol. 1868. 1993, pp. 2–12. DOI: 10.1117/12.150601.

[119] R. Ischebeck et al. "Study of the transverse coherence at the TTF free electron laser". In: *Nuclear Instruments and Methods in Physics Research Section A: Accelerators, Spectrometers, Detectors and Associated Equipment* 507.1-2 (July 2003), pp. 175–180. ISSN: 01689002. DOI: `10.1016/S0168-9002(03)00866-0`.

[120] G. Geloni, V. Kocharyan, and E. Saldin. "Self-seeding scheme for the soft X-ray line at the European XFEL". In: *arXiv.org* February (2012). arXiv: `1202.5209v1`.

[121] W Decking and T Limberg. *European XFEL Post-TDR Description*. Tech. rep. February. Hamburg: European X-Ray Free-Electron Laser Facility GmbH, 2013. URL: `https://docs.xfel.eu/alfresco/d/a/workspace/SpacesStore/7f5974d5-23b7-48e5-a54c-a752b83761bc/TN-2013-004-01\_TDR\_Design\_Changes.pdf`.

[122] Grating Solver Development Company. *Gsolver*. 2012. URL: `http://www.gsolver.com`.

[123] E. Gullikson. *X-Ray database*. Berkeley, California. URL: `http://www.henke.lbl.gov/optical\$\backslash\_\$constants/`.

[124] Nanotech and ESRF. *The ray-tracing program SHADOW*. Wisconsin, 2002. URL: `http://www.esrf.eu/computing/scientific/raytracing/`.

[125] I. Agapov et al. "The Full Potential of the Baseline SASE Undulators of the European XFEL". In: *arXiv.org* April (2014). arXiv: `1404.1177`.

[126] *X-ray Attenuation and Absorption for Materials of Dosimetric Interest*. URL: `http://www.nist.gov/pml/data/index.cfm`.

[127] T. Tanaka and RIKEN SPring-8 Center. *SPECTRA - synchrtron radiation calculation code*. Koto, Japan, 2015. URL: `http://radiant.harima.riken.go.jp/spectra/`.

[128] S. Serkez et al. "Soft x-ray self-seeding simulation methods and their application for the Linac Coherent Light Source". In: *Physical Review Special Topics - Accelerators and Beams* 18.3 (Mar. 2015), p. 030708. ISSN: 1098-4402. DOI: `10.1103/PhysRevSTAB.18.030708`.

[129] R. Ganter and Others. *SwissFEL Conceptual Design Report*. Tech. rep. 10. Paul Scherrer Institut, 2012. URL: `https://www.psi.ch/swissfel/HomeEN/SwissFEL\_CDR\_web\_small.pdf`.

[130] J.-H. Han, H.-S. Kang, and I. S. Ko. "Status of the Pal-Xfel Project". In: *Proceedings of IPAC2012* (2012), pp. 1735–1737. URL: `http://accelconf.web.cern.ch/accelconf/ipac2012/papers/tuppp061.pdf`.

[131] H.-S. Kang, K.-W. Kim, and I. S. Ko. "Current status of PAL_XFEL project". In: *Proceedings of IPAC2014* (2014), pp. 6–8. URL: `http://accelconf.web.cern.ch/AccelConf/IPAC2014/papers/thpro019.pdf`.

[132] J. N. Galayda. "LCLS-II Project". In: *Talk at IPAC 2014* June (2014). URL: http://accelconf.web.cern.ch/accelconf/IPAC2014/talks/tuoca01_talk.pdf.

[133] T. Raubenheimer. "The LCLS-II : A New CW X-ray FEL Facility at SLAC Linac Coherent Light Source Facility". In: *Talk at International FEL Conference, Basel, Switzerland* (2014). URL: http://accelconf.web.cern.ch/AccelConf/FEL2014/talks/web01_talk.pdf.

[134] I Moreno et al. "Teaching Fourier optics through ray matrices". In: *European Journal of Physics* 26.2 (2005), p. 261. URL: http://stacks.iop.org/0143-0807/26/i=2/a=005.

[135] A. E. Siegman. "ABCD-matrix elements for a curved diffraction grating". In: *J. Opt. Soc. Am. A* 2.10 (1985), p. 1793. DOI: 10.1364/JOSAA.2.001793.

[136] A. April and N. McCarthy. "ABCD-matrix elements for a chirped diffraction grating". In: *Optics Communications* 271.2 (2007), pp. 327–331. ISSN: 00304018. DOI: 10.1016/j.optcom.2006.10.049.